Near infrared (NIR) hyperspectral imaging and X-ray computed tomography combined with statistical and multivariate data analysis to study *Fusarium* infection in maize

by

Paul James Williams

Dissertation presented for the degree of *Doctor of Philosophy (Food Science)*

in the Faculty of AgriSciences

at

Stellenbosch University

Supervisor: Prof. Marena Manley
Co-supervisor: Prof. Trevor J Britz
Co-supervisor: Prof. Paul Geladi

March 2013

DECLARATION

By submitting this thesis/dissertation electronically, I declare that the entirety of the work contained therein is my own, original work, that I am the sole author thereof (save to the extent explicitly otherwise stated), that reproduction and publication thereof by Stellenbosch University will not infringe any third party rights and that I have not previously in its entirety or in part submitted it for obtaining any qualification.

Paul James Williams

March 2013

ACKNOWLEDGEMENTS

Firstly I would like to thank our heavenly Father for granting me the aptitude, motivation, health and most importantly, the strength to succeed;

I would like to thank my parents, my sister and Angelique van der Scholtz, for their continual support, love, motivation, patience, encouragement, and understanding throughout this study and especially after we lost Lyle;

A special word of thanks to Angelique for always believing in me, supporting me, encouraging me and insisting that my seminars would be “AWESOME”!

Thank you to Andrew Swarts for being there to offload when work got rough and for words of encouragement! It’s your turn now buddy…

I would like to express my most sincere gratitude to the following people and institutions for their contribution to the successful completion of this study:

My supervisor, Prof. Manley for her professional supervision and guidance, invaluable advice, patience, motivation, confidence in my abilities throughout my postgraduate studies and for her understanding and support during a very difficult time when I lost my younger brother;

My co-supervisor Prof. Britz for his expert advice, guidance, motivation and his enthusiasm for NIR and NIR hyperspectral imaging and its applications in microbiology,

My co-supervisor Prof. Geladi for his expert NIR hyperspectral imaging advice, assisting with interpretation of data and his help with all things Matlab and Chemometrics;

Prof Alvaro Viljoen and Ilze Vermaak (Tshwane University of Technology, Pretoria) for use of the SisuChema instrument;

Prof Altus Viljoen and Lindy Rose (Department of Plant Pathology, Stellenbosch University) for supplying fungal cultures and assisting with spore preparation

Frikkie de Beer, Jakobus Hoffman, Robert Nshimirimana and Lunga Bam (South African Nuclear Energy Cooperation, Pelindaba, South Africa) for: imaging maize kernels with X-ray micro-computed tomography system; data analysis; advice and proof reading the X-ray chapter. Necsa offers free beam time to post-graduate researchers;

The Maize Trust for a bursaries and project funding (2009-2011);

The University of Stellenbosch (Merit Bursary, 2009 - 2011);

The National Research Foundation (NRF) (Scarce Skills Bursary, 2009 - 2012) are hereby acknowledged for financial support (any opinion, findings and conclusions or recommendations

expressed in this material are those of the author(s) and therefore the NRF does not accept any liability in regard thereto);

South African-Swedish Research Partnership Programme Bilateral Agreement, NRF, South Africa (UID 70863) and the Swedish Research Council (VR sida 348-2009-6461) provided funding for exchange of researchers throughout the study;

To ALL the staff and postgraduate students of the Food Science Department, thank you for all the help, advice, encouragement, motivation and support;

Dr. Gunnar Sigge for his advice, motivation, encouragement and for giving me an office for the last two weeks;

Anchen Lombard for assisting with travel arrangements, for frequent coffee breaks, and for being a running buddy (her new addiction!);

Daleen Du Preez for all her help especially with printing credits!

Petro Du Buisson for translating my Abstract to Afrikaans, Baie dankie!

Chisala, Rick Ross, Ng'Andwe and Eben Brooks for totally non-academic chats and all things sport! Gunner for life!

To all my friends who haven't seen me properly for the past four years, I AM DONE!

DEDICATION

This thesis is dedicated to my brother, Lyle Williams, who would have been so proud of this achievement.

May his soul rest in peace.

29-01-1987 to 02-12-2010

For nothing is hidden that will not be made manifest, nor is anything secret that will not be known and come to light.

Luke 8:17

ABSTRACT

Maize (*Zea mays* L.) is used for human and animal consumption in diverse forms, from specialised foods in developed countries, to staple food in developing countries. Unfortunately, maize is prone to infection by different *Fusarium* species that can produce harmful mycotoxins. *Fusarium verticillioides* is capable of asymptomatic infection, where infected kernels show no sign of fungal growth, but are contaminated with mycotoxins. If fungal contamination is not detected early on, mycotoxins can enter the food chain. Rapid and accurate methods are required to detect, identify and distinguish between pathogens to enable swift decisions regarding the fate of a batch or consignment of cereal.

Near infrared (NIR) hyperspectral imaging and multivariate image analysis (MIA) were evaluated to investigate the fungal development in maize kernels over time. When plotting principal component (PC) 4 against PC5, with percentages sum of squares (%SS) 0.49% and 0.34%, three distinct clusters were apparent in the score plot and this was associated with degree of infection. Prominent peaks at 1900 nm and 2136 nm confirmed that the source of variation was due to changes in starch and protein. Variable importance plots (VIP) confirmed the peaks observed in the PCA loading line plots. Early detection of fungal contamination and activity (20 h after inoculation) was possible before visual symptoms of infection appeared.

Using NIR hyperspectral imaging and MIA it was possible to differentiate between species of *Fusarium* associated with maize. It was additionally applied to examine the fungal growth kinetics on culture media. Partial least squares discriminant analysis (PLS-DA) prediction results showed that it was possible to discriminate between species, with *F. verticillioides* the least correctly predicted (between 16-47% pixels correctly predicted). For *F. subglutinans* 78-100% and for *F. proliferatum* 60-80% pixels were correctly predicted. Three prominent bands at 1166, 1380 and 1918 nm were considered to be responsible for the differences between the growth zones. Variations in the bands at 1166 and 1380 nm were correlated with the depletion of carbohydrates as the fungus grew while the band at 1918 nm was a possible indication of spore and new mycelial formation. By plotting the pixels from the individual growth zones as a function of time, it was possible to visualise the emergence and interaction of the growth zones as separate growth profiles.

The microstructure of fungal infected maize kernels was studied over time using high resolution X-ray micro-computed tomography (µCT). The presence of voids and airspaces could be seen in two dimensional (2D) X-ray transmission images and in the three dimensional (3D) tomograms. Clear differences were detected between kernels imaged after 20 and 596 h of inoculation. This difference in voids as the fungus progressed showed the effect of fungal damage on the microstructure of the maize kernels.

Imaging techniques are important for rapid, accurate and objective evaluation of products for quality and safety. NIR hyperspectral imaging offers rapid chemical evaluation of samples in 2D

images while µCT offers 3D microstructural information. By combining these image techniques more value was added and this led to a comprehensive evaluation of *Fusarium* infection in maize.

UITTREKSEL

Mielies (*Zea mays* L.) word in verskeie vorms deur mens en dier verbruik, van gespesialiseerde voedsel in ontwikkelde lande, tot stapelvoedsel in ontwikkelende lande. Ongelukkig is mielies onderhewig aan besmetting deur verskeie *Fusarium* spesies wat skadelike mikotoksiene kan produseer. *Fusarium verticilloioides* is in staat tot asimptomatiese infeksie waar die besmette pit geen teken van fungusgroei toon nie, maar (reeds) met mikotoksiene besmet is. Indien fungusbesmetting nie vroegtydig opgespoor word nie, kan mikotoksiene die voedselketting betree. Vinnige en akkurate metodes word benodig om patogene op te spoor, te identifiseer en ook om onderskeid tussen patogene te tref om sodoende (effektiewe) besluite aangaande die gebruik van ‘n lot of besending graan te neem.

Naby-infrarooi (NIR) hiperspektrale beelding en meerveranderlike beeld ontleding (MIA) is geëvalueer om fungusontwikkeling in mieliepitte oor tyd te ondersoek. Wanneer hoofkomponent (PC) 4 teenoor PC5 gestip word, met persentasies som van kwadrate (%SS) 0.49% en 0/34%, is drie afsonderlike groepein die telling grafiek waargeneem. Dit is geassosieer met die graad van besmetting. Prominente pieke by 1900 nm en 2136 nm het bevestig dat veranderinge in stysel en proteïene die bron van die variasie was. Veranderlike belangrikheidsgrafieke (VIP) het die pieke wat in die PCA beladingslyngrafieke waargeneem is, bevestig. Vroegtydige opsporing (bespeuring) van fungusbesmetting en aktiwiteit (20 h na inokulasie) was moontlik voor visuele besmettingsimptome verskyn het.

Onderskeid tussen *Fusarium* spesies wat met mielies geassosieer word, was moontlik deur gebruik te maak van NIR hiperspektrale beelding en MIA. Dit is bykomend toegepas om fungusgroeikinetika op kwekingsmedia te bestudeer. Parsiële kleinste kwadrate diskriminantanalise (PLS-DA) voorspellingsresultate het getoon dat dit moontlik was om tussen spesies te onderskei, met *F. verticillioides* die minste korrek voorspel (tussen 19-47% beeldelemente korrek voorspel). Vir *F. subglutinans* is 78-100% en vir *F. proliferatum* is 60-80% beeldelemente korrek voorspel. Drie prominente bande by 1166, 1380 en 1918 nm is oorweeg as oorsaak vir die verskille tussen die groeisones. Variasies in die bande by 1166 en 1380 nm is gekorreleer met die vermindering van koolhidrate soos die fungus groei, terwyl die band by 1918 nm ‘n moontlike aanduiding van spoor en nuwe miseliale vorming is. Deur die beeldelemente van die individuele groeisones as ‘n funksie van tyd te stip, was dit moontlik om die verskyning en interaksie van die groeisones as aparte groeiprofiele te visualiseer.

Hoë-resolusie X-straal mikro-berekende tomografie (µCT) is gebruik om die mikrostruktuur van fungusbesmette mieliepitte oor tyd te ondersoek. Die voorkoms van leemtes en lugruimtes kon in die twee-dimensionele (2D) X-straal transmissie beelde en in die drie-dimensionele (3D) tomogramme gesien word. Duidelike verskille is waargeneem tussen pitte wat na 20 en 596 h na inokulasie verbeeld is. Hierdie verskil in leemtes soos die fungus vorder, het die effek van fungusskade op die mikrostruktuur van mieliepitte getoon.

Beeldingstegnieke is belangrik vir vinnige, akkurate en objektiewe evaluasie van produkte vir kwaliteit en veiligheid. NIR hiperspektrale beelding bied vinnige chemiese evaluering van monsters in 2D beelde, terwyl µCT 3D mikrostrukturele inligting gee. Meer waarde is toegevoeg deur hierdie beeldingstegnieke te kombineer en dit het gelei tot ‘n omvangryke evaluering van *Fusarium* besmetting in mielies.

TABLE OF CONTENTS

LIST OF FIGURES

LIST OF TABLES

LIST OF ABBREVIATIONS USED

2D:	two dimensional
3D:	three dimensional
ATP:	Adenosine triphosphate
CFU:	colony forming unit
CNS:	control non-sterilised
CNSD:	control non-sterilised germ down
CNSU:	control non-sterilised germ up
CS:	control sterilised
CSD:	control sterilised down
CSU:	control sterilised up
D:	germ down
dH_2O:	distilled water
DON:	Deoxynivalenol
ELISA:	enzyme linked immunosorbent assay
FT-NIR:	Fourier transform near infrared
GLCM:	grey level co-occurrence matrix
HgCdTe:	mercury-cadmium-telluride
LDA:	linear discriminant analysis
MCT:	mercury-cadmium-telluride
MIA:	multivariate image analysis
NaOCl:	sodium hypochlorite
NIR:	near infrared
NS:	non-sterilised
NSD:	non-sterilised germ down
NSU:	non-sterilised germ up
PC:	principal component
PCA:	principal component analysis
PCR:	polymerase chain reaction
PDA:	potato dextrose agar
PGP:	prism grating prism
PLS:	partial least squares
PLS-DA:	partial least squares discriminant analysis
Q^2:	coefficient of determination for prediction
RIA:	radioimmunoassay
RMSEP:	root mean square error of prediction
ROI:	region of interest
S:	sterilised

SD:	sterilised germ down
SEM:	scanning electron microscopy
SEP:	standard error of prediction
SNV:	standard normal variate
SS:	sum of squares
SS:	sum of squares
SU:	sterilised germ up
SVM:	support vector machines
SWIR:	short wave infrared
TEM:	transmission electron microscopy
U:	germ up
VIP:	variable importance plot
vis-NIR:	visible and near infrared
µCT:	micro-computed tomography

CHAPTER 1
INTRODUCTION

Maize (*Zea mays* L.), a dietary staple in Africa, is an important crop grown throughout the world (Schierbaum, 2007; Wagacha & Muthomi, 2008; Hellin *et al.*, 2012). It is used for human consumption in diverse forms, from specialised foods to staple food, as well as for animal feed (Hotz & Gibson, 2001; Malvar *et al.*, 2008; Lidia *et al.*, 2012). Unfortunately maize is commonly associated with a number of *Fusarium* species, predominantly *F. verticillioides, F. proliferatum* and *F. subglutinans* (Sydenham *et al.*, 1990; Fandohan *et al.*, 2003; Boutigny *et al.*, 2012). The presence of these pathogens is often associated with high incidence of mycotoxins, particularly fumonisins (Rheeder *et al.*, 2002). Fumonisins have cancer-promoting activity, and have been shown to cause leukoencephalomalacia in horses, pulmonary edema syndrome in pigs, and liver cancer in rats (Gelderblom *et al.*, 1988; Gelderblom *et al.*, 2001a; Gelderblom *et al.*, 2001b; Marasas, 2001; Gelderblom *et al.*, 2004). It is also believed to be associated with squamous carcinoma of the oesophagus in humans (Isaacson, 2005). Testing for these pathogens is thus necessary.

Conventional methods for enumeration and the identification of microorganisms to the species level can take as long as two weeks before the fate of a cereal batch or sample is known (Velusamy *et al.*, 2010). These methods are time-consuming as they require specialised growth media, staining and inspection using microscopy; leading to destruction of the sample and tedious sample preparation. Rapid, yet accurate methods and techniques are required to ensure products adhere to food safety regulations and are safe for human and animal consumption (Fung, 2000).

Near infrared (NIR) spectroscopy is a spectroscopic technique that utilises the part of the electromagnetic spectrum between the visible and infrared regions between 700-2500 nm (Wahr *et al.*, 1996; Pasquini, 2003; Cen & He, 2007; Roggo *et al.*, 2007). The technique is based on the measurement of bond vibrations between the atoms of organic molecules consisting mainly of C-H, C=O, O-H and N-H. NIR spectroscopy has been used for non-destructive analysis of various constituents of food materials (Scotter, 1997; Cen & He, 2007) and has been reported as an analytical technique for mycotoxin detection in cereals (Lattanzio *et al.*, 2009). Fumonisins were detected in single maize kernels infected with *Fusarium verticillioides* using reflectance and transmittance NIR spectroscopy (Dowell *et al.*, 2002). NIR spectroscopy is limited in the spatial dimension offering no information regarding the location of the constituent or contaminant investigated. Measurements are made on only a small area of the sample that might not even cover an entire kernel, and averaged. Thus, the entire sample is not necessarily measured and the result given as a single spectrum. In contrast, NIR hyperspectral imaging is a technique capable of incorporating localisation, thus measuring entire samples, rapidly and accurately (Gowen *et al.*, 2007; Boldrini *et al.*, 2012). Multiple single kernels can also be analysed simultaneously.

NIR hyperspectral imaging is a form of spectral imaging that captures images at many wavelength bands in the NIR region (Koehler *et al.*, 2002; Geladi *et al.*, 2004). NIR hyperspectral

images or hypercubes are composed of hundreds of neighbouring wavebands for each spatial position of an object studied where each pixel in an NIR hyperspectral image contains the spectrum of that exact location (Burger & Geladi, 2006; Gowen *et al.*, 2007; Boldrini *et al.*, 2012; Elmasry *et al.*, 2012). Using multivariate image analysis (MIA) to analyse the hypercubes, the composition of a sample can be characterised by the ensuing spectra that acts as finger prints.

NIR hyperspectral imaging has proven to be valuable for applications particularly in the food, pharmaceutical and agricultural fields (Gowen *et al.*, 2007; Gowen *et al.*, 2008; Elmasry *et al.*, 2012). It has been reported as a food safety inspection tool (Feng & Sun, 2012) and has been recognised for its potential use in microbiological applications (Yao *et al.*, 2008; Yoon *et al.*, 2010; Feng *et al.*, 2012). The rapid and non-destructive nature of NIR hyperspectral imaging makes it suitable for simulation studies and implementation in production lines (online, at-line).

In an earlier study, NIR hyperspectral imaging and MIA was used to distinguish between *Fusarium* infected and healthy maize kernels (Williams *et al.*, 2010). Classification accuracies of 73% and 86% were reported for a staring imager (960-1662 nm) and a pushbroom system (1000-2498 nm), respectively. *F. verticillioides* is capable of asymptomatic infection where the kernel portrays no visible signs of infection; however these kernels are often already contaminated with fumonisins. These kernels frequently go unnoticed into the food chain. Detection at this early stage is important.

A number of fungal species were investigated to distinguish uninfected maize kernels from infected kernels 48 h after inoculation by hyperspectral imaging in the spectral range 400-1000 nm (Del Fiore *et al.*, 2010). Differentiation was, however, only possible for kernels infected with *Aspergillus niger* and *A. flavus*. The spectral range used may have contributed to this; using the full NIR spectrum may give additional chemical information for better detection of infected kernels. *Fusarium* infection in maize is a global concern and accurate and rapid methods for early detection of contaminated kernels are needed.

Once it has been determined that maize kernels are contaminated with *Fusarium* spp., it is also important to identify the species present. Of the three species commonly associated with maize contamination, *F. verticillioides* and *F. proliferatum* produce the highest concentrations of fumonisins while *F. subglutinans* produces much lower concentrations (Rheeder *et al.*, 2002). Presently *Fusarium* spp. are identified microbiologically which involves plating out on appropriate growth medium prior to further analyses such as staining and inspection using microscopy. If an organism cannot be identified using the culture techniques, samples are often evaluated with molecular techniques such as polymerase chain reaction (PCR). Culture techniques are thus a necessary step prior to the more complex PCR analysis. An alternative to PCR is thus required to identify between pathogens on culture media to enable immediate decisions regarding the fate of the samples.

Campylobacter colonies were detected on growth media with detection accuracies between 97 and 99% after 24 h of incubation using NIR hyperspectral imaging in the 400-900 nm spectral

range (Yoon *et al.*, 2010). Classification of *Campylobacter* and non- *Campylobacter* colonies was based on a band ratio algorithm at 426 and 458 nm. In a similar study, the ability to differentiate between five toxigenic fungi on growth media with a classification rate of 97.7% was reported (Yao *et al.*, 2008). All five fungi could be classified using three narrow bands centred at 743, 458 and 541 nm. The latter two wavelengths are part of the visible spectrum, as are the wavelengths indicated in the study of Yoon et al. (2010). Since the fungi studied differed in colour, it is possible the differentiation was based on colour differences observed in the colonies.

On potato dextrose agar *F. verticillioides, F. proliferatum* and *F. subglutinans* produce white mycelium that may become grey or violet as the colony ages (Desjardins, 2006). The colour of the colony under surface varies from white to orange and violet. The same change in colour will, however, be observed for all species. A distinction based on colour cannot be made and a spectral range that is not reliant on colour is required. Using the NIR range to image these fungi on culture media would be ideal as chemical information regarding growth and development can be determined. A question still unanswered is whether NIR hyperspectral imaging in the 1100-2500 nm spectral range would permit accurate differentiation between the three *Fusarium* spp. as well as characterisation of growth kinetics on culture media.

In instances where contaminants are located deep within a sample, the long, low energy levels of wavelengths (700-2500 nm) in the NIR region are not adequate and shorter, high energy wavelengths are required. X-rays have a wavelength in the range of 0.01 to 10 nm and are able to traverse through samples (Kotwaliwale *et al.*, 2011).

As a technique predominantly used for medical applications, X-rays are now more commonly being used for internal evaluation of food and agricultural products (Haff & Toyofuku, 2008; Kotwaliwale *et al.*, 2011). Similar to NIR hyperspectral imaging, X-ray imaging offers a rapid, non-destructive means of evaluating samples. Recently an automatic scanner to detect pest infestation in agricultural products has been developed (Chuang *et al.*, 2011). For a more detailed study of the internal microstructure of samples X-ray computed tomography (μCT) is used (Laverse *et al.*, 2012). The sample is rotated 180 or 360 degrees and multiple slices are progressively imaged as the object is rotated through the X-rays (Haff & Toyofuku, 2008; Kotwaliwale *et al.*, 2011). These slices are mathematically reconstructed to form three dimensional (3D) images (Kak & Slaney, 1988). This form of imaging not only allows for the evaluation of the internal structure of samples, but also permits virtual exploration non-destructively.

X-ray imaging was used for the detection of fungal infection in wheat with accuracies of between 92.2-98.9% (Narvankar *et al.*, 2009). A number of image features were extracted and used to classify kernels as infected or non-infected. A study on the detection of internal wheat seed infestation by *Rhyzopertha dominica* using X-ray imaging, reported classification accuracies of up to 98% (Karunakaran *et al.*, 2004). The differentiation between infested and non-infested wheat kernels was evident in the X-ray images and appeared as density variations. X-ray computed tomography has been used to investigate the microstructure of processed meat and the

differences between the microstructures of a variety of salamis and their fat distributions have been reported (Frisullo *et al.*, 2009). In a similar study, the distribution of intramuscular fat in beef muscles was investigated (Frisullo *et al.*, 2010). Correlation coefficients of between 0.92 and 0.99 were obtained when comparing percentage object volume determined with µCT to the soxhlet extraction method for intramuscular fat. Hidden information is revealed by the use of X-ray imaging and X-ray computed tomography for non-destructive internal and microstructural evaluation of food and agricultural produce.

Microstructural changes in *Fusarium* infected maize kernels have been reported using an array of destructive scanning electron (SEM) and transmission electron microscopy (TEM) techniques (Duncan & Howard, 2010). The non-destructive nature of µCT makes it ideal to investigate the internal structure of *Fusarium* infected maize kernels over time.

The aim of this dissertation was to study *Fusarium* infection in whole maize kernels using near infrared (NIR) hyperspectral imaging and µCT combined with statistical and multivariate data analysis. Specific objectives were to:

- investigate the fungal development in maize kernels over time using NIR hyperspectral imaging and multivariate data analysis;
- differentiate between species and strains of the genus *Fusarium* associated with maize;
- examine the growth characteristics of three *Fusarium* species by NIR hyperspectral imaging and multivariate image analysis; and
- investigate the change in the internal structure of maize kernels infected with *F. verticillioides* studied over time with µCT.

References

Boldrini, B., Kessler, W., Rebner, K. & Kessler, R. (2012). Hyperspectral imaging: a review of best practice, performance and pitfalls for inline and online applications. *Journal of Near Infrared Spectroscopy*, **20**, 438-508.

Boutigny, A.L., Beukes, I., Small, I., Zühlke, S., Spiteller, M., Van Rensburg, B.J., Flett, B. & Viljoen, A. (2012). Quantitative detection of *Fusarium* pathogens and their mycotoxins in South African maize. *Plant Pathology*, **61**, 522-531.

Burger, J. & Geladi, P. (2006). Hyperspectral NIR imaging for calibration and prediction: a comparison between image and spectrometer data for studying organic and biological samples. *Analyst*, **131**, 1152-1160.

Cen, H.Y. & He, Y. (2007). Theory and application of near infrared reflectance spectroscopy in determination of food quality. *Trends in Food Science and Technology*, **18**, 72-83.

Chuang, C.-L., Ouyang, C.-S., Lin, T.-T., Yang, M.-M., Yang, E.-C., Huang, T.-W., Kuei, C.-F., Luke, A. & Jiang, J.-A. (2011). Automatic X-ray quarantine scanner and pest infestation detector for agricultural products. *Computers and Electronics in Agriculture*, **77**, 41-59.

Del Fiore, A., Reverberi, M., Ricelli, A., Pinzari, F., Serranti, S., Fabbri, A.A., Bonifazi, G. & Fanelli, C. (2010). Early detection of toxigenic fungi on maize by hyperspectral imaging analysis. *International Journal of Food Microbiology*, **144**, 64-71.

Desjardins, A.E. (2006). Selected Mycotoxigenic *Fusarium* Species. In: *Fusarium Mycotoxins: Chemistry, Genetics and Biology*. Pp. 192-194. St. Paul, Minnesota U.S.A: The American Phytopathological Society.

Dowell, F.E., Pearson, T.C., Maghirang, E.B., Xie, F. & Wicklow, D.T. (2002). Reflectance and transmittance spectroscopy applied to detecting fumonisin in single corn kernels infected with *Fusarium verticillioides*. *Cereal Chemistry*, **79**, 222-226.

Duncan, K.E. & Howard, R.J. (2010). Biology of maize kernel infection by *Fusarium verticillioides*. *Molecular Plant-Microbe Interactions*, **23**, 6-16.

Elmasry, G., Kamruzzaman, M., Sun, D.W. & Allen, P. (2012). Principles and applications of hyperspectral imaging in quality evaluation of agro-food products: a review. *Critical Reviews in Food Science and Nutrition*, **52**, 999-1023.

Fandohan, P., Hell, K., Marasas, W. & Wingfield, M. (2003). Infection of maize by *Fusarium* species and contamination with fumonisin in Africa. *African Journal of Biotechnology*, **2**, 570-579.

Feng, Y.-Z., ElMasry, G., Sun, D.-W., Walsh, D. & Morcy, N. (2012). Near-infrared hyperspectral imaging and partial least squares regression for rapid and reagentless determination of *Enterobacteriaceae* on chicken fillets. *Food Chemistry*, http://dx.doi.org/10.1016/j.foodchem.2012.1011.1040.

Feng, Y.-Z. & Sun, D.-W. (2012). Application of hyperspectral imaging in food safety inspection and control: a review. *Critical Reviews in Food Science and Nutrition*, **52**, 1039-1058.

Frisullo, P., Laverse, J., Marino, R. & Nobile, M.A.D. (2009). X-ray computed tomography to study processed meat microstructure. *Journal of Food Engineering*, **94**, 283-289.

Frisullo, P., Marino, R., Laverse, J., Albenzio, M. & Del Nobile, M.A. (2010). Assessment of intramuscular fat level and distribution in beef muscles using X-ray microcomputed tomography. *Meat Science*, **85**, 250-255.

Fung, D.Y.C. (2000). Rapid methods and automation in microbiology: a review. *Irish Journal of Agricultural and Food Research*, **39**, 301-307.

Geladi, P., Burger, J. & Lestander, T. (2004). Hyperspectral imaging: calibration problems and solutions. *Chemometrics and Intelligent Laboratory Systems*, **72**, 209-217.

Gelderblom, W.C.A., Abel, S., Smuts, C.M., Marnewick, J., Marasas, W.F.O., Lemmer, E.R. & Ramljak, D. (2001a). Fumonisin induced hepatocarcinogenesis: mechanisms related to cancer initiation and promotion. *Environmental Health Perspectives*, **109**, 291-300.

Gelderblom, W.C.A., Jaskiewicz, K., Marasas, W.F.O., Thiel, P.G., Horak, R.M., Vleggaar, R. & Kriek, N.P.J. (1988). Fumonisins novel mycotoxins with cancer-promoting activity produced by *Fusarium moniliforme*. *Applied and Environmental Microbiology*, **54**, 1806-1811.

Gelderblom, W.C.A., Rheeder, J.P., Leggott, N., Stockenstrom, S., Humphreys, J., Shephard, G.S. & Marasas, W.F.O. (2004). Fumonisin contamination of a corn sample associated with the induction of hepatocarcinogenesis in rats-role of dietary deficiencies. *Food and Chemical Toxicology*, **42**, 471-479.

Gelderblom, W.C.A., Seier, J.V., Snijman, P.W., Van Schalkwyk, D.J., Shephard, G.S. & Marasas, W.F.O. (2001b). Toxicity of culture material of *Fusarium verticillioides* strain MRC 826 to nonhuman primates. *Environmental Health Perspectives*, **109**, 267-276.

Gowen, A.A., O'Donnell, C.P., Cullen, P.J. & Bell, S.E.J. (2008). Recent applications of chemical imaging to pharmaceutical process monitoring and quality control. *European Journal of Pharmaceutics and Biopharmaceutics*, **69**, 10-22.

Gowen, A.A., O'Donnell, C.P., Cullen, P.J., Downey, G. & Frias, J.M. (2007). Hyperspectral imaging: an emerging process analytical tool for food quality and safety control. *Trends in Food Science and Technology*, **18**, 590-598.

Haff, R. & Toyofuku, N. (2008). X-ray detection of defects and contaminants in the food industry. *Sensing and Instrumentation for Food Quality and Safety*, **2**, 262-273.

Hellin, J., Shiferaw, B., Cairns, J.E., Reynolds, M., Ortiz-Monasterio, I., Banziger, M., Sonder, K. & La Rovere, R. (2012). Climate change and food security in the developing world: potential of maize and wheat research to expand options for adaptation and mitigation. *Journal of Development and Agricultural Economics*, **4**, 311-321.

Hotz, C. & Gibson, R.S. (2001). Assessment of home-based processing methods to reduce the phytate content and phytate/zinc molar ratio of white maize (*Zea mays*). *Journal of Agricultural and Food Chemistry*, **49**, 692-698.

Isaacson, C. (2005). The change of the staple diet of black South Africans from sorghum to maize (corn) is the cause of the epidemic of squamous carcinoma of the oesophagus. *Medical Hypotheses*, **64**, 658-660.

Kak, A.C. & Slaney, M. (1988). *Computerized tomographic imaging.* Pp. 344. New York: The Institute of Electrical and Electronics Engineers, Inc.

Karunakaran, C., Jayas, D.S. & White, N.D.G. (2004). Detection of internal wheat seed infestation by *Rhyzopertha dominica* using X-ray imaging. *Journal of Stored Products Research*, **40**, 507-516.

Koehler, F.W., Lee, E., Kidder, L.H. & Lewis, N.E. (2002). Near infrared spectroscopy: the practical chemical imaging solution. *Spectroscopy Europe*, **14**, 12-19.

Kotwaliwale, N., Singh, K., Kalne, A., Jha, S.N., Seth, N. & Kar, A. (2011). X-ray imaging methods for internal quality evaluation of agricultural produce. *Journal of Food Science and Technology*, http://dx.doi.org/10.1007/s13197-13011-10485-y.

Lattanzio, V.M.T., Pascale, M. & Visconti, A. (2009). Current analytical methods for trichothecene mycotoxins in cereals. *TRAC Trends in Analytical Chemistry*, **28**, 758-768.

Laverse, J., Mastromatteo, M., Frisullo, P. & Del Nobile, M.A. (2012). X-ray microtomography to study the microstructure of mayonnaise. *Journal of Food Engineering*, **108**, 225-231.

Lidia, E.A., Ellis, D.D., Duvick, S., Goggi, A.S., Hurburgh, C.R. & Gardner, C.A. (2012). Feasibility of near infrared spectroscopy for analyzing corn kernel damage and viability of soybean and corn kernels. *Journal of Cereal Science*, **55**, 160-165.

Malvar, R.A., Revilla, P., Moreno-Gonzalez, J., Butron, A., Sotelo, J. & Ordas, A. (2008). White maize: genetics of quality and agronomic performance. *Crop Science*, **48**, 1373-1381.

Marasas, W.F.O. (2001). Discovery and occurence of the fumonisins: a historical perspective. *Environmental Health Perspectives*, **109**, 239-243.

Narvankar, D.S., Singh, C.B., Jayas, D.S. & White, N.D.G. (2009). Assessment of soft X-ray imaging for detection of fungal infection in wheat. *Biosystems Engineering*, **103**, 49-56.

Pasquini, C. (2003). Near Infrared Spectroscopy: fundamentals, practical aspects and analytical applications. *Journal of the Brazilian Chemical Society*, **14**, 198-219.

Rheeder, J.P., Marasas, W.F.O. & Vismer, H.F. (2002). Production of fumonisin analogs by *Fusarium* species. *Applied and Environmental Microbiology*, **68**, 2101-2105.

Roggo, Y., Chalus, P., Maurer, L., Lema-Martinez, C., Edmond, A. & Jent, N. (2007). A review of near infrared spectroscopy and chemometrics in pharmaceutical technologies. *Journal of Pharmaceutical and Biomedical Analysis*, **44**, 683-700.

Schierbaum, F. (2007). World corn production, uses and ending stocks: recorded figures for fiscal years 2004/05 and 2005/06. *Starch-Starke*, **59**, 192-195.

Scotter, C.N.G. (1997). Non-destructive spectroscopic techniques for the measurement of food quality. *Trends in Food Science and Technology*, **8**, 285-292.

Sydenham, E.W., Gelderblom, W.C.A., Thiel, P.G. & Marasas, W.F.O. (1990). Evidence for the natural occurrence of fumonisin-B1, a mycotoxin produced by *Fusarium moniliforme*, in corn. *Journal of Agricultural and Food Chemistry*, **38**, 285-290.

Velusamy, V., Arshak, K., Korostynska, O., Oliwa, K. & Adley, C. (2010). An overview of foodborne pathogen detection: in the perspective of biosensors. *Biotechnology Advances*, **28**, 232-254.

Wagacha, J.M. & Muthomi, J.W. (2008). Mycotoxin problem in Africa: current status, implications to food safety and health and possible management strategies. *International Journal of Food Microbiology*, **124**, 1-12.

Wahr, J.A., Tremper, K.K., Samra, S. & Delpy, D.T. (1996). Near-Infrared spectroscopy: theory and applications. *Journal of Cardiothoracic and Vascular Anesthesia*, **10**, 406-418.

Williams, P., Manley, M., Fox, G. & Geladi, P. (2010). Indirect detection of *Fusarium verticillioides* in maize (*Zea mays* L.) kernels by near infrared hyperspectral imaging. *Journal of Near Infrared Spectroscopy*, **18**, 49-58.

Yao, H., Hruska, Z., Kincaid, R., Brown, R. & Cleveland, T. (2008). Differentiation of toxigenic fungi using hyperspectral imagery. *Sensing and Instrumentation for Food Quality and Safety*, **2**, 215-224.

Yoon, S., Lawrence, K., Line, J., Siragusa, G., Feldner, P., Park, B. & Windham, W. (2010). Detection of *Campylobacter* colonies using hyperspectral imaging. *Sensing and Instrumentation for Food Quality and Safety*, **4**, 35-49.

CHAPTER 2
LITERATURE REVIEW

Introduction

Cereals are the staple diet of most of the world's population and also a major source of dietary protein (Moore *et al.*, 1995; reviewed by Shewry, 2007). Unfortunately they sustain the growth of different unwanted and sometimes harmful fungi (Firrao *et al.*, 2010). In addition to the economic losses due to spoilage, fungal growth is associated with the production of mycotoxins that are toxic and carcinogenic to humans and animals (Chu, 1991; Fung & Clark, 2004). Losses of up to US$ 2.7 billion caused by *Fusarium* head blight was reported for the period 1998-2000 for only wheat and barley (Nganje *et al.*, 2004). In an economic model developed (reviewed by Wu, 2007), it was estimated that in a normal year (without a significant *Fusarium* ear rot outbreak), losses due to fumonisin in animal feed would total US$ 1–20 million. In a year with significant *Fusarium* ear rot outbreak, losses would total US$ 31–46 million.

Maize is one of the main dietary staple foods in the world (Schierbaum, 2007; reviewed by Hellin *et al.*, 2012). Together with rice, maize and wheat provide at least 30% of the food calories to more than 4.5 billion people in 100 developing countries (reviewed by Hellin *et al.*, 2012). Maize is used for human consumption in diverse forms, from specialised foods in developed countries, to staple food in undeveloped countries (Hotz & Gibson, 2001; Malvar *et al.*, 2008). Besides being used for human consumption, maize is also used for animal feed (Lidia *et al.*, 2012). Unfortunately maize is commonly associated with and prone to infection by a number of *Fusarium* species, predominantly *F. verticillioides, F. proliferatum* and *F. subglutinans* (Sydenham *et al.*, 1990; Fandohan *et al.*, 2003; Van Rensburg, 2006). The presence of these pathogens is often associated with the high incidence of mycotoxins, specifically fumonisins (Rheeder *et al.*, 2002). Fumonisins have cancer-promoting activity, and have been shown to cause leukoencephalomalacia in horses, pulmonary edema syndrome in pigs, and liver cancer in rats (Gelderblom *et al.*, 1988; Gelderblom *et al.*, 2001a; Gelderblom *et al.*, 2001b; Marasas, 2001; Gelderblom *et al.*, 2004)

Conventional methods for enumeration and the identification of microorganisms to the species level can take as long as two weeks before the fate of a cereal batch or sample is known (reviewed by Velusamy *et al.*, 2010). These methods are time-consuming; they require specialised growth media, staining and inspection using microscopy, leading to destruction of the sample and tedious sample preparation. Rapid, yet accurate methods and techniques are required to ensure products adhere to food safety regulations and are safe for human and animal consumption (Fung, 2000).

Near infrared (NIR) spectroscopy is a proven technique for non-destructive analysis of various constituents of food materials (Scotter, 1990; reviewed by Cen & He, 2007). Although high in spectral resolution, traditional NIR is limited in the spatial dimension, offering no information regarding the location of the constituent or contaminant investigated. Measurements are made

across a small area on the sample and averaged. In contrast NIR hyperspectral imaging is a technique capable of incorporating localisation, thus measuring entire samples, rapidly and accurately (reviewed by Gowen *et al.*, 2007; Boldrini *et al.*, 2012).

Some of the most widely known conventional microbiological techniques used in food microbiology are discussed in this literature review. The advantages as well as the drawbacks are addressed, and in doing so the requirement for rapid, non-destructive techniques is recognised. Then the use of rapid, non-destructive spectroscopic techniques such NIR spectroscopy and NIR hyperspectral imaging and multivariate image analysis is discussed. This is followed by some applications regarding the use of NIR and NIR hyperspectral imaging on food and agricultural products. Finally, the use of more sophisticated methods such as X-ray imaging and X-ray micro-computed tomography is outlined with applications on food and agricultural products. An important method to extract useful information from images, image analysis, is described with reference to image texture and grey level co-occurrence matrices. This is all done with special mention to work regarding fungal infected cereal grains.

Conventional and current microbiological techniques

Food safety mostly concerns the analysis of food produce for the presence of undesirable microorganisms. This involves the detection and identification of bacteria and fungi and their associated toxins. Thus, microbiology and specifically food microbiology has become an essential facet in the food industry and food related research. Techniques range from simple methods such as standard plate counts or aerobic plate counts to complex approaches such as Adenosine triphosphate (ATP) bioluminescence (Gracias & McKillip, 2004). Although ATP bioluminescence is regarded as rapid since results are obtained in less than 15 min, sample preparation is cumbersome and involves construction of standard curves with dilutions of bacteria of known concentrations. Only then can the level of contamination be assessed in a food sample or on a contact surface. The conventional culture techniques, although laborious, have been and are still used in the food industry and food related research because they offer cost-effectiveness, easy use and familiarity (Gracias & McKillip, 2004).

Culture and colony techniques

There are numerous bacteriological media used for detection, enumeration and identification of foodborne microbes and pathogens from various products (McLandsborough, 2005; Merck, 2007). Although not as advanced as molecular techniques and biosensor technology, culture methods remain reliable and accurate for foodborne pathogen detection and give both qualitative and quantitative information on the number and the nature of the microorganisms present in a food sample (de Boer & Beumer, 1999; Gracias & McKillip, 2004; reviewed by Velusamy *et al.*, 2010). They remain standard techniques and reference methods implemented in the food industry for quality and safety control management, and are frequently used for the detection, isolation and enumeration of various organisms from food and agricultural products such as milk (Hayes *et al.*,

1986), poultry (Schrank *et al.*, 2001) and maize (Alborch *et al.*, 2010). Over the years there have been improvements to conventional techniques, making them more selective and thus suited for isolating particular pathogens (Fung, 2000).

Selective media

Various selective plating media are available for foodborne pathogens such as *Listeria* (Farber & Peterkin, 1991), *Staphylococcus aureus* (Baird & Lee, 1995), yeasts (Beuchat, 1993), *Bacillus cereus* (van Netten & Kramer, 1992) and *Fusarium* (Andrews & Pitt, 1986; Thrane, 1996; Vujanovic *et al.*, 2002). An improvement in the detection of *L. monocytogenes* by the addition of a "new" selective media to standard isolation procedures has been described to enhance the detection ratio and reduce time and cost of analysis (Vlaemynck *et al.*, 2000). Recently a number of commercially available and custom made media was tested for their ability to support growth of *Escherichia coli* O157:H7, *L. monocytogenes*, *Salmonella enterica* and *Yersinia enterocolitica* (Gehring *et al.*, 2012). The growth media evaluated were capable of enriching the organisms to *ca.* 1×10^5 in a mixed culture at 30°C for 18 h. This was considered significant, since it is within the detection limits of rapid molecular and immunological methods.

Although culturing and plating methods are sensitive and selective, they are time-consuming. Detection can take several days or several weeks depending on the species to be isolated (Deisingh & Thompson, 2002). In addition, sample and media preparation, inoculation of plates, colony counting and biochemical characterisation makes these techniques labour intensive and tedious. These are notable disadvantages to the food industry, where rapid information on the possible presence of pathogens on raw materials and finished products is essential.

Immunological methods

Immunological methods are generally used for the determination of microbial contamination of food products (Candlish, 1991; reviewed by Mandal *et al.*, 2011). Due to the specific nature and high sensitivity of the antibody/antigen reaction, these techniques are useful for routine microbiological analysis of foods. Four types of immunoassays have been reported: agglutination, radioimmunoassay (RIA), enzyme linked immunosorbent assay (ELISA) and affinity chromatography (Candlish, 1991; reviewed by Sidari & Caridi, 2011). Of these, ELISA is by far the most popular and frequently used. It has been extensively used for detection of *Salmonella* in food samples (Beumer *et al.*, 1991; Feng, 1997). These and other immunological methods have been reported (Notermans & Wernars, 1991; Swaminathan & Feng, 1994; Feng, 1997; Deisingh & Thompson, 2002) to be used to detect the presence of moulds in fruits, vegetables and grains (Notermans & Heuvelman, 1985), *Aspergillus parasiticus* in cereals (Tsai & Yu, 1999) and *Fusarium* species in maize corn (Meirelles *et al.*, 2006). Immunological methods have been used to detect foodborne pathogens and the toxins they produce (Hansen, 1990; Notermans & Wernars, 1991). Deoxynivalenol (DON) and fumonisin concentrations have been determined in maize using

ELISA (Pleadin *et al.*, 2012) where correlations coefficients of 0.97 and 0.93 were reported for DON and fumonisins, respectively, using two ELISA kits from different manufacturers.

These methods are beneficial in that they are rapid, sensitive and organism specific. They are not just capable of detecting pathogens, but also detecting and quantifying the toxins they produce. In spite of this, these methods lack the ability to detect pathogens in real-time (Velusamy *et al.*, 2010). Possible problems that may arise are: low sensitivity of assays, low affinity of antibody to pathogen or other analyte measured and interference from contaminants.

Polymerase chain reaction (PCR)

In PCR, target DNA or parts thereof, are amplified in the presence of species specific primers, allowing for high-sensitivity recognition of pathogens (Candrian, 1995; Olsen *et al.*, 1995; Scheu *et al.*, 1998; Elmerdahl Olsen, 2000). As an assay for food microbiology, PCR has been comprehensively implemented and investigated. It has been successfully utilised for the detection of *L. monocytogenes* in food (Niederhauser *et al.*, 1992; Bansal, 1996). A fluorogenic PCR assay was effectively evaluated for the detection of *Salmonella* species in chicken, milk and ground beef (Chen *et al.*, 1997). In addition, a nested-PCR method was developed for the detection of *Shigella* spp. in food (Lindqvist, 1999). The nested-PCR method detected *Shigella flexneri* in lettuce inoculated with 2, 20 and 200 cfu g^{-1} after 1, 7 and 18 days of storage, respectively. There have been various modifications to this technique, making it even more sensitive, rapid and specific for detection and quantification of foodborne pathogens (de Boer & Beumer, 1999; Ercolini, 2004; reviewed by Lazcka *et al.*, 2007; reviewed by Velusamy *et al.*, 2010). A newer development of this is real-time PCR, proving a beneficial amendment for food microbiology (Hanna *et al.*, 2005). Real-time PCR was used to quantify *Fusarium* species of maize samples from two susceptible cultivars from 14 localities in South Africa (Boutigny *et al.*, 2012). A similar study reported the ability to quantify 11 individual *Fusarium* spp. in wheat and maize samples using real-time PCR (Nicolaisen *et al.*, 2009). Reverse-transcriptase PCR was used to detect viable cells of *Escherichia coli* O157:H7 (Yaron & Matthews, 2002). Multiplex PCR based assays have also been used for the early detection of aflatoxigenic fungi on maize kernels (Del Fiore *et al.*, 2010a), and for the detection of mycotoxigenic *Fusarium* species in rice and fingermillet (Ramana *et al.*, 2011).

There are continual advancements in methodologies and techniques to achieve more rapid, sensitive and species specific PCR methods such as quantitative PCR (reviewed by Postollec *et al.*, 2011). Despite its benefits, from an industrial point of view, routine detection of microbes using PCR can be expensive and complicated, requiring skilled workers to carry out the tests. A problem inherent to all PCR methods is the presence of factors that inhibit nucleic acid synthesis by the polymerase enzyme (Hanna *et al.*, 2005). Such inhibitory factors can be found in foods, culture media, and various chemical compounds, including those used to extract DNA (Rossen *et al.*, 1992). Specialised equipment and reagents as well as an aseptic working environment are needed. Because all the traditional methods to detect foodborne pathogens are often time-

consuming and labour intensive, there is a need for rapid, reliable, robust and simple alternatives. Spectroscopy offers such alternatives: NIR spectroscopy and NIR hyperspectral imaging.

NIR spectroscopy

Principles

NIR is a spectroscopic technique that utilises the part of the electromagnetic spectrum between the visible and infrared regions between 700 and 2500 nm (Wahr *et al.*, 1996; Pasquini, 2003; reviewed by Cen & He, 2007; reviewed by Roggo *et al.*, 2007). The technique is based on the measurement of bond vibrations between the atoms of organic molecules consisting mainly of C-H, C=O, O-H and N-H. These bonds are subject to vibrational energy changes when irradiated by NIR frequencies. Two vibration patterns exist in these bonds: stretching vibration and bending vibration. NIR absorption occurs when the vibrations at a given frequency coincide with those of a molecular bond in the material being scanned.

Applications

As a tool for use in the food industry, NIR spectroscopy has been recognised for its ability as a rapid, non-destructive means of quality assessment (Scotter, 1990; Scotter, 1997; reviewed by Woodcock *et al.*, 2008). It has gained much attention in food and agricultural applications as an instrument for online and inline monitoring of food and beverages (reviewed by Huang *et al.*, 2008). As a means of non-destructive measurement of quality of fruit and vegetables, NIR spectroscopy was shown to be suitable and reliable (reviewed by Nicolaï *et al.*, 2007). It has been recognised for its potential to predict quality of meat and meat products (reviewed by Prieto *et al.*, 2009), and in the dairy industry it was also shown to be effective in a number of quality related applications including adulterant detection (Rodriguez-Otero *et al.*, 1997). The technique is well-established as a means of quality assessment and prediction in the food industry.

Much work has been done regarding the identification, discrimination and quantification of harmful microbes and their associated toxins in food and agricultural products. The use of Fourier transform near infrared (FT-NIR) spectroscopy and multivariate pattern recognition techniques were evaluated for the rapid detection and identification of bacterial contamination in liquids (Rodriguez-Saona *et al.*, 2001). Principal component analysis (PCA) on second derivative spectra grouped samples into clusters based on cell wall composition of each of the respective bacteria (Rodriguez-Saona *et al.*, 2001). In a similar study the detection and identification of bacteria in an isolated system was investigated with accuracies of 100% for the classification of three *Pseudomonas* spp. (Alexandrakis *et al.*, 2008). In a study on tomatoes, Hahn (2002) showed that it was possible to discriminate between tomatoes infected with *Rhizopus stolonifer* and *F. oxysporum* or spore-free samples with accuracies up to 90% using visible and NIR spectra. This could have posed some problems due to the use of the visible range; all the tomatoes would have to be at the same stage of ripeness as different colours would cause a deviation in the spectral profile.

The use of visible spectroscopy is often regarded as inadequate, nevertheless useful information can be obtained from a carefully designed experiment. The NIR region is more chemical rich despite the overlapping bands and broad peaks. Using the vis-NIR region from 600 to 1000 nm, Lin *et al.* (2004) reported that they were able to perceive changes in microbial load on chicken muscle when calculating principal components (PC's). A partial least squares (PLS) model with eight latent variables had a correlation coefficient of 0.91 and a standard error of prediction (SEP) of 0.48 log CFU.g^{-1}. This work illustrates the potential to rapidly and non-invasively detect spoilage on food products. In another study the level of bacterial contamination on shredded cabbage was measured in the 700-1100 nm range (Suthiluk *et al.*, 2008). Two extraction methods were compared and SEP's of 0.46 log CFU.g^{-1} for the stomacher solution and 0.44 log CFU.g^{-1} for the washing solution were reported with correlation coefficients of 0.95 and 0.92, respectively. By correlating NIR with conventional microbiological techniques, the practicality of NIR was demonstrated as a useful tool to complement conventional food microbiology methods.

NIR was successfully evaluated on cereal as a rapid technique for the detection of kernel rots and mycotoxin in maize (Berardo *et al.*, 2005) while scab, vomitoxin and ergosterol were predicted in single wheat kernels (Dowell *et al.*, 1999). Fumonisins were detected in single maize kernels infected with *F. verticillioides* using reflectance and transmittance NIR spectroscopy (Dowell *et al.*, 2002) and aflatoxin B1 was detected in maize and barley (Fernández-Ibañez *et al.*, 2009). Recently, DON concentrations were estimated using NIR spectroscopy and partial least squares regression (Beyer *et al.*, 2010).

These methods, although successful and high in spectral resolution, are limited in the spatial dimension, offering no information regarding the location of the substance or contaminant investigated. Measurements are made across a small area on the sample and averaged, thus the entire sample is not measured but parts thereof and the result is always given as a single spectrum. A technique capable of incorporating localisation, thus measuring entire samples, rapidly and accurately is NIR hyperspectral imaging. With fungal infections that may be localised in a large sample, spectral averaging could produce a signal that was below the detection limit. The localisation of pixels in imaging would produce a local signal that was far above the detection limit.

NIR hyperspectral imaging

NIR hyperspectral imaging, first used for remote sensing (Goetz *et al.*, 1985), is an imaging technique that combines digital imaging and spectroscopy. It was later adapted for use in the laboratory and has since been applied in a number of applications: mostly used in the pharmaceutical, food and agricultural industries. NIR hyperspectral imaging is superior to traditional NIR bulk spectroscopy because it not only collects spectral data but also spatial information from a sample (Geladi *et al.*, 2007; Burger & Gowen, 2011), thus permitting spatial visualisation of constituents within a measured sample.

Principles

NIR hyperspectral imaging and its various imaging configurations has proven to be a valuable instrument with applications specific to the food, pharmaceutical and agricultural fields (reviewed by Gowen *et al.*, 2007; Gowen *et al.*, 2008; Elmasry *et al.*, 2012). There are three imaging configurations or means of generating a hyperspectral image from a sample, i.e. the whiskbroom imaging (point scan), pushbroom imaging (line scan) and staring imaging (wavelength scan) (Geladi *et al.*, 2007; reviewed by Gowen *et al.*, 2007; reviewed by ElMasry & Sun, 2010; reviewed by Boldrini *et al.*, 2012). The whiskbroom configuration is typically suited for microscopic imaging. In this format, the hyperspectral image is built by collecting spatial and spectral information from the sample, point by point (pixel by pixel). This is a time-consuming process suited for small samples, yielding a high spatial resolution. The pushbroom design is most suited for online applications as the instrument captures spatial and spectral information line-by-line (reviewed by Elmasry *et al.*, 2011). Thus, the sample may move under the camera's field of view for data collection. This configuration could be installed on a conveyor belt system for quality control. A complete hyperspectral image can take up to 20 seconds to acquire, depending on the field-of-view and magnification. This makes it perfect for online or at-line applications, where it offers rapid and non-destructive quantitative and qualitative assessment. A typical line scan system is depicted in Figure 2.1. The camera is comprised of a two-dimensional (2D) array Mercury-Cadmium-Telluride (MCT) detector with a prism-grating prism (PGP) monochromator. The illumination source is important as it should provide homogenous lighting and should not heat the sample. An image is acquired one line at a time while scanning the sample on a translation stage. Each line is comprised of 320 pixels. In the scanning dimension the number of lines is dependent on the selected scanning length. With the staring imaging configuration or focal plane array the sample and all spectrometer components remain stationary while an image of the entire field of view is acquired (reviewed by Boldrini *et al.*, 2012). An image of the sample at each wavelength (depending on the capability of the detector and spectrograph) is recorded resulting in images slices, i.e. there is one image per wavelength stacked sequentially.

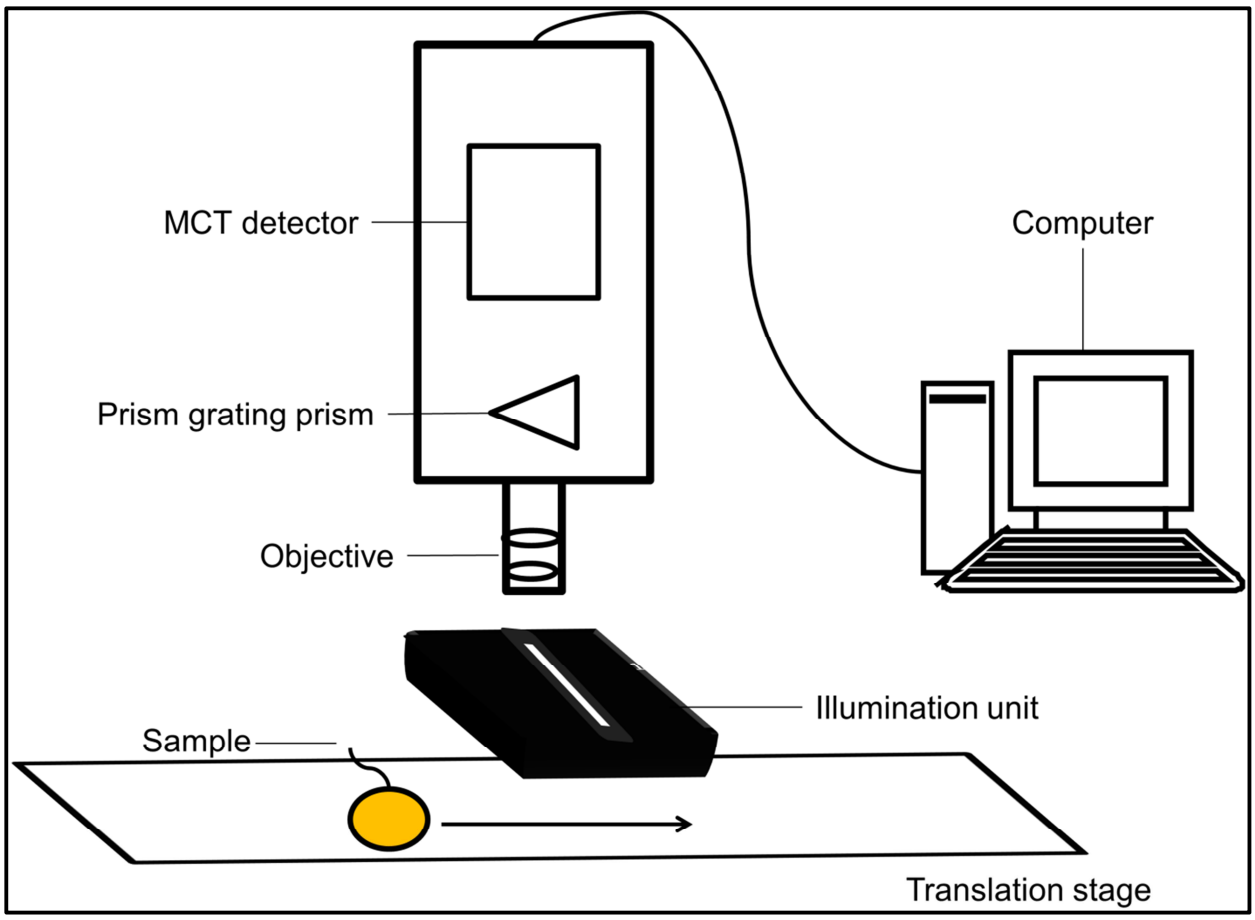

Figure 2.1. Diagram illustrating the components of a line scan imaging system.

NIR hyperspectral images

NIR hyperspectral images are composed of hundreds of neighbouring wavebands for each spatial position of an object studied (Geladi *et al.*, 2004). The acquired hyperspectral image is known as a hypercube (Burger & Geladi, 2006). This is a three-dimensional (3D) data cube comprised of two spatial dimensions (*x* and *y* of *m* rows and *n* columns) and one spectral dimension (λ) as shown in Figure 2.2. The spectral dimension acts like a chemical fingerprint allowing one to identify chemical and biochemical constituents present in the sample. Together with the spatial dimensions, the spectral dimension permits spatial visualisation of the chemical/biochemical constituents. The hyperspectral images can be seen as chemical maps, providing information regarding the composition of the sample, the location of the constituents and the relative amounts of the constituents (Koehler *et al.*, 2002). The intensity of a pixel in the hypercube plotted as a function of the wavelength dimension represents a standard NIR spectrum and the intensity for all pixels at a single wavelength represents an image of absorption. A hypercube, from e.g. a SisuCHEMA pushbroom imaging system comprises, e.g. 301 x 320 pixels x 242 wavelengths. This results in a data set composed of 96 320 spectra at 242 wavelength channels. Enormous amounts of data are obtained from a single sample, posing potential data analysis problems. This magnitude of data requires a combination of multivariate chemometrics and visualisation tools to adequately mine for

meaningful information. Multivariate image analysis (MIA) offers a platform to do this in an efficient way.

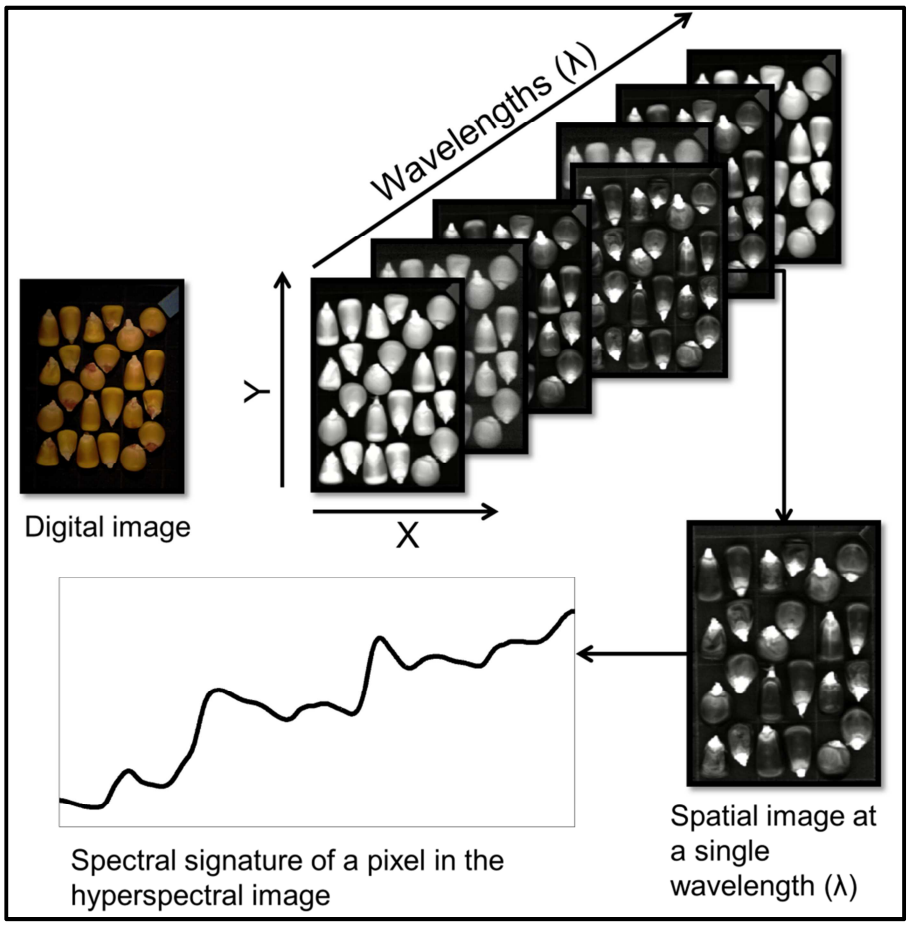

Figure 2.2. Representation of a hypercube illustrating the relationship between spatial and spectral dimensions.

Multivariate image analysis (MIA)

Multivariate image analysis (MIA) are data analysis techniques employed for the exploration and interpretation of hypercubes (Geladi & Grahn, 1996; Burger & Geladi, 2007a). Because of the sheer size of these hypercubes and the succeeding data set, dimensionality reduction techniques are required. The data reduction technique should decompose the data maintaining the original variance within fewer variables. PCA is well-suited for this purpose and is essential for data reduction and examination of NIR spectra (Cowe & McNicol, 1985). However, for hyperspectral images, an unfolding step is required first. Prior to any data treatment, the hypercube is first reorganised into a matrix **X**, where the pixel information (*x*, *y*) are the observations and the wavelengths are the variables. The data are first mean-centred then decomposed into a scores matrix (**T**), a loadings matrix (**P'**) and a residual matrix (**E**) according to equation 1:

$$X = TP' + E \quad \text{…[eq. 1]}$$

The scores matrix can be used to construct score plots and are refolded into score images. Score plots illustrate the score values of the PC's plotted against each other while score images show the score values plotted as contour maps of the sample imaged for each PC. In certain image analysis software packages the two plots are interactive; selecting pixels with, e.g. high density values in the scores plot will highlight the corresponding pixels in the score image allowing visualisation of location within the sample. While the scores describe the relationship of the objects in the decomposed matrix, the loadings represent the variation in the wavelength dimension. This is visualised by plotting the loading values against the wavelengths. When used in combination, the scores and loadings permit the visualisation, localisation and identification of desired parameters within an image. The loadings also indicate the cause of the variation. PCA applied to hypercubes is illustrated in Figure 2.3.

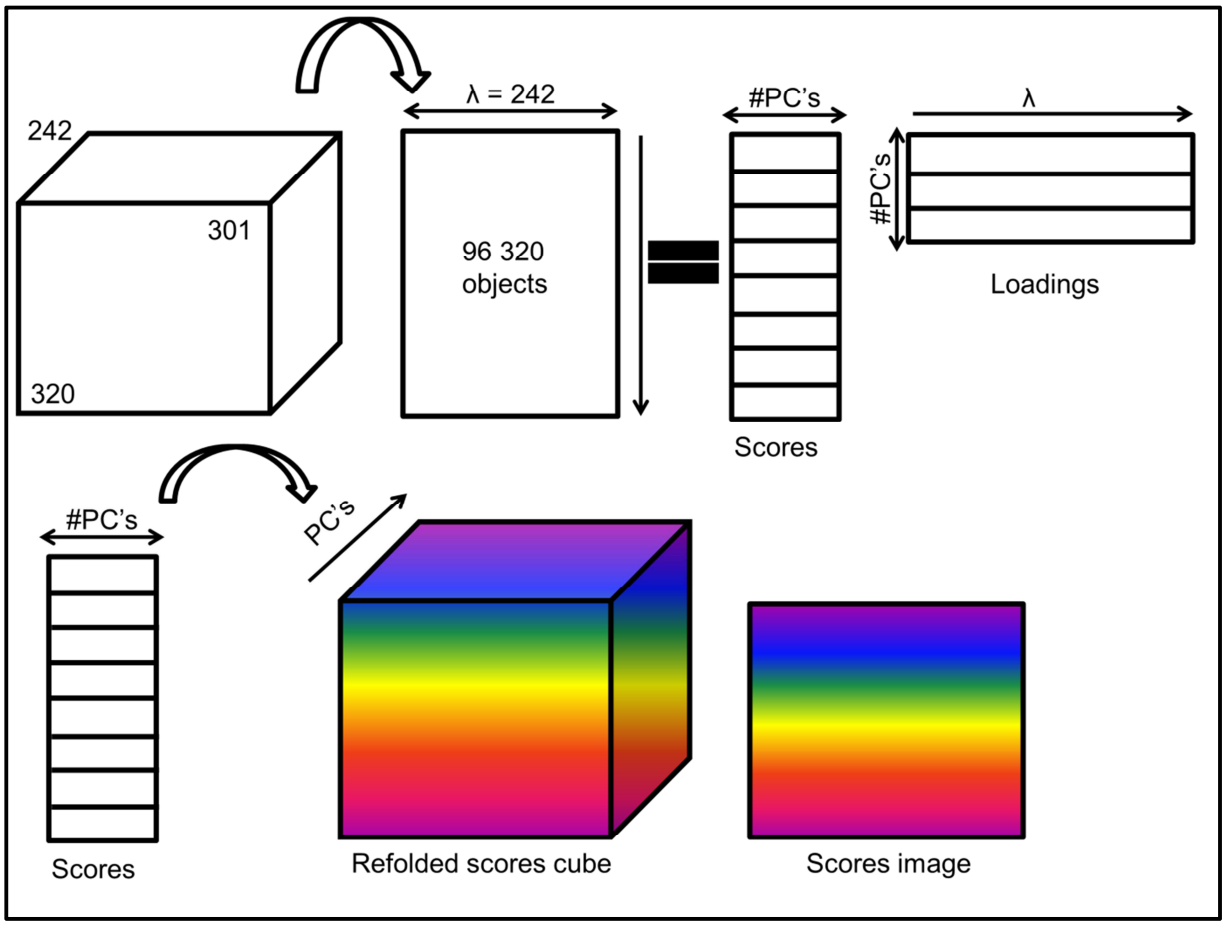

Figure 2.3. Principal component analysis applied to a hypercube.

Pre-processing

Once the hypercube has been unfolded an array of pre-processing techniques may be applied to remove effects of scattering, to improve signal-to-noise ratio and to eliminate physical inconsistencies caused by non-uniform lighting. The most widely used spectral pre-processing techniques are the Savtizky-Golay derivatives (Savitzky & Golay, 1964), standard normal variate (SNV) (Barnes *et al.*, 1989) and multiplicative scatter correction (MSC) (Geladi *et al.*, 1985). These techniques were shown to be useful on NIR hyperspectral image data (Burger & Geladi, 2007b).

Classification

NIR hyperspectral imaging lends itself to defect or contamination detection. It is perfectly suited for discriminant studies, to compare products with each other in order to identify irregularities or impurities by means of classification. This can be done by, e.g. calculating partial least squares discriminant analysis (PLS-DA) models on the unfolded cube (Chevallier *et al.*, 2006). PLS-DA is similar to PLS, that uses the latent variable approach to find fundamental relations between two matrices (**X** and **Y**) (Martens, 2001; Wold *et al.*, 2001; Liu & Rayens, 2007). PLS uses the y-data structure to decompose **X** so that the outcome constitutes an optimal regression vector. PLS-DA operates similarly, however instead of measured y-data, dummy variables are used which are indicators of groups (Chevallier *et al.*, 2006). This allows for prediction of group membership, and thus classification of pixels to classes. Similar to PCA, it is also possible to build synthetic images showing the predicted groups. There are numerous other classification techniques and data handling methods for hyperspectral images (reviewed by Burger & Gowen, 2011; Elmasry *et al.*, 2012).

Applications

Hyperspectral imaging has been described as an instrument well-suited for food safety inspection using an array of spectral imaging modalities such as NIR, fluorescence and Raman hyperspectral imaging (reviewed by Feng & Sun, 2012). Of the hyperspectral imaging techniques available, NIR hyperspectral imaging is the most applicable for rapid analyses because the other modalities are time-consuming and require sample preparation prior to measurement. The food safety related NIR hyperspectral imaging work that has been done can, in essence, be considered as microbiological applications since the work deals with the identification, differentiation and quantification of microbes on and in food matrices. NIR hyperspectral imaging may complement conventional microbiological techniques.

The relevance of NIR hyperspectral imaging (1000-2350 nm) to detect food-borne pathogens on food cards was investigated (Dubois *et al.*, 2005). The technique was effective in discriminating between *E. coli*, *S. typhimurium*, *L. innocua*, *B. subtilis*, *B. cereus*, *L. monocytogenes* and *S. entiritidis* based on spectral differences. The potential for discriminating between different food-borne pathogens without the use of complicated techniques such as PCR is evident. Detecting

these potentially hazardous organisms on or in food products is the ultimate goal and NIR hyperspectral imaging could serve as an immediate, rapid means of detection in the food factory or laboratory.

The detection of faecal contamination on poultry carcasses has been investigated (Park *et al.*, 2004; Park *et al.*, 2006; Park *et al.*, 2007a; Park *et al.*, 2007b). Recently, a line-scan hyperspectral imaging system for real-time faecal detection on poultry carcasses in-line was developed (Park *et al.*, 2011). Detection of 10 mg of faecal and ingesta contaminations at an impressive processing speed of 140 birds per minute was reported. The feasibility of such a system for food safety inspection in a commercial poultry plant, where contaminated carcasses can be removed immediately, was demonstrated. Similar systems would be beneficial for other produce such as cereals, where contaminated samples could be removed by high-pressure air valves.

An automated NIR system for selecting individual wheat kernels based on protein content and hardness has been developed (Dowell *et al.*, 2006). The system used air valves to separate single kernels based on hardness and protein content. Pearson (2009) also developed an imaging system that separated grains based on colour differences and defects. The throughput rate achieved corresponded to an inspection rate of approximately 8 $kg.h^{-1}$ of wheat and 40 $kg.h^{-1}$ of popcorn with accuracies of 88% for separating red wheat and 91% for separating white wheat. For popcorn, the system achieved 74% accuracy when removing popcorn with blue-eye damage and 91% accuracy at recognising good popcorn. These systems would be ideal for automated separation of contaminated cereal. Sorting systems based on optical measurements for the detection and removal of fungal and insect infested grains have been reported (Pasikatan & Dowell, 2001). Although these systems were predominantly designed with traditional NIR spectroscopic techniques, they can be adapted to imaging platforms.

Occasionally infected cereal grains exhibit no visual symptoms of infection, and if not objectively inspected, may enter the food chain. These grains are important since they may still contain high levels of mycotoxins (Bacon & Hinton, 1996). Early detection of fungal contamination is vital to prevent infected grains with potentially high mycotoxin concentrations, from entering the food chain. Using a staring imager and a line-scan system, a distinction between kernels infected with *F. verticillioides* and sound kernels with accuracies of 73% and 86% for both instruments respectively, was reported (Williams *et al.*, 2010). The line-scan instrument was found to be more accurate and this was ascribed to the extended wavelength region. Working in the vis-NIR region (400-1000 nm), Del Fiore *et al.* (2010b) reported the ability to discriminate between infected and non-infected commercial maize kernels after 48 h of inoculation with *A. flavus* and *A. niger*. Two wavelengths, 410 and 470 nm, characterised by a high discriminating power were used. These are associated with the blue and violet regions of the visible spectrum, thus the discrimination was based on a colour change as the fungi proliferated and grew on the kernels.

Detecting fungal contamination on other cereals has also been done and this is of increasing importance as cereals form a large part of nourishment worldwide. A summary of NIR

hyperspectral imaging applications concerning fungal detection, identification and discrimination in cereals can be found in Table 2.1. Fungal damaged wheat was investigated with a short wave NIR hyperspectral imaging system within the 700-1100 nm spectral range and digital colour imaging (Singh *et al.*, 2011). The band at 870 nm was considered significant and was subsequently used for feature extraction and classification. Colour imaging performed better than the NIR hyperspectral imaging system. This was likely due to the vast difference in colour of the wheat kernels as a result of fungal contamination. A study using the vis-NIR region with spectral ranges of 400-1000 and 1000-1700 nm achieved classification accuracies of 95% between sound and *Fusarium* damaged wheat kernels (Delwiche *et al.*, 2011). No difference between the two spectral regions was found and it was suggested that either one would be useful. However, the NIR region was preferred due to chemical changes observed. The spectral absorption near 1200 nm, attributed to ergosterol (a primary constituent in fungi cell membranes), was shown to be useful in spectral recognition of *Fusarium* damage. In a similar investigation, 92% classification accuracy was attained between sound and *Fusarium* damaged wheat kernels (Shahin & Symons, 2011). A hyperspectral system in the vis-NIR (400-1000 nm) wavelength range was used. The distribution of PCA scores of individual kernels were computed and used to develop linear discriminant models (LDA) to predict extent of damage. Ultimately, it was shown that classification based on six selected wavelengths (484, 567, 684, 817, 900 and 950 nm) was comparable to the entire spectrum. In an online application, the presence and quantity of ergot bodies were detected in wheat in the spectral range (1100-2400 nm) (Vermeulen *et al.*, 2011). In a remote sensing application, fungal disease severity in wheat was classified and quantified in the 360-900 nm spectral range (Muhammed & Larsolle, 2003).

Using multispectral imaging, bacterial spoilage on pork meat was monitored and total viable counts with a SEP of 7.47% was predicted (Dissing *et al.*, 2012). In a similar study investigating beef spoilage, predictions with an r^2 of 0.95 and SEP of 0.30 for $\log_{10}$ total viable count were reported (Peng *et al.*, 2011). An imaging system operating in the spectral range 400-1100 nm was used. Not only was the bacterial load predicted, it was also localised and the contaminated regions of the samples could be visualised. Fresh produce and minimally processed products pose a risk to consumers as they are vehicles of foodborne pathogens. A recent study evaluated hyperspectral imaging in the 400-1000 nm spectral region for the detection of *E. coli* on packaged fresh spinach (Siripatrawan *et al.*, 2011). The microbial load was predicted using artificial neural networks with an r^2 of 0.97 and prediction maps were constructed illustrating the distribution of *E. coli* on the spinach. These studies demonstrate the advantages of NIR hyperspectral imaging: the spatial and the spectral dimensions enable simpler and more efficient visualisation and interpretation of the data.

Table 2.1. An overview of NIR hyperspectral imaging applications regarding the evaluation of cereal for fungal infection

Cereal type	Application	Wavelength range (nm)	Classification	References
Maize	Detection of kernels infected with *F. verticillioides*	960-1662; 1000-2498	PCA[a]; PLS-DA[b]	(Williams *et al.*, 2010)
Maize	Early detection of toxigenic fungi	400-1000	PCA[a]; DA[c]	(Del Fiore *et al.*, 2010b)
Wheat	Discrimination and quantification of fungal disease	360-900	ICA[d]; PCA[a]; FVBA[e]	(Muhammed & Larsolle, 2003)
Wheat	Detection of *Fusarium* in single kernels	430-900; 900-1750	Fuzzy c-means clustering; PLS[f]	(Polder *et al.*, 2005)
Wheat	Classification of sound and stained kernels	420-2500	PDA[g]	(Berman *et al.*, 2007)
Wheat	Detection of sprouted and midge damaged kernels	1000-1600; 1100-1700	PCA[a;] LDA[h]; QDA[i]	(Singh *et al.*, 2009; Singh *et al.*, 2010)
Wheat	*Fusarium* damage assessment	400-1000; 1000-1700	LDA[h]	(Delwiche *et al.*, 2011)
Wheat	Detection of *Fusarium* damage in Canadian Western Red Spring wheat	400-1000	PCA[a]; LDA[h]; PLS[f]; PLS-DA[b]	(Shahin & Symons, 2011; Shahin & Symons, 2012)
Wheat	Fungal damage detection	400-700; 700-1100	PCA[a]; LDA[h]	(Singh *et al.*, 2011)
Wheat	Online detection and quantification of ergot bodies	1100-2400	PLS-DA[b]; SVM[j]	(Vermeulen *et al.*, 2011)
Wheat	Detection of mildew	450-950	MLR[k]; PLS[f]; FLDA[l]	(Zhang *et al.*, 2012)
Rice	Early detection of rice blast	900-1700	PCA[a]; LDA[h]	(Yang *et al.*, 2012)

[a] Principal component analysis; [b] Partial least squares discriminant analysis; [c] Discriminant analysis; [d] Independent component analysis; [e] Feature vector based analysis; [f] Partial least squares; [g] Penalised discriminant analysis; [h] Linear discriminant analysis; [i] Quadratic discriminant analysis; [j] Support vector machines; [k] Multivariate linear regression; [l] Fisher linear discriminant analysis

The aforementioned studies considered the detection, identification and differentiation of microbial spoilage or contamination on food products, which in itself are complex matrices. In order to investigate and differentiate microorganisms in a more controlled manner and environment, plating out on the appropriate growth medium and incubating at the optimum temperature is necessary. This is typically done in a food factory to assess microbial load, and to identify contaminants. If an organism cannot be identified using the culture techniques, samples are often evaluated with molecular techniques such as PCR. Culture techniques are thus a necessary step prior to more complex analyses.

Campylobacter colonies were detected on growth media with detection accuracies between 97-99% after 24 h of incubation (Yoon *et al.*, 2010). Petri-dishes inoculated with *Campylobacter* and non-*Campylobacter* colonies were imaged in the 400-900 nm spectral range. A band ratio algorithm at 426 and 458 nm was used. Two types of growth media were evaluated (Blood agar and Campy-Cefex agar), and it was found that colonies plated on Blood agar yielded better detection accuracies. The two wavelengths used in the algorithm were from the visible spectrum, thus it is likely that changes in colour was detected in the agar rather than chemical changes. *Campylobacter* is known for its haemolytic activity on Blood agar. In a similar study, the ability to differentiate between five toxigenic fungi on growth media with a classification rate of 97.7% was reported (Yao *et al.*, 2008). All five fungi could be classified using three narrow bands centred at 743, 458 and 541 nm. The latter two wavelengths are part of the visible spectrum and the fungi studied differed in colour. It is possible the differentiation was based on colour differences observed in the colonies on the growth medium. In both studies 458 nm was used for classification and differentiation was based on colour changes.

The simplicity of NIR hyperspectral imaging and MIA render them as useful techniques for food quality and safety inspection. The rapid and non-destructive nature of the NIR hyperspectral imaging techniques makes them suitable for implementation in production lines (online, at-line and simulation studies). The long wavelengths involved in NIR hyperspectral imaging are however a major limitation. In instances where contaminants are located at deeper levels within a sample, the low energy levels of wavelengths in the NIR region are not sufficient and shorter, high energy wavelengths are required.

X-ray imaging and X-ray micro-computed tomography

Principles

X-rays are produced when high-energy electrons strike a target material usually a metal in an X-ray tube (reviewed by Haff & Toyofuku, 2008). Electrons shedding from a heated filament anode in the X-ray tube are exposed to a high voltage in a vacuum, causing them to accelerate and strike the cathode metal at high energies. As the high energy electrons decelerate in the metal, the electrons of the metal atoms are excited to higher energy levels, and then decay to their ground states with the emission of X-ray photons. X-rays have a wavelength in the range of 0.01 to 10 nm

and behave like particles as well as waves while interacting with matter (reviewed by Kotwaliwale *et al.*, 2011). Electromagnetic waves with wavelengths ranging from 0.1 to 10 nm are called soft X-rays. Due to low penetration power and ability to reveal the internal density changes, soft X-rays are more suitable to be used on agricultural products (reviewed by Kotwaliwale *et al.*, 2011).

When an object is irradiated with X-rays, the X-rays interact with the matter and a decrease in the total energy of the X-ray beam occurs as it passes through the object (Kotwaliwale *et al.*, 2011). This decrease in energy is known as attenuation, and is a measure that describes how easily a material can be penetrated by a beam of radiation (McCullough, 1975). A high attenuation coefficient means that the beam is rapidly attenuated (weakened) as it passes through the medium while a small attenuation coefficient means that the medium is relatively transparent to the beam. Objects with high attenuation coefficients are usually denser than those with low attenuation coefficients.

Existing microscopes are used to look at object surfaces or transmission images through thin sections, thus internal 3D structure can only be studied destructively. Data obtained in this manner might not always be consistent because of the destructive nature of the sample preparation (Lim & Barigou, 2004). Consistent 2D and 3D microstructural data can be obtained from X-ray micro tomography (μCT). These are derived from a set of thin planar cross-sections which expose material density information (Lim & Barigou, 2004). Multiple slices are progressively imaged as the object is rotated through the X-rays. These slices are mathematically reconstructed to form 3D images (Kak & Slaney, 1988). This form of imaging not only allows for the evaluation of the internal structure of objects but also permits exploration of the object non-destructively. High resolution μCT tomography is a sophisticated technique for the structural investigation of objects (Lim & Barigou, 2004). The method has some advantages over other techniques such as light or electron microscopy. These include the ability to investigate samples in their natural state at atmospheric pressure and temperature; the much greater spatial resolution; and the ability of X-rays to penetrate through any material and capture 3D details of the inner microstructure (Lim & Barigou, 2004).

Applications

X-ray and μCT imaging techniques are commonly associated with medical applications, but have also been successfully implemented in material science, chemical engineering, geology and biology (Kotwaliwale *et al.*, 2011; Laverse *et al.*, 2012). In recent years much attention has been focused on extending this imaging technique to food science, as a useful technique to aid in the study of food microstructure.

An X-ray imaging inspection method was developed by Thomas *et al.* (1993) to successfully evaluate mangos for an internal disorder, spongy tissue. Differences between affected and healthy fruit appeared as differences in grey values in the X-ray images where darker regions corresponded to spongy tissue and lighter areas where associated with healthy fruit. In another study, Thomas *et al.* (1995) made use of the difference in density to distinguish between weevil

infested and non-infested mango fruit. Lighter material in the X-ray images was attributed as healthy while dark to black was recognised as infested or damaged by the weevils. The appearance of airspaces and voids was also black and was associated with the cavities and corresponding grey values in the X-ray image. The increase in these voids and airspaces was caused by the weevils. A high resolution real-time X-ray system was developed for the detection of the granary weevil infested wheat kernels and was compared to a radiographic system (Haff & Slaughter, 2004). The percentage of images correctly classified averaged 84.4% for the real−time system compared to 90.2% for the film observations. Soft X-ray imaging was used for the detection of fungal infection in wheat (Narvankar *et al.*, 2009). Accuracies of between 92.2-98.9% were obtained using a two-class Mahalanobis discriminant classifier. In a study to detect sprouted wheat kernels, also using soft X-ray image analysis, accuracies of between 90 and 95%, and 87 and 92% were obtained for a four-layer back propagation neural network model and a statistical classifier model, respectively (Neethirajan *et al.*, 2007). A study on the detection of internal wheat seed infestation by *Rhyzopertha dominica* using X-ray imaging, reported classification accuracies of up to 98% (Karunakaran *et al.*, 2004). The differentiation between infested and non-infested wheat kernels was evident in the X-ray images and appeared as density variations. Hidden information is revealed by the use of X-ray imaging for non-destructive internal evaluation of food and agricultural produce, however these are 2D images that offers no depth or the possibility of exploring the imaged object in virtual space.

3D X-ray microstructural applications of food are increasingly investigated to understand the functionality of food components and ingredients (Mebatsion *et al.*, 2009; Pittia *et al.*, 2011; Chawanji *et al.*, 2012; Frisullo *et al.*, 2012a; Frisullo *et al.*, 2012b; Laverse *et al.*, 2012) and the internal quality evaluation of agricultural produce (reviewed by Kotwaliwale *et al.*, 2011). X-ray computed tomography has been used to investigate the microstructure of processed meat and the differences between the microstructures of a variety of salamis and their fat distributions have been reported (Frisullo *et al.*, 2009). In a similar study, the distribution of intramuscular fat in beef muscles was investigated (Frisullo *et al.*, 2010). Correlation coefficients of between 0.92 and 0.99 were obtained when comparing percentage object volume determined with µCT to the soxhlet extraction method for intramuscular fat. The microstructure of mayonnaise was studied using µCT (Laverse *et al.*, 2012). The researchers were able to analyse the distribution of fat and quantify the percentage fat, using the µCT data that corresponded well with the manufacturers' specifications. Furthermore, the µCT data was correlated with rheological properties.

Regarding the µCT investigations on cereal, a few studies stand out. Neethirajan *et al.* (2006) studied the airflow resistance of various grains in grain bulks. They reported that the ratio of total airspace area to the total number of air paths is the best predictor for the difference in the airflow resistance in horizontal and vertical directions in the grain bulks. Cleveland (IV) *et al.* (2008) recognised the potential of using tomographic techniques to investigate the structural analysis of maize kernels and to differentiate between kernels infected with *Aspergillus flavus* and sound

ones. Infected kernels had lower neutron attenuation than those not infected. This was attributed to lower hydrogen concentrations because of fungal degradation.

Image analysis

Visualisation and analysis of µCT data is possible using dedicated software packages. Information such as object volume, object surface to volume ratio, porosity, structure thickness and particle size can be extracted (Laverse *et al.*, 2012). These measures are however not suited for all applications.

The large amounts of image data generated from the X-ray imaging techniques pose data handling problems. Methods are required to extract meaningful information from the images. The aim of image analysis is to describe an image scene on the basis of information extracted from images or image sequences (Rosenfeld, 1984). Because of the immense size of images, analysing an image in its original form can be very time-consuming (Jayas *et al.*, 2000). To make the process simple and less time-consuming, the image is often reduced to a smaller selected region of interest (ROI) and information is extracted from the objects to be analysed. The extracted attributes, features or descriptors are used as inputs to algorithms for classifying the objects into different categories. Texture analysis, which extracts textural descriptors from grey level co-occurrence matrices (GLCMs), is the most popular (Bharati *et al.*, 2004).

Texture and GLCMs

Texture is one of the important characteristics used in identifying objects or ROIs in an image, and can be assessed as either fine, coarse, smooth, rippled, grainy or lineated (Haralick, 1979). Image texture can be defined as a function of the spatial organisation and variation in pixel intensity or grey values (Haralick *et al.*, 1973; Tuceryan & Jain, 1993). Figure 2.4 illustrates four different textures often observed in images. Texture contains essential information about the structural organisation of surfaces, and these features, based on grey tone spatial dependencies, have a general applicability in image classification and for discrimination (Haralick *et al.*, 1973; Gadkari, 2004).

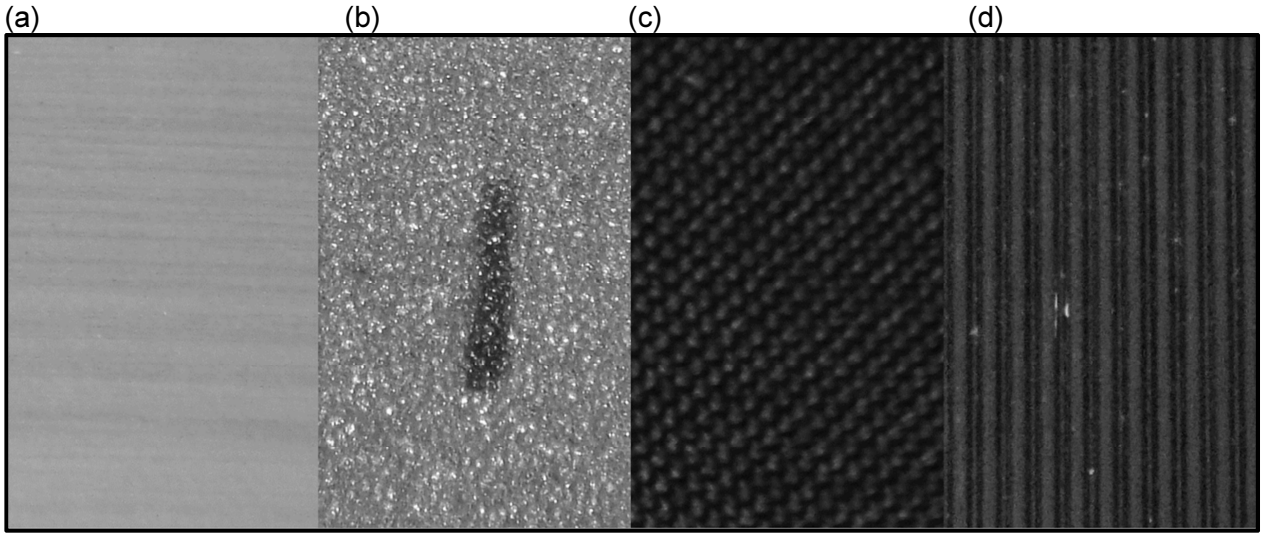

Figure 2.4. Examples of different textures observed in images; (a) smooth, (b) coarse, (c) grainy and (d) lineated.

Textural features are extracted from GLCMs that are grey tone spatial-dependence probability-distribution matrices. The GLCM is defined as a 2D histogram of grey levels for a pair of pixels, which are separated by a fixed spatial relationship. This method is based on the use of second-order statistics of the greyscale image histograms (Bharati *et al.*, 2004). The GLCM of an image is an approximation of the second-order joint probability, P_δ (*i, j*) of the intensity values of two pixels (*i* and *j*), a distance δ apart along a given direction θ, *i.e.*, the probability that *i* and *j* have the same intensity (Haralick *et al.*, 1973; Bharati *et al.*, 2004). This joint probability is expressed as a matrix $\mathbf{P}_\delta$, with row and column dimensions equal to the number of discrete grey levels (intensities) in the original image. A 4x4 greyscale image with only four grey levels (0-3) is shown in Figure 2.5a, where each block represents a pixel with a particular intensity. The GLCM is computed by finding the frequency each pixel combination occurs in the image. This is represented by Figure 2.5b which is the general form for computing the GLCM. Each cell indicates the combination of the reference and the neighbouring pixels and is used for locating these combinations in the original image. GLCMs can be calculated using four displacement vectors with δ =1, or 2 pixels, and θ =0°, 45°, 90°, or 135° (Haralick *et al.*, 1973). Figure 2.5c depicts a GLCM computed in an East-West direction θ =0° and δ =1. This is a non-symmetric co-occurrence matrix because it was calculated only in one direction, east to west. GLCMs are symmetrical matrices, and to calculate this, the GLCM must be computed in the opposite direction too. The two non-symmetrical matrices are summed, resulting in a symmetrical matrix (Fig. 2.5d). The symmetric GLCM is first normalised by dividing each element in the matrix by the sum of all elements, before texture measures are calculated.

(a)

0	0	1	1
0	0	1	1
0	2	2	2
2	2	3	3

(b)

Grey tone	0	1	2	3
0	0,0	0,1	0,2	0,3
1	1,0	1,1	1,2	1,3
2	2,0	2,1	2,2	2,3
3	3,0	3,1	3,2	3,3

(c)

2	2	1	0
0	2	0	0
0	0	3	1
0	0	0	1

(d)

4	2	1	0
2	4	0	0
1	0	6	1
0	0	1	2

(e)

0.167	0.083	0.042	0
0.083	0.167	0	0
0.042	0	0.250	0.042
0	0	0.042	0.083

Figure 2.5. Schematic representation indicating how the GLCM is computed. (a) Greyscale image with 4 grey levels (0-3). (b) The general form of the GLCM where each cell represents the frequency a pixel of a certain grey level occurs with a neighbouring pixel. (c) The computed non-symmetric co-occurrence matrix and (d) the symmetric co-occurrence matrix illustrating the frequency of grey level pixels occurring in the original image. (e) The normalised symmetric GLCM. GLCMs computed at an angle $\theta = 0°$ and a distance $\delta = 1$ pixel.

A set of 14 textural features have been proposed that contain information about image textural characteristics such as homogeneity, grey-tone linear dependencies, contrast, number and nature of boundaries present and the complexity of the image (Haralick *et al.*, 1973). Often only a few of these descriptors are necessary for analysing texture in an image (Bharati *et al.*, 2004). Four of the most commonly used descriptors are contrast, correlation, energy and homogeneity (equations 2-5).

$$\textbf{Contrast} = \sum_{i,j} |i-j|^2 \boldsymbol{P}(i,j) \quad \text{…[eq. 2]}$$

$$\textbf{Correlation} = \sum_{i,j} \frac{(i-\mu i(j-\mu j)\boldsymbol{P}(i,j)}{\sigma_i \sigma_j} \quad \text{…[eq. 3]}$$

$$\textbf{Energy} = \sum_{i,j} \boldsymbol{P}(i,j)^2 \quad \text{…[eq. 4]}$$

$$\textbf{Homogeneity} = \sum_{i,j} \frac{\boldsymbol{P}(i,j)}{1+|i-j|} \quad \text{…[eq. 5]}$$

Where:

i, j: neighbouring grey tone values

$\boldsymbol{P}(i,j)$: i,jth entry in the normalised GLCM

$\sigma_i \sigma_j$ and μ_i σ_j: are the means and standard deviations

Contrast measures the spatial frequency of an image and is the difference moment of the GLCM (Gadkari, 2004). It is the difference between the highest and the lowest values of a contiguous set of pixels and it measures the amount of local variations present in the image (Haralick *et al.*, 1973). Correlation is a measure of the grey tone linear-dependencies in the image (Haralick et al., 1973), i.e. how correlated a pixel is to its neighbour over the whole image. Energy is also called angular second-moment (ASM) and is a measure of the homogeneity of the image (Haralick et al., 1973). Energy values close to or equal to 1 indicates a homogenous image. Thus the grey level distribution is constant across the image. Homogeneity is also known as the inverse difference moment and is inversely correlated to contrast (Gadkari, 2004). It returns a value that measures the closeness of the distribution of elements in the GLCM to the GLCM diagonal. The diagonal elements all represent pixel pairs with no grey level difference. If there are high probabilities in these elements, then the image does not show much contrast; most pixels are identical to their neighbours.

Applications

Texture analysis, applied to imaging data, has been applied frequently in the food industry for quality evaluation and inspection (Zheng *et al.*, 2006a). Meat quality was successfully determined using texture analysis (Shiranita *et al.*, 1998). Recently, textural features were used to estimate tea quality (Laddi *et al.*, 2013). It was reported that discrimination of tea grains was best under Darkfield illumination. Wavelet texture analysis was used for classification of wheat classes (Choudhary *et al.*, 2009). Using wavelet features from score images yielded classification accuracies of 79.9%. In a similar study, textural features were used as input for neural networks and discriminant analyses (Zapotoczny, 2011). Classification accuracies of up to 100% were reported for 11 wheat varieties.

These are only a few applications highlighting the use of image texture analysis on food and agricultural products. Considerable research regarding image texture applied to food and

agricultural products have been done and such research continues with various image processing applications for quality evaluation and inspection (Du & Sun, 2004; Zheng *et al.*, 2006b).

Conclusion

With the on-going pressure on the food chain, rapid, non-destructive techniques for microbiological evaluation are increasing, to ensure safe food. NIR hyperspectral imaging offers the rapidity and non-destructiveness required.

NIR hyperspectral imaging is widely available and recognised as instrumental during rapid food safety inspection. Microbiology laboratories, specifically food microbiology laboratories will only benefit from the use of NIR hyperspectral imaging when it is used complementary to conventional methods for identification and differentiation of pathogens and foodborne pathogens. These systems could serve as rapid, initial detectors of contamination prior to more complex molecular techniques. The ability to assess the spectral and spatial dimensions with relative ease and powerful visualisation tools makes data exploration and interpretation effortless. The spatial feature of NIR hyperspectral imaging enables characterisation of complex heterogeneous samples, while the spectral feature allows for the identification of a wide range of multi-constituent surface and sub-surface features. Additional research regarding early detection of fungal contamination is required. In addition, research regarding growth and identification of fungi and bacteria on growth media is lacking.

X-ray computed tomography is a powerful analytical technique for studying the microstructure of food and agricultural produce. It is being increasingly used as a research tool; however it is not always readily available for researcher and beam time on commercial equipment is usually costly. Evaluation is time-consuming but offers non-destructive, 3D visualisation of imaged objects. It permits the study of fine detail of samples in high resolution, making it suitable for research. Practically it would be ideal to use 2D X-ray imaging techniques in the food industry because it is rapid and analyses can be done in real-time. Thus far no work regarding the X-ray microstructure of fungal infected cereals has been done.

Image analysis is vital for extracting information from images. Texture is an important image feature and a characteristic used in identifying objects or ROIs in images. Together these offer a rapid, objective and statistical means of analysing images.

References

Alborch, L., Bragulat, M.R. & Cabañes, F.J. (2010). Comparison of two selective culture media for the detection of *Fusarium* infection in conventional and transgenic maize kernels. *Letters in Applied Microbiology*, **50**, 270-275.

Alexandrakis, D., Downey, G. & Scannell, A.G.M. (2008). Detection and identification of bacteria in an isolated system with near-infrared spectroscopy and multivariate analysis. *Journal of Agricultural and Food Chemistry*, **56**, 3431-3437.

Andrews, S. & Pitt, J.I. (1986). Selective medium for isolation of *Fusarium* species and dematiaceous hyphomycetes from cereals. *Applied and Environmental Microbiology*, **51**, 1235-1238.

Bacon, C.W. & Hinton, D.M. (1996). Symptomless endophytic colonization of maize by *Fusarium moniliforme*. *Canadian Journal of Botany*, **74**, 1195-1202.

Baird, R.M. & Lee, W.H. (1995). Media used in the detection and enumeration of *Staphylococcus aureus*. *International Journal of Food Microbiology*, **26**, 15-24.

Bansal, N.S. (1996). Development of a polymerase chain reaction assay for the detection of *Listeria monocytogenes* in foods. *Letters in Applied Microbiology*, **22**, 353-356.

Barnes, R.J., Dhanoa, M.A. & Lister, S.J. (1989). Standard normal variate transformatoin and de-trending of near-infrared diffuse reflectance spectra. *Applied Spectroscopy*, **43**, 772-777.

Berardo, N., Pisacane, V., Battilani, P., Scandolara, A., Pietri, A. & Marocco, A. (2005). Rapid detection of kernel rots and mycotoxins in maize by near-infrared reflectance spectroscopy. *Journal of Agricultural and Food Chemistry*, **53**, 8128-8134.

Berman, M., Connor, P., Whitbourn, L., Coward, D., Osborne, B. & Southan, M. (2007). Classification of sound and stained wheat grains using visible and near infrared hyperspectral image analysis. *Journal of Near Infrared Spectroscopy*, **15**, 351-358.

Beuchat, L.R. (1993). Selective media for detecting and enumerating foodborne yeasts. *International Journal of Food Microbiology*, **19**, 1-14.

Beumer, R.R., Brinkman, E. & Rombouts, F.M. (1991). Enzyme-linked immunoassays for the detection of *Salmonella* spp.: a comparison with other methods. *International Journal of Food Microbiology*, **12**, 363-374.

Beyer, M., Pogoda, F., Ronellenfitsch, F.K., Hoffmann, L. & Udelhoven, T. (2010). Estimating deoxynivalenol contents of wheat samples containing different levels of *Fusarium*-damaged kernels by diffuse reflectance spectrometry and partial least square regression. *International Journal of Food Microbiology*, **142**, 370-374.

Bharati, M.H., Liu, J.J. & MacGregor, J.F. (2004). Image texture analysis: methods and comparisons. *Chemometrics and Intelligent Laboratory Systems*, **72**, 57-71.

Boldrini, B., Kessler, W., Rebner, K. & Kessler, R. (2012). Hyperspectral imaging: a review of best practice, performance and pitfalls for inline and online applications. *Journal of Near Infrared Spectroscopy*, **20**, 438-508.

Boutigny, A.L., Beukes, I., Small, I., Zühlke, S., Spiteller, M., Van Rensburg, B.J., Flett, B. & Viljoen, A. (2012). Quantitative detection of *Fusarium* pathogens and their mycotoxins in South African maize. *Plant Pathology*, **61**, 522-531.

Burger, J. & Geladi, P. (2006). Hyperspectral NIR imaging for calibration and prediction: a comparison between image and spectrometer data for studying organic and biological samples. *Analyst*, **131**, 1152-1160.

Burger, J. & Geladi, P. (2007a). Hyperspectral image data conditioning and regression analysis. In: *Techniques and applications of hyperspectral image analysis* (edited by H.F. Grahn & P. Geladi). Pp. 127-153. Chichester, West Sussex, England: John Wiley & Sons, Ltd.

Burger, J. & Geladi, P. (2007b). Spectral pre-treatments of hyperspectral near infrared images: analysis of diffuse reflectance scattering. *Journal of Near Infrared Spectroscopy*, **15**, 29.

Burger, J. & Gowen, A. (2011). Data handling in hyperspectral image analysis. *Chemometrics and Intelligent Laboratory Systems*, **108**, 13-22.

Candlish, A.A.G. (1991). Immunological methods in food microbiology. *Food Microbiology*, **8**, 1-14.

Candrian, U. (1995). Polymerase chain reaction in food microbiology. *Journal of Microbiological Methods*, **23**, 89-103.

Cen, H.Y. & He, Y. (2007). Theory and application of near infrared reflectance spectroscopy in determination of food quality. *Trends in Food Science and Technology*, **18**, 72-83.

Chawanji, A.S., Baldwin, A.J., Brisson, G. & Webster, E. (2012). Use of X-ray micro tomography to study the microstructure of loose-packed and compacted milk powders. *Journal of Microscopy*, **248**, 49-57.

Chen, S., Yee, A., Griffiths, M., Larkin, C., Yamashiro, C.T., Behari, R., Paszko-Kolva, C., Rahn, K. & De Grandis, S.A. (1997). The evaluation of a fluorogenic polymerase chain reaction assay for the detection of *Salmonella* species in food commodities. *International Journal of Food Microbiology*, **35**, 239-250.

Chevallier, S., Bertrand, D., Kohler, A. & Courcoux, P. (2006). Application of PLS-DA in multivariate image analysis. *Journal of Chemometrics*, **20**, 221-229.

Choudhary, R., Mahesh, S., Paliwal, J. & Jayas, D.S. (2009). Identification of wheat classes using wavelet features from near infrared hyperspectral images of bulk samples. *Biosystems Engineering*, **102**, 115-127.

Chu, F.S. (1991). Mycotoxins: food contamination, mechanism, carcinogenic potential and preventive measures. *Mutation Research/Genetic Toxicology*, **259**, 291-306.

Cleveland (IV), T.E., Hussey, D.S., Chen, Z.Y., Jacobson, D.L., Brown, R.L., Carter-Wientjes, C., Cleveland, T.E. & Arif, M. (2008). The use of neutron tomography for the structural analysis of corn kernels. *Journal of Cereal Science*, **48**, 517-525.

Cowe, I. & McNicol, J. (1985). The use of principal components in the analysis of near-infrared spectra. *Applied Spectroscopy*, **39**, 257-266.

de Boer, E. & Beumer, R.R. (1999). Methodology for detection and typing of foodborne microorganisms. *International Journal of Food Microbiology*, **50**, 119-130.

Deisingh, A.K. & Thompson, M. (2002). Detection of infectious and toxigenic bacteria. *Analyst*, **127**, 567-581.

Del Fiore, A., Reverberi, M., De Rossi, P., Tolaini, V., Fabbri, A.A. & Fanelli, C. (2010a). Polymerase chain reaction-based assay for the early detection of aflatoxigenic fungi on maize kernels. *Quality Assurance and Safety of Crops and Foods*, **2**, 22-27.

Del Fiore, A., Reverberi, M., Ricelli, A., Pinzari, F., Serranti, S., Fabbri, A.A., Bonifazi, G. & Fanelli, C. (2010b). Early detection of toxigenic fungi on maize by hyperspectral imaging analysis. *International Journal of Food Microbiology*, **144**, 64-71.

Delwiche, S., Kim, M. & Dong, Y. (2011). *Fusarium* damage assessment in wheat kernels by Vis/NIR hyperspectral imaging. *Sensing and Instrumentation for Food Quality and Safety*, **5**, 63-71.

Dissing, B.S., Papadopoulou, O.S., Tassou, C., Ersbøll, B.K., Carstensen, J.M., Panagou, E.Z. & Nychas, G.-J. (2012). Using multispectral imaging for spoilage detection of pork meat. *Food and Bioprocess Technology*, 1-12.

Dowell, F., Maghirang, E., Graybosch, R., Baenziger, P., Baltensperger, D. & Hansen, L. (2006). An automated near-infrared system for selecting individual kernels based on specific quality characteristics. *Cereal Chemistry*, **83**, 537-543.

Dowell, F., Ram, M. & Seitz, L. (1999). Predicting scab, vomitoxin, and ergosterol in single wheat kernels using near-infrared spectroscopy. *Cereal Chemistry*, **76**, 573-576.

Dowell, F.E., Pearson, T.C., Maghirang, E.B., Xie, F. & Wicklow, D.T. (2002). Reflectance and transmittance spectroscopy applied to detecting fumonisin in single corn kernels infected with *Fusarium verticillioides*. *Cereal Chemistry*, **79**, 222-226.

Du, C.-J. & Sun, D.-W. (2004). Recent developments in the applications of image processing techniques for food quality evaluation. *Trends in Food Science and Technology*, **15**, 230-249.

Dubois, J., Neil Lewis, E., Fry Jr, F.S. & Calvey, E.M. (2005). Bacterial identification by near-infrared chemical imaging of food-specific cards. *Food Microbiology*, **22**, 577-583.

Elmasry, G., Barbin, D.F., Sun, D.-W. & Allen, P. (2011). Meat quality evaluation by hyperspectral imaging technique: an overview. *Critical Reviews in Food Science and Nutrition*, **52**, 689-711.

Elmasry, G., Kamruzzaman, M., Sun, D.W. & Allen, P. (2012). Principles and applications of hyperspectral imaging in quality evaluation of agro-food products: a review. *Critical Reviews in Food Science and Nutrition*, **52**, 999-1023.

ElMasry, G. & Sun, D.-W. (2010). Principles of hyperspectral imaging technology. In: *Hyperspectral Imaging for Food Quality Analysis and Control* (edited by S. Professor Da-Wen). Pp. 3-43. San Diego: Academic Press.

Elmerdahl Olsen, J. (2000). DNA-based methods for detection of food-borne bacterial pathogens. *Food Research International*, **33**, 257-266.

Ercolini, D. (2004). PCR-DGGE fingerprinting: novel strategies for detection of microbes in food. *Journal of Microbiological Methods*, **56**, 297-314.

Fandohan, P., Hell, K., Marasas, W. & Wingfield, M. (2003). Infection of maize by *Fusarium* species and contamination with fumonisin in Africa. *African Journal of Biotechnology*, **2**, 570-579.

Farber, J. & Peterkin, P. (1991). Listeria monocytogenes, a food-borne pathogen. *Microbiological reviews*, **55**, 476.

Feng, P. (1997). Impact of molecular biology on the detection of foodborne pathogens. *Molecular Biotechnology*, **7**, 267-278.

Feng, Y.-Z. & Sun, D.-W. (2012). Application of hyperspectral imaging in food safety inspection and control: a review. *Critical Reviews in Food Science and Nutrition*, **52**, 1039-1058.

Fernández-Ibañez, V., Soldado, A., Martínez-Fernández, A. & de la Roza-Delgado, B. (2009). Application of near infrared spectroscopy for rapid detection of aflatoxin B1 in maize and barley as analytical quality assessment. *Food Chemistry*, **113**, 629-634.

Firrao, G., Torelli, E., Gobbi, E., Raranciuc, S., Bianchi, G. & Locci, R. (2010). Prediction of milled maize fumonisin contamination by multispectral image analysis. *Journal of Cereal Science*, **52**, 327-330.

Frisullo, P., Barnabà, M., Navarini, L. & Del Nobile, M.A. (2012a). Coffea arabica beans microstructural changes induced by roasting: an X-ray microtomographic investigation. *Journal of Food Engineering*, **108**, 232-237.

Frisullo, P., Laverse, J., Barnabà, M., Navarini, L. & Del Nobile, M.A. (2012b). Coffee beans microstructural changes induced by cultivation processing: an X-ray microtomographic investigation. *Journal of Food Engineering*, **109**, 175-181.

Frisullo, P., Laverse, J., Marino, R. & Nobile, M.A.D. (2009). X-ray computed tomography to study processed meat microstructure. *Journal of Food Engineering*, **94**, 283-289.

Frisullo, P., Marino, R., Laverse, J., Albenzio, M. & Del Nobile, M.A. (2010). Assessment of intramuscular fat level and distribution in beef muscles using X-ray microcomputed tomography. *Meat Science*, **85**, 250-255.

Fung, D.Y.C. (2000). Rapid methods and automation in microbiology: a review. *Irish Journal of Agricultural and Food Research*, **39**, 301-307.

Fung, F. & Clark, R.F. (2004). Health effects of mycotoxins: a toxicological overview. *Clinical Toxicology*, **42**, 217-234.

Gadkari, D. (2004). *Image quality analysis using GLCM. MSc in Modeling and Simulation*. University of Central Florida, Orlando, Florida, USA.

Gehring, A.G., Albin, D.M., Bhunia, A.K., Kim, H., Reed, S.A. & Tu, S.-I. (2012). Mixed culture enrichment of *Escherichia coli* O157:H7, *Listeria monocytogenes*, *Salmonella enterica*, and *Yersinia enterocolitica*. *Food Control*, **26**, 269-273.

Geladi, P., Burger, J. & Lestander, T. (2004). Hyperspectral imaging: calibration problems and solutions. *Chemometrics and Intelligent Laboratory Systems*, **72**, 209-217.

Geladi, P. & Grahn, H.F. (1996). *Multivariate image analysis.* Chichester, West Sussex: John Wiley & Sons Ltd.

Geladi, P., Grahn, H.F. & Burger, J. (2007). Multivariate images, hyperspectral imaging: background and equipment. In: *Techniques and applications of hyperspectral image analysis* (edited by H.F. Grahn & P. Geladi). Pp. 1-14. Chichester, West Sussex: John Wiley & Sons Ltd.

Geladi, P., MacDougall, D. & Martens, H. (1985). Linearization and scatter-correction for near-infrared reflectance spectra of meat. *Applied Spectroscopy*, **39**, 491-500.

Gelderblom, W.C.A., Abel, S., Smuts, C.M., Marnewick, J., Marasas, W.F.O., Lemmer, E.R. & Ramljak, D. (2001a). Fumonisin induced hepatocarcinogenesis: mechanisms related to cancer initiation and promotion. *Environmental Health Perspectives*, **109**, 291-300.

Gelderblom, W.C.A., Jaskiewicz, K., Marasas, W.F.O., Thiel, P.G., Horak, R.M., Vleggaar, R. & Kriek, N.P.J. (1988). Fumonisins novel mycotoxins with cancer-promoting activity produced by *Fusarium moniliforme*. *Applied and Environmental Microbiology*, **54**, 1806-1811.

Gelderblom, W.C.A., Rheeder, J.P., Leggott, N., Stockenstrom, S., Humphreys, J., Shephard, G.S. & Marasas, W.F.O. (2004). Fumonisin contamination of a corn sample associated with the induction of hepatocarcinogenesis in rats-role of dietary deficiencies. *Food and Chemical Toxicology*, **42**, 471-479.

Gelderblom, W.C.A., Seier, J.V., Snijman, P.W., Van Schalkwyk, D.J., Shephard, G.S. & Marasas, W.F.O. (2001b). Toxicity of culture material of *Fusarium verticillioides* strain MRC 826 to nonhuman primates. *Environmental Health Perspectives*, **109**, 267-276.

Goetz, A.F., Vane, G., Solomon, J.E. & Rock, B.N. (1985). Imaging spectrometry for Earth remote sensing. *Science*, **228**, 1147-1153.

Gowen, A.A., O'Donnell, C.P., Cullen, P.J. & Bell, S.E.J. (2008). Recent applications of chemical imaging to pharmaceutical process monitoring and quality control. *European Journal of Pharmaceutics and Biopharmaceutics*, **69**, 10-22.

Gowen, A.A., O'Donnell, C.P., Cullen, P.J., Downey, G. & Frias, J.M. (2007). Hyperspectral imaging: an emerging process analytical tool for food quality and safety control. *Trends in Food Science and Technology*, **18**, 590-598.

Gracias, K.S. & McKillip, J.L. (2004). A review of conventional detection and enumeration methods for pathogenic bacteria in food. *Canadian Journal of Microbiology*, **50**, 883-890.

Haff, R. & Toyofuku, N. (2008). X-ray detection of defects and contaminants in the food industry. *Sensing and Instrumentation for Food Quality and Safety*, **2**, 262-273.

Haff, R.P. & Slaughter, D.C. (2004). Real-time x-ray inspection of wheat for infestation by the granary weevil, *Sitophilus granarius* (L.). *Transactions of the ASAE*, **47**, 531-537.

Hahn, F. (2002). Fungal spore detection on tomatoes using spectral fourier signatures. *Biosystems Engineering*, **81**, 249-259.

Hanna, S.E., Connor, C.J. & Wang, H.H. (2005). Real-time polymerase chain reaction for the food microbiologist: technologies, applications, and limitations. *Journal of Food Science*, **70**, R49-R53.

Hansen, T.J. (1990). Immunochemical methods for mycotoxin detection in food products. *Trends in Food Science and Technology*, **1**, 83-88.

Haralick, R.M. (1979). Statistical and structural approaches to texture. *Proceedings of the IEEE*, **67**, 786-804.

Haralick, R.M., Shanmugam, K. & Dinstein, I.H. (1973). Textural features for image classification. *IEEE Transactions on Systems, Man and Cybernetics*, **3**, 610-621.

Hayes, P.S., Feeley, J.C., Graves, L.M., Ajello, G.W. & Fleming, D.W. (1986). Isolation of *Listeria monocytogenes* from raw milk. *Applied and Environmental Microbiology*, **51**, 438-440.

Hellin, J., Shiferaw, B., Cairns, J.E., Reynolds, M., Ortiz-Monasterio, I., Banziger, M., Sonder, K. & La Rovere, R. (2012). Climate change and food security in the developing world: potential of maize and wheat research to expand options for adaptation and mitigation. *Journal of Development and Agricultural Economics*, **4**, 311-321.

Hotz, C. & Gibson, R.S. (2001). Assessment of home-based processing methods to reduce the phytate content and phytate/zinc molar ratio of white maize (*Zea mays*). *Journal of Agricultural and Food Chemistry*, **49**, 692-698.

Huang, H., Yu, H., Xu, H. & Ying, Y. (2008). Near infrared spectroscopy for on/in-line monitoring of quality in foods and beverages: A review. *Journal of Food Engineering*, **87**, 303-313.

Jayas, D.S., Paliwal, J. & Visen, N.S. (2000). Multi-layer neural networks for image analysis of agricultural products. *Journal of Agricultural Engineering Research*, **77**, 119-128.

Kak, A.C. & Slaney, M. (1988). *Computerized tomographic imaging.* Pp. 344. New York: The Institute of Electrical and Electronics Engineers, Inc.

Karunakaran, C., Jayas, D.S. & White, N.D.G. (2004). Detection of internal wheat seed infestation by *Rhyzopertha dominica* using X-ray imaging. *Journal of Stored Products Research*, **40**, 507-516.

Koehler, F.W., Lee, E., Kidder, L.H. & Lewis, N.E. (2002). Near infrared spectroscopy: the practical chemical imaging solution. *Spectroscopy Europe*, **14**, 12-19.

Kotwaliwale, N., Singh, K., Kalne, A., Jha, S.N., Seth, N. & Kar, A. (2011). X-ray imaging methods for internal quality evaluation of agricultural produce. *Journal of Food Science and Technology*, http://dx.doi.org/10.1007/s13197-13011-10485-y.

Laddi, A., Sharma, S., Kumar, A. & Kapur, P. (2013). Classification of tea grains based upon image texture feature analysis under different illumination conditions. *Journal of Food Engineering*, **115**, 226-231.

Laverse, J., Mastromatteo, M., Frisullo, P. & Del Nobile, M.A. (2012). X-ray microtomography to study the microstructure of mayonnaise. *Journal of Food Engineering*, **108**, 225-231.

Lazcka, O., Campo, F.J.D. & Muñoz, F.X. (2007). Pathogen detection: a perspective of traditional methods and biosensors. *Biosensors and Bioelectronics*, **22**, 1205-1217.

Lidia, E.A., Ellis, D.D., Duvick, S., Goggi, A.S., Hurburgh, C.R. & Gardner, C.A. (2012). Feasibility of near infrared spectroscopy for analyzing corn kernel damage and viability of soybean and corn kernels. *Journal of Cereal Science*, **55**, 160-165.

Lim, K.S. & Barigou, M. (2004). X-ray micro-computed tomography of cellular food products. *Food Research International*, **37**, 1001-1012.

Lin, M., Al-Holy, M., Mousavi-Hesary, M., Al-Qadiri, H., Cavinato, A.G. & Rasco, B.A. (2004). Rapid and quantitative detection of the microbial spoilage in chicken meat by diffuse reflectance spectroscopy (600–1100 nm). *Letters in Applied Microbiology*, **39**, 148-155.

Lindqvist, R. (1999). Detection of *Shigella* spp. in food with a nested PCR method – sensitivity and performance compared with a conventional culture method. *Journal of Applied Microbiology*, **86**, 971-978.

Liu, Y. & Rayens, W. (2007). PLS and dimension reduction for classification. *Computational Statistics*, **22**, 189-208.

Malvar, R.A., Revilla, P., Moreno-Gonzalez, J., Butron, A., Sotelo, J. & Ordas, A. (2008). White maize: genetics of quality and agronomic performance. *Crop Science*, **48**, 1373-1381.

Mandal, P., Biswas, A., Choi, K. & Pal, U. (2011). Methods for rapid detection of foodborne pathogens: an overview. *American Journal of Food Technology*, **6**, 87-102.

Marasas, W.F.O. (2001). Discovery and occurence of the fumonisins: a historical perspective. *Environmental Health Perspectives*, **109**, 239-243.

Martens, H. (2001). Reliable and relevant modelling of real world data: a personal account of the development of PLS Regression. *Chemometrics and Intelligent Laboratory Systems*, **58**, 85-95.

McCullough, E.C. (1975). Photon attenuation in computed tomography. *Medical physics*, **2**, 307-320.

McLandsborough, L. (2005). *Food microbiology laboratory.* Pp. 173. Boca Raton: CRC Press.

Mebatsion, H.K., Verboven, P., Melese Endalew, A., Billen, J., Ho, Q.T. & Nicolaï, B.M. (2009). A novel method for 3-D microstructure modeling of pome fruit tissue using synchrotron radiation tomography images. *Journal of Food Engineering*, **93**, 141-148.

Meirelles, P.G., Ono, M.A., Ohe, M.C.T., Maroneze, D.M., Itano, E.N., Garcia, G.T., Sugiura, Y., Ueno, Y., Hirooka, E.Y. & Ono, E.Y.S. (2006). Detection of *Fusarium* sp. contamination in corn by enzyme-linked immunosorbent assay. *Food and Agricultural Immunology*, **17**, 79-89.

Merck (2007). *Microbiology Manual.* Darmstadt, Germany: Merck KGaA.

Moore, G., Devos, K.M., Wang, Z. & Gale, M.D. (1995). Cereal genome evolution: grasses, line up and form a circle. *Current Biology*, **5**, 737-739.

Muhammed, H.H. & Larsolle, A. (2003). Feature vector based analysis of hyperspectral crop reflectance data for discrimination and quantification of fungal disease severity in wheat. *Biosystems Engineering*, **86**, 125-134.

Narvankar, D.S., Singh, C.B., Jayas, D.S. & White, N.D.G. (2009). Assessment of soft X-ray imaging for detection of fungal infection in wheat. *Biosystems Engineering*, **103**, 49-56.

Neethirajan, S., Jayas, D.S. & White, N.D.G. (2007). Detection of sprouted wheat kernels using soft X-ray image analysis. *Journal of Food Engineering*, **81**, 509-513.

Neethirajan, S., Karunakaran, C., Jayas, D.S. & White, N.D.G. (2006). X-ray computed tomography image analysis to explain the airflow resistance differences in grain bulks. *Biosystems Engineering*, **94**, 545-555.

Nganje, W.E., Bangsund, D.A., Leistritz, F.L., Wilson, W.W. & Tiapo, N.M. (2004). Regional economic impacts of *Fusarium* head blight in wheat and barley. *Applied Economic Perspectives and Policy*, **26**, 332-347.

Nicolaï, B.M., Beullens, K., Bobelyn, E., Peirs, A., Saeys, W., Theron, K.I. & Lammertyn, J. (2007). Nondestructive measurement of fruit and vegetable quality by means of NIR spectroscopy: a review. *Postharvest Biology and Technology*, **46**, 99-118.

Nicolaisen, M., Suproniene, S., Nielsen, L.K., Lazzaro, I., Spliid, N.H. & Justesen, A.F. (2009). Real-time PCR for quantification of eleven individual *Fusarium* species in cereals. *Journal of Microbiological Methods*, **76**, 234-240.

Niederhauser, C., Candrian, U., Höfelein, C., Jermini, M., Bühler, H.P. & Lüthy, J. (1992). Use of polymerase chain reaction for detection of *Listeria monocytogenes* in food. *Applied and Environmental Microbiology*, **58**, 1564-1568.

Notermans, S. & Heuvelman, C.J. (1985). Immunological detection of moulds in food by using the enzyme-linked immunosorbent assay (ELISA); preparation of antigens. *International Journal of Food Microbiology*, **2**, 247-258.

Notermans, S. & Wernars, K. (1991). Immunological methods for detection of foodborne pathogens and their toxins. *International Journal of Food Microbiology*, **12**, 91-102.

Olsen, J.E., Aabo, S., Hill, W., Notermans, S., Wernars, K., Granum, P.E., Popovic, T., Rasmussen, H.N. & Olsvik, Ø. (1995). Probes and polymerase chain reaction for detection of food-borne bacterial pathogens. *International Journal of Food Microbiology*, **28**, 1-78.

Park, B., Kise, M., Lawrence, K., Windham, W., Smith, D. & Thai, C. (2007a). Real-time multispectral imaging system for online poultry fecal inspection using unified modeling language. *Sensing and Instrumentation for Food Quality and Safety*, **1**, 45-54.

Park, B., Lawrence, K., Windham, W. & Smith, D. (2004). Multispectral imaging system for fecal and ingesta detection on poultry carcasses. *Journal of Food Process Engineering*, **27**, 311-327.

Park, B., Lawrence, K., Windham, W. & Smith, D. (2006). Performance of hyperspectral imaging system for poultry surface fecal contaminant detection. *Journal of Food Engineering*, **75**, 340-348.

Park, B., Windham, W.R., Lawrence, K.C. & Smith, D.P. (2007b). Contaminant classification of poultry hyperspectral imagery using a spectral angle mapper algorithm. *Biosystems Engineering*, **96**, 323-333.

Park, B., Yoon, S.-C., Windham, W., Lawrence, K., Kim, M. & Chao, K. (2011). Line-scan hyperspectral imaging for real-time in-line poultry fecal detection. *Sensing and Instrumentation for Food Quality and Safety*, **5**, 25-32.

Pasikatan, M.C. & Dowell, F.E. (2001). Sorting systems based on optical methods for detecting and removing seeds infested internally by insects or fungi: a review. *Applied Spectroscopy Reviews*, **36**, 399-416.

Pasquini, C. (2003). Near Infrared Spectroscopy: fundamentals, practical aspects and analytical applications. *Journal of the Brazilian Chemical Society*, **14**, 198-219.

Pearson, T. (2009). Hardware-based image processing for high-speed inspection of grains. *Computers and Electronics in Agriculture*, **69**, 12-18.

Peng, Y.K., Zhang, J., Wang, W., Li, Y.Y., Wu, J.H., Huang, H., Gao, X.D. & Jiang, W.K. (2011). Potential prediction of the microbial spoilage of beef using spatially resolved hyperspectral scattering profiles. *Journal of Food Engineering*, **102**, 163-169.

Pittia, P., Sacchetti, G., Mancini, L., Voltolini, M., Sodini, N., Tromba, G. & Zanini, F. (2011). Evaluation of microstructural properties of coffee beans by synchrotron X-Ray microtomography: a methodological approach. *Journal of Food Science*, **76**, 222-231.

Pleadin, J., Perši, N., Zadravec, M., Sokolović, M., Vulić, A., Jaki, V. & Mitak, M. (2012). Correlation of deoxynivalenol and fumonisin concentration determined in maize by ELISA methods. *Journal of Immunoassay and Immunochemistry*, **33**, 414-421.

Polder, G., Van der Heijden, G., Waalwijk, C. & Young, I. (2005). Detection of *Fusarium* in single wheat kernels using spectral imaging. *Seed Science and Technology*, **33**, 655-668.

Postollec, F., Falentin, H., Pavan, S., Combrisson, J. & Sohier, D. (2011). Recent advances in quantitative PCR (qPCR) applications in food microbiology. *Food Microbiology*, **28**, 848-861.

Prieto, N., Roehe, R., Lavín, P., Batten, G. & Andrés, S. (2009). Application of near infrared reflectance spectroscopy to predict meat and meat products quality: A review. *Meat Science*, **83**, 175-186.

Ramana, M.V., Balakrishna, K., Murali, H.C.S. & Batra, H.V. (2011). Multiplex PCR-based strategy to detect contamination with mycotoxigenic *Fusarium* species in rice and fingermillet collected from southern India. *Journal of the Science of Food and Agriculture*, **91**, 1666-1673.

Rheeder, J.P., Marasas, W.F.O. & Vismer, H.F. (2002). Production of fumonisin analogs by *Fusarium* species. *Applied and Environmental Microbiology*, **68**, 2101-2105.

Rodriguez-Otero, J.L., Hermida, M. & Centeno, J. (1997). Analysis of dairy products by near-infrared spectroscopy: a review. *Journal of Agricultural and Food Chemistry*, **45**, 2815-2819.

Rodriguez-Saona, L.E., Khambaty, F.M., Fry, F.S. & Calvey, E.M. (2001). Rapid detection and identification of bacterial strains by fourier transform near-infrared spectroscopy. *Journal of Agricultural and Food Chemistry*, **49**, 574-579.

Roggo, Y., Chalus, P., Maurer, L., Lema-Martinez, C., Edmond, A. & Jent, N. (2007). A review of near infrared spectroscopy and chemometrics in pharmaceutical technologies. *Journal of Pharmaceutical and Biomedical Analysis*, **44**, 683-700.

Rosenfeld, A. (1984). Image analysis: Problems, progress and prospects. *Pattern Recognition*, **17**, 3-12.

Rossen, L., Nørskov, P., Holmstrøm, K. & Rasmussen, O.F. (1992). Inhibition of PCR by components of food samples, microbial diagnostic assays and DNA-extraction solutions. *International Journal of Food Microbiology*, **17**, 37-45.

Savitzky, A. & Golay, M. (1964). Smoothing and differentiation of data by simplified least squares procedures. *Analytical Chemistry*, **36**, 1627-1639.

Scheu, P.M., Berghof, K. & Stahl, U. (1998). Detection of pathogenic and spoilage micro-organisms in food with the polymerase chain reaction. *Food Microbiology*, **15**, 13-31.

Schierbaum, F. (2007). World corn production, uses and ending stocks: recorded figures for fiscal years 2004/05 and 2005/06. *Starch-Starke*, **59**, 192-195.

Schrank, I.S., Mores, M.A.Z., Costa, J.L.A., Frazzon, A.P.G., Soncini, R., Schrank, A., Vainstein, M.H. & Silva, S.C. (2001). Influence of enrichment media and application of a PCR based method to detect *Salmonella* in poultry industry products and clinical samples. *Veterinary Microbiology*, **82**, 45-53.

Scotter, C. (1990). Use of near infrared spectroscopy in the food industry with particular reference to its applications to on/in-line food processes. *Food Control*, **1**, 142-149.

Scotter, C.N.G. (1997). Non-destructive spectroscopic techniques for the measurement of food quality. *Trends in Food Science and Technology*, **8**, 285-292.

Shahin, M.A. & Symons, S.J. (2011). Detection of *Fusarium* damaged kernels in Canada Western Red Spring wheat using visible/near-infrared hyperspectral imaging and principal component analysis. *Computers and Electronics in Agriculture*, **75**, 107-112.

Shahin, M.A. & Symons, S.J. (2012). Detection of *Fusarium* damage in Canadian wheat using visible/near-infrared hyperspectral imaging. *Journal of Food Measurement and Characterization*, DOI 10.1007/s11694-11012-19126-z.

Shewry, P.R. (2007). Improving the protein content and composition of cereal grain. *Journal of Cereal Science*, **46**, 239-250.

Shiranita, K., Miyajima, T. & Takiyama, R. (1998). Determination of meat quality by texture analysis. *Pattern Recognition Letters*, **19**, 1319-1324.

Sidari, R. & Caridi, A. (2011). Methods for detecting enterohaemorrhagic *Escherichia coli* in food. *Food Reviews International*, **27**, 134-153.

Singh, C.B., Jayas, D.S., Paliwal, J. & White, N.D.G. (2009). Detection of sprouted and midge-damaged wheat kernels using near infrared hyperspectral imaging. *Cereal Chemistry*, **86**, 256-260.

Singh, C.B., Jayas, D.S., Paliwal, J. & White, N.D.G. (2010). Detection of midge-damaged wheat kernels using short-wave near-infrared hyperspectral and digital colour imaging. *Biosystems Engineering*, **105**, 380-387.

Singh, C.B., Jayas, D.S., Paliwal, J. & White, N.D.G. (2011). Fungal damage detection in wheat using short-wave near-infrared hyperspectral and digital colour imaging. *International Journal of Food Properties*, **15**, 11-24.

Siripatrawan, U., Makino, Y., Kawagoe, Y. & Oshita, S. (2011). Rapid detection of *Escherichia coli* contamination in packaged fresh spinach using hyperspectral imaging. *Talanta*, **85**, 276-281.

Suthiluk, P., Saranwong, S., Kawano, S., Numthuam, S. & Satake, T. (2008). Possibility of using near infrared spectroscopy for evaluation of bacterial contamination in shredded cabbage. *International Journal of Food Science and Technology*, **43**, 160-165.

Swaminathan, B. & Feng, P. (1994). Rapid detection of food-borne pathogenic bacteria. *Annual Review of Microbiology*, **48**, 401-426.

Sydenham, E.W., Gelderblom, W.C.A., Thiel, P.G. & Marasas, W.F.O. (1990). Evidence for the natural occurrence of fumonisin-B1, a mycotoxin produced by *Fusarium moniliforme*, in corn. *Journal of Agricultural and Food Chemistry*, **38**, 285-290.

Thomas, P., Kannan, A., Degwekar, V.H. & Ramamurthy, M.S. (1995). Non-destructive detection of seed weevil-infested mango fruits by X-ray imaging. *Postharvest Biology and Technology*, **5**, 161-165.

Thomas, P., Saxena, S., Chandra, R., Rao, R. & Bhatia, C. (1993). X-ray imaging for detecting spongy tissue, an internal disorder in fruits of Alphonso mango (*Mangifera indica L.*). *Journal of Horticultural Science and Biotechnology*, **68**, 803-806.

Thrane, U. (1996). Comparison of three selective media for detecting *Fusarium* species in foods: a collaborative study. *International Journal of Food Microbiology*, **29**, 149-156.

Tsai, G.-J. & Yu, S.-C. (1999). Detecting *Aspergillus parasiticus* in cereals by an enzyme-linked immunosorbent assay. *International Journal of Food Microbiology*, **50**, 181-189.

Tuceryan, M. & Jain, A.K. (1993). Texture analysis. In: *Handbook of pattern recognition and computer vision* (edited by C.H. Chen, L.F. Pau & P.S.P. Wang). Pp. 235-276. World Scientific Publishing Company.

van Netten, P. & Kramer, J.M. (1992). Media for the detection and enumeration of *Bacillus cereus* in foods: a review. *International Journal of Food Microbiology*, **17**, 85-99.

Van Rensburg, B.J. (2006). *Distribution and quantification of Fusarium verticillioides in South African maize and its effect on grain quality and toxicity*. *MSc in Environmental Sciences*. North-West University, Potchefstroom, South Africa.

Velusamy, V., Arshak, K., Korostynska, O., Oliwa, K. & Adley, C. (2010). An overview of foodborne pathogen detection: in the perspective of biosensors. *Biotechnology Advances*, **28**, 232-254.

Vermeulen, P., Pierna, J.A.F., van Egmond, H.P., Dardenne, P. & Baeten, V. (2011). Online detection and quantification of ergot bodies in cereals using near infrared hyperspectral imaging. *Food Additives and Contaminants: Part A*, **29**, 232-240.

Vlaemynck, G., Lafarge, V. & Scotter, S. (2000). Improvement of the detection of *Listeria monocytogenes* by the application of ALOA, a diagnostic, chromogenic isolation medium. *Journal of Applied Microbiology*, **88**, 430-441.

Vujanovic, V., Hamel, C., Jabaji-Hare, S. & St-Arnaud, M. (2002). Development of a selective myclobutanil agar (MBA) medium for the isolation of *Fusarium* species from asparagus fields. *Canadian Journal of Microbiology*, **48**, 841-847.

Wahr, J.A., Tremper, K.K., Samra, S. & Delpy, D.T. (1996). Near-Infrared spectroscopy: theory and applications. *Journal of Cardiothoracic and Vascular Anesthesia*, **10**, 406-418.

Williams, P., Manley, M., Fox, G. & Geladi, P. (2010). Indirect detection of *Fusarium verticillioides* in maize (*Zea mays* L.) kernels by near infrared hyperspectral imaging. *Journal of Near Infrared Spectroscopy*, **18**, 49-58.

Wold, S., Sjöström, M. & Eriksson, L. (2001). PLS-regression: a basic tool of chemometrics. *Chemometrics and Intelligent Laboratory Systems*, **58**, 109-130.

Woodcock, T., Downey, G. & O'Donnell, C. (2008). Better quality food and beverages: the role of near infrared spectroscopy. *Journal of Near Infrared Spectroscopy*, **16**, 1-29.

Wu, F. (2007). Measuring the economic impacts of *Fusarium* toxins in animal feeds. *Animal Feed Science and Technology*, **137**, 363-374.

Yang, Y., Chai, R. & He, Y. (2012). Early detection of rice blast (*Pyricularia*) at seedling stage in Nipponbare rice variety using near-infrared hyper-spectral image. *African Journal of Biotechnology*, **11**, 6809-6817.

Yao, H., Hruska, Z., Kincaid, R., Brown, R. & Cleveland, T. (2008). Differentiation of toxigenic fungi using hyperspectral imagery. *Sensing and Instrumentation for Food Quality and Safety*, **2**, 215-224.

Yaron, S. & Matthews, K.R. (2002). A reverse transcriptase-polymerase chain reaction assay for detection of viable *Escherichia coli* O157:H7: investigation of specific target genes. *Journal of Applied Microbiology*, **92**, 633-640.

Yoon, S., Lawrence, K., Line, J., Siragusa, G., Feldner, P., Park, B. & Windham, W. (2010). Detection of *Campylobacter* colonies using hyperspectral imaging. *Sensing and Instrumentation for Food Quality and Safety*, **4**, 35-49.

Zapotoczny, P. (2011). Discrimination of wheat grain varieties using image analysis and neural networks. Part I. Single kernel texture. *Journal of Cereal Science*, **54**, 60-68.

Zhang, J.-C., Pu, R.-l., Wang, J.-h., Huang, W.-j., Yuan, L. & Luo, J.-h. (2012). Detecting powdery mildew of winter wheat using leaf level hyperspectral measurements. *Computers and Electronics in Agriculture*, **85**, 13-23.

Zheng, C., Sun, D.-W. & Zheng, L. (2006a). Recent applications of image texture for evaluation of food qualities—a review. *Trends in Food Science and Technology*, **17**, 113-128.

Zheng, C., Sun, D.-W. & Zheng, L. (2006b). Recent developments and applications of image features for food quality evaluation and inspection – a review. *Trends in Food Science and Technology*, **17**, 642-655.

CHAPTER 3

INVESTIGATION OF FUNGAL DEVELOPMENT IN MAIZE KERNELS USING NIR HYPERSPECTRAL IMAGING AND MULTIVARIATE DATA ANALYSIS*

Abstract

Near infrared (NIR) hyperspectral imaging and hyperspectral image analysis were evaluated for their potential to track changes in fungal contamination on and fungal activity immediately under the surface of whole maize kernels (*Zea mays* L.) infected with *Fusarium verticillioides*. Hyperspectral images of clean and infected kernels were acquired using a SisuChema hyperspectral pushbroom imaging system with a spectral range of 1000-2498 nm at predetermined time intervals after infection. Background, bad pixels and shading of acquired absorbance images were removed using exploratory principal component analysis (PCA). When plotting PC4 against PC5, with percentage sum of squares (%SS) 0.49% and 0.34%, three distinct clusters were apparent in the score plot and this was associated with degree of infection. Loading line plots, with prominent peaks at 1900 nm and 2136 nm, confirmed that the source of variation was due to changes in starch and protein. Partial least squares (PLS) regression models, with time as the *Y* variable, were calculated and also indicated that changes over time were apparent. Variable importance plots (VIP) confirmed the peaks observed in the PCA loading line plots. More systematic future experiments are needed to confirm this, but it can already be concluded that early detection of fungal contamination and activity is possible.

*Published as: Williams, P.J., Geladi, P., Britz, T.J. & Manley, M. (2012). Investigation of fungal development in maize kernels using NIR hyperspectral imaging and multivariate data analysis. *Journal of Cereal Science*, **55**, 272-278.

Introduction

Maize (*Zea mays* L.) is a vital source of energy and is one of the most important dietary staple foods in the world (Schierbaum, 2007). It is used for human consumption in diverse forms, from specialised foods in developed countries, to staple food in undeveloped countries (Malvar *et al.*, 2008). In addition to being used for human consumption, maize is also used for animal feed.

Fusarium verticillioides, a pathogen of maize, is a concern primarily since it produces secondary metabolites toxic to animals and humans (Munkvold, 2003; Bacon *et al.*, 2008; Duncan & Howard, 2010). As it infects maize, which represents a significant component in the human food supply chain, the need for understanding the biology of host-pathogen interaction exists (Duncan & Howard, 2010). *Fusarium verticillioides* is an endophyte since its hyphae occur systemically in the leaves, stems, roots and cobs of the maize plant (Bacon *et al.*, 1992; Bacon & Hinton, 1996; Munkvold & Desjardins, 1997; Schulthess *et al.*, 2002; Fandohan *et al.*, 2003). *Fusarium verticillioides*, however, is capable of causing asymptomatic as well as symptomatic infections (Bacon *et al.*, 1992; Bacon & Hinton, 1996; Munkvold & Desjardins, 1997; Fandohan *et al.*, 2003). Thus, if the fungal contamination of maize plants and kernels is not detected early on, contamination in the form of mycotoxins can enter the food chain. *Fusarium* mycotoxins are a relevant problem in the cereal supply chain and are known to be carcinogenic to humans and animals. Many methods have been utilised to determine fungal contamination and the presence of fungi on cereals. Traditional methods include microbiological techniques (diagnostic media and microscopy) (Bacon *et al.*, 1992; Medina-Martinez & Martinez, 2000; Muthomi *et al.*, 2008) or immunological methods for detection of toxin (Sydenham *et al.*, 1996; Paepens *et al.*, 2004; Castells *et al.*, 2008). These techniques are known to be time consuming, labour intensive and to produce harmful by-products. They are also usually expensive.

Near infrared (NIR) hyperspectral imaging is an imaging technique in which spectral and spatial information are combined to obtain NIR hyperspectral images (Koehler *et al.*, 2002; Geladi *et al.*, 2004; Geladi *et al.*, 2007; Gowen *et al.*, 2007). NIR hyperspectral images are three-dimensional arrays of the form, $\mathbf{X}$ ($m \times n \times \lambda$), where m and n are the spatial axes information and the λ axis represents the spectral information. The 3-dimensional structure of the hypercube requires reorganisation to a 2-dimensional matrix, adapting the image for further pre-treatments. Statistical treatments such as principal component analysis (PCA), an unsupervised classification or dimensionality reduction technique (Cowe & McNicol, 1985), can be applied to the data. It reduces the data to a much smaller number of principal components (PCs) and can also be used as an exploratory technique. Principal component (PC) score images and score plots are used interactively to investigate sample images for special features or irregularities in samples. If anomalies are observed, during interpretation of cleaned images (irrelevant pixels have been removed), they will most likely be due to chemical variation. This observed variation can be explained by studying the accompanying loading line plots. Partial least squares regression (PLS) is a powerful regression technique that uses the latent variable approach to find the fundamental

relations between two matrices (**X** and **Y**) (Martens, 2001; Wold *et al.*, 2001; Liu & Rayens, 2007). PLS uses the y-data structure to decompose **X** so that the outcome constitutes an optimal regression vector.

NIR hyperspectral imaging is fast becoming an important non-destructive technique for the investigation of fungal contamination on cereals. It has been applied to maize kernels for the indirect detection of *Fusarium verticillioides* with accuracies up to 86% (Williams *et al.*, 2010). Using the visible-near infrared spectral range (400-1000 nm), hyperspectral imaging was investigated for the early detection of toxigenic fungi on maize (Del Fiore *et al.*, 2010). In another study, the application of multispectral imaging (720-940 nm) was studied to predict the fumonisin content of milled maize (Firrao *et al.*, 2010). Similar studies have been done on wheat, where a hyperspectral imaging system in the range of 400 to 1000 nm has been used to detect early infection by *Fusarium* (Bauriegel *et al.*, 2011). NIR hyperspectral imaging and support vector machines (SVM) have been evaluated for the classification of fungal infected wheat kernels with classification rates of 92.9% for *Aspergillus niger*; 87.2% for *A. glaucus* and 99.3% and 100% for two *Penicillium* species, respectively (Zhang *et al.*, 2007). In a similar study two-class and four-class classification models yielded classification rates of 97.8% and 95%, respectively, to distinguish between infected and non-infected wheat kernels.

The aim of this work was to detect fungal contamination of maize kernels prior to the appearance of visual symptoms and to monitor chemical changes associated with fungal activity using NIR hyperspectral imaging and multivariate data analysis techniques.

Material and Methods

Maize kernel sterilisation

White maize kernels of intermediate hardness were used for the study. Prior to any treatment, the kernels were randomly split into two groups, a) kernels to be sterilised (S) and (b) kernels without sterilisation, i.e. non-sterilised (NS). To completely remove both surface and internally borne fungi from the kernels, they were first surfaced sterilised by rinsing in a combination of 70% ethanol and 1% NaOCl solution followed by rinsing with sterile distilled water (dH_2O). Thereafter the sterilised kernels were imbibed in sterile dH_2O for 4 h, kept in a water bath at 60^{o}C for 5 min (Bacon *et al.*, 1994) and left to dry in a laminar flow for 1 h. The kernels were subsequently considered sterile and ready for inoculation. From each of the groups (S and NS), a subset was taken and used as controls (CS and CNS).

Fungal spore suspension and inoculation

Fungal spore suspensions were prepared from petri-dishes cultured with *F. verticillioides* (MRC 0826) kindly supplied by the Department of Plant Pathology, Stellenbosch University. Prior to spore preparation the culture was transferred onto potato dextrose agar (PDA) (Merck) and incubated at 28°C. After 7 days, sterile water with Tween 20 (6 drops.L^{-1}) was used to wash spores from the

agar surface. The spore suspension was poured through two layers of sterile cheesecloth to remove mycelium, thereafter the suspension was adjusted to 10^6 spores.mL^{-1} using a haemocytometer (Boeco, Germany). Finally the kernels (from groups S and NS) were inoculated by dipping into the spore suspension for 30 s and allowed to dry at room temperature. Thereafter 40 kernels (two sets of 20 each) randomly selected from each group were placed on two respective petri-dishes (20 kernels per petri-dish). On one petri-dish the kernels were orientated germ-up (U) while on the other the kernels were oriented germ-down (D). This was done for each treatment (SU, SD, NSU, NSD, CSU, CSD, CNSU and CNSD) after which the petri-dishes were incubated at 28°C. Each treatment therefore consisted of 2 petri-dishes; each with 20 kernels orientated either germ-up or germ-down. After the images were collected from all petri-dishes, one kernel was removed from the second petri-dish at each time interval. These were used to test for the presence of the fungus by placing the kernel onto PDA and incubating at 28°C for three days. This resulted in the second petri-dish of T8 only having 11 kernels available for validation.

NIR hyperspectral system and imaging

Hyperspectral images were acquired with the SisuChema short wave infrared (SWIR) camera (Specim, Spectral Imaging Ltd, Oulu, Finland). The camera comprised an imaging spectrograph coupled to a 2-D array Mercury-cadmium-telluride (HgCdTe) detector. Individual images were acquired within a spectral range of 1000-2500 nm at 10 nm resolution, spectral sampling per pixel of 6.3 nm and a field of view of 100 mm x 100 mm. Images of the entire petri-dish, without removing the lid, were collected to prevent contamination and were taken at predetermined time intervals after inoculation. Nine images (T0-T8) were collected at nine specified time intervals (0, 17, 20, 23, 26, 40, 43, 69, and 90 h). The time intervals indicate periods of time after inoculation. It would have been ideal to ensure the intervals to be evenly spread; due to technical issues (power failure) it was not possible. The power failure caused a problem with wavelength accuracy, therefore the 40 hr image, could not be used. White and dark references were captured prior to each sample image and were subsequently used for image correction and calibration. For the white reference a 100% standard (Spectralon, Labsphere, North Sutton NH, USA) was used and for the dark reference the shutter was closed.

Hyperspectral image analysis

Images were analysed using the Evince v.2.5.0 (UmBio AB, Umeå, Sweden) hyperspectral image analysis software package and MATLAB v 7.10 (The MathWorks, Massachusetts, USA). The image calibration and correction to absorbance was done automatically in the Evince software package according to equation 1:

$$I_{\lambda,n} = -\log_{10}\left[\left(\frac{S_{\lambda,n} - B_{\lambda,n}}{W_{\lambda,n} - B_{\lambda,n}}\right)\right] \quad \text{…[eq. 1]}$$

Where

n = pixel index variable (n = 1...N)

$I_{\lambda,n}$ = standardised absorbance intensity, pixel n, at wavelength λ

$S_{\lambda,n}$ = sample image, pixel n, at wavelength λ

$B_{\lambda,n}$ = dark reference image, pixel n, at wavelength λ

$W_{\lambda,n}$ = white reference image, pixel n, at wavelength λ

Individual images per treatment were merged to form a mosaic image. Each mosaic thus included the control and the respective images taken at each time interval for each treatment. A principal component analysis (PCA) model with six components was calculated for each of the mosaic images. Using the brushing technique (Manley *et al.*, 2009; Williams *et al.*, 2009; Williams *et al.*, 2010; Manley *et al.*, 2011); all irrelevant pixels were removed and PCA was recalculated on the cleaned images. PCA score plots, score images and loading line plots were used to locate and identify regions of interest.

For making partial least squares (PLS) regression models a dependent variable is needed. The only dependent variable available was time after inoculation and PLS models were calculated with time as the *Y* variable. Because the *y*-variable is the same for every pixel in an image taken at a certain time, it was decided to use the average spectrum (8 object model) instead of all individual spectra. This stabilises the models (Burger & Geladi, 2005), but leaves very few objects in the X-block. An improvement to this 8 object model was tried by splitting the images of the petri-dishes into four rectangular segments. This provides four average spectra for each time point and gives a data matrix comprising 32 objects.

PLS models with 8 objects were calculated for each treatment (SU, SD, NSU, NSD) individually. The models were calculated using the images of the first set of petri-dishes; excluding the control plates. Spectra of all kernels, within a treatment, were averaged for each time interval (0; 17; 20; 23; 26; 43; 69; 90 h). Calibration models were thus calculated on matrices of 8 x 206 with time interval as the *y*-vector. The *y*-vector models were independently validated on the second set of petri-dishes. Limited sample spectra were available to be used during validation for T6 to T8 due to kernels being removed from the second set of petri-dishes to confirm presence of fungi after each imaging interval. Therefore the validation set only comprised images of T0 to T4; not as many kernels were removed from the earlier time intervals. The validation set thus comprised matrices of 5 x 206. Standard normal variate (SNV) and mean centring was applied to all models. It was not ideal to develop a single model including all treatments (SU, SD, NSU, NSD) due to too large differences between the average spectra of the respective treatments. PLS models were thus evaluated individually for each treatment using the images of the first set of petri-dishes and independent validation was done on the second set of petri-dishes comprising different kernels.

For the 32 object PLS models, the images of each petri-dish were divided into quadrants (rectangles consisting of approximately the same amount of pixels), which were averaged resulting

in a total of 32 spectra. SNV and mean-centering were applied, the PLS models was calculated with 4 latent variables. The higher number of objects allowed the use of leave-one-out cross validation.

Results and discussion

Hyperspectral image analysis

Principal component analysis

PCA models with 6 PCs and 206 variables, for all mosaic images, yielded similar %SS (NSD 99.5; NSU 99.7; SD 99.6; SU 99.5) for all treatments. Once irrelevant pixels were removed, 112 559, 111 481, 109 975 and 94 677 pixels remained for NSD, NSU, SD and SU respectively. After evaluating the PCA score plots, score images and loading line plots, comparable results were found between the different treatments. For that reason, the PCA results for only one treatment (SU) will be presented in this paper.

Once irrelevant pixels were removed, including the pedicle and parts of the germ, score images were more interpretable. Using the brushing technique all possible combinations of score plots were evaluated with the corresponding score images. After evaluating loading line plots, it was observed that much disturbance and noise was apparent at the higher wavelengths from variables 207 to 242 (2285-2502 nm). This adversely affected the model as it was not possible to distinguish between the samples at the different time intervals. Score images of PC3 to PC6 could not be interpreted since they were extremely noisy. This could be attributed to NIR absorption by the plastic in the petri-dishes. To confirm this, pieces of a crushed polystyrene petri-dish were loaded in a FOSS NIRSystems sample holder and covered with a Spectralon reflective disk. The spectrum was measured with a FOSS NIRSystems 5000 spectrometer (FOSS NIRSystems, Inc. Laurel, MD, USA), from 1100-2498 nm with 2 nm steps, using a rotating sample holder. The obtained spectrum was the average of 32 scans. The resultant spectrum (Fig. 3.1a) showed strong absorption peaks in the 1660 nm and 1685 nm regions, C-H stretch first overtone related to a *cis*-RCH=CHR structure and C-H stretch first overtone associated with an aromatic structure, respectively (Osborne *et al.*, 1993). Both these features are abundant in the structure of polystyrene, hence the strong absorbance at these wavelengths. In addition a range of high absorbing peaks were observed in the region 2200 nm to 2500 nm also associated with double bonds. The presence of these peaks was prominent in the average spectra of the maize kernel images (Fig. 3.1b). These peaks are not typically present in the NIR spectra of maize kernels. These variables were thus removed from the mosaic images and excluded from subsequent calculations. The removal of these wavelengths vastly improved the score images and reduced the noise.

(a)

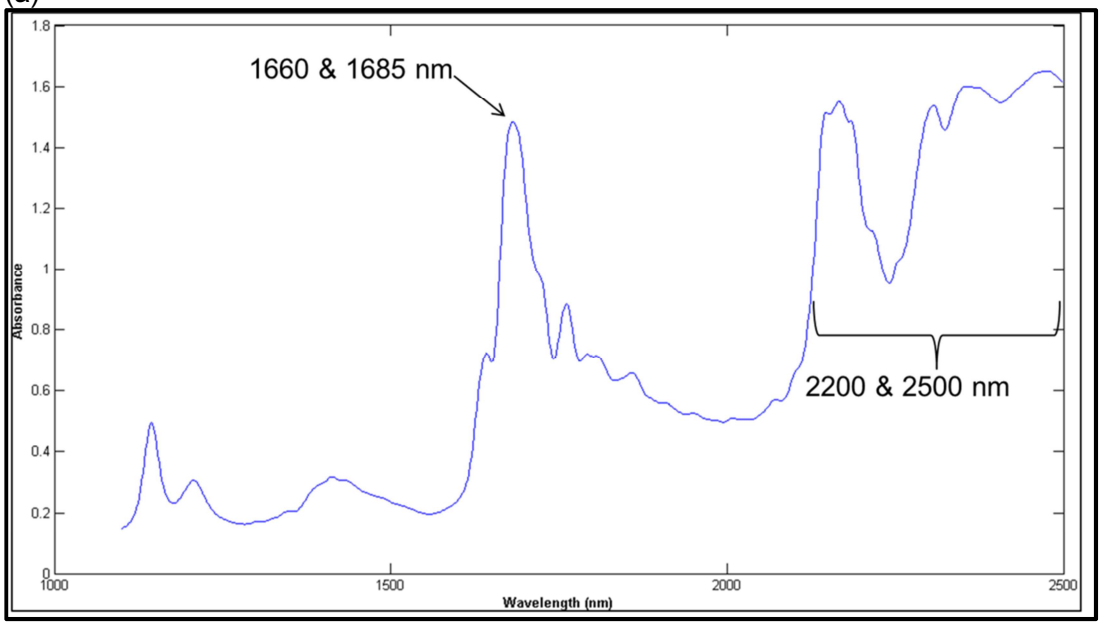

(b)

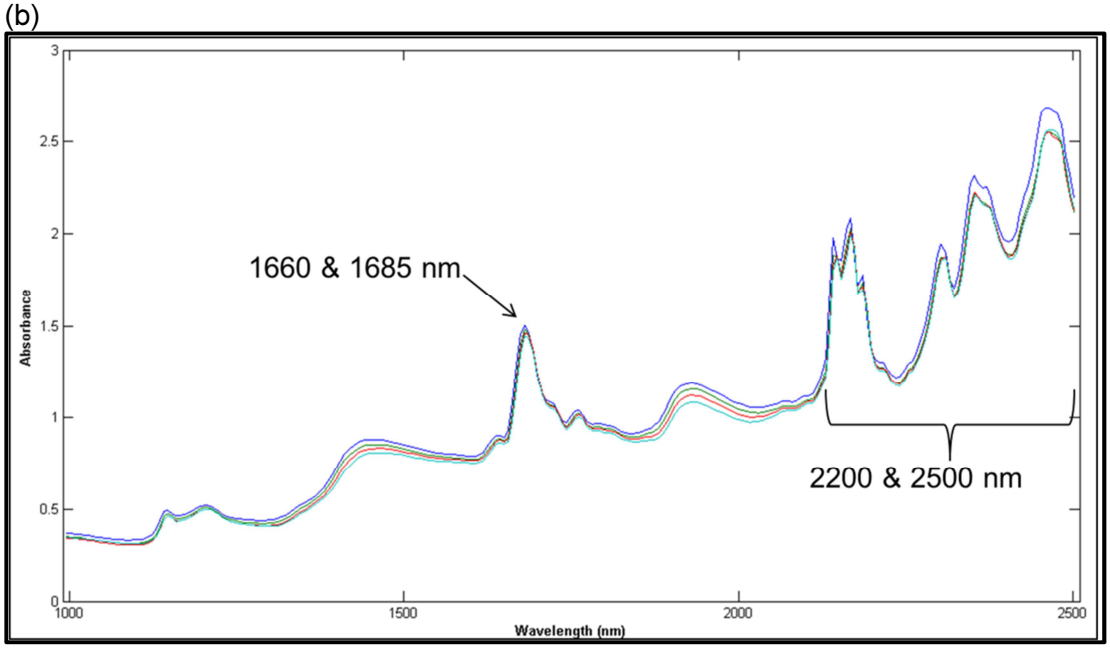

Figure 3.1. (a) Spectrum of a polystyrene petri-dish (blue) indicating prominent absorbance peaks in the 1660 nm and 1685 nm regions, C-H stretch first overtone related to a cis-RCH=CHR structure and C-H stretch first overtone associated with an aromatic structure, respectively. High absorption peaks were also observed from 2200 to 2500 nm associated with double bonds (HC=CH); (b) Mean spectra of selected maize kernels prior to removal of wavelengths 2285 to 2502 nm. Similar peaks to those found in the polystyrene spectrum are observed at 1660 nm and the region from 2200 to 2500 nm associated with HC=CH double and aromatic bonds.

In the new PCA models, when plotting PC4 against PC5 (%SS 0.49% and 0.34%), three distinct clusters were apparent in the score plot (Fig. 3.2a). In the score image of PC4 (Fig. 3.2b) there is a distinct decrease in score values from left to right *i.e.* from control kernels to kernels inoculated and incubated for 90 h. This is illustrated by the change in colour from red in the control

samples to blue in the kernels inoculated and incubated for 90 h. The brushing technique allowed the determination of the representation of each cluster in the score plot in the corresponding score image as the selected pixels in the score plot were subsequently highlighted in the score image. This technique was used to create classification plots, by assigning each cluster to a class in the score plot and projecting it onto the score image to form a classification image (Figs. 3.2c & d). The green cluster in the classification plot is associated with the control samples in the classification image; the black cluster is associated with T0 and T1 (T0&T1) while the red cluster is associated with the remaining time intervals. The single cluster (red) observed in the score plot for images collected after 20, 23, 26, 43, 69, and 90 h of inoculation indicates that little additional fungal contamination or activity change took place after 20 h of incubation (T2). In the classification plot (Fig. 3.2c) there is thus a change in degree of infection from right to left in the direction of PC4, i.e. from positive to negative score values. These changes, from the non-infected control samples (green cluster) to T0&T1 (black cluster) and then to those that have been incubated for longer periods of time (red cluster), i.e. longer than 20 h, can be described as an infection gradient. Since variation attributed to physical differences has been removed, these differences should be as a result of chemical changes on and immediately under the surface of the kernels; either due to the presence of fungal spores or changes caused by the proliferating fungi. This cause of variation can be established by interpreting the loading line plots.

The loading line plot for PC4 (Fig. 3.3) showed 3 prominent positive peaks at 1405 nm, 1668 nm and 1900 nm. The peak at 1405 nm, with an O-H stretch first overtone attributed to an ROH structure, is most likely associated with starch (Osborne *et al.*, 1993). The peak at 1668 nm, C-H stretch first overtone related to a *cis*-RCH=CHR structure, was associated with the petri-dish and the peak at 1900 nm, an O-H stretch + 2 x C-O stretch. A very prominent peak at 2136 nm was also apparent and most likely due to protein because of a N-H stretch and a C=O stretch associated with amino acid. It is clear that the main cause of variation is changes in starch and protein composition or contents. This could signal a decrease in levels of stored food reserves in the kernels as incubation time increased. It is known that *Fusarium* infection depletes food reserves for fungal growth (Boyacioglu & Hettiarachchy, 1995). In all other treatments similar results and trends were found even though variation may arise in the rate of infection in individual kernels.

PC1 to PC3 explained variation due to the effect of grain topography (kernel curvature, shape and texture) on spectral variation of NIR hyperspertral images. This effect was illustrated earlier using PCA and classification gradients (Manley *et al.*, 2012).

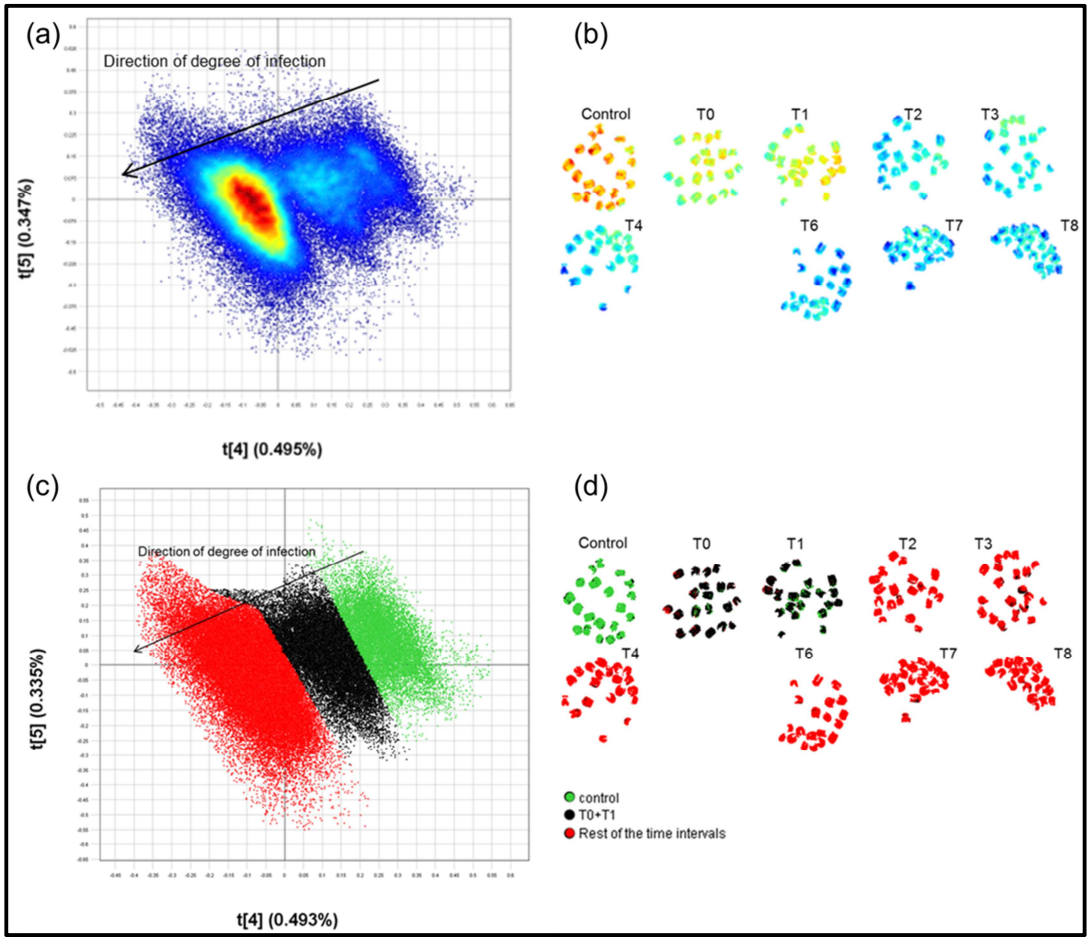

Figure 3.2. (a) PCA score plot of PC4 vs. PC5 (0.49% and 0.34%) showing three clusters and (b) corresponding score image of PC4 showing decrease in score values from left to right, where warm colours (yellow to red) correspond with positive score values and cold colours (blue) correspond to negative score. values; (c) classification plot of PC4 vs. PC5 with classes and degree of infection in the direction of PC4 and (d) classes projected onto score image showing the control (green), T0&T1 (black) and the remaining time intervals up to 90 h post inoculation (red).

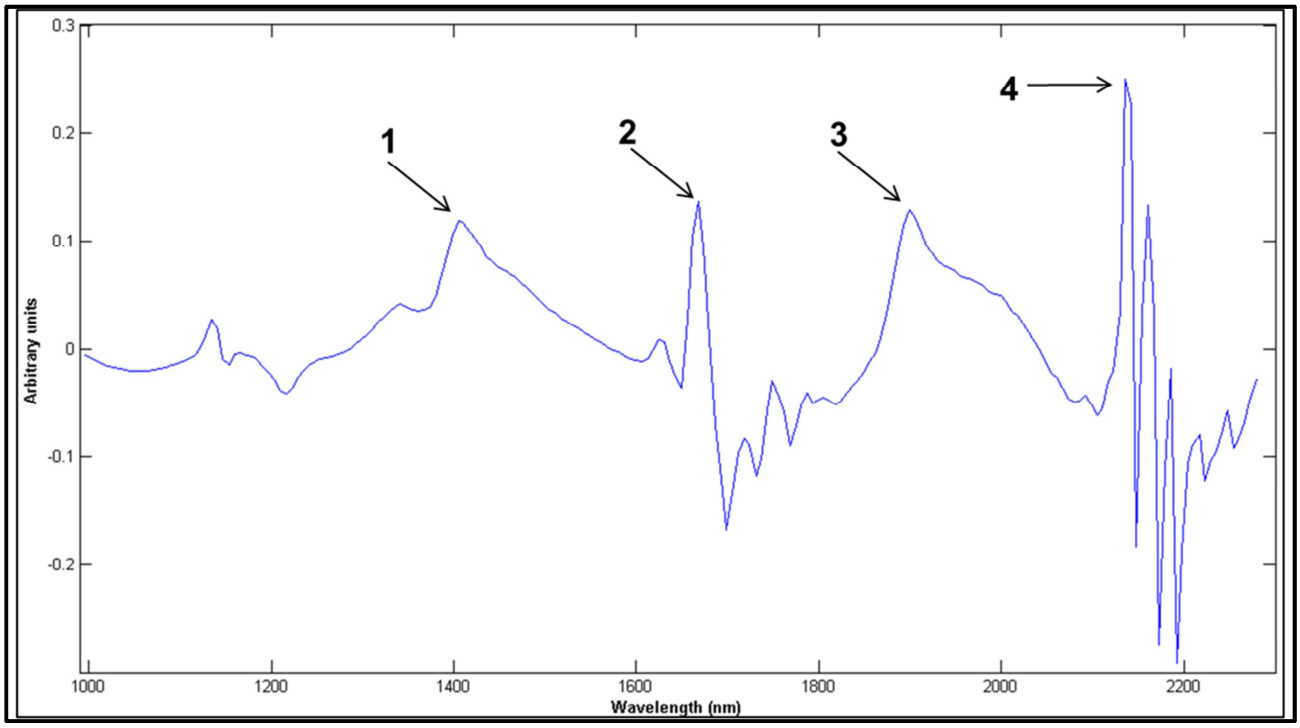

Figure 3.3 Loading line plot for PC4 illustrating 4 prominent positive peaks. (1) 1405 nm, O-H stretch first overtone attributed to an ROH structure, most likely associated with starch; (2) 1668 nm, C-H stretch first overtone related to a *cis*-RCH=CHR structure associated with the petri-dish and (3) 1900 nm, O-H stretch + 2 x C-O stretch associated with starch; and (4) 2136 nm, most likely due to protein because of an N-H stretch and a C=O stretch associated with amino acid.

Partial least squares regression

The PLS regression model statistics for both the 8 and 32 object models are depicted in Table. 3.1. Treatment NSD, for the 8 object model, had the best overall statistics and ability to predict degree of infection with an error of 7.4 h. There were deviations between the calibration and validation sets; however, most of these differences were within the range of the average spectra (Fig. 3.4a). This might seem a large error; however, this information can justify the trend in the score image of PC4, where it illustrates that after from T2 onwards there was no distinguishable difference between the remaining time intervals (T2 to T8). Thus from 20 h of inoculation the changes to be detected by NIR hyperspectral imaging seemed to have taken place and additional changes (if any) are not detected. Thus the main contrast is observed between the images of the control, T0&T1 and the images taken at the rest of the time intervals. The time intervals following 17 h of inoculation may be considered as a group since the difference between them and the control and T0&T1 is greater than the differences within the group (T2 to T8). In a similar study it was found that significant spectral differences were found between sterile kernels and kernels inoculated with *Aspergillus flavus* 3357 after 2 days of contamination (Del Fiore *et al.*, 2010).

Table. 3.1. PLS statistics for the model with 8 and 32 object models for all treatments

Sample	LV's	RMSEC [a]	RMSEP [a]	R^2	Q^{2} [b]
Models with 8 objects					
NSD [c]	3	4.0	7.4	0.98	0.80
SD1 [d]	4	4.2	7.0	0.98	0.71
SU [e]	4	3.7	8.2	0.98	0.63
NSU [f]	4	3.9	54.9	0.98	0.33
SD2 [g]	4	4.2	12.9	0.98	0.94
Sample	LV's	RMSEC[a]	RMSECV[a]	R^2	Q^{2} [b]
Models with 32 objects					
NSD [c]	4	9.3	13.2	0.89	0.78
SD1 [d]	4	7.6	10.4	0.92	0.86
SU [e]	2	8.7	9.9	0.98	0.87
NSU [f]	4	11.5	14.6	0.83	0.73

[a] Root Mean Square Error of Calibration and Root Mean Square Error of Prediction both measured in h

[b] Coefficient of determination for prediction or cross-validated data

[c] Non sterilised germ down

[d] Sterilised germ down

[e] Sterilised germ up

[f] Non-sterilised germ up

[g] Sterilised germ down, but validated with entire data set and not just T0-T4

(a) (b)

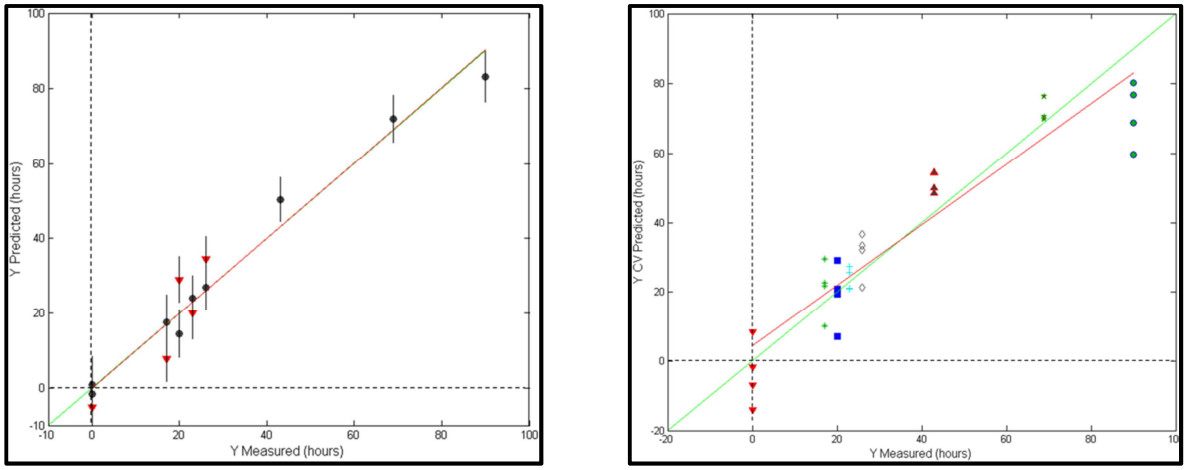

Figure 3.4. (a) Predicted time vs. measured time for the 8 object model for the NSD treatment with 3 PLS components and an RMSEP of 7.4 h; (b) Predicted time vs. measured time for the 32 object model for the SU treatment with 2 PLS components with a Q^2 of 0.87 and an RMSECV of 9.9 h.

In the present study differences were already apparent after 17 h (T1). Differences were not due to moisture as no moisture peaks were apparent in either the loading line plots or the regression vectors. In an earlier study a coefficient of determination (R^2) of 0.44, an RMSEP of 0.19 µg.kg^{-1} and a RPD of 0.88 were obtained for a linear regression model fitting image data with fumonisin content of maize flour (Firrao *et al.*, 2010). These images were not taken over time and degree of infection was not investigated. It does, however, show the potential of such models. In the current study, the PLS models, although done on few samples (8 objects), illustrated the potential of predicting degree of infection in addition to providing supplementary information to understand the PCA plots.

The NSU validated model performed inadequately and could not be used to predict degree of infection; this could be due to inconsistencies between the average spectra of the calibration set and the validation set. These inconsistencies could have been due to variation in image cleaning. This highlights the importance of accurate and consistent cleaning of images. The other treatments (SD and SU) performed reasonably well with Q^2 values (where Q^2 is the coefficient of determination for the prediction) of 0.71 and 0.63 respectively and RMSEP's of 7.0 h and 8.2 h respectively.

It was observed that treatments NSD and SD performed more effectively than SU and NSU, therefore indicating that, although not apparent in the PCA, orientation of the kernels, in terms of germ up or germ down, affects the model. This is most likely due to the interference of bonds related to oil which is predominantly found in the germ region; additionally the difference in topographic anatomy of germ side and the non-germ side could also have given rise to these discrepancies. The germ side is also more prone to shading and non-uniform scatter due to the presence of an indent and this of course varies from kernel to kernel since some kernels have

more pronounced indents than others. Treatment SD was also validated including images for the entire time series and not just from T0 to T4. This model had a very good coefficient of determination of 0.94, however the RMSEP (12.9 h) was high (Table. 3.1). Nevertheless, this still illustrates a linear change in the time series indicating degree of infection.

Variable importance plots (VIP) ascertain which variables had the most influence on a model and were subsequently studied. This technique is useful since the **b** vectors are dependent on **X** and are often complicated to interpret. The regression coefficients represent the importance each predictor has in the prediction of only the response. The VIP, on the other hand, represents the contribution of each predictor in fitting the PLS model for both **X** and **Y** (Wold *et al.*, 2001). This is a weighted sum of squares of the PLS-weights, with the weights calculated from the amount of Y-variance of each PLS component. The VIP for treatment NSD (Fig. 3.5) illustrates the same peaks as found in the loading line plot for PC4; 1405 nm (O-H stretch first overtone attributed to an ROH structure and most likely associated with starch); 1668 nm (C-H stretch first overtone related to a *cis*-RCH=CHR structure, associated with the petri-dish); 1900 nm (O-H stretch + 2 x C-O stretch); and 2136 nm (N-H stretch and a C=O stretch associated with amino acid, thus protein). This confirms that the differences in the time intervals are due to changes in the starch, most likely the depletion thereof as the fungus proliferates and more spores germinate.

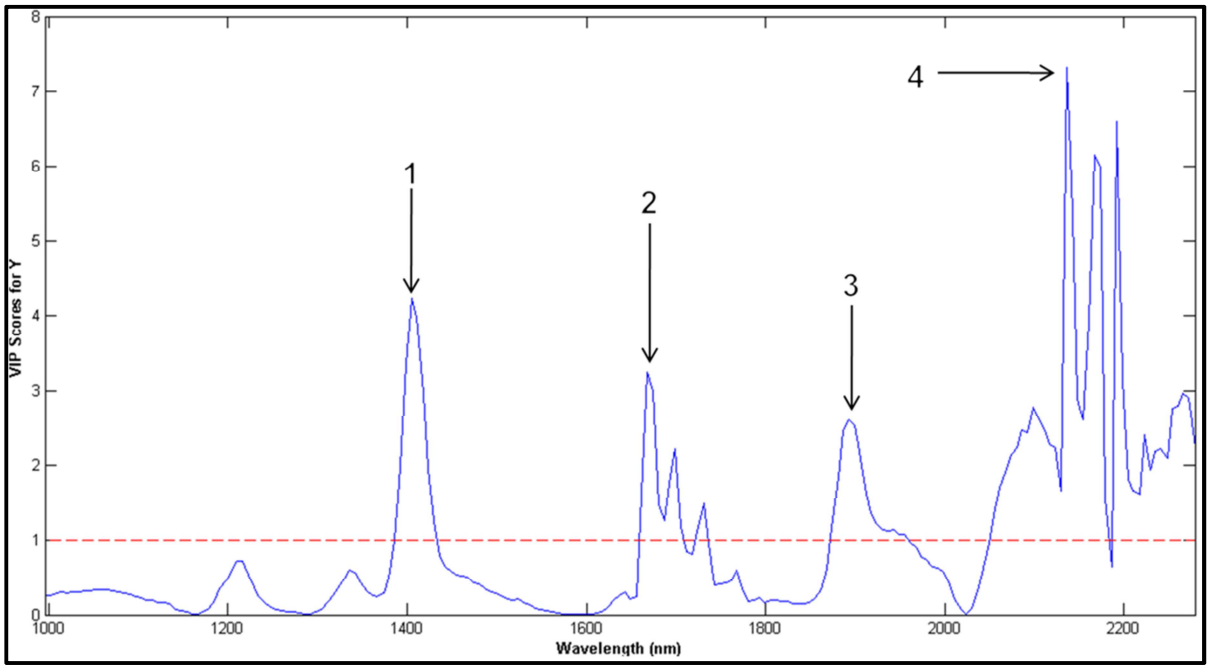

Figure 3.5 Variable importance plot of the Y-variables indicating the peaks 1405 nm (1), 1668 nm (2), 1900 nm (3) and 2136 nm (4) as observed also in the loading line plot of PC4.

The results for the 32 object models confirm that the model with only 8 objects are valid to illustrate potential of NIR hyperspectral imaging. Because the 8 petri-dish averages were now replaced by 32 averages (four quadrants per petri-dish), the RMSEC and RMSECV values are

higher, but the models are still of acceptable prediction accuracy as the Q^2 values improved with similar number of components (Table. 3.1; Fig. 3.4b).

The benefit of NIR hyperspectral imaging is the speed of measurement, *ca.* 10 seconds per petri-dish. The fungal infection could occur at any point on the kernel, thus one needs pixels covering the entire kernel to make a valid model. With the current method the entire sample is imaged at once and ca. 967 spectra per kernel are collected. Conventional or handheld spectrometers would require a large number of representative samples to be analysed and would need to be pointed correctly at the kernels. This could be time consuming difficult as maize kernels differ in size and shape.

Conclusion

Using NIR hyperspectral imaging it was possible to monitor changes in fungal infected maize kernels over time. PCA models, without pre-processing, showed three distinct clusters making it possible to discriminate between the images of the control, T0&T1 (17 h after inoculation) and the images of the samples inoculated for 20 to 90 h. Variables identified as vital to this study are 1405 nm (associated with starch); 1660-1668 nm (associated with an aromatic structure); 1900 nm (associated with starch; and 2136 nm (associated with protein).

To an extent, it was possible to establish PLS models that could predict degree of infection. Although a limited number of spectra were used for these models, it illustrates the potential of such an application. Variation between samples and within treatments negatively impacted models since biological samples vary from each other and each kernel may react differently to fungal invasion. An important observation that cannot be avoided when working with image data is image cleaning. This greatly affected the models developed and must be considered carefully as it often cannot be reproduced.

PCA models, where no time variable was included in building the model, and PLS models against the time variable gave comparable results. A comparable interpretation indicating infection that changes the starch structure or content was noted.

References

Bacon, C.W., Bennett, R.M., Hinton, D.M. & Voss, K.A. (1992). Scanning electron microscopy of *Fusarium moniliforme* within asymptomatic corn kernels and kernels associated with leukoencephalomalacia. *Plant Disease*, **76**, 144-148.

Bacon, C.W., Glenn, A.E. & Yates, I.E. (2008). *Fusarium verticillioides*: managing the endophytic association with maize for reduced fumonisins accumulation. *Toxin Reviews*, **27**, 411-446.

Bacon, C.W. & Hinton, D.M. (1996). Symptomless endophytic colonization of maize by *Fusarium moniliforme*. *Canadian Journal of Botany*, **74**, 1195-1202.

Bacon, C.W., Hinton, D.M. & Richardson, M.D. (1994). A corn seedling assay for resistance to *Fusarium moniliforme*. *Plant Disease*, **78**, 302-305.

Bauriegel, E., Giebel, A., Geyer, M., Schmidt, U. & Herppich, W.B. (2011). Early detection of *Fusarium* infection in wheat using hyper-spectral imaging. *Computers and Electronics in Agriculture*, **75**, 304-312.

Boyacioglu, D. & Hettiarachchy, N.S. (1995). Changes in some biochemical components of wheat grain that was infected with *Fusarium graminearum*. *Journal of Cereal Science*, **21**, 57-62.

Burger, J. & Geladi, P. (2005). Hyperspectral NIR image regression part I: calibration and correction. *Journal of Chemometrics*, **19**, 355-363.

Castells, M., Marín, S., Sanchis, V. & Ramos, A.J. (2008). Distribution of fumonisins and aflatoxins in corn fractions during industrial cornflake processing. *International Journal of Food Microbiology*, **123**, 81-87.

Cowe, I. & McNicol, J. (1985). The use of principal components in the analysis of near-infrared spectra. *Applied Spectroscopy*, **39**, 257-266.

Del Fiore, A., Reverberi, M., Ricelli, A., Pinzari, F., Serranti, S., Fabbri, A.A., Bonifazi, G. & Fanelli, C. (2010). Early detection of toxigenic fungi on maize by hyperspectral imaging analysis. *International Journal of Food Microbiology*, **144**, 64-71.

Duncan, K.E. & Howard, R.J. (2010). Biology of maize kernel infection by *Fusarium verticillioides*. *Molecular Plant-Microbe Interactions*, **23**, 6-16.

Fandohan, P., Hell, K., Marasas, W. & Wingfield, M. (2003). Infection of maize by *Fusarium* species and contamination with fumonisin in Africa. *African Journal of Biotechnology*, **2**, 570-579.

Firrao, G., Torelli, E., Gobbi, E., Raranciuc, S., Bianchi, G. & Locci, R. (2010). Prediction of milled maize fumonisin contamination by multispectral image analysis. *Journal of Cereal Science*, **52**, 327-330.

Geladi, P., Burger, J. & Lestander, T. (2004). Hyperspectral imaging: calibration problems and solutions. *Chemometrics and Intelligent Laboratory Systems*, **72**, 209-217.

Geladi, P., Grahn, H.F. & Burger, J. (2007). Multivariate images, hyperspectral imaging: background and equipment. In: *Techniques and applications of hyperspectral image analysis* (edited by H.F. Grahn & P. Geladi). Pp. 1-14. Chichester, West Sussex: John Wiley & Sons Ltd.

Gowen, A.A., O'Donnell, C.P., Cullen, P.J., Downey, G. & Frias, J.M. (2007). Hyperspectral imaging: an emerging process analytical tool for food quality and safety control. *Trends in Food Science and Technology*, **18**, 590-598.

Koehler, F.W., Lee, E., Kidder, L.H. & Lewis, E.N. (2002). Near infrared spectrsocopy: the practical chemical imaging solution. *Spectoscopy Europe*, **14**, 12-19.

Liu, Y. & Rayens, W. (2007). PLS and dimension reduction for classification. *Computational Statistics*, **22**, 189-208.

Malvar, R.A., Revilla, P., Moreno-Gonzalez, J., Butron, A., Sotelo, J. & Ordas, A. (2008). White maize: genetics of quality and agronomic performance. *Crop Science*, **48**, 1373-1381.

Manley, M., du Toit, G. & Geladi, P. (2011). Tracking diffusion of conditioning water in single wheat kernels of different hardnesses by near infrared hyperspectral imaging. *Analytica Chimica Acta*, **686**, 64-75.

Manley, M., McGoverin, C.M., Engelbrecht, P. & Geladi, P. (2012). Influence of grain topography on near infrared hyperspectral images. *Talanta*, **89**, 223-230.

Manley, M., Williams, P., Nilsson, D. & Geladi, P. (2009). Near infrared hyperspectral imaging for the evaluation of endosperm texture in whole yellow maize (*Zea maize* L.) kernels. *Journal of Agricultural and Food Chemistry*, **57**, 8761-8769.

Martens, H. (2001). Reliable and relevant modelling of real world data: a personal account of the development of PLS Regression. *Chemometrics and Intelligent Laboratory Systems*, **58**, 85-95.

Medina-Martinez, M.S. & Martinez, A.J. (2000). Mold occurrence and aflatoxin B1 and fumonisin B1 determination in corn samples in Venezuela. *Journal of Agricultural and Food Chemistry*, **48**, 2833-2836.

Munkvold, G.P. (2003). Epidemiology of *Fusarium* diseases and their mycotoxins in maize ears. *European Journal of Plant Pathology*, **109**, 705-713.

Munkvold, G.P. & Desjardins, A.E. (1997). Fumonisins in maize: can we reduce their occurrence? *Plant Disease*, **81**, 556-565.

Muthomi, J.W., Ndung'u, J.K., Gathumbi, J.K., Mutitu, E.W. & Wagacha, J.M. (2008). The occurrence of *Fusarium* species and mycotoxins in Kenyan wheat. *Crop Protection*, **27**, 1215-1219.

Osborne, B.G., Fearn, T. & Hindle, P.H. (1993). *Practical NIR Spectroscopy with Applications in Food and Beverage Analysis.* Pp. 29-33. Essex, England: Longman Scientific & Technical.

Paepens, C., Saeger, S.D., Sibanda, L., Barna-Vetró, I., Léglise, I., Van Hove, F. & Peteghem, C.V. (2004). A flow-through enzyme immunoassay for the screening of fumonisins in maize. *Analytica Chimica Acta*, **523**, 229-235.

Schierbaum, F. (2007). World corn production, uses and ending stocks: recorded figures for fiscal years 2004/05 and 2005/06. *Starch-Starke*, **59**, 192-195.

Schulthess, F., Cardwell, K.F. & Gounou, S. (2002). The effect of endophytic *Fusarium verticillioides* on infestation of two maize varieties by Lepidopterous Stemborers and Coleopteran grain feeders. *Phytopathology*, **92**, 120-128.

Sydenham, E.W., Shephard, G.S., Thiel, P.G., Bird, C. & Miller, B.M. (1996). Determination of fumonisins in corn: evaluation of competitive immunoassay and HPLC techniques. *Journal of Agricultural and Food Chemistry*, **44**, 159-164.

Williams, P., Geladi, P., Fox, G. & Manley, M. (2009). Maize kernel hardness classification by near infrared (NIR) hyperspectral imaging and multivariate data analysis. *Analytica Chimica Acta*, **653**, 121-130.

Williams, P., Manley, M., Fox, G. & Geladi, P. (2010). Indirect detection of *Fusarium verticillioides* in maize (*Zea mays* L.) kernels by near infrared hyperspectral imaging. *Journal of Near Infrared Spectroscopy*, **18**, 49-58.

Wold, S., Sjöström, M. & Eriksson, L. (2001). PLS-regression: a basic tool of chemometrics. *Chemometrics and Intelligent Laboratory Systems*, **58**, 109-130.

Zhang, H., Paliwal, J., Jayas, D.S. & White, N.D.G. (2007). Classification of fungal infected wheat kernels using near-infrared reflectance hyperspectral imaging and support vector machine. *Transactions of the ASABE*, **50**, 1779-1785.

CHAPTER 4

NEAR-INFRARED (NIR) HYPERSPECTRAL IMAGING AND MULTIVARIATE IMAGE ANALYSIS TO STUDY GROWTH CHARACTERISTICS AND DIFFERENCES BETWEEN SPECIES AND STRAINS OF MEMBERS OF THE GENUS *FUSARIUM**

Abstract

Near-infrared (NIR) hyperspectral imaging was used to study three strains of each of three *Fusarium* spp. (*F. subglutinans*, *F. proliferatum*, *F. verticillioides*) inoculated on potato dextrose agar in Petri dishes after either 72 or 96 h of incubation. Multivariate image analysis was used for cleaning the images and for making principal component analysis (PCA) score plots and score images and local partial least squares discriminant analysis (PLS-DA) models. The score images, including all strains, showed how different the strains were from each other. Using classification gradients it was possible to show the change in mycelium growth over time. Loading line plots for principal component (PC) 1 and PC2 explained variation between the different *Fusarium* spp. as scattering and chemical differences (protein production), respectively. PLS-DA prediction results (including only the most important strain of each species) showed that it was possible to discriminate between species with *F. verticillioides* the least correctly predicted (between 16-47% pixels correctly predicted). For *F. subglutinans* 78-100% pixels were correctly predicted; depending on the training and test set used. Similarly the percentage correctly predicted values of *F. proliferatum* were 60-80%. Visualisation of the mycelium radial growth in the PCA score images was made possible due to the use of NIR hyperspectral imaging. This is not possible with bulk spectroscopy in the visible or NIR regions.

*Published as: Williams, P., Geladi, P., Britz, T. & Manley, M. (2012). Near-infrared (NIR) hyperspectral imaging and multivariate image analysis to study growth characteristics and differences between species and strains of members of the genus *Fusarium*. *Analytical and Bioanalytical Chemistry*, **404**, 1759-1769.

Introduction

Fungi are ubiquitous in nature and grow on most substrates under optimal conditions (Nelson *et al.*, 1994). They are common in tropical and temperate regions and are also found in desert, alpine and arctic areas where harsh climatic conditions prevail. *Fusarium* spp. are mostly regarded as soil borne fungi where they are abundant and associated with plants as either parasites or saprophytes (Nelson *et al.*, 1994; Bacon *et al.*, 2008).

Mycotoxin production by *Fusarium* spp. is of primary concern to the food industry. They are known to produce fumonisins, trichothecenes and zearalenones, as well as other minor mycotoxins. Of these the fumonisins are of particular importance and concern. These toxins are natural contaminants of cereal grains worldwide and are mostly found in maize and products derived from maize. Fumonisins have cancer-promoting activity (Gelderblom *et al.*, 1988). Furthermore, *F. verticillioides* strain MRC 0826, isolated from mouldy maize, was shown to cause ELEM in horses, porcine pulmonary edema (PPE) syndrome in pigs, and liver cancer in rats (Gelderblom *et al.*, 1988; Gelderblom *et al.*, 2001a; Gelderblom *et al.*, 2001b; Marasas, 2001; Gelderblom *et al.*, 2004).

The taxonomy of *Fusarium* spp. has always been a disputable issue (Nelson et al., 1994; Summerell et al., 2003) and is known as a genus in which it is difficult to distinguish species (Snyder & Hansen, 1940). The taxonomy has been inundated by varying species concepts, with as few as nine or well over 1000 species being recognised (Summerell et al., 2003). Because of its abundance and the inordinate economic importance of the members of this genus, it is essential to be able to easily and accurately identify the various species.

Conventional identification methods at species level involves plating out on appropriate media, description of colonies (texture, colour and pigment) and microscopic description of conidiogenous cells and conidia (Hennequin *et al.*, 1999). Because variation of important characteristics such as pigmentation and growth rate is often seen within a given species, only well-trained mycologists are able to perform the identification. Other more complex techniques involve molecular techniques such as polymerase chain reaction (PCR) assays (Möller *et al.*, 1999; Mulè *et al.*, 2004), DNA sequencing (Hennequin *et al.*, 1999; de Oliveira Rocha *et al.*, 2011) and mass spectrometry (Marinach-Patrice *et al.*, 2009; Santos *et al.*, 2010). Not only are these techniques time consuming, they are expensive, require specialised technicians, specialised instrumentation and tedious sample preparation. Rapid techniques are thus required for identification and differentiation of fungal species.

Near-infrared (NIR) hyperspectral imaging is an imaging technique in which spectral and spatial information are combined to obtain NIR hyperspectral images (Koehler *et al.*, 2002; Geladi *et al.*, 2004; Geladi *et al.*, 2007; Gowen *et al.*, 2007). NIR hyperspectral images are three-dimensional arrays of the form, $\mathbf{X}$ ($m \times n \times \lambda$), where m and n are the spatial axes information and the

λ axis represents the spectral information. The three-dimensional structure of the hypercube requires reorganisation to a two-dimensional matrix to adapt the image for further pre-treatments.

Statistical treatments such as principal component analysis (PCA), an unsupervised classification or dimensionality reduction technique (Cowe & McNicol, 1985), can be applied to the data. It reduces the data to a much smaller number of principal components (PCs) and can be used as an exploratory technique. PC score images and score plots are used interactively to investigate sample images for special features or irregularities in samples. If anomalies are observed during interpretation of cleaned images (irrelevant pixels have been removed), they will most likely be due to relevant variation between samples which could be either chemical or physical. This observed variation can be explained by studying the accompanying PC loading line plots.

Partial least squares (PLS) regression is a powerful regression technique that uses the latent variable approach to find the fundamental relations between two matrices (**X** and **Y**) (Martens, 2001; Wold *et al.*, 2001; Liu & Rayens, 2007). PLS uses the y-data structure to decompose **X** so that the outcome constitutes an optimal regression vector. Partial least squares discriminant analysis (PLS-DA) operates similarly; however, instead of measured y-data, dummy variables are used which are indicators of groups (Chevallier *et al.*, 2006). This allows for prediction of group membership and thus classification of pixels.

Recently, NIR hyperspectral imaging has been used more frequently in food applications with particular reference to food safety aspects such as detection of fungi on maize kernels (Bartnicki-Garcia, 1968; Williams *et al.*, 2010), early detection of fungal infection on maize (Bauriegel *et al.*, 2011) detection of chicken heart disease (Chao *et al.*, 2001), the detection of faecal matter and ingesta on chicken carcasses (Park *et al.*, 2002; Park *et al.*, 2004; Park *et al.*, 2007), the detection of faecal contamination on apples (Kim *et al.*, 2002; Kim *et al.*, 2005; Liu *et al.*, 2007) and for the detection of foreign objects in semolina (Bhuvaneswari *et al.*, 2011) and chicken fillets (Yoon *et al.*, 2008). Thus far not much work has been done applying NIR hyperspectral imaging in microbiological studies.

An earlier study investigated NIR hyperspectral imaging as a tool for high-throughput analysis of self-contained microbial identification of test cards for microorganisms of concern in food (Dubois *et al.*, 2005). In this preliminary work, a NIR chemical imaging system operating in the spectral range 1000–2350 nm was used to acquire NIR chemical images of bacterial cells deposited on a ‘card’, containing both the calibration and test samples. Results showed that some bacteria could be identified from differences observed at unique wavelengths and that a standard operating procedure could be developed for a particular ‘card’ to differentiate and hence identify the various organisms it contains using discrete wavelengths. In another study the detection of *Campylobacter* was investigated with detection accuracies between 97 and 99% (Yoon *et al.*, 2010). In this study, an instrument operating in the 400-900 nm wavelength range was used, employing the visible and NIR regions. The disadvantage of this range is that it includes the visible

wavelength region, and these models rely on colour as a discriminating tool. A study on the differentiation of toxigenic fungi used a similar wavelength range of 400-1000 nm and achieved classification accuracies of 97.7% (Yao *et al.*, 2008). Five fungal species were selected, i.e. *Penicillium chrysogenum, F. verticillioides, Aspergillus parasiticus, Trichoderma viride* and *Aspergillus flavus* and all could be classified using three narrow bands (bandwidth = 2.43 nm) centred at 743, 458 and 541 nm. The last two wavelengths are associated with blue and green respectively and resulted in the high accuracy of the classification since four of the five organisms appeared blue/green when cultured on the appropriate medium.

The purpose of the current study was to investigate the use of NIR hyperspectral imaging and multivariate image analysis techniques to differentiate between species and strains of the genus *Fusarium* associated with maize.

Materials and methods

Sample preparation

Three strains of each of three *Fusarium* spp. as shown in Table 4.1 were kindly supplied by the Department of Plant Pathology, Stellenbosch University, South Africa. The strains were streaked out from a frozen stock solution onto potato dextrose agar (PDA) (Merck (Pty) Ltd, Cape Town, South Africa) and incubated at 28°C in Petri dishes for a total of 96 h.

NIR hyperspectral imaging system and image collection

Hyperspectral images were acquired with the SisuCHEMA short wave infrared camera (Specim, Spectral Imaging Ltd, Oulu, Finland). The camera comprised an imaging spectrograph coupled to a 2-D array mercury-cadmium-telluride detector. Individual images were acquired within a spectral range of 1000-2498 nm at 10 nm resolution, 6.3 nm wavelength intervals and a field-of-view of 100 × 100 mm. Images of the entire Petri dish, without removing the lid, were collected at 3 and 5 days after inoculation. In a few cases where isolates were streaked out in polystyrene petri dishes, the lid was removed before image collection. Internal dark and white reference standards were imaged prior to each sample.

Hyperspectral image analysis

Images were analysed using the Evince v.2.5.5 hyperspectral image analysis software package (UmBio AB, Umeå, Sweden) and MATLAB v 7.10 (The MathWorks, Massachusetts, USA). The image calibration and correction to absorbance was done automatically in the Evince software package as described in Williams *et al.* (2012b).

Construction of mosaics and image cleaning

Selected individual images within the wavelength range 1103-2483 nm were merged to form mosaics. The first mosaic comprised three strains of each of the *Fusarium* spp. The second mosaic contained only the most important strains (MRC 0115, MRC 2301, and MRC 0826) of each

species imaged. This included colonies of the same strains in the same Petri dishes, but imaged after 72 h and 96 h of incubation, respectively. These strains were selected based on frequency of isolation from contaminated maize (Fandohan *et al.*, 2003). The third mosaic comprised of images of the same strains cultured. The training set was cultured and imaged 18 months prior to the test set. The test set was the same image used as training set in the second mosaic. The fourth mosaic comprised the same training set as the third mosaic (three main strains inoculated on three separate Petri dishes) and the same three strains inoculated in a single Petri dish as the test set.

A PCA model with six components was calculated, on mean centred data, for each of the mosaics (1-4). Using the brushing technique (Geladi & Grahn, 1996; Esbensen & Lied, 2007) all irrelevant pixels (background, agar, reflection from Petri dish, bad pixels) were removed using score plots and score images of all six principal components (PCs). To ensure efficient cleaning of the images, this cleaning process was repeated five to ten times and PCA was recalculated after each repetition on the cleaned images.

Multivariate image analysis

PCA and PLS-DA with species as dummy variables were used as provided in the Evince v.2.5.5 software package. To enable PLS-DA classification with three classes, the samples (pixels) for class one were represented by the row vector (1, 0, 0). Similarly the samples for class two were represented by (0, 1, 0) and those of class three by (0, 0, 1). The PLS-DA model would thus result in three separate regression coefficients, one for each class for all pixels. These were then used to predict a new set of data which were refolded to form the prediction image, showing the location of the classes.

Table 4.1. Details on the *Fusarium* spp. and respective strains investigated

Species and strains	Isolation locality	Reference
Fusarium subglutinans		
MRC 0115	Transkei, Zazulwana, Butterworth	(Marasas *et al.*, 1986)
MRC 2293	USA	(Marasas *et al.*, 1986)
MRC 6194 (KSU E-00990; ATCC 201270; FRC M-3696)	St Elmo, Illinois, USA	(Nirenberg & O'Donnell, 1998)
Fusarium proliferatum		
MRC 2301	California, USA	(Marasas *et al.*, 1986)
MRC 6908	Ghana	na
MRC 7140	Pietermaritzburg, RSA	na
Fusarium verticillioides		
MRC 0826	Transkei	(Marasas *et al.*, 1986)
MRC 8267	North Benin	na
MRC 8559 (KSU A-00149; FRC M-3125)	California, USA	(Nirenberg & O'Donnell, 1998)

MRC: Medical Research Council, Tygerberg, South Africa

ATCC: American Type Culture Collection

KSU: Kansas State University culture collection, Department of Plant Pathology, Kansas State University, Manhattan, Kansas, USA

FRC: *Fusarium* Research Center, Pennsylvania State University, USA

Different preprocessing methods, i.e. standard normal variate (SNV), multiplicative scatter correction (MSC) and Savitzky-Golay derivatives were tested to improve models, and the number of components to be used was determined using test sets. Confusion matrices constructed from the test set prediction results were used to evaluate the respective models in terms of percentage pixels not classified, percentage pixels correctly classified and percentage false negatives. The percentage pixels correctly classified were calculated based on total number of pixels in the test set as well as with number of pixels not classified in the test set removed. For the PLS-DA models, prediction images are shown for the training set to illustrate how well the respective models performed. Prediction images for the test sets show the accuracy of the PLS-DA models. PLS-DA models use R^2 and root mean square error of prediction (RMSEP) per response variable as

diagnostics. The optimum number of PLS-DA components was selected based on the number of components that resulted in the highest R^2, lowest RMSEP and prediction image with best classification of the samples (highest percentage correctly classified pixels).

Results and discussion

Hyperspectral image analysis

Typical mycelia growth on PDA of *Fusarium subglutinans* (MRC 0115), *Fusarium proliferatum* (MRC 2301) and *F. verticillioides* (MRC 0826), after incubation for 72 h at 28°C is shown in Figure 4.1. A first observation is that the growth is not homogeneous. There is a visible difference between the centre and edges of each colony, but the colonies could otherwise not be visually distinguished based on shape and colour. Visible distinction, between *F. subglutinans and F. proliferatum,* is not clear. The non-homogeneous nature of the colonies makes studying the distinction between *Fusarium* spp. an ideal application for NIR hyperspectral imaging and multivariate image analysis.

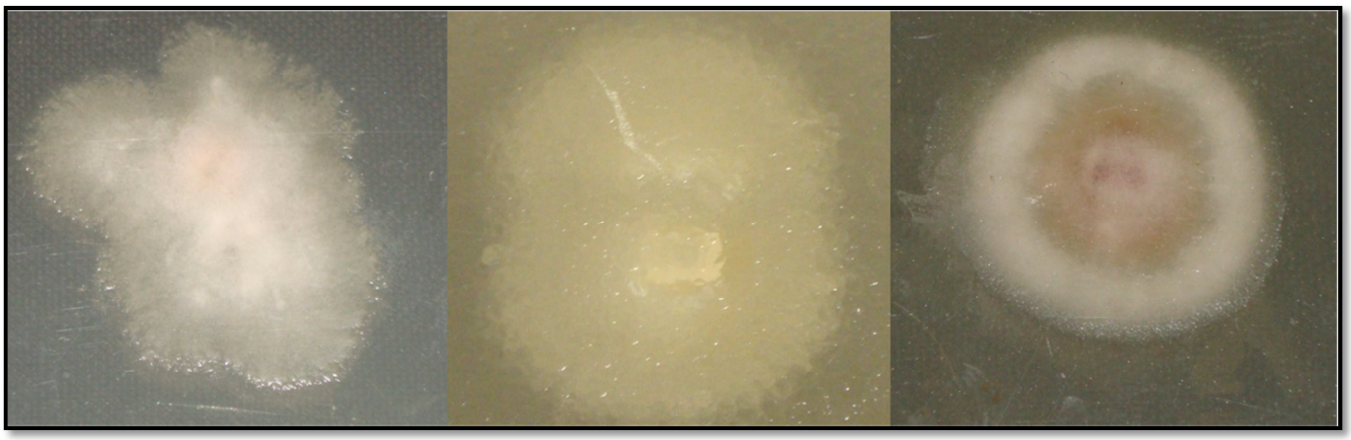

Figure. 4.1. Digital images of mycelium colonies of *F. subglutinans*, *F. proliferatum* and *F. verticillioides* after 72 h incubation at 28°C.

Mosaic 1

By doing a PCA, on mean-centred data, most information on differences between the colonies was found in PC1 (98.7% sum of squares (SS)) and partly in PC2 (0.79% SS). PC3 and lower variance PCs showed no relevant information. Figure 4.2 shows the PC1 score image of Mosaic 1. The mosaic was set up as a nested analysis of variance with the species in rows and the three strains of the same species within each row. The left column comprises the most important strain within each species (most often observed in maize), while the other columns are made up of the more rare strains. Inclusion of the strains less “commonly" associated with maize environments in the mosaic makes distinction between the different species impossible. Preprocessing of the data did not improve these results. Distinction between the three species for the more "common" strains was already clear in the PC1 score image (left column in Fig. 4.2). Mycelium growth of colonies starts in the centre of the colony with youngest growth toward the edges of the colonies. This

phenomenon, referred to as radial growth (Pirt, 1967), could clearly be seen within the images of the respective colonies (Fig. 4.2). This is clearer for some colonies and less clear for others. Temperature plays an important role in the growth, growth rate and the ability of these fungal species to produce mycotoxins (Alberts et al., 1990). For that reason all plates were incubated at the same temperature to minimise the variation. In spite of this precaution, it was observed in the score image that all colonies differed markedly. The temperature in this study, i.e. 28°C was chosen based on the optimal growth rate for the species involved, reported to be in the range 25-30°C (Kriek *et al.*, 1977; Alberts *et al.*, 1990; Viljoen *et al.*, 1997; Marín *et al.*, 1999a; Marín *et al.*, 1999b; Marin *et al.*, 1999). Selecting an optimum temperature is important when fungi are cultured for a specific purpose such as maximal mycotoxin production. The present study did not have such a purpose and 28°C was selected as similar, controlled growth rates were observed at this temperature for all three species. Figure 4.3a shows obvious density clusters in the score plot, direction of PC1. In the direction of PC2 less clear clustering is seen. Classification gradients (Manley *et al.*, 2011; Manley *et al.*, 2012) were constructed to visualise and understand the meaning and relevance of these clusters (Fig. 4.3b). Classification gradients were defined in the direction of PC1 by dividing the score value range into six successive groups based on the observed clusters. For interpretation of the groups, the classification plot (Fig. 4.3b), obtained after the groups were selected in the score plot, were projected onto the score image to produce a classification image (Fig. 4.3c). Figure 4.3c clearly shows the mycelium radial growth with the older growth of the colonies at the centre of the colony, where the original inoculation was done, and the newer growth toward the edge of the colony showing latest growth after 72 h. These clear differences between the mycelium growth rings further complicated the data classification between species with all the strains included. Because of the different results for the species/strain combinations, growth rings were studied in more detail by doing a PCA for each colony separately (Williams *et al.*, 2012a).

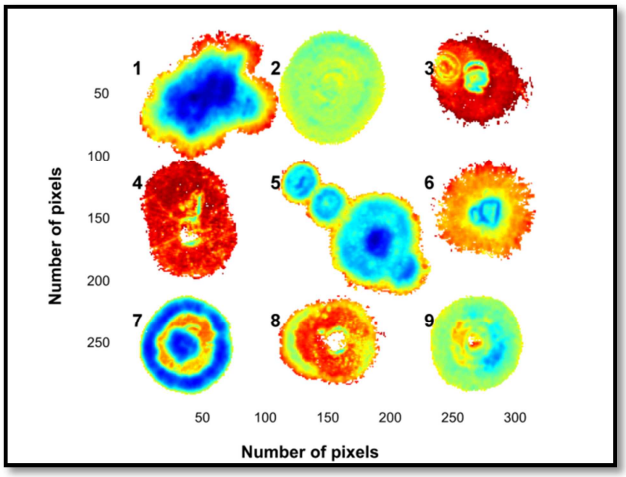

Figure. 4.2. Principal component 1 score image of Mosaic 1 illustrating differences between and within the colonies. Similarities between some of the colonies are also noticeable. Species are shown in rows and strains of the same species within each row. The left column comprises the most important strain within each species. *F. subglutinans* (MRC 0115) are top left followed by *F. proliferatum* (MRC 2301) and *F. verticilioides* (MRC 0826).

PCA analysis of Fusarium spp.

PCA calculated for the most important strain of each the three *Fusarium* spp., imaged 18 months prior, is shown in the PC1 (98.7%SS) vs. PC2 (0.846 %SS) score plot (Fig. 4.4a) and two score images for PC1 (Fig. 4.4b) and PC2 (Fig. 4.4c), respectively. The score plot showed two clusters in the direction of PC2, and the corresponding score image showed that this was a contrast between *F. subglutinans* and the combination of *F. proliferatum* and *F. verticillioides*. The loading line plot of PC2 explained this contrast due to variation in N-H stretch first overtone (1430 nm) and CONH stretch second overtone (1918 nm) (Osborne *et al.*, 1993). These peaks were both positively loaded corresponding with *F. proliferatum* and *F. verticillioides*, both having positive scores in the score plot (Fig. 4.4d). This means that both these latter species produced more protein during mycelium growth which allowed differentiation from *F. subglutinans*.

The PC1 direction explained the difference between older and newer mycelium growth as can also be seen in the PC1 score image. This was confirmed by means of the loading line plot of PC1, showing a typical shape similar to a mean spectrum which indicated a difference in scattering properties between the different growth stages (Fig. 4.4d). This difference in scattering properties could also have been caused by the difference in height of the mycelium growth from the centre to the edges of the colonies or due to the presence of spores in the older growth (centre).

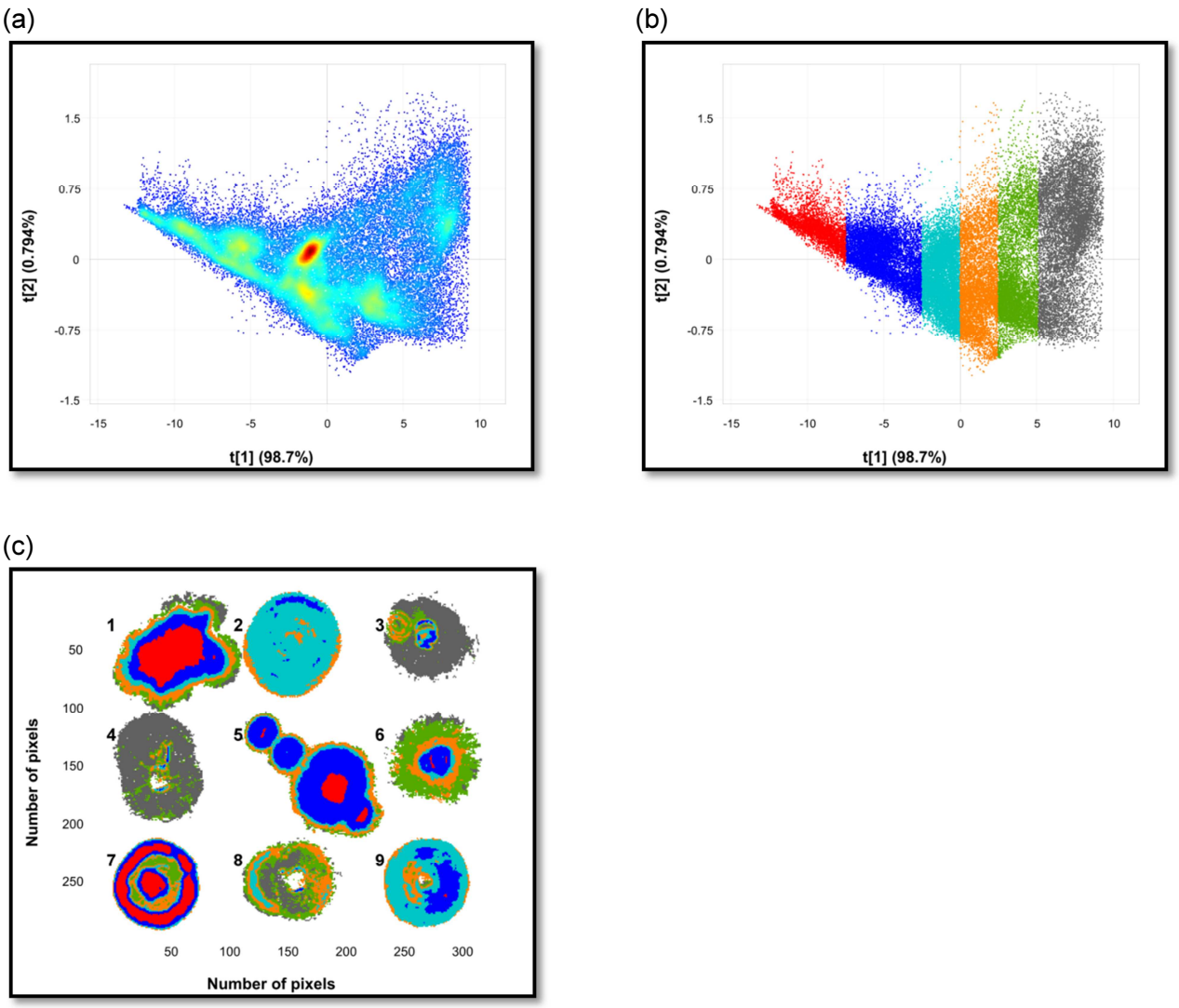

Figure. 4.3. (a) PC1 vs. PC2 scatter plot for Mosaic 1 showing a number of clusters in the PC1 direction, (b) six selected classification gradients in the PC1 direction based on observed clusters and (c) the classification gradients projected onto the score image. Some colonies have a number of clear mycelium growth rings shown as gradient classes (colonies 1, 5, 6 & 7) while others belong mainly to a single gradient class (colony 2) with no apparent difference in mycelium growth over time.

With NIR hyperspectral imaging, the shape, height and curvature of the sample play an important role. It has been shown that the topography of the sample is explained by the higher variance PCs which accounted for most of the variation in the data (McGoverin *et al.*, 2011; Manley *et al.*, 2012). The PC that captured the variation due to chemical differences contributed a low %SS, but still contributed to effective classification. In the present study, the required information to discriminate between the fungal species was explained in PC2 in spite of the low %SS (0.846%). It is frequently seen in imaging applications that the most relevant PC or PCs are those with a low %SS (Gowen *et al.*, 2008; Manley *et al.*, 2009; Williams *et al.*, 2009; Baranowski *et al.*, 2012).

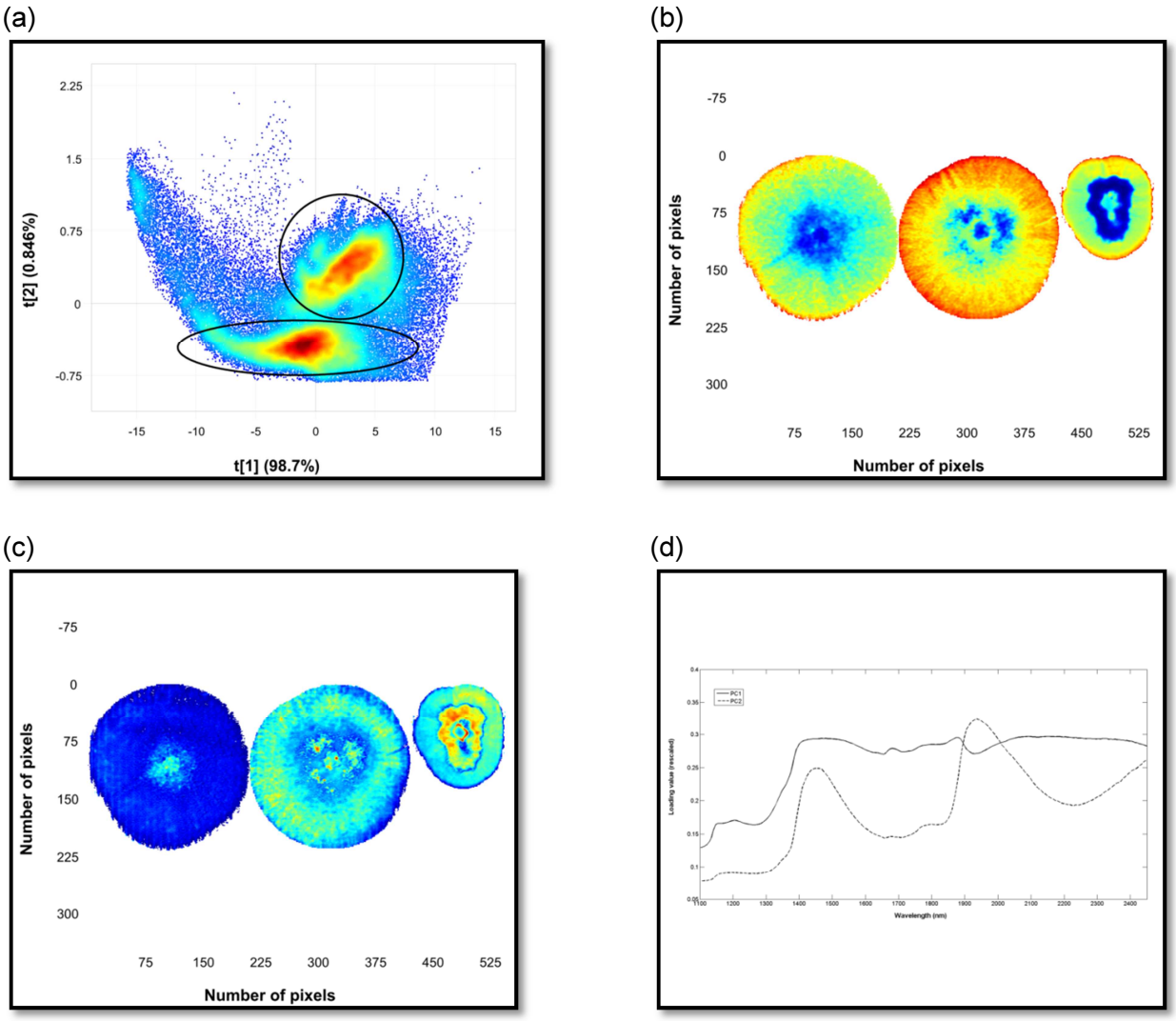

Figure. 4.4 (a) Principal component analysis score plot (PC1 vs. PC2), (b) PC1 score image, (c) PC2 score image and (d) loading line plots of PC1 and PC2 for the most important strain of each of the three *Fusarium* species. Left to right: *F. subglutanins*, *F. proliferatum* and *F. verticillioides*.

Mosaic 2

To test the effect of growth period of mycelium colonies on PLS-DA classification, Mosaic 2 was made of images of the three *Fusarium* spp. (MRC 0115, MRC 2301 & MRC 0826), scanned at two different times. The training images were collected 72 h after inoculation, while the test set images were collected from the same colonies 96 h after inoculation. The PLS-DA model was calculated with four components on raw, mean-centred data. Dummy (0/1) variables were used as reference data to classify class membership. Preprocessing by SNV, MSC or by Savitzky-Golay derivatives showed no improvement in prediction.

The R^2 of 0.48 for the model for the training data was due to it not being able to clearly distinguish between *F. verticillioides* and *F. subglutinans* as can be seen in Figure 4.5. For the same reason the RMSEP in Table 4.2 is only acceptable for *F. proliferatum*. The prediction images for *F. subglutinans* (green) and *F. proliferatum* (blue) showed a reasonable number of correctly predicted pixels for both the training and test sets (Fig. 4.5). For *F. verticilli*oides (yellow), the training image showed misclassification, while the test image showed a large number of pixels not

classified (red). Most of the incorrectly predicted pixels in the *F. proliferatum* image were in the centre of the colony, where older mycelium growth was found. *F. verticillioides* showed a number of pixels as not classified (red) with only a few correct predictions. The reason for this high number of not classified pixels could be due to the radial growth that showed marked clustering inside the colony (Figs. 4.1 & 4.3c).

From the Evince confusion matrix for the test set, it was calculated that for *F. subglutinans* 99.9% of the pixels were correctly classified with 0.1% pixels not classified. For *F. proliferatum*, 86.7% of the pixels were correctly classified, not taking the non-classified pixels (7.2%) into consideration. For *F. verticillioides*, the predictions were much poorer with only 44% correctly classified (54% not classified pixels not included). More detailed prediction statistics results are shown in Table 4.2.

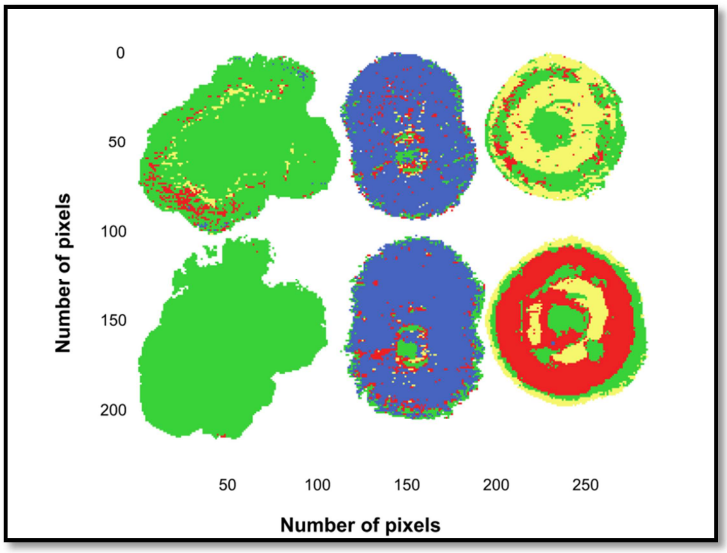

Figure. 4.5 PLS-DA training and test prediction images for Mosaic 2. Classification based on the training data are in the upper row for *F. subglutinans*, *F. proliferatum* and *F. verticillioides* (from left to right) (colonies incubated for 72 h) and the bottom row is the classification for the test data (the same colonies incubated for 96 h).

Mosaic 3

Images combined in Mosaic 3 comprised two sets of the three *Fusarium* spp., acquired 18 months apart (Fig. 4.6a). The images in the top row were used as the training set and the images in the bottom row as the test set. This test set is the same that has been used as the training set in Mosaic 2 (as shown in Fig. 4.5). This means that the model was tested with an independent test set. The PLS-DA model was calculated with four components on mean-centred data. For this mosaic, the R^2 of 0.66 was reasonable. Again, the RMSEP was lowest for *F. proliferatum*. For the training data (top row, Fig. 4.6a) *F. subglutinans* showed good predictions. Predictions for *F. proliferatum* were still reasonable, while those for *F. verticillioides* were the worst, although slightly better than the predictions shown in Figure 4.5.

For the test set, *F. subglutinans* had a good classification; *F. proliferatum* was slightly worse, but still good, while *F. verticillioides* showed a large number of pixels classified as *F. subglutinans* and only a smaller number of pixels as *F. verticillioides*. From the Evince confusion matrix for the test set it was calculated that for *F. subglutinans* 98.6% of the pixels were correctly classified (Table 4.2). For *F. proliferatum*, 66.6% were correctly classified, not taking the 13% pixels not classified into consideration. The predictions for *F. verticillioides* were much poorer (16.8% correctly classified) although only 0.2% pixels were not classified. The poor performance of *F. verticillioides* is likely due to inconsistent differences between older and newer growth (as seen in Fig. 4.1 & 4.3c). Because of the use of an independent test set, the results are slightly worse than for Mosaic 2. Again the *F. verticillioides* result was the worst.

Table 4.2 PLS-DA predictions results for Mosaics 2, 3 and 4, showing qualitative classification of Fusarium spp. with NIR hyperspectral imaging.

	RMSEP	**% Not classified**	**% Correct predictions of only classified pixels**	**% False negatives**	**% Correct predictions of total pixels**
Mosaic 2					
F. subglutinans	0.39	0.1	99.9	0	99.9
F. proliferatum	0.25	7.2	86.7	13.3	80.4
F. verticillioides	0.45	54.7	44	56	20
Mosaic 3					
F. subglutinans	0.58	0.6	98.6	1.4	98.0
F. proliferatum	0.44	1.3	66.6	33.4	57.9
F. verticillioides	0.40	0.2	16.8	83.2	16.7
Mosaic 4					
F. subglutinans	0.32	4.9	80.1	19.9	76.2
F. proliferatum	0.45	19.4	86.5	13.5	69.8
F. verticillioides	0.46	16.7	39.1	60.9	32.5

Mosaic four

The training data in Mosaic 4 was the same as for Mosaic 3, thus the same four-component model was used to predict class membership. This time the test set was an image of the three *Fusarium* spp. (MRC 0115, MRC 2301, MRC 0826) inoculated in a single Petri dish after incubation for 120 h (Fig. 4.6b). A large number of pixels were not classified for *F. verticillioides* (16.7%) and even more for *F. proliferatum* (19.4%). In the previous PLS-DA predictions, the pixels in the *F. subglutinans* image were almost 100% correctly predicted, while in this mosaic only 80.1% of the pixels were

correctly predicted with 4.9% pixels not classified. For *F. verticillioides* and *F. proliferatum*, 39.1% and 86.5% pixels were correctly predicted (from only classified pixels). For *F. verticillioides*, there was a large number of pixels predicted as false negatives (60.9%). These pixels were falsely predicted as *F. proliferatum*. A false negative is when the outcome is incorrectly classified as a negative when it is in fact positive. Thus, majority of the pixels in *F. verticillioides* were classified as not being part of the class, when in fact they are. The PLS-DA prediction results of Mosaics 2 to 4 are compared in Table 4.2.

Non-classified pixels are not desirable and especially *F. verticillioides* had many of those in two of the mosaics, while *F. subglutinans* rarely had any non-classified pixels. A high proportion of non-classified pixels give a false impression of correct predictions when the percentage of correct predictions is calculated based only on classified pixels (column three in Table 4.2). This was clear when the percentage of correct predictions was calculated from the total number of pixels (column 5 in Table 4.2). The percentage of correctly classified *F. subglutinans* always did best, due to the low percentage of non-classified pixels.

The benefit of using PLS for dimension reduction and discrimination is that it performs better than PCA when within class variation is higher than between class variation (Barker & Rayens, 2003). In this study the within class variation for *F. verticillioides* seemed to be much higher than for the other species as can be seen in the calibration and prediction images in Figures 4.5 and 4.6. The PLS-DA models, however, failed in classifying *F. verticillioides* efficiently. It seemed that the models could either not classify the pixels of the *F. verticillioides* image as a known class or attempted to predict it as belonging to the *F. subglutinans* or *F. proliferatum* class.

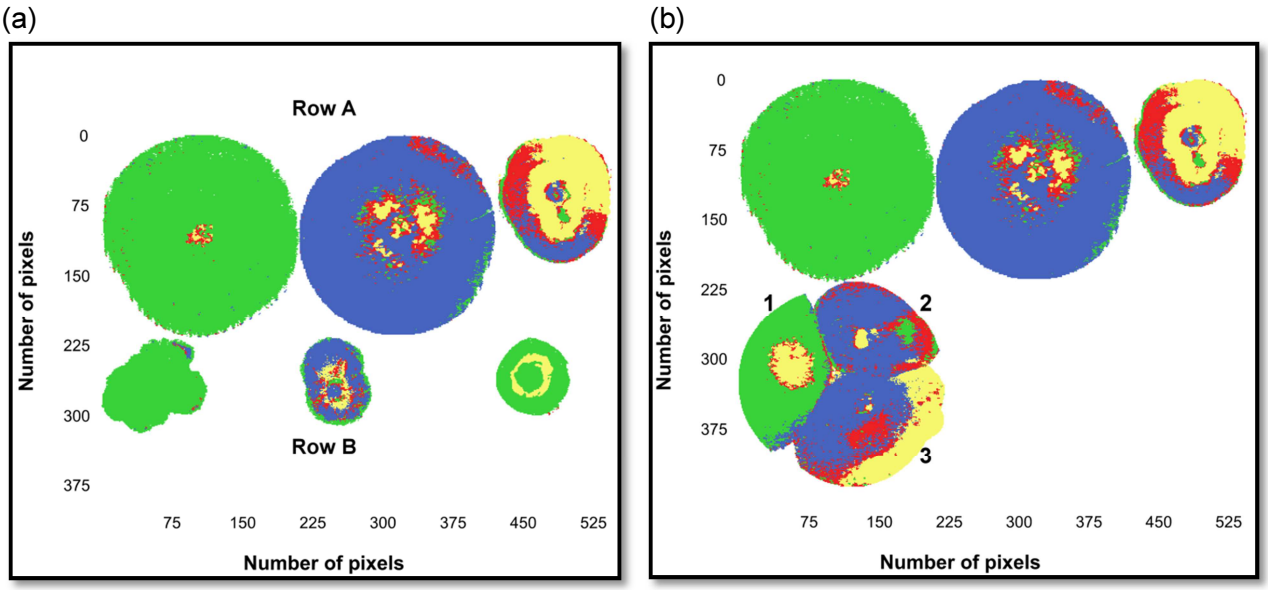

Figure. 4.6 (a) PLS-DA prediction images for Mosaic 3. The top row (row A) shows images of colonies for *F. subglutinans*, *F. proliferatum* and *F. verticillioides* (from left to right) used as training data and the bottom row (row B) was the test data. (b) PLS-DA prediction images for Mosaic 4. The test data shows the image of the three *Fusarium* spp. inoculated in a single Petri dish (1 = *F. subglutinans*; 2 = *F. proliferatum*; 3 = *F. verticillioides*).

Conclusion

Using the NIR region, three *Fusarium* spp. could be discriminated from each other with reasonable accuracy by hyperspectral imaging and the use of test sets. Including a number of different strains in the training set complicated identification in PCA score images. This complication was enhanced due to the presence of clear radial growth rings with older growth in the middle and younger growth on the edge of the mycelium colonies. Global diagnostics for the PLS-DA models such as R^2 and RMSEP serve as a guide of modelling accuracy for images because of the large number of pixels and should be used in conjunction with the prediction image. Occasionally, a model has an unsatisfactory RMSEP, but still shows acceptable prediction results in the prediction image for a large number of pixels. The use of NIR hyperspectral imaging allows one to visualise radial growth rings in the PCA score images. This would not have been possible with bulk spectroscopy in the visible or NIR regions. Because of this, imaging is far superior to integrating reflectance spectroscopy. An additional advantage of multivariate image analysis is the possibility to interpret PC loading line plots for a possible chemical or physical explanation. Although removing irrelevant pixels from hyperspectral images enhance the ability to detect chemical variation by PCA, inherent physical differences cannot be avoided. Thus, a sound knowledge of the sample(s) is essential for adequate multivariate image analysis. Future research should include experiments on different growth media incubated at variable temperatures and water activities.

References

Alberts, J.F., Gelderblom, W.C., Thiel, P.G., Marasas, W.F., Van Schalkwyk, D.J. & Behrend, Y. (1990). Effects of temperature and incubation period on production of fumonisin B1 by *Fusarium moniliforme*. *Applied and Environmental Microbiology*, **56**, 1729-1733.

Bacon, C.W., Glenn, A.E. & Yates, I.E. (2008). *Fusarium verticillioides*: managing the endophytic association with maize for reduced fumonisins accumulation. *Toxin Reviews*, **27**, 411-446.

Baranowski, P., Mazurek, W., Wozniak, J. & Majewska, U. (2012). Detection of early bruises in apples using hyperspectral data and thermal imaging. *Journal of Food Engineering*, **110**, 345-355.

Barker, M. & Rayens, W. (2003). Partial least squares for discrimination. *Journal of Chemometrics*, **17**, 166-173.

Bartnicki-Garcia, S. (1968). Cell wall chemistry, morphogenesis, and taxonomy of fungi. *Annual Review of Microbiology*, **22**, 87-108.

Bauriegel, E., Giebel, A., Geyer, M., Schmidt, U. & Herppich, W.B. (2011). Early detection of *Fusarium* infection in wheat using hyper-spectral imaging. *Computers and Electronics in Agriculture*, **75**, 304-312.

Bhuvaneswari, K., Fields, P.G., White, N.D.G., Sarkar, A.K., Singh, C.B. & Jayas, D.S. (2011). Image analysis for detecting insect fragments in semolina. *Journal of Stored Products Research*, **47**, 20-24.

Chao, K., Chen, Y.R., Hruschka, W.R. & Park, B. (2001). Chicken heart disease characterization by multi-spectral imaging. *Applied Engineering in Agriculture*, **17**, 99-106.

Chevallier, S., Bertrand, D., Kohler, A. & Courcoux, P. (2006). Application of PLS-DA in multivariate image analysis. *Journal of Chemometrics*, **20**, 221-229.

Cowe, I. & McNicol, J. (1985). The use of principal components in the analysis of near-infrared spectra. *Applied Spectroscopy*, **39**, 257-266.

de Oliveira Rocha, L., Reis, G.M., da Silva, V.N., Braghini, R., Teixeira, M.M.G. & Corrêa, B. (2011). Molecular characterization and fumonisin production by *Fusarium verticillioides* isolated from corn grains of different geographic origins in Brazil. *International Journal of Food Microbiology*, **145**, 9-21.

Dubois, J., Neil Lewis, E., Fry Jr, F.S. & Calvey, E.M. (2005). Bacterial identification by near-infrared chemical imaging of food-specific cards. *Food Microbiology*, **22**, 577-583.

Esbensen, K.H. & Lied, T.T. (2007). Principles of multivariate image analysis (MIA) in remote sensing, technology and industry. In: *Techniques and applications of hyperspectral image analysis* (edited by H.F. Grahn & P. Geladi). Pp. 17-41. Chichester, West Sussex: John Wiley & Sons, Ltd.

Fandohan, P., Hell, K., Marasas, W. & Wingfield, M. (2003). Infection of maize by *Fusarium* species and contamination with fumonisin in Africa. *African Journal of Biotechnology*, **2**, 570-579.

Geladi, P., Burger, J. & Lestander, T. (2004). Hyperspectral imaging: calibration problems and solutions. *Chemometrics and Intelligent Laboratory Systems*, **72**, 209-217.

Geladi, P. & Grahn, H.F. (1996). *Multivariate image analysis.* Chichester, West Sussex: John Wiley & Sons Ltd.

Geladi, P., Grahn, H.F. & Burger, J. (2007). Multivariate images, hyperspectral imaging: background and equipment. In: *Techniques and applications of hyperspectral image analysis* (edited by H.F. Grahn & P. Geladi). Pp. 1-14. Chichester, West Sussex: John Wiley & Sons Ltd.

Gelderblom, W.C.A., Abel, S., Smuts, C.M., Marnewick, J., Marasas, W.F.O., Lemmer, E.R. & Ramljak, D. (2001a). Fumonisin induced hepatocarcinogenesis: mechanisms related to cancer initiation and promotion. *Environmental Health Perspectives*, **109**, 291-300.

Gelderblom, W.C.A., Jaskiewicz, K., Marasas, W.F.O., Thiel, P.G., Horak, R.M., Vleggaar, R. & Kriek, N.P.J. (1988). Fumonisins novel mycotoxins with cancer-promoting activity produced by *Fusarium moniliforme*. *Applied and Environmental Microbiology*, **54**, 1806-1811.

Gelderblom, W.C.A., Rheeder, J.P., Leggott, N., Stockenstrom, S., Humphreys, J., Shephard, G.S. & Marasas, W.F.O. (2004). Fumonisin contamination of a corn sample associated with the induction of hepatocarcinogenesis in rats-role of dietary deficiencies. *Food and Chemical Toxicology*, **42**, 471-479.

Gelderblom, W.C.A., Seier, J.V., Snijman, P.W., Van Schalkwyk, D.J., Shephard, G.S. & Marasas, W.F.O. (2001b). Toxicity of culture material of *Fusarium verticillioides* strain MRC 826 to nonhuman primates. *Environmental Health Perspectives*, **109**, 267-276.

Gowen, A.A., O'Donnell, C.P., Cullen, P.J., Downey, G. & Frias, J.M. (2007). Hyperspectral imaging: an emerging process analytical tool for food quality and safety control. *Trends in Food Science and Technology*, **18**, 590-598.

Gowen, A.A., O'Donnell, C.P., Taghizadeh, M., Cullen, P.J., Frias, J.M. & Downey, G. (2008). Hyperspectral imaging combined with principal component analysis for bruise damage detection on white mushrooms (*Agaricus bisporus*). *Journal of Chemometrics*, **22**, 259-267.

Hennequin, C., Abachin, E., Symoens, F., Lavarde, V., Reboux, G., Nolard, N. & Berche, P. (1999). Identification of *Fusarium* species involved in human infections by 28S rRNA gene sequencing. *Journal of Clinical Microbiology*, **37**, 3586-3589.

Kim, M.S., Lefcourt, A.M., Chao, K., Chen, Y.R., Kim, I. & Chan, D.E. (2002). Multispectral detection of fecal contamination on apples based on hyperspectral imagery. Part I. Application of visible and near-infrared reflectance imaging. *Transactions of the ASAE*, **45**, 2027-2037.

Kim, M.S., Lefcourt, A.M., Chen, Y.-R. & Tao, Y. (2005). Automated detection of fecal contamination of apples based on multispectral fluorescence image fusion. *Journal of Food Engineering*, **71**, 85-91.

Koehler, F.W., Lee, E., Kidder, L.H. & Lewis, N.E. (2002). Near infrared spectroscopy: the practical chemical imaging solution. *Spectroscopy Europe*, **14**, 12-19.

Kriek, N.P.J., Marasas, W.F.O., Steyn, P.S., Van Rensburg, S.J. & Steyn, M. (1977). Toxicity of a moniliformin-producing strain of *Fusarium moniliforme* var. *subglutinans* isolated from maize. *Food and Cosmetics Toxicology*, **15**, 579-587.

Liu, Y., Chen, Y.R., Kim, M.S., Chan, D.E. & Lefcourt, A.M. (2007). Development of simple algorithms for the detection of fecal contaminants on apples from visible/near infrared hyperspectral reflectance imaging. *Journal of Food Engineering*, **81**, 412-418.

Liu, Y. & Rayens, W. (2007). PLS and dimension reduction for classification. *Computational Statistics*, **22**, 189-208.

Manley, M., du Toit, G. & Geladi, P. (2011). Tracking diffusion of conditioning water in single wheat kernels of different hardnesses by near infrared hyperspectral imaging. *Analytica Chimica Acta*, **686**, 64-75.

Manley, M., McGoverin, C.M., Engelbrecht, P. & Geladi, P. (2012). Influence of grain topography on near infrared hyperspectral images. *Talanta*, **89**, 223-230.

Manley, M., Williams, P., Nilsson, D. & Geladi, P. (2009). Near infrared hyperspectral imaging for the evaluation of endosperm texture in whole yellow maize (*Zea maize* L.) kernels. *Journal of Agricultural and Food Chemistry*, **57**, 8761-8769.

Marasas, W.F.O. (2001). Discovery and occurence of the fumonisins: a historical perspective. *Environmental Health Perspectives*, **109**, 239-243.

Marasas, W.F.O., Thiel, P.G., Rabie, C.J., Nelson, P.E. & Toussoun, T.A. (1986). Moniliformin production in *Fusarium* section *Liseola*. *Mycologia*, **78**, 242-247.

Marín, S., Homedes, V., Sanchis, V., Ramos, A. & Magan, N. (1999a). Impact of *Fusarium moniliforme* and *F. proliferatum* colonisation of maize on calorific losses and fumonisin production under different environmental conditions. *Journal of Stored Products Research*, **35**, 15-26.

Marín, S., Magan, N., Bellí, N., Ramos, A.J., Canela, R. & Sanchis, V. (1999b). Two-dimensional profiles of fumonisin B1 production by *Fusarium moniliforme* and *Fusarium proliferatum* in relation to environmental factors and potential for modelling toxin formation in maize grain. *International Journal of Food Microbiology*, **51**, 159-167.

Marin, S., Magan, N., Serra, J., Ramos, A., Canela, R. & Sanchis, V. (1999). Fumonisin B1 production and growth of *Fusarium moniliforme* and *Fusarium proliferatum* on maize, wheat, and barley grain. *Journal of Food Science*, **64**, 921-924.

Marinach-Patrice, C., Lethuillier, A., Marly, A., Brossas, J.Y., Gené, J., Symoens, F., Datry, A., Guarro, J., Mazier, D. & Hennequin, C. (2009). Use of mass spectrometry to identify clinical *Fusarium* isolates. *Clinical Microbiology and Infection*, **15**, 634-642.

Martens, H. (2001). Reliable and relevant modelling of real world data: a personal account of the development of PLS Regression. *Chemometrics and Intelligent Laboratory Systems*, **58**, 85-95.

McGoverin, C., Engelbrecht, P., Geladi, P. & Manley, M. (2011). Characterisation of non-viable whole barley, wheat and sorghum grains using near-infrared hyperspectral data and chemometrics. *Analytical and Bioanalytical Chemistry*, **401**, 2283-2289.

Möller, E.M., Chełkowski, J. & Geiger, H.H. (1999). Species-specific PCR assays for the fungal pathogens *Fusarium moniliforme* and *Fusarium subglutinans* and their application to diagnose maize ear rot disease. *Journal of Phytopathology*, **147**, 497-508.

Mulè, G., Susca, A., Stea, G. & Moretti, A. (2004). A species-specific PCR assay based on the calmodulin partial gene for identification of *Fusarium verticillioides*, *F. proliferatum* and *F. subglutinans*. *European Journal of Plant Pathology*, **110**, 495-502.

Nelson, P.E., Dignani, M.C. & Anaissie, E.J. (1994). Taxonomy, biology, and clinical aspects of *Fusarium* species. *Clinical Microbiology Reviews*, **7**, 479-504.

Nirenberg, H.I. & O'Donnell, K. (1998). New *Fusarium* species and combinations within the *Gibberella fujikuroi* species complex. *Mycologia*, 434-458.

Osborne, B.G., Fearn, T. & Hindle, P.H. (1993). *Practical NIR Spectroscopy with Applications in Food and Beverage Analysis.* Pp. 29-33. Essex, England: Longman Scientific & Technical.

Park, B., Kise, M., Lawrence, K., Windham, W., Smith, D. & Thai, C. (2007). Real-time multispectral imaging system for online poultry fecal inspection using unified modeling language. *Sensing and Instrumentation for Food Quality and Safety*, **1**, 45-54.

Park, B., Lawrence, K.C., Windham, W.R. & Buhr, R.J. (2002). Hyperspectral imaging for detecting fecal and ingesta contaminants on poultry carcasses. *Transactions of the ASAE*, **45**, 2017-2026.

Park, B., Lawrence, K.C., Windham, W.R. & Smith, D.P. (2004). Multispectral imaging system for fecal and ingesta detection on poultry carcasses. *Journal of Food Process Engineering*, **27**, 311-327.

Pirt, S.J. (1967). A kinetic study of the mode of growth of surface colonies of bacteria and fungi. *Journal of General Microbiology*, **47**, 181-197.

Santos, C., Paterson, R.R.M., Venâncio, A. & Lima, N. (2010). Filamentous fungal characterizations by matrix-assisted laser desorption/ionization time-of-flight mass spectrometry. *Journal of Applied Microbiology*, **108**, 375-385.

Snyder, W.C. & Hansen, H.N. (1940). The species concept in *Fusarium*. *American Journal of Botany*, **27**, 64-67.

Summerell, B.A., Salleh, B. & Leslie, J.F. (2003). A utilitarian approach to *Fusarium* identification. *Plant Disease*, **87**, 117-128.

Viljoen, A., Marasas, W.F.O., Wingfield, M.J. & Viljoen, C.D. (1997). Characterization of *Fusarium subglutinans* f. sp. *pini* causing root disease of *Pinus patula* seedlings in South Africa. *Mycological Research*, **101**, 437-445.

Williams, P., Geladi, P., Britz, T. & Manley, M. (2012a). Growth characteristics of three *Fusarium* species evaluated by near-infrared hyperspectral imaging and multivariate image analysis. *Applied Microbiology and Biotechnology*, **96**, 803-813.

Williams, P., Geladi, P., Fox, G. & Manley, M. (2009). Maize kernel hardness classification by near infrared (NIR) hyperspectral imaging and multivariate data analysis. *Analytica Chimica Acta*, **653**, 121-130.

Williams, P., Manley, M., Fox, G. & Geladi, P. (2010). Indirect detection of *Fusarium verticillioides* in maize (*Zea mays* L.) kernels by near infrared hyperspectral imaging. *Journal of Near Infrared Spectroscopy*, **18**, 49-58.

Williams, P.J., Geladi, P., Britz, T.J. & Manley, M. (2012b). Investigation of fungal development in maize kernels using NIR hyperspectral imaging and multivariate data analysis. *Journal of Cereal Science*, **55**, 272-278.

Wold, S., Sjöström, M. & Eriksson, L. (2001). PLS-regression: a basic tool of chemometrics. *Chemometrics and Intelligent Laboratory Systems*, **58**, 109-130.

Yao, H., Hruska, Z., Kincaid, R., Brown, R. & Cleveland, T. (2008). Differentiation of toxigenic fungi using hyperspectral imagery. *Sensing and Instrumentation for Food Quality and Safety*, **2**, 215-224.

Yoon, S., Lawrence, K., Line, J., Siragusa, G., Feldner, P., Park, B. & Windham, W. (2010). Detection of *Campylobacter* colonies using hyperspectral imaging. *Sensing and Instrumentation for Food Quality and Safety*, **4**, 35-49.

Yoon, S., Lawrence, K., Smith, D., Park, B. & Windham, W. (2008). Embedded bone fragment detection in chicken fillets using transmittance image enhancement and hyperspectral reflectance imaging. *Sensing and Instrumentation for Food Quality and Safety*, **2**, 197-207.

CHAPTER 5
GROWTH CHARACTERISTICS OF THREE *FUSARIUM* SPECIES EVALUATED BY NEAR-INFRARED HYPERSPECTRAL IMAGING AND MULTIVARIATE IMAGE ANALYSIS*

Abstract

Colony growth of three *Fusarium* spp. on potato dextrose agar was followed by collecting near-infrared (NIR) hyperspectral images of the colonies at regular intervals after inoculation up to 55 h. After principal component analysis (PCA), two clusters were apparent in the score plot along principal component 1. Using the brushing technique, these clusters were divided into four groups of pixels with similar score values. These could be visualised as growth zones within the colonies in the corresponding score image. Three spectral bands, i.e. 1166, 1380 and 1918 nm, were prominent in the multiplicative scatter corrected and Savitzky-Golay second derivative spectra. These indicated chemical changes, associated with carbohydrates (1166 and 1380 nm) and protein (1918 nm), that occurred as the mycelium grew and matured. The protein band was more prominent in the mature fungal material while the carbohydrate band was less pronounced. The younger material and the agar were characterised by the carbohydrate spectral band. Integrating whole mycelium colonies as the sum of pixels over time made it possible to construct curves that resembled growth curves; this included the lag phase, active growth phase, deceleration phase and phase of constant growth. Growth profiles constructed from individual growth zones indicated more detailed growth characteristics. The use of NIR hyperspectral imaging and multivariate image analysis (MIA) allowed one to visualise radial growth rings in the PCA score images. This would not have been possible with bulk spectroscopy. Interpreting spectral data enabled better understanding of microbial growth characteristics on agar medium. NIR hyperspectral imaging combined with MIA is a powerful tool for the evaluation of growth characteristics of fungi.

*Published as: Williams, P., Geladi, P., Britz, T. & Manley, M. (2012). Growth characteristics of three *Fusarium* species evaluated by near-infrared hyperspectral imaging and multivariate image analysis. *Applied Microbiology and Biotechnology*, **96**, 803-813.

Introduction

Fusarium spp. are among the most common fungi (Booth, 1977) and are of major economic importance (Nganje *et al.*, 2004). They are known for their intimate association with cereals as a plant pathogen and have been isolated from maize (Adejumo *et al.*, 2007), wheat (Jenkinson & Parry, 1994) and barley (Salas *et al.*, 1999). In addition to their pathogenicity, they are capable of producing toxic secondary metabolites known as mycotoxins. Fumonisins, probably the most well-known mycotoxin of this genus, have been associated with oesophageal cancer in humans, pulmonary edema syndrome in pigs, liver cancer in rats and leukoencephalomalacia in horses (Marasas, 1995; Marasas, 2001).

Filamentous fungi, similar to bacteria, yeasts and other non-filamentous organisms, are characterised by exponential growth in submerged homogeneous liquid cultures; provided the filaments are uniformly dispersed and do not aggregate to form pellets (Pirt, 1966). It is putative that colonies of filamentous fungi growing on solid media in Petri dish cultures spread outwards at a constant rate, often termed the linear rate of growth (Pirt, 1967). Individual hypha increase and extend at a constant rate (linear growth) but branching produces exponential growth in a mass of hyphae (Plomley, 1959; Trinci, 1969). The formation of a colony can be described on the basis of growth of the hyphae and was clarified by proposing the term growth unit (Plomley, 1959). This term is based on the growth of individual hypha; hypha increase in length at a constant rate, while the increase in length of all the hyphae (mycelium) is proportionate to its amount and is associated with branching (Plomley, 1959). Much work on the growth characteristics and kinetics of fungal growth has been done. These involved classic techniques coupled with measurements from photographs and microscopes (Plomley, 1959; Trinci, 1969; Gow & Gooday, 1982) and time lapse cameras (Trinci, 1971; Trinci, 1974; Steele & Trinci, 1975); cytochemical processing and photo microscopy (Zalokar, 1959b; Yanagita & Kogané, 1962) and enzyme assays (Zalokar, 1959a). These techniques are painstaking and time consuming and often involved using an enlarger with a projection screen for measurement of colonies with a ruler. In certain instances measurements were done with low-power microscopes with a micrometre eyepiece at 37°C (Pirt, 1967).

Spectroscopic techniques, specifically near-infrared (NIR) spectroscopy, are rapid and increasingly being used to detect and identify pathogens and mycotoxins on food and agricultural products. The use of Fourier transform near infrared (FT-NIR) spectroscopy and multivariate pattern recognition techniques were evaluated for the rapid detection and identification of bacterial contamination in liquids (Rodriguez-Saona *et al.*, 2001). Principal component analysis (PCA) on second derivative spectra reproducibly grouped samples into clusters based on cell wall composition of each of the respective bacteria. In a similar study, the identification and detection of bacteria in an isolated system was investigated with accuracies of 100% for the classification of three *Pseudomonas* spp. (Alexandrakis *et al.*, 2008). In another study, the level of bacterial contamination on shredded cabbage was measured in the range of 700-1000 nm (Suthiluk *et al.*, 2008). NIR spectroscopy was successfully evaluated as a rapid technique for the detection of

kernel rots and mycotoxin in maize (Berardo *et al.*, 2005), while scab, vomitoxin and ergosterol were predicted in single wheat kernels (Dowell *et al.*, 1999). Fumonisins were detected in single maize kernels infected with *Fusarium verticillioides* using reflectance and transmittance near infrared spectroscopy (Dowell *et al.*, 2002), and aflatoxin B1 was detected in maize and barley (Fernández-Ibañez *et al.*, 2009). Recently, deoxynivalenol concentrations were estimated using NIR spectroscopy and partial least squares regression (Beyer *et al.*, 2010). These methods, although high in spectral resolution, are limited in the spatial dimension, offering no information regarding the location of the substance or contaminant investigated. Measurements are made at a single point or limited area on the sample and averaged; thus the entire sample is not measured but parts thereof and the result is always given as a single spectrum. A technique capable of incorporating localisation, thus measuring entire samples, rapidly and accurately is NIR hyperspectral imaging.

NIR hyperspectral imaging, an analytical system, relatively new to the measurement of food and agricultural products, is a spectroscopic technique that couples spectroscopy and imaging (Goetz *et al.*, 1985; Geladi *et al.*, 2007). Light reflected from or transmitted through the sample is directed towards the imaging spectrograph, where an image is formed. Pixel dimensions are dependent on the size of the detector, and wavelength dimensions rely on the type of detector. Data are collected in cubes, by acquiring an image of the sample comprised of the *x* and *y* pixel coordinates (spatial dimension) and the wavelength (spectral) dimension (λ) (Burger & Geladi, 2005). The spectral dimension serves as a fingerprint for the various chemical bonds present. Together these enable identification and localisation of chemical constituents occurring in a sample. A data cube, also known as a hypercube, from a SisuCHEMA imaging system comprises, e.g. 301 x 320 pixels x 242 wavelengths; each pixel represents a spectrum. This hypercube would thus result in a data set composed of 96 320 spectra at 242 wavelength channels. It is apparent that enormous amounts of data are obtained from a single sample using NIR hyperspectral imaging, posing potential data analysis problems. The data needs multivariate image analysis (MIA) for interpretation.

Multivariate and hyperspectral image analysis are techniques employed for the exploration and interpretation of hypercubes (Geladi & Grahn, 1996; Burger & Geladi, 2007). PCA is essential for data reduction and examination of NIR spectra (Cowe & McNicol, 1985) and forms the basis of MIA. Prior to any data treatment, the hypercube is first reorganised into a matrix **X**, where the pixel information (*x*, *y*) are the observations and the wavelengths are the variables. The data are first mean-centred then decomposed into a scores matrix (**T**), a loadings matrix (**P'**) and a residual matrix (**E**) according to equation 1:

$$\boldsymbol{X = TP' + E} \qquad \text{…[eq. 1]}$$

The scores matrix can be used to construct score plots and reorganised into score images. Score plots illustrate the score values of the principal components (PCs) plotted against each other

while score images show the score values plotted as contour maps of the sample imaged for each PC. The two plots are interactive; selecting pixels with high score values in the scores plot will highlight the pixels in the scores image allowing visualisation of location within the sample. While the scores describe the relationship of the objects in the decomposed matrix, the loadings represents the variation in the wavelength dimension. This is visualised by plotting the loading values against the wavelengths. When used in combination, the scores and loadings permit the visualisation, localisation and identification of desired parameters within an image.

NIR hyperspectral imaging, when used as a tool for food quality and safety (Du & Sun, 2004; Gowen *et al.*, 2007; Wang & Paliwal, 2007), often concerns some microbiological aspects. Recently, NIR hyperspectral imaging was evaluated for the rapid detection of *E. coli* on packaged fresh spinach with an R^2 of 0.97 and root mean square error of prediction of 0.038 (Log(CFU/g)) (Siripatrawan *et al.*, 2011). On cereal grains, NIR hyperspectral imaging has been used for the indirect (Williams *et al.*, 2010) and early (Del Fiore *et al.*, 2010; Williams *et al.*, 2012b) detection of toxigenic fungi on maize kernels; on wheat kernels it has been used to assess damage caused by *Fusarium* spp. (Delwiche *et al.*, 2011; Shahin & Symons, 2011). A preliminary study for the identification of bacteria on food cards showed it was possible to differentiate between bacteria based on their NIR spectra (Dubois *et al.*, 2005). In a study on beef, NIR hyperspectral imaging was used to predict the total viable count per gram of beef with an R^2 of 0.95 and standard error of prediction of 0.30 $\log_{10}$ (total viable count) (Peng *et al.*, 2011).

The aforementioned studies considered the detection, identification and differentiation of microbial spoilage or contamination on food products, which in itself are complex matrices. In order to investigate and differentiate microorganisms in a more controlled manner and environment, plating out on the appropriate growth medium and incubating at the optimum temperature is necessary. Yao *et al.* (2008) studied five different toxigenic fungi on growth media and was able to differentiate between all with a classification rate of 97.7%. A similar study concerning the detection of *Campylobacter* colonies on growth media reported accuracies of between 97 and 99% (Yoon *et al.*, 2010). Both studies, although novel, suffer a shortcoming in that they utilised parts of the visible spectrum for differentiation and detection of the microbes investigated. The NIR region is more chemical rich and utilising this region allows for a more comprehensive study of a given sample. In a recent study using NIR hyperspectral imaging for the differentiation of species of the *Fusarium* genus, clear differences within each mycelium complicated the data classification between species with all the strains included in the mosaic (Williams *et al.*, 2012a). These indicated chemical differences within the mycelium as it grows and this required further investigation.

The aim of this work was thus to study the growth characteristics of three *Fusarium* spp. on a growth medium using NIR hyperspectral imaging and MIA.

Materials and methods

Sample preparation

Fungal isolates were kindly supplied by the Department of Plant Pathology, Stellenbosch University, South Africa. The isolates included the following organisms: *F. verticillioides* (MRC 0826), *Fusarium subglutinans* (MRC 0115) and *Fusarium proliferatum* (MRC 2301). The strains were streaked out on potato dextrose agar (PDA) (Merck (Pty) Ltd, Cape Town, South Africa) and incubated at 28°C in Petri dishes for a total of 55 h.

NIR hyperspectral imaging system and image collection

The SisuCHEMA short wave infrared camera (Specim, Spectral Imaging Ltd, Oulu, Finland) was used to acquire hyperspectral images. A 2-D array mercury-cadmium-telluride detector inside the camera was used with a prism-grating-prism monochromator. Individual images were acquired within a spectral range of 996-2502 nm at 10 nm resolution, spectral sampling per pixel of 6.3 nm and a field of view of 100 mm x 100 mm. Images of the entire Petri dish, without removing the lid, were collected at approximately 2-hour intervals immediately post-inoculation. Image acquisition of the same Petri dish was performed from 09:00 to 17:00 for three days to generate a total of 15 time points, i.e. 15 images spanning 55 h for each of the three species. The time points with corresponding actual times in hours were as follows: T0 (0 h), T1 (2 h), T2 (4 h), T3 (6 h), T4 (8 h), T5 (23 h), T6 (25 h), T7 (27 h), T8 (29 h), T9 (31 h), (T10 (47 h), T11 (49 h), T12 (51 h), T13 (53 h) and T14 (55 h).Internal dark and white reference standards were imaged prior to each sample. A typical hypercube had dimensions of 301 × 320 pixels × 242 wavelengths.

Hyperspectral image analysis

Images were analysed using the Evince v.2.5.5 (UmBio AB, Umeå, Sweden) hyperspectral image analysis software package. The image calibration and correction to absorbance was done automatically in the Evince software package according to (Williams *et al.*, 2012b).

Cleaning and construction of mosaics

Raw hypercubes were cleaned from background (agar), shading, bad pixels and reflection from the Petri dish to segment the colonies in new smaller hypercubes. In addition, wavelengths that disturbed the analyses were removed. These included 996-1097 nm and 2489-2502 nm where the detector is less sensitive resulting in noisy spectral regions. Individual time images were merged to form mosaics which included the entire time series. This was done for each of the three *Fusarium* species separately.

Data analysis

PCA was calculated on mean-centred data with 6 principal components (PC's) using Evince v.2.5.5. Score images, score plots and loading line plots were used to investigate the growth of the

colonies over time. Average spectra and growth curves were constructed using MATLAB v 7.10 (The MathWorks, MA, USA).

Results

A slice of one of the original hypercubes (T10), randomly selected at 1374 nm, is shown in Figure 5.1. This image, at the 1374 nm channel, shows a typical dark grey *Fusarium* colony in the centre of a Petri dish. The mosaics of all the time points combined for each of the three *Fusarium* spp. were analysed by PCA after mean centering. As similar results were observed for all three species in terms of difference between time points, the mosaic results for only one of the species are shown, i.e. *F. subglutinans*.

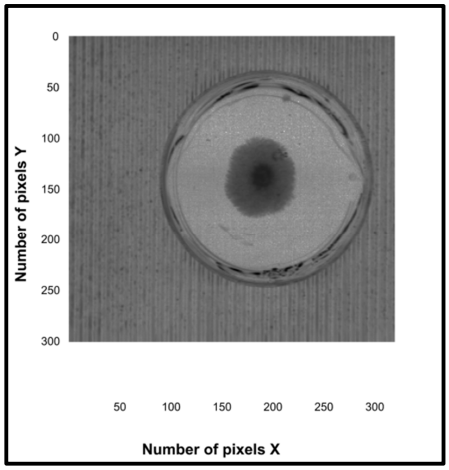

Figure 5.1. Slice of the hypercube at 1374 nm of one of the original hypercubes prior to cleaning. Dark grey spot in the centre of the Petri dish is the colony studied.

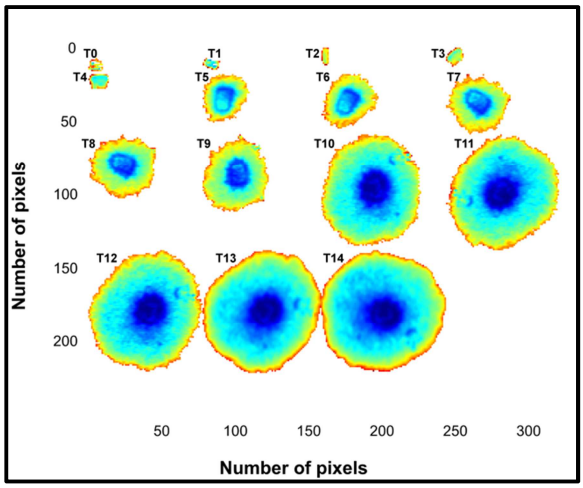

Figure 5.2. Score image of PC1 showing mosaic of 15 time points for *F. subglutinans*. From left to right: upper row = T0-T3; second row = T4-T7; third row = T8-T11 and fourth row = T12-T14.

PC1 explained 99.4% of the total sum of squares (%SS) and is depicted in the score image shown in Figure 5.2. The centre of the colonies appears to be changing with time. This can be seen from T5 where the centre has low score values (cold colours; cyan) that decrease even more till T14 (dark blue). The surrounding mycelia are different to the centre with slightly higher score

values. The highest score values (warm colours; yellow/red) can be found at the extreme edges of the colonies and are likely a mixture of pixels associated with agar and mycelium. The score plot of PC1 vs. PC2 shows clustering only in the direction of PC1 (Fig. 5.3a). The %SS of PC2 was small (0.26%) and no clustering could be observed. The small cluster was associated with the centre of the fungal colonies, when selected in the score plot and projected onto the score image. The much larger cluster (including both negative and positive score values from -5 to +5) was associated with the remainder of the fungal colony (score images with projections not shown). To better evaluate the differences along PC1, a tentative division of pixels into four groups, with similar score values within a group, was made (Fig. 5.3a). In this way groups of pixels with similar score values were defined in an unsupervised manner (Manley *et al.*, 2011; Manley *et al.*, 2012). The divisions were made as such to include only negative or positive score values. Each group was over-laid with a different colour (Fig. 5.3b) and projected onto the score image (Fig. 5.3c). From this image, it is clear that the differences observed in the direction of PC1 are due to differences in radial growth. From T10 to T14, there were four distinct concentric circles within each colony. For T0-T4, the colonies were very small and no radial growth was observed.

The variation captured by PC1 was described by five prominent peaks (two positively loaded and three negatively loaded) in the loading line plot (Fig. 5.3d) calculated from Savitzky-Golay second derivative (3rd order polynomial; 15 point smoothing) spectra. The positively loaded peaks were at *ca*. 1279 nm (2 × C-H stretch + C-H deformation-CH_3) and 1943 nm (O-H stretch + O-H deformation-H_2O) and are most likely associated with carbohydrates and moisture, respectively. The negatively loaded peaks were located at *ca*. 1198 nm (C-H stretch second overtone, CH_3), 1380 nm (2 × C-H + C-H deformation, CH_2) and 1837 nm (O-H stretch + 2 × C-O stretch, cellulose) all associated with carbohydrates. These describe the variation between only the small cluster and the larger cluster (Fig. 5.3a) observed along PC1; thus the negatively loaded peaks are associated with the small cluster while the positively loaded peaks are associated with the larger cluster. For a detailed description of the spectral variation within and between each of the four defined groups of pixels, calculating and evaluating mean spectra of each group was required.

Mean spectra of the four groups of pixels were constructed by selecting each group in the score plot (Fig. 5.3b), calculating the mean and plotting them from 1100 to 2200 nm. An average spectrum of the agar was calculated in a similar manner and included in the plot. The mean spectra were exported to MATLAB v 7.10 (The MathWorks) for further analyses. To remove effects of scattering and to compare the mean spectra from approximately the same baseline, the data were treated with the multiplicative scatter correction (MSC) algorithm (Geladi *et al.*, 1985). These spectra are shown in Figure 5.4a where red is the mean spectrum from the oldest region or the centre spot of the culture; blue is the region just surrounding the centre, *i.e.* newer material or newer growth; cyan is the area closest to the edge; mustard is the outermost region of growth and edge (colours correspond with those in Fig. 5.3b); and black is the agar.

The Savitzky-Golay technique (Savitzky & Golay, 1964) was used to calculate second derivatives (3rd order polynomial; 15 point smoothing) from 1100 to 2200 nm (Fig. 5.4b). These spectra are shown with the average agar spectrum (Fig. 5.4.b) and without (Fig. 5.4c) to emphasise mycelium features. As would be expected, there is a marked difference between the agar spectrum and the spectra associated with the fungi. At *ca*. 1166 nm and approximately 1380 nm (2 × C-H + C-H deformation, CH_2), there is a gradual decrease in 2nd derivative values from the agar spectrum, youngest, young, intermediate and old mycelium spectra. A prominent band at *ca*. 1918 nm is apparent and is most likely ascribed to protein because of the presence of a CONH (peptide bond) structure arising from a C=O stretch, second overtone. A peak at 1405 nm was unique to the agar spectrum. This peak was characterised by an O-H stretch, first overtone due to the presence of an ROH functional group. It is likely due to the polysaccharide content of the agar medium. Similar results were found for both *F. verticillioides* and *F. proliferatum* (results not shown).

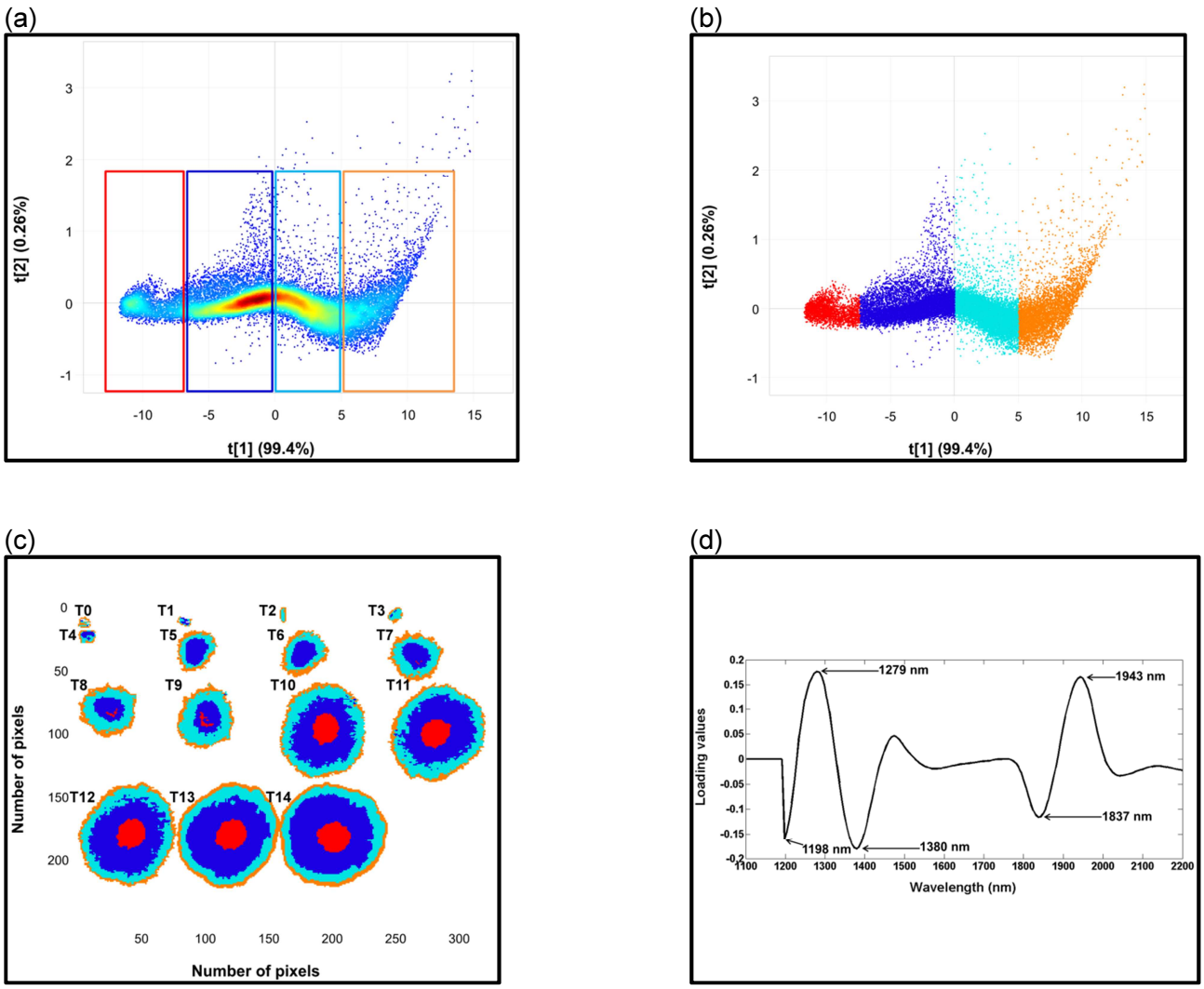

Figure. 5.3 (a) Score plot of PC1 vs. PC2 for the mosaic of *F. subglutinans* time series with division of pixels indicated. (b) Grouping of pixels with similar score values along PC1 applied to the score plot. (c) Projection of pixel groups onto image space allowing visualisation of the variation in PC1. Where red is old; blue is the region just surrounding the centre or newer growth; cyan is the area closest to the edge; mustard is the outermost region of growth and edge. (d) Loading line plot of PC1 showing the variables (carbohydrates and moisture) responsible for the variation between the small cluster (negative loadings) and the larger cluster (positive loadings) in the score plot.

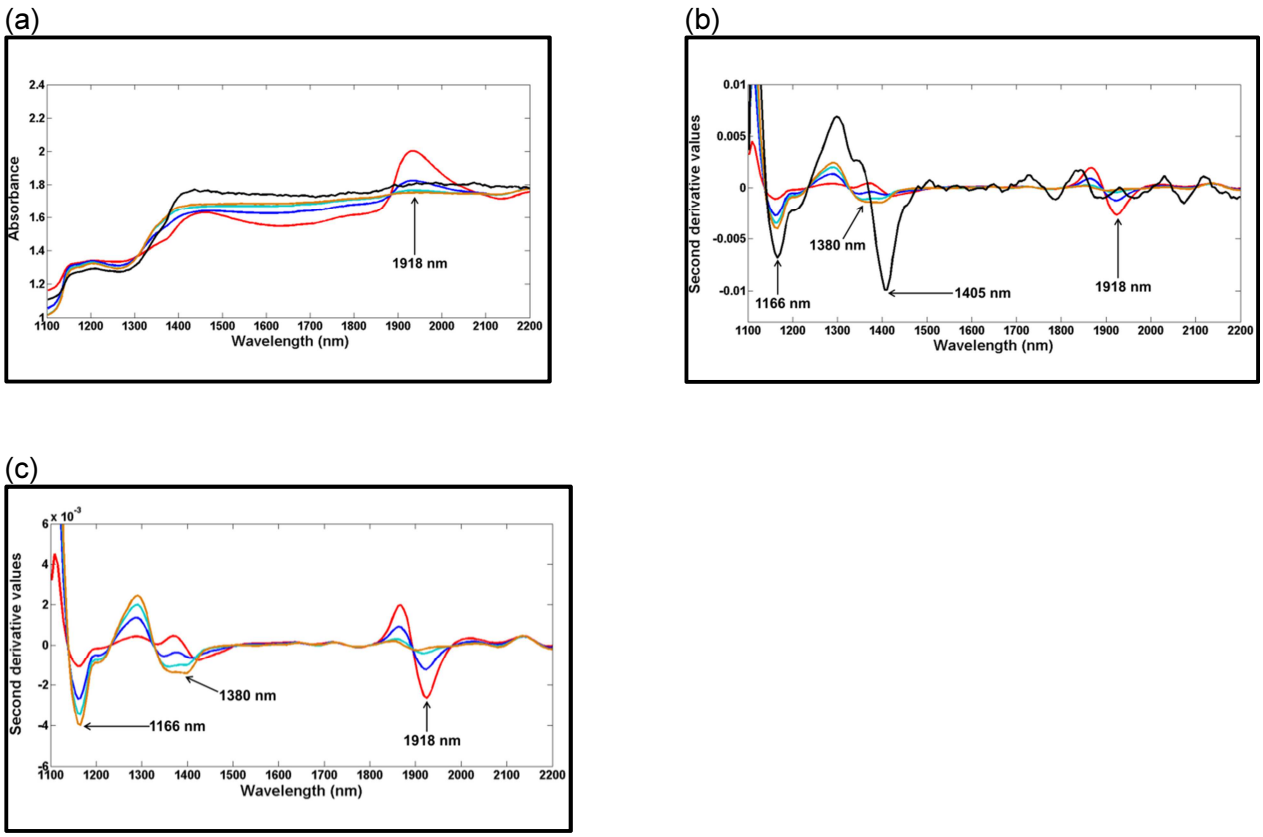

Figure 5.4. (a) Multiplicative scatter corrected (MSC) mean spectra of only the agar as well as the four groups of pixels in Fig. 3a. (b) Savitzky-Golay second derivatives (3rd polynomial; 15 points) of mean spectra of the four groups of pixels (same as colours in Fig. 3b) and agar (black line). (c) The same as (b) with agar spectrum removed.

To determine whether exponential growth could be observed in the NIR hyperspectral images, the growth of the mycelium was expressed as the number of pixels at each time point. This was done for each colony for all three species. This resulted in Figure 5.5, which represents a growth profile of mycelium (expressed as number of pixels) for each of the three *Fusarium* spp. It is important to keep in mind that the mycelium growth was shown to consist of radial growth rings (Figs. 5.3b & c) which suggests that different growth patterns could exist. The score images with only T5, T9 and T14 included were subsequently used to explain the growth characteristics occurring in more detail (Fig. 5.6a). The left colony (T5) shows how the mycelium grew around the inoculation point and built concentric growth rings. The edge (mustard colour) is the youngest or newest growth but it is very thin and is mixed with spectral information from the agar. The cyan ring is young growth but older than the mustard region and the blue zone is intermediate age growth. The middle colony (T9) shows that the young growth zone (cyan) has expanded and depicts old growth appearing (red) in the centre around the inoculation point. The right colony (T14) shows a mature mycelium with a larger area of older growth (red) in the middle, which is clearly different to the younger growth. The area of intermediate growth (blue) has increased substantially as well as the area of young growth (cyan) while the edge covers a small area (mustard).

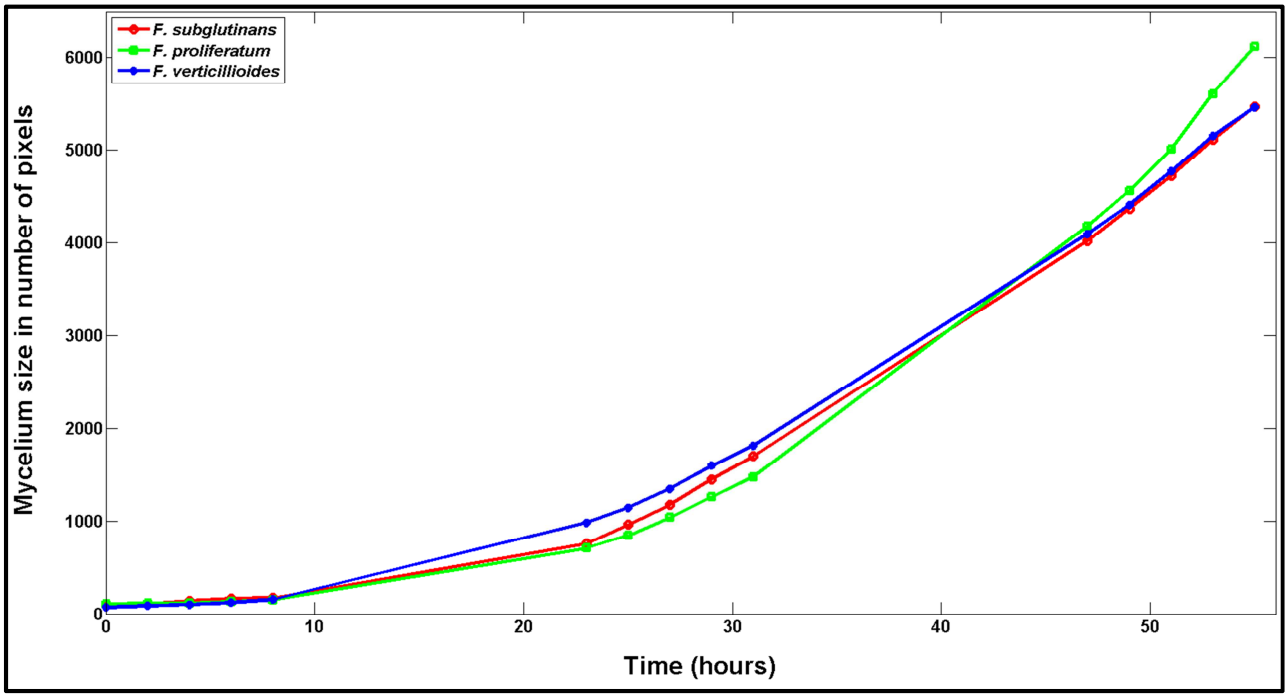

Figure 5.5. Growth of colonies of *F. subglutinans* (red), *F. proliferatum* (green) and *F. verticillioides* (blue) up to 55 h of inoculation (expressed as sum of pixels).

The pixels of the individual growth zones were segmented and measured as a function of time to give a more detailed depiction of the growth characteristics (Fig. 5.6b). During the first 8 h after inoculation, as with the previous growth curve, the fungi are in a lag phase. At 23 h after inoculation the "active-growth", seen as a sharp increase in pixel number over time, phase begins; here the young (cyan), intermediate (blue) and very young (mustard) mycelial growth dominated and appeared to be covering the mycelium area equally. From this point, the new growth was rapidly spreading concentrically. As this continued, the extending zone increased and moved outward to clean agar medium. As the extending zone and the productive zone increased concentrically, they aged and transformed into the fruiting zone. The productive zone dominated from 27 h after inoculation, following a phase of increased growth, by covering the largest area in the mycelium and this continued till 31 h post inoculation. Simultaneously, the extending zone and fruiting zone increased gradually till 31 h after inoculation. At this point, the old growth or aged zone emerged, increasing in area and thickness. From 47 h after inoculation, the fruiting zone covered the largest area of the mycelium followed by the productive zone. Here the growth decelerated till 55 h post inoculation; the productive zone seems to plateaux and entered a phase of constant growth rate while the fruiting zone steadily increased in area as the mycelium aged. The aged zone increased from 23 h to 47 h after inoculation and continued to increase in area as the mycelium matured. The extending zone increased steadily from 23 h to 55 h post inoculation but did not cover a large area of the mycelium. Here, the radial extension would have continued until environmental conditions become unfavourable. A digital image of *F. subglutinans* (Fig. 5.7) shows the difference in mycelium growth from the centre (aged zone) toward the edge (extension zone).

(a)

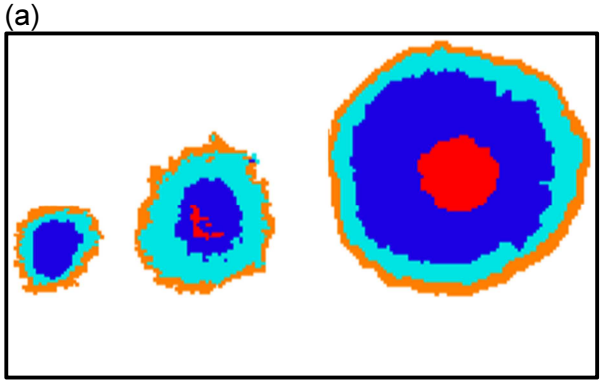

(b)

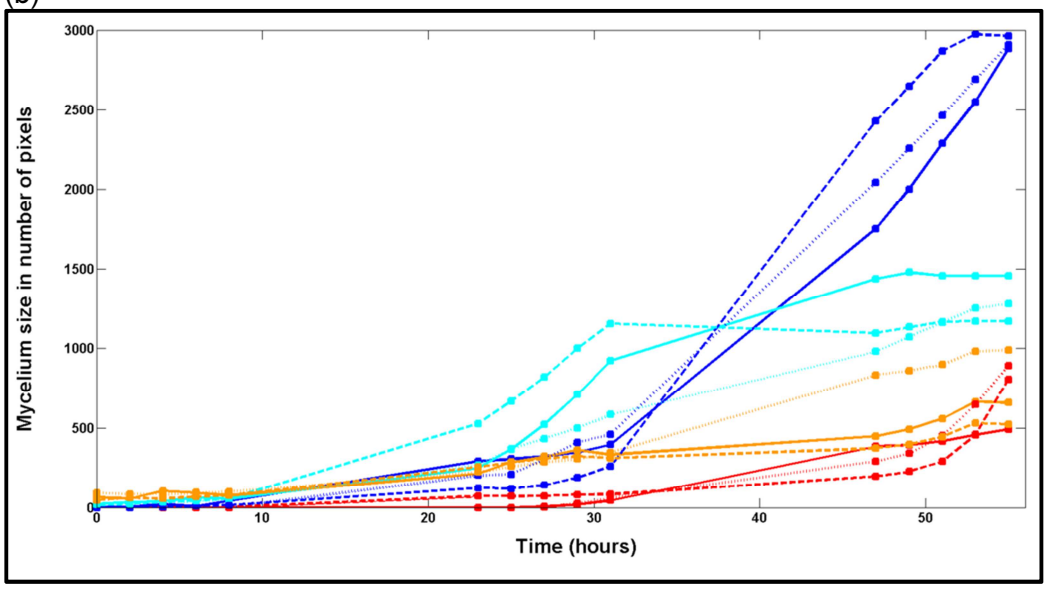

Figure 5.6. (a) Very young (mustard), young (cyan), intermediate (blue) and old (red) growth after 23 (T5; left), 31 (T9; centre) and 55 (T14; right) h. (b) Individual growth curves of oldest mycelium (red), intermediate (blue) young (cyan) and very young (mustard). Dotted line is *F. proliferatum*, dashed line is *F. verticillioides* and solid line is *F. subglutinans*.

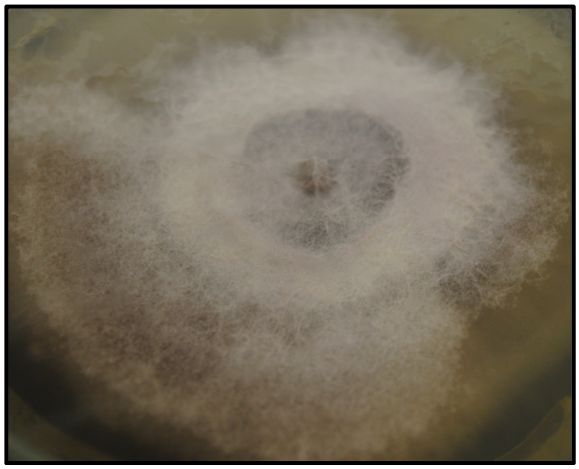

Figure 5.7. Digital colour image of a *F. subglutinans* colony on PDA, showing thicker growth in the centre as opposed to the edges where agar is visible through the mycelium growth. (Sony Cybershot, DSC-W210).

Discussion

Using NIR hyperspectral imaging for the differentiation of three *Fusarium* spp. on agar medium Williams *et al.* (2012a) demonstrated the potential of this technique for microbiological applications. Clear differences within each mycelium, however, complicated the data classification between species with all the strains included in the mosaic. Figure 5.3c shows similarities to classification images observed in Williams *et al.* (2012a) where different regions were observed based on chemical differences within each region.

The loading line plot explains the difference between the two prominent clusters in Figure 5.3a along PC1. Thus, the variation along this component changes from negative to positive score values and is associated with changes in carbohydrates and moisture. As the mycelium grows and ages, there is a change in carbohydrate (content or structure) and moisture. It has been reported that mycelia of the inner colony contains more cell wall substance (polysaccharides) than the outer regions (Yanagita & Kogané, 1962). The cell wall composition of the inner growth regions is more complex than those of the outer regions and is likely due to changes in carbohydrates. Although the score plot allowed a primitive subdivision into four defined groups of pixels with similar score values, the corresponding loading line plot was not adequately informative to describe this variation between the groups. It was deemed better to look at average spectra of the different defined groups of pixels. The loadings only showed an average gradient. The average spectra of the four groups showed more detail.

From Figure 5.4a it appears that the spectra from the older regions of growth have a unique shape compared to the newer growth regions and that the newer growth region's spectral shape is similar to that of the agar spectrum. It is expected that the mycelium growth in the centre of the Petri dish would be denser than in the outer regions. As the mycelium grows outwards, the growth progressively gets thinner and less dense allowing reflection from the agar to be detected by the instrument. This phenomenon could be due to the mycelium thickening as it ages; more of the agar is covered thus less to no reflection from the agar reaches the detector. It was also reported that the middle and central zones contains the highest concentration of polysaccharides compared to the other growth zones (Yanagita & Kogané, 1962). Mycelia of the inner zones (older growth) of the fungal colony contain much more cell wall substances than those of the outer zones (newer growth). The presence of the spectral band at 1918 nm is unique as it is not present in the agar and increases gradually in the sequence from younger to older mycelium spectra; indicating an increase in protein. This increase could be due to the thicker mycelium growth or the presence of spores. These spectral differences confirm the potential of using NIR hyperspectral imaging to identify growth characteristics of fungal colonies on growth media.

It is well known that bacterial and fungal colonies exhibit exponential growth (Pirt, 1967). This is also the case for filamentous fungi, provided the filaments do not aggregate to form pellets (Pirt, 1966). Curves similar to those in Figure 5.5 were reported by Trinci (1969; 1971) while investigating kinetics of fungal growth. In a batch culture experiment, investigating the width of the

peripheral growth zone on the radial growth rate of fungal colonies, growth curves for *Geotrichum lactis* at 25°C were shown (Trinci, 1971). The growth curves were based on the mycelium dry weight over incubation time and divided into four phases: lag, exponential growth, deceleration and very slow autolysis. Measuring the colony radius from the circumference of the inoculum on solid media, the growth of *Aspergillus nidulans* over time, showed a comparable curve (Trinci, 1969). Here too, the colony growth was divided into four phases, however in this case it was observed that the final growth phase was characterised by a constant growth rate. The curves in this study (Fig. 5.5) closely resemble the curve of *A. nidulans* found by (Trinci, 1969) and could also easily be divided into four phases of growth. The number of pixels in Figure 5.5 represents the sum of the pixels in the mycelium area. From T0 to T4, the lag phase is evident. However, since too few data points were collected, exponential growth could not be inferred. This region, T5-T9, was referred to as the active-growth phase. As can be noticed in the graph, this phase had already begun at T4 and continued during the period of no measurement till T5. It is speculated that the deceleration phase occurred during the period when no measurement was taken, between 31 and 47 h post-inoculation. Thereafter, from T10 to T14, a state of constant growth rate is observed. Continuing the experiment for a few more hours would have been ideal to emphasise the state of constant growth rate. The curves for the three fungi were similar. Slight differences were, however, observed at the active-growth phase, where *F. verticillioides* seemed to the have the most mycelium pixels (983) followed by *F. subglutinans* (757) and *F. proliferatum* (705). At the end of this phase, it seems that the curve for *F. proliferatum* continues in the exponential phase until *ca.* 41 h after inoculation when the deceleration phase begins. At T14, *F. proliferatum* consists of 6119 mycelium pixels while *F. subglutinans* and *F. verticillioides* both comprised 5463 mycelium pixels.

The progression of mycelium growth development as observed in Figure 5.6a indicates clear growth zones as shown by the defined groups of pixels. These are similar to the three distinguished zones of a mould colony when viewed horizontally: peripheral, middle and central zones (Yanagita & Kogané, 1962), where the widths of the zones are determined by the physiological state in the colony. The peripheral zone was described as the outer, thin hyphal network border and a region of hyphal mat bearing no conidia while in the middle zone, conidia was said to be forming or have just formed. The central zone was characterised as an area with an abundance of conidia. This description is valid for T5 where three zones were apparent but not so for T9 and T14. It should be noted that these initial observations made by Yanagita and Kogané (1962) were based solely on visual information. After histochemical studies, they concluded that a mould colony could be divided into four zones based on the functions of the various parts (Yanagita & Kogané, 1962). The zones were: the extending zone, the productive zone, the fruiting zone and the aged zone. The extending zone is represented by the outermost periphery, which consists of a thin hyphal network extending centrifugally; the productive zone is characterised by a piled up hyphal network and the formation of aerial hyphae. The fruiting zone was distinguished by the formation of fruiting bodies. The aged zone is the central part of the colony; here the mycelial

mat is less susceptible to staining and only the conidia are prone to intense staining. This applies for T9 to T14; for T5, the mycelium has not matured enough yet to have developed the aged zone. Using T14 as a diagrammatic representation (Fig. 5.6a) to confirm the results of Yanagita and Kogané (1962), the peripheral zone would be the mustard region, the productive zone the cyan region, the fruiting zone the blue region and the aged zone the red region.

By plotting the pixels from the individual growth zones as a function of time, it was possible to study the growth characteristics in more detail. From Figure 5.6b, more information regarding the growth rate of each zone is given as opposed to Figure 5.5 where a global growth profile is shown. The individual growth profiles illustrate, more clearly, how the growth rates of the different zones differs with respect to each other. Differences in growth rates can clearly be seen as from approximately 30 h after inoculation. As for the global growth profiles (Fig. 5.5), the active growth phases can also be seen in the profiles for the individual zones with the deceleration phase just starting at 50 h.

Using NIR hyperspectral imaging and MIA techniques, it was possible to efficiently study colony growth of three *Fusarium* spp. on solid growth medium over time. Grouping of pixels with similar score values made visualisation of growth zones in colonies possible. This would not have been possible with bulk spectroscopic techniques. Spectral analyses showed how the growth zones differed from each other over time. Three prominent bands at 1166 nm, 1380 nm (carbohydrates) and 1918 nm (protein) were found, and these were responsible for the differences between the growth zones. By integrating images of whole mycelium colonies as the sum of pixels over time, it was possible to construct curves that resembled microbial growth curves. Despite a lack of all data points at certain time intervals, this work shows that using NIR hyperspectral imaging and MIA techniques, growth characteristics of fungi can be studied in a simpler manner than earlier work. Future work should incorporate inoculation on different growth media, incubation at different temperatures for variable periods and imaging for prolonged, regular intervals.

References

Adejumo, T.O., Hettwer, U. & Karlovsky, P. (2007). Occurrence of *Fusarium* species and trichothecenes in Nigerian maize. *International Journal of Food Microbiology*, **116**, 350-357.

Alexandrakis, D., Downey, G. & Scannell, A.G.M. (2008). Detection and identification of bacteria in an isolated system with near-infrared spectroscopy and multivariate analysis. *Journal of Agricultural and Food Chemistry*, **56**, 3431-3437.

Berardo, N., Pisacane, V., Battilani, P., Scandolara, A., Pietri, A. & Marocco, A. (2005). Rapid detection of kernel rots and mycotoxins in maize by near-infrared reflectance spectroscopy. *Journal of Agricultural and Food Chemistry*, **53**, 8128-8134.

Beyer, M., Pogoda, F., Ronellenfitsch, F.K., Hoffmann, L. & Udelhoven, T. (2010). Estimating deoxynivalenol contents of wheat samples containing different levels of *Fusarium*-damaged kernels by diffuse reflectance spectrometry and partial least square regression. *International Journal of Food Microbiology*, **142**, 370-374.

Booth, C. (1977). *The genus Fusarium.* Kew, Surrey, England: Commonwealth Mycological Institute.

Burger, J. & Geladi, P. (2005). Hyperspectral NIR image regression part I: calibration and correction. *Journal of Chemometrics*, **19**, 355-363.

Burger, J. & Geladi, P. (2007). Hyperspectral image data conditioning and regression analysis. In: *Techniques and applications of hyperspectral image analysis* (edited by H.F. Grahn & P. Geladi). Pp. 127-153. Chichester, West Sussex, England: John Wiley & Sons, Ltd.

Cowe, I. & McNicol, J. (1985). The use of principal components in the analysis of near-infrared spectra. *Applied Spectroscopy*, **39**, 257-266.

Del Fiore, A., Reverberi, M., Ricelli, A., Pinzari, F., Serranti, S., Fabbri, A.A., Bonifazi, G. & Fanelli, C. (2010). Early detection of toxigenic fungi on maize by hyperspectral imaging analysis. *International Journal of Food Microbiology*, **144**, 64-71.

Delwiche, S., Kim, M. & Dong, Y. (2011). *Fusarium* damage assessment in wheat kernels by Vis/NIR hyperspectral imaging. *Sensing and Instrumentation for Food Quality and Safety*, **5**, 63-71.

Dowell, F., Ram, M. & Seitz, L. (1999). Predicting scab, vomitoxin, and ergosterol in single wheat kernels using near-infrared spectroscopy. *Cereal Chemistry*, **76**, 573-576.

Dowell, F.E., Pearson, T.C., Maghirang, E.B., Xie, F. & Wicklow, D.T. (2002). Reflectance and transmittance spectroscopy applied to detecting fumonisin in single corn kernels infected with *Fusarium verticillioides*. *Cereal Chemistry*, **79**, 222-226.

Du, C.-J. & Sun, D.-W. (2004). Recent developments in the applications of image processing techniques for food quality evaluation. *Trends in Food Science and Technology*, **15**, 230-249.

Dubois, J., Neil Lewis, E., Fry Jr, F.S. & Calvey, E.M. (2005). Bacterial identification by near-infrared chemical imaging of food-specific cards. *Food Microbiology*, **22**, 577-583.

Fernández-Ibañez, V., Soldado, A., Martínez-Fernández, A. & de la Roza-Delgado, B. (2009). Application of near infrared spectroscopy for rapid detection of aflatoxin B1 in maize and barley as analytical quality assessment. *Food Chemistry*, **113**, 629-634.

Geladi, P. & Grahn, H.F. (1996). *Multivariate image analysis.* Chichester, West Sussex: John Wiley & Sons Ltd.

Geladi, P., Grahn, H.F. & Burger, J. (2007). Multivariate images, hyperspectral imaging: background and equipment. In: *Techniques and applications of hyperspectral image analysis* (edited by H.F. Grahn & P. Geladi). Pp. 1-14. Chichester, West Sussex: John Wiley & Sons Ltd.

Geladi, P., MacDougall, D. & Martens, H. (1985). Linearizaton and scatter-correction for near-infrared reflectance spectra of meat. *Applied Spectroscopy*, **39**, 491-500.

Goetz, A.F., Vane, G., Solomon, J.E. & Rock, B.N. (1985). Imaging spectrometry for Earth remote sensing. *Science*, **228**, 1147-1153.

Gow, N.A.R. & Gooday, G.W. (1982). Growth kinetics and morphology of colonies of the filamentous form of *Candida albicans*. *Journal of General Microbiology*, **128**, 2187-2194.

Gowen, A.A., O'Donnell, C.P., Cullen, P.J., Downey, G. & Frias, J.M. (2007). Hyperspectral imaging: an emerging process analytical tool for food quality and safety control. *Trends in Food Science and Technology*, **18**, 590-598.

Jenkinson, P. & Parry, D.W. (1994). Isolation of *Fusarium* species from common broad-leaved weeds and their pathogenicity to winter wheat. *Mycological Research*, **98**, 776-780.

Manley, M., du Toit, G. & Geladi, P. (2011). Tracking diffusion of conditioning water in single wheat kernels of different hardnesses by near infrared hyperspectral imaging. *Analytica Chimica Acta*, **686**, 64-75.

Manley, M., McGoverin, C.M., Engelbrecht, P. & Geladi, P. (2012). Influence of grain topography on near infrared hyperspectral images. *Talanta*, **89**, 223-230.

Marasas, W.F.O. (1995). Fumonisins: Their implications for human and animal health. *Natural Toxins*, **3**, 193-198.

Marasas, W.F.O. (2001). Discovery and occurence of the fumonisins: a historical perspective. *Environmental Health Perspectives*, **109**, 239-243.

Nganje, W.E., Bangsund, D.A., Leistritz, F.L., Wilson, W.W. & Tiapo, N.M. (2004). Regional economic impacts of *Fusarium* head blight in wheat and barley. *Applied Economic Perspectives and Policy*, **26**, 332-347.

Peng, Y.K., Zhang, J., Wang, W., Li, Y.Y., Wu, J.H., Huang, H., Gao, X.D. & Jiang, W.K. (2011). Potential prediction of the microbial spoilage of beef using spatially resolved hyperspectral scattering profiles. *Journal of Food Engineering*, **102**, 163-169.

Pirt, S.J. (1966). A Theory of the mode of growth of fungi in the form of pellets in submerged culture. *Proceedings of the Royal Society of London. Series B. Biological Sciences*, **166**, 369-373.

Pirt, S.J. (1967). A kinetic study of the mode of growth of surface colonies of bacteria and fungi. *Journal of General Microbiology*, **47**, 181-197.

Plomley, N. (1959). Formation of the colony in the fungus *Chaetomium*. *Australian Journal of Biological Sciences*, **12**, 53-64.

Rodriguez-Saona, L.E., Khambaty, F.M., Fry, F.S. & Calvey, E.M. (2001). Rapid detection and identification of bacterial strains by fourier transform near-infrared spectroscopy. *Journal of Agricultural and Food Chemistry*, **49**, 574-579.

Salas, B., Steffenson, B., Casper, H., Tacke, B., Prom, L., Fetch Jr, T. & Schwarz, P. (1999). *Fusarium* species pathogenic to barley and their associated mycotoxins. *Plant Disease*, **83**, 667-674.

Savitzky, A. & Golay, M. (1964). Smoothing and differentiation of data by simplified least squares procedures. *Analytical Chemistry*, **36**, 1627-1639.

Shahin, M.A. & Symons, S.J. (2011). Detection of *Fusarium* damaged kernels in Canada Western Red Spring wheat using visible/near-infrared hyperspectral imaging and principal component analysis. *Computers and Electronics in Agriculture*, **75**, 107-112.

Siripatrawan, U., Makino, Y., Kawagoe, Y. & Oshita, S. (2011). Rapid detection of *Escherichia coli* contamination in packaged fresh spinach using hyperspectral imaging. *Talanta*, **85**, 276-281.

Steele, G. & Trinci, A. (1975). Morphology and growth kinetics of hyphae of differentiated and undifferentiated mycelia of *Neurospora crassa*. *Journal of General Microbiology*, **91**, 362.

Suthiluk, P., Saranwong, S., Kawano, S., Numthuam, S. & Satake, T. (2008). Possibility of using near infrared spectroscopy for evaluation of bacterial contamination in shredded cabbage. *International Journal of Food Science and Technology*, **43**, 160-165.

Trinci, A. (1971). Influence of the width of the peripheral growth zone on the radial growth rate of fungal colonies on solid media. *Journal of General Microbiology*, **67**, 325-344.

Trinci, A. (1974). A study of the kinetics of hyphal extension and branch initiation of fungal mycelia. *Journal of General Microbiology*, **81**, 225-236.

Trinci, A.P.J. (1969). A kinetic study of the growth of *Aspergillus nidulans* and other fungi. *Journal of General Microbiology*, **57**, 11-24.

Wang, W. & Paliwal, J. (2007). Near-infrared spectroscopy and imaging in food quality and safety. *Sensing and Instrumentation for Food Quality and Safety*, **1**, 193-207.

Williams, P., Geladi, P., Britz, T. & Manley, M. (2012a). Near-infrared (NIR) hyperspectral imaging and multivariate image analysis to study growth characteristics and differences between species and strains of members of the genus *Fusarium*. *Analytical and Bioanalytical Chemistry*, **404**, 1759-1769.

Williams, P., Manley, M., Fox, G. & Geladi, P. (2010). Indirect detection of *Fusarium verticillioides* in maize (*Zea mays* L.) kernels by near infrared hyperspectral imaging. *Journal of Near Infrared Spectroscopy*, **18**, 49-58.

Williams, P.J., Geladi, P., Britz, T.J. & Manley, M. (2012b). Investigation of fungal development in maize kernels using NIR hyperspectral imaging and multivariate data analysis. *Journal of Cereal Science*, **55**, 272-278.

Yanagita, T. & Kogané, F. (1962). Growth and cytochemical differentiation of mold colonies. *The Journal of General and Applied Microbiology*, **8**, 201-213.

Yao, H., Hruska, Z., Kincaid, R., Brown, R. & Cleveland, T. (2008). Differentiation of toxigenic fungi using hyperspectral imagery. *Sensing and Instrumentation for Food Quality and Safety*, **2**, 215-224.

Yoon, S., Lawrence, K., Line, J., Siragusa, G., Feldner, P., Park, B. & Windham, W. (2010). Detection of *Campylobacter* colonies using hyperspectral imaging. *Sensing and Instrumentation for Food Quality and Safety*, **4**, 35-49.

Zalokar, M. (1959a). Enzyme activity and cell differentiation in *Neurospora*. *American Journal of Botany*, **46**, 555-559.

Zalokar, M. (1959b). Growth and differentiation of *Neurospora* hyphae. *American Journal of Botany*, **46**, 602-610.

CHAPTER 6
INTERNAL EVALUATION OF FUNGAL CONTAMINATED MAIZE KERNELS USING HIGH RESOLUTION X-RAY MICRO-COMPUTED TOMOGRAPHY

Abstract

The microstructure of fungal infected maize kernels was studied over time using high resolution X-ray micro-computed tomography. Physical changes in the kernels were realised with two dimensional (2D) X-ray transmission images and further quantified in the three dimensional (3D) tomograms together with related histograms and texture analyses. The damage to the germ and endosperm of the maize kernels affected the integrity and physical texture of this region. This contributed to changes in density that could be observed by X-rays due to the different attenuation of X-rays. The presence of voids and airspaces could be seen in 2D X-ray transmission images and clear differences were detected between kernels imaged after 20 and 596 h of inoculation. In the 3D tomograms these difference in voids with fungal progression was clearer and the effect of fungal damage on the microstructure was evident.

Using histogram analyses it was found that infected regions had a grey value profile shifted to the lower end of grey levels i.e. these regions were darker. The infected material was less dense and attenuated the X-rays less.

Principal component analysis on the extracted textural descriptors showed a distinct separation along PC1, with percentage sum of squares of 92.61%, and was associated with the correlation textural descriptor. This depicted a change in correlation with increasing infection time. This could be used to distinguish between infected and non-infected regions over time. Combining high resolution X-ray computed tomography with texture analysis made it possible to distinguish infected from non-infected regions.

Introduction

The fact that X-rays of a certain photon energy can travel through organic and biological materials and expose unseen impurities or defects has led to their widespread use for quality control inspection (Haff & Toyofuku, 2008). X-ray imaging is a non-destructive technique, which makes it even more attractive as an instrument for rapid quality and safety evaluation. The use of X-rays for the detection of defects and contaminants in food products have been restricted mainly to the packaged foods sector (Haff & Toyofuku, 2008). The need for non-destructive internal product inspection has driven a substantial research effort in the food and agricultural industry (Zwiggelaar *et al.*, 1996; Bull *et al.*, 1997; Haff & Toyofuku, 2008; Kotwaliwale *et al.*, 2011).

When an object is exposed to X-rays, the X-rays interact with the matter and there is an exponential decrease in the total energy of the beam as it travels through the object (Kotwaliwale *et al.*, 2011). This decrease in energy is known as attenuation, and is affected by the atomic number of the various atoms, the thickness as well as of the density of the object irradiated. The fact that X-ray attenuation is affected by the density of an object makes it ideal to investigate objects that are comprised of different materials which differ in density.

In a study to detect weevil infestation in mangos, Thomas *et al.* (1995) made use of this difference in density to distinguish between weevil infested and non-infested mango fruit. The authors credited the difference in density to the activity of the weevil in the fruit, disintegrating the seed. Lighter regions in the X-ray images were attributed as healthy while dark to black was recognised as infested or damaged by the weevils. The appearance of airspaces and voids was also black and the authors recognised the relationship between the cavities and corresponding grey value in the X-ray image. The increase in these voids and airspaces were caused by the weevils.

Soft X-ray imaging with wavelengths ranging from 0.1-10 nm was used for the detection of fungal infection in wheat (Narvankar *et al.*, 2009). Accuracies of between 92.2 and 98.9% were obtained using a two-class Mahalanobis discriminant classifier. In a study to detect sprouted wheat kernels, also using soft X-ray image analysis, accuracies of between 90 and 95%, and 87 and 92% were obtained for a four-layer back propagation neural network model and a statistical classifier model, respectively (Neethirajan *et al.*, 2007). A study on the detection of internal wheat seed infestation by *Rhyzopertha dominica* using X-ray imaging, reported classification accuracies of up to 98% (Karunakaran *et al.*, 2004a). The differentiation between infested and non-infested wheat kernels was evident in the X-ray images and appeared as density variations. Much hidden information is revealed by the use of X-ray imaging for non-destructive internal evaluation of food and agricultural produce, however these are 2D images that offer no depth or the possibility of exploring the imaged object in virtual space.

Existing microscopes are used to look at object surfaces or transmission images through thin sections, thus internal 3D structure can only be studied destructively. Data obtained in this manner might not always be consistent because of the destructive nature of the sample preparation (Lim &

Barigou, 2004). Consistent 2D and 3D microstructural data can be obtained from X-ray micro tomography. These are derived from a set of thin planar cross-sections which expose material density information (Lim & Barigou, 2004). X-ray computed tomography is a method of achieving 3D image data. An object is rotated 180 or 360° while being irradiated with X-ray beams. Multiple slices are progressively imaged as the object is rotated through the X-rays. These slices are mathematically reconstructed to form 3D images (Kak & Slaney, 1988). This form of imaging not only allows for the evaluation of the internal structure of objects but also permits exploration of the object non-destructively. High resolution X-ray micro-computed tomography (μCT) is a sophisticated technique for the structural investigation of objects (Lim & Barigou, 2004). The method has some advantages over other techniques such as light or electron microscopy. These include the ability to investigate samples in their natural state at atmospheric pressure and temperature; the much greater spatial resolution; and the ability of X-rays to penetrate through any material and capture 3D details of the inner microstructure (Lim & Barigou, 2004).

During μCT a series of 2D X-ray images are acquired as the sample is rotated through 180 or 360°(Jacobs *et al.*, 1995; Kalender, 2006).The sequence of slices, comprising the entire sample, can be presented as a whole or as virtual slices at different depths and orientations. Processing and analysing μCT data with dedicated software, permits the reconstruction of cross-sections at depth increments as low as 15 μm along any desired orientation (Frisullo *et al.*, 2009). An array of μCT slices of the same sample, in any direction, provides much more information than just one scanning electron microscopy or optical imaging picture. The reconstruction of these 2D images are done using the Inverse Radon transform theorem (Kak & Slaney, 1988; Helgason, 1999). The Radon transform of a function $f(x, y)$ is the set of line integrals with generalisation to higher dimensions. It reconstructs a function from its projections.

3D microstructural investigations of food are currently of increasing interest to understand the functionality of food components and ingredients (Pittia *et al.*, 2011) and the internal quality evaluation of agricultural produce (Kotwaliwale *et al.*, 2011). X-ray computed tomography has been used to investigate the microstructure of processed meat (Frisullo *et al.*, 2009) and the authors reported differences between the microstructure and the fat distribution of a variety of salamis. In a similar study, the distribution of intramuscular fat in beef muscles was investigated (Frisullo *et al.*, 2010). Correlation coefficients of between 0.92 and 0.99 were obtained when comparing percentage object volume determined with μCT to the soxhlet extraction method for intramuscular fat. The microstructure of mayonnaise was studied using X-ray μCT (Laverse *et al.*, 2012). The researchers were able to analyse the distribution of fat and quantify the percentage fat using the μCT data that corresponded well with the manufacturers' specifications. Furthermore, the μCT data was correlated with rheological properties.

Regarding the μCT investigations on cereal, only a few studies stand out. Neethirajan *et al.* (2006) studied the airflow resistance of various grains in stored grain. They reported that the ratio of total airspace area to the total number of air paths is the best predictor for the difference in the

airflow resistance in horizontal and vertical directions in the grain bulk. Cleveland *et al.* (2008) recognised the potential of using tomographic techniques to investigate the structural analysis of maize kernels and to differentiate between kernels infected with *Aspergillus flavus* and sound ones. Infected kernels had lower neutron attenuation than those not infected. This was attributed to lower hydrogen concentrations because of fungal degradation.

Fusarium verticillioides, a pathogen of maize, is a concern primarily because it produces secondary metabolites toxic to animals and humans (Munkvold, 2003; Bacon *et al.*, 2008; Duncan & Howard, 2010). As it infects maize, which represents a significant component in the human food supply chain, the need for understanding the biology of host-pathogen interaction exists (Duncan & Howard, 2010). *Fusarium* mycotoxins are a relevant problem in the cereal supply chain. Traditional methods of detection and identification include microbiological techniques (diagnostic media and microscopy) (Bacon *et al.*, 1992; Medina-Martinez & Martinez, 2000; Muthomi *et al.*, 2008) or immunological methods for detection of toxin (Sydenham *et al.*, 1996; Paepens *et al.*, 2004; Castells *et al.*, 2008). These techniques are known to be expensive, time-consuming, labour intensive and to produce harmful by-products. Recent studies have shown the potential of near infrared (NIR) hyperspectral imaging and multivariate data analyses for the early detection of toxigenic fungi on maize kernels (Del Fiore *et al.*, 2010; Williams *et al.*, 2012). Although these techniques are powerful, they offer limited information about the microstructure of the kernels or the structural changes that occur due to fungal degradation.

The aim of this study was to investigate the change in the internal structure of maize kernels infected with *Fusarium verticillioides* studied over time. And, to distinguish between infected and non-infected regions within these kernels using high resolution X-ray micro-computed tomography, image analysis, texture analysis and multivariate data analysis techniques.

Materials and methods

Samples and preparation

White maize kernels of intermediate hardness were used for the study. To completely remove both surface and internally borne fungi from the kernels, they were first surface sterilised by rinsing in a combination of 70% ethanol and 1% NaOCl solution, followed by rinsing with sterile distilled water. Thereafter the surface sterilised kernels were imbibed in sterile distilled H_2O for 4 h, soaked in a water bath at 60°C for 5 min (Bacon *et al.*, 1994) and left to dry in a laminar flow hood for 1 h. The kernels were considered sterile and ready for inoculation.

Fungal spore suspensions were prepared from petri-dishes cultured with *F. verticillioides* (MRC 0826) kindly supplied by the Department of Plant Pathology, Stellenbosch University. Prior to spore preparation the culture was transferred onto potato dextrose agar (PDA) (Merck, Cape Town, South Africa) and incubated at 28°C. After 7 days, sterile water with Tween 20 (6 drops.L^{-1}) was used to wash spores from the agar surface. The spore suspension was poured through two layers of sterile cheesecloth to remove mycelium, thereafter the suspension was adjusted to 2×10^6

spores.mL^{-1} using a haemocytometer (Boeco, Germany). Finally the kernels were inoculated by dipping into the spore suspension for 30 s and allowed to dry at room temperature. The kernels were kept in a moist environment and incubated at ambient temperature until imaged.

Micro X-ray computed tomography

Samples were scanned using the Nikon XTH 225 ST micro-focus X-ray system (Nikon Metrology NV, Leuven, Belgium) at the Micro-focus X-ray tomography facility (MIXRAD) at The South African Nuclear Energy Corporation (Necsa, Pelindaba, North West Province, South Africa). The system depicted in Figure 6.1 is comprised of a lead-lined cabinet, an external control module, an external cooler and a reconstruction PC. The lead-lined cabinet houses the X-ray tube and sample manipulator. A flat panel detector with dimensions 2048 x 2048 pixels and a pixel size of 200 micron was used (PerkinElmer Inc,. Massachusetts, USA). Power settings of 150 kV and 70 µA were used with 1000 angular projections within 360° and an exposure time of 2000 ms per projection. For this specific study, a silver target was chosen to be the best material for the generation of X-rays.

Five kernels were imaged individually at predetermined intervals after inoculation up to 25 days after inoculation, resulting in a time series of images. Due to slight movement of the samples during the scanning process, a number of scans resulted in poor reconstructions of image volumes, and only the time points as set out in Table 6.1 were available for analyses.

Figure 6.1. High resolution X-ray micro-computed tomography system used for acquiring X-ray images and tomograms.

Table 6.1. Time points that kernel were imaged with corresponding time in hours after inoculation

Time point	Actual time (h) after inoculation
t1	20
t6	73
t7	92
t11	168
t15	260
t18	333
t19	356
t20	380
t25	502
t29	596

Image processing

The series of 2D X-ray image projections were reconstructed at MIXRAD (Necsa, Pelindaba, North West Province, South Africa) and corrected for beam hardening effects using CT-Pro reconstruction v 2.0 software (Nikon Metrology NV, Leuven, Belgium). 3D image volumes were analysed using VGStudio Max v. 2.1.4 (Volume Graphics GmbH, Heidelberg, Germany). Image stacks of various orientations (top, front and side) of the sample were extracted with a spatial resolution of 0.008 mm in all directions. These slices were further analysed in ImageJ (ImageJ, U. S. National Institutes of Health, Bethesda, Maryland, USA) and Matlab v 7.10 (The MathWorks, Massachusetts, USA).

Image analysis

Conventional image and area analyses

Images were analysed with conventional 2D image analysis tools in ImageJ (ImageJ, U. S. National Institutes of Health, Bethesda, Maryland, USA) and converted to 8-bit grey scale images (256 grey values; 0-255). Then the images were segmented to remove background. The segmentation also involved binarising the images where all pixel values below a certain grey level value were assigned to 0 (white) and the remaining pixels assigned to 1 (black). The binary images were used for area measurements where the percentage of area degradation was calculated according to equation 1.

$$D = At - \frac{Ap}{At} \times 100 \quad \text{...[eq. 1]}$$

Where:

D = degradation %

At = total area

Ap = area of pores

Histogram analyses

Regions of interest (ROIs) were selected in the original images and cropped to 712 × 532 pixels. Here the ROI was also reduced to 70 slices per image from approximately 2 000 slices per image. The 70 slices were selected as such to include a region mostly comprised of the germ and endosperm as illustrated in Figure 6.2**.** These were exported to Matlab v 7.10 (The MathWorks, Massachusetts, USA) for histogram analyses.

Texture analyses of the original ROIs

Image texture features were extracted for selected slices in the time series and analysed. Image texture features based on the original greyscale images were computed using built-in entropy and standard deviation functions in the Image Processing Toolbox v. 7.0 of Matlab.

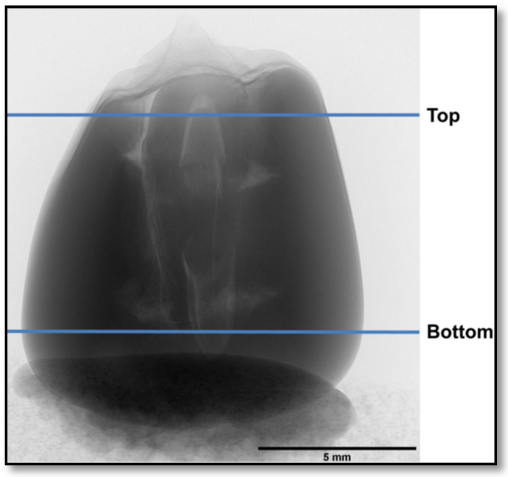

Figure 6.2. X-ray transmission image of maize kernel indicating the approximate region the 70 slices that were extracted. Slices numbered in ascending order from bottom to top (1-70).

Texture analysis using grey-level co-occurrence matrices and principal component analysis

Grey level co-occurrence matrices (GLCM's) as proposed by (Haralick *et al.*, 1973) were calculated for all the images in the time series. Co-occurrence matrices describe the occurrence of grey levels between pixels separated in the image by a given distance (Haralick *et al.*, 1973; Tournier *et al.*, 2012). These were then used as input to calculate 4 textural features, contrast, correlation, energy and homogeneity (equations 2-5). Haralick *et al.* (1973) described 14 such

textural features, however only a few are necessary to describe differences between images (Bharati *et al.*, 2004). The outputs of these were used to calculate principal component analysis (PCA).

$$\textbf{Contrast} = \sum_{i,j} |i-j|^2 p(i,j) \quad \text{...[eq. 2]}$$

$$\textbf{Correlation} = \sum_{i,j} \frac{(i-\mu i(j-\mu j)p(i,j)}{\sigma_i \sigma_j} \quad \text{...[eq. 3]}$$

$$\textbf{Energy} = \sum_{i,j} p(i,j)^2 \quad \text{...[eq. 4]}$$

$$\textbf{Homogeneity} = \sum_{i,j} \frac{p(i,j)}{1+|i-j|} \quad \text{...[eq. 5]}$$

Where:

i, j: neighbouring grey tone values

$p(i,j)$: i,jth entry in the normalized GLCM

$\sigma_i \sigma_j$ and μ_i σ_j: are the means and standard deviations

Results and discussion

Conventional image and area analyses

X-ray micro-computed tomography allows for the generation of 3D virtual volumes that can be sliced in any direction revealing the information in 2D as a slice in 3D. Figure 6.3 shows a series of raw 2D X-ray transmission slices of the maize kernel at the same position after 20 (Fig. 6.3a), 168 (Fig. 6.3b), 380 (Fig. 6.3c) and 596 (Fig. 6.3d) hours of inoculation. Areas of high X-ray attenuation are black while those with no or low X-ray attenuation are white. Attenuation is the weakening in intensity of the X-ray beams as it passes through the kernel. The area around the kernel is air that does not attenuate the X-ray beams (dark = less X-rays coming to the detector; white = more X-rays coming to the detector through the sample). The dark areas are those where the beam is more attenuated than the white areas, thus they are denser. The germ and immediate surrounding area were of particular interest. This region was shown to be highly infected in a previous study (Duncan & Howard, 2010). As seen in Fig. 6.3a there were a number of low attenuating areas (white regions). These white areas were associated with airspaces, voids and less dense material than the surrounding areas. There is an observable change in this region when advancing through the time series. Although there appears to be little differences between t1 (values for t as shown in Table 6.1) (Fig. 6.3a) and t11 (Fig. 6.3b), there were subtle changes in the germ. At t11 the germ has more high intensity grey values (a maximum grey value of 147) than t1 (126), thus there is

lower attenuation at t11. This is even more apparent in t20 (164) (Fig. 6.3c) and in t29 (158) (Fig. 6.3d) where the entire germ region is considerably less attenuated than that found in t1 and t11. This is ascribed to the fact that the fungus breaks down and metabolises the kernel's reserves for energy use (Boyacioglu & Hettiarachchy, 1995). This softens the germ and endosperm region influencing the integrity of the kernel and ultimately the internal density of the structure (Hesseltine & Shotwell, 1973; Lillehoj *et al.*, 1976). Thus, there are more voids in the kernel after being inoculated with the fungus for 596 h. The total high intensity grey values in the germ are substantially less for t1 (mean grey value of 68) than for t29 (mean grey value of 103). This can be attributed to the breakdown of starch, as there is less material to attenuate the photon energy. This was seen in all five kernels, only the results for one is shown throughout. Similar differences in X-ray images were reported by Karunakaran *et al.* (2004a) when comparing insect infested wheat kernels to un-infested kernels. The damage caused by the insects appeared as low attenuating regions in the images.

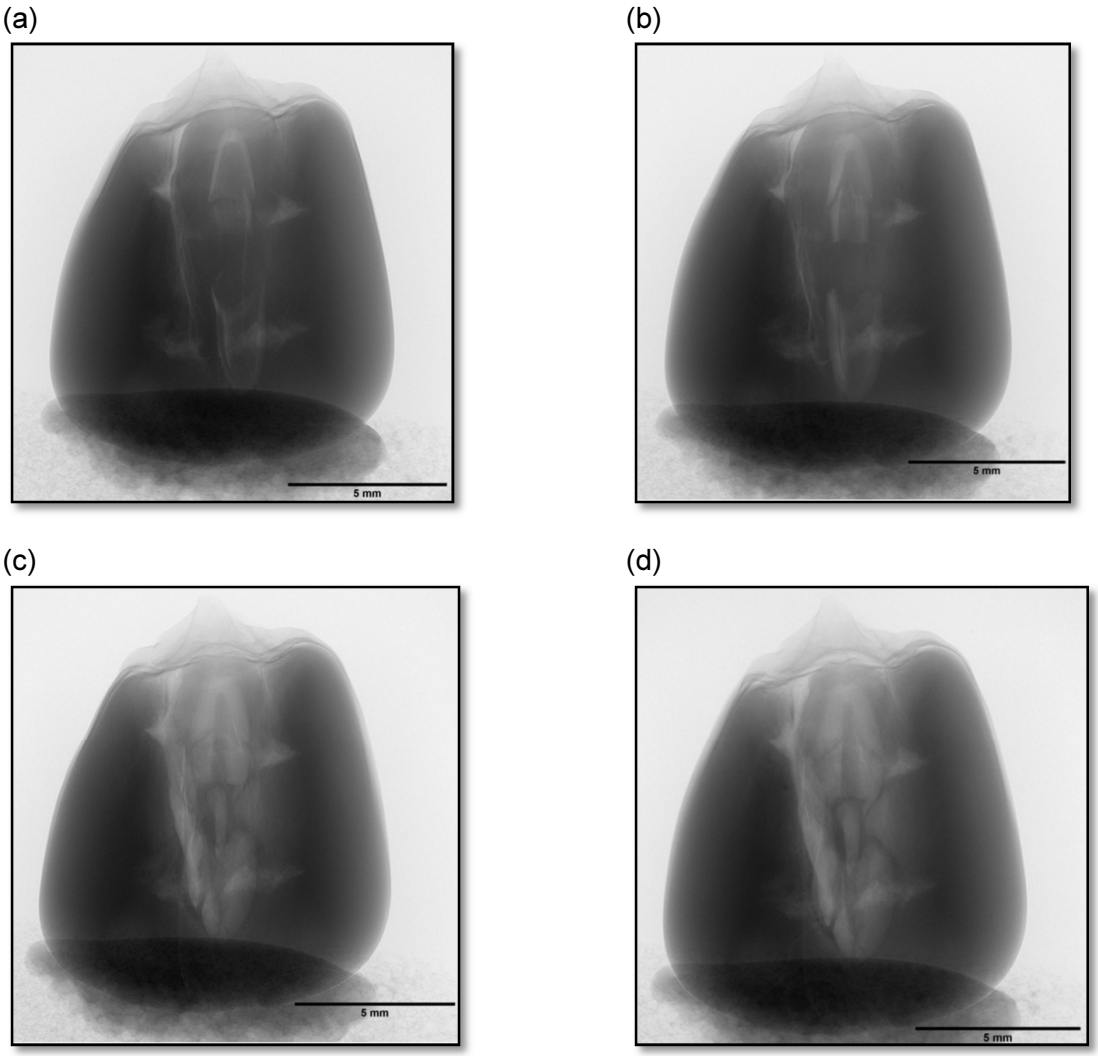

Figure 6.3. X-ray transmission images of (a) a maize kernel after 20 h inoculation and (b) the same kernel 168 h after inoculation. (c) X-ray image after 380 h inoculation and (d) after 596 h inoculation. Lighter regions correspond to low/no X-ray attenuation and darker regions to high attenuation.

Figure 6.4a shows binary images with the pores and voids excluded (Fig. 6.4b) and with pores and voids included after 20 h of inoculation, respectively. Figures 6.4c and 6.4d are binary images of the same kernel after 596 h of inoculation. An initial approach was to assess the area (with and without pores) for all the time points. The quotient would give an indication to the degree or severity of the fungal infection. Theoretically, more pores or voids should become apparent as the fungus grows. This was already visible in the X-ray transmission images (Fig. 6.3) and could give an indication to the degree of infection. However, it should be noted that pores and voids are inherent to maize kernels and other cereals due to the porous nature of the endosperm that influences kernel hardness (Chang, 1988). Thus an increase in the existing pores and the appearance of additional pores due to the growing fungi was expected. The outcome of this analysis gave rise to area plots that described the area of the kernel on the basis of presence or absence of voids and pores. And, this was linked to fungal infection. A healthier kernel would be characterised by *ca.* 100% area while a severely infected kernel by <90%. An area plot for t1 for all 70 slices (Fig. 6.5) shows a slight decrease in “healthy” material (slice 1-10), then an increase and plateaux (slices 20-50) followed by a decrease from slices 50-70. It should be noted that the maximum and minimum values for t1 are 99.40 and 94.22% respectively. The decrease in area was due to the position of the slices on either end of the kernel as depicted in Fig. 6.2.

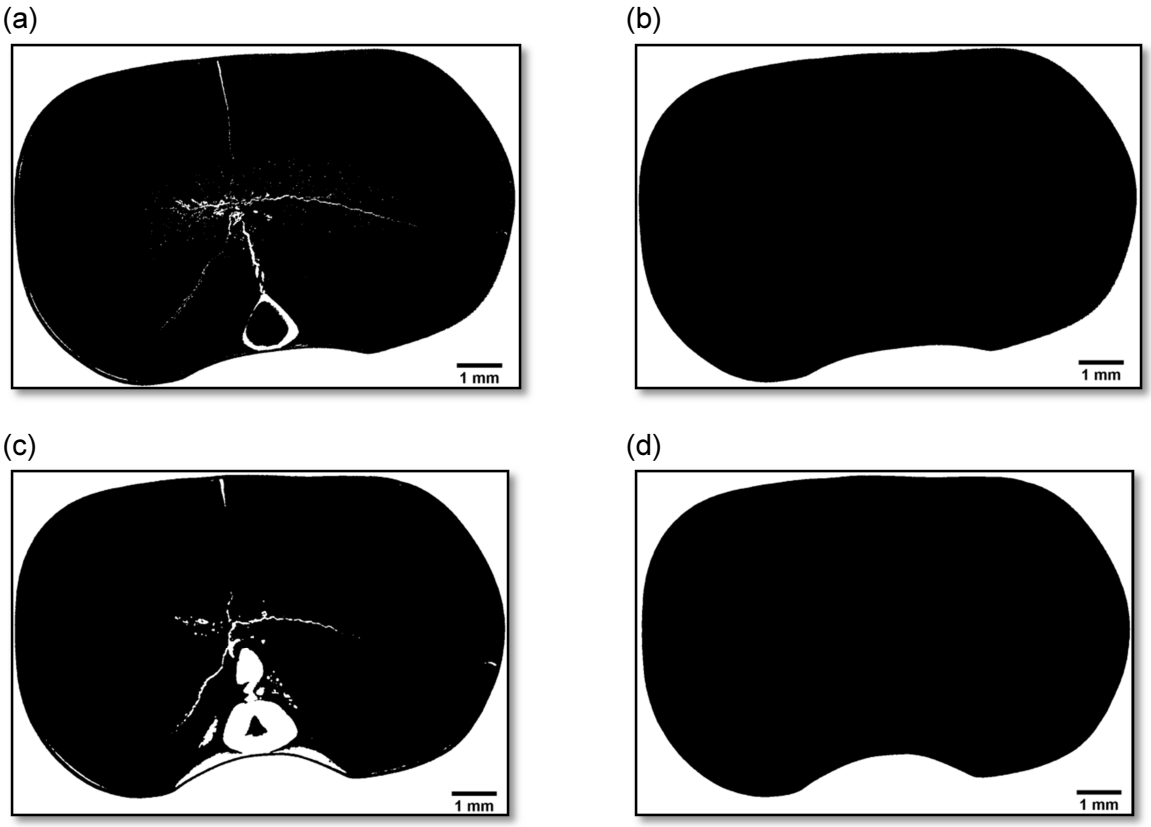

Figure 6.4. (a) Binary image without the pores and voids, the pores and voids are in white and (b) the same image slice with the pores included for t1. (c) Binary image without pores and voids and (d) with voids for t29.

Slices from the bottom of the kernel generally had less voids than those from the top because there are more voids and airspaces in the germ region. This was evident in the X-ray transmission image in Fig. 6.3. Thus the slight deviations in the area plot for t1 (Fig. 6.5) would be expected throughout the time series. It is expected that at the advanced time points, e.g. t29, the deviations would be more evident. This is illustrated in Fig. 6.6 where the area plot of t29 is shown. There was an overall decrease in area for all slices when compared with t1. The maximum and minimum percentage area values for t29 were 96.08 and 85.95%, respectively. This was a considerable decline compared to t1. Although this may be regarded as a modest change, it is likely due to the action of the fungus. This difference is depicted in the tomograms of t1 and t29 in Figures 6.7a and b, respectively. There is a substantial difference in the number and size of the voids in t29 compared to those of t1. It has been reported that fungal infection of maize kernels causes the kernel to lose its integrity (Hesseltine & Shotwell, 1973; Lillehoj *et al.*, 1976). The glassy endosperm becomes friable and porous due to the degradation caused by the proliferating fungus. This is potentially what occurred in the kernel over time. Similar trends were observed in the other time points; Figure 6.8 illustrates this where Fig. 6.8a is the area plot for t11, 168 h after inoculation and Fig. 6.8b t20. These plots closely resemble those of t1 and t29; however percentage area for t11 was slightly lower than that of t1 for all the slices, indicating that it was to a certain extent more damaged than t1. The maximum and minimum values for t11 were 98.05 and 93.29% respectively, compared with the 99.40 and 94.22% of t1. There are clear differences between t11 and t20 (Figs. 6.8a and b) and this is even more evident in the tomograms when viewed at approximately the same slice in the image stack (Figs. 6.9a and b). It should be noted that in terms of attenuation and density for the 3D X-ray tomogram images white is high attenuating (high density) while black is low/no attenuating (low density).

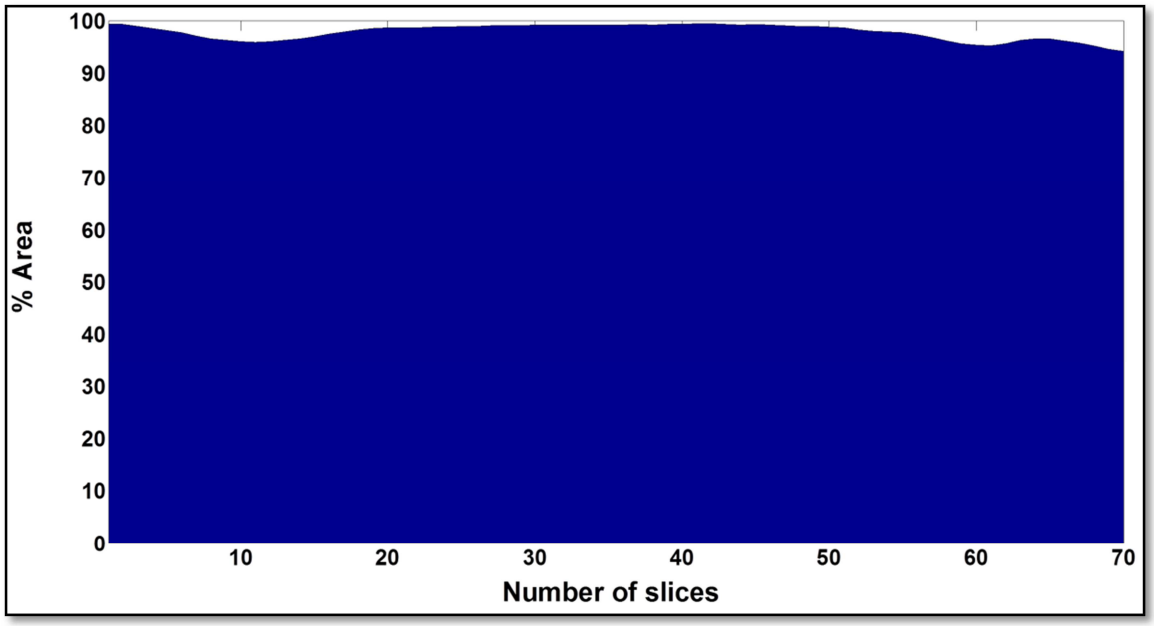

Figure 6.5. Area plot for t1, 20 h after inoculation for all slices.

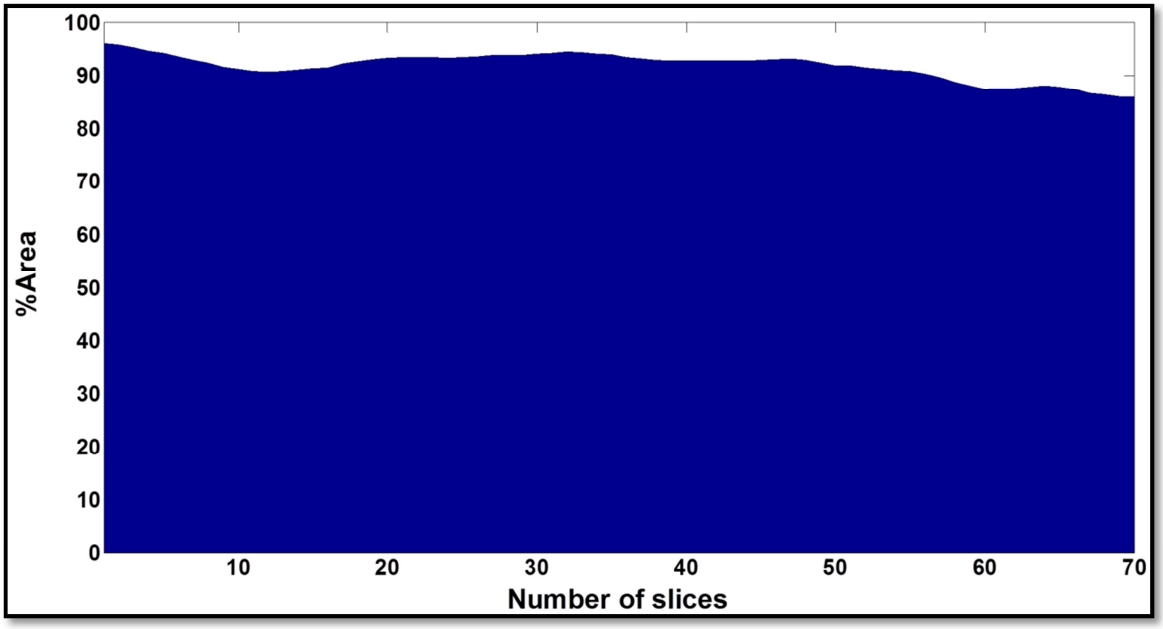

Figure 6.6. Area plot for t29, 596 h after inoculation for all slices.

(a) (b)

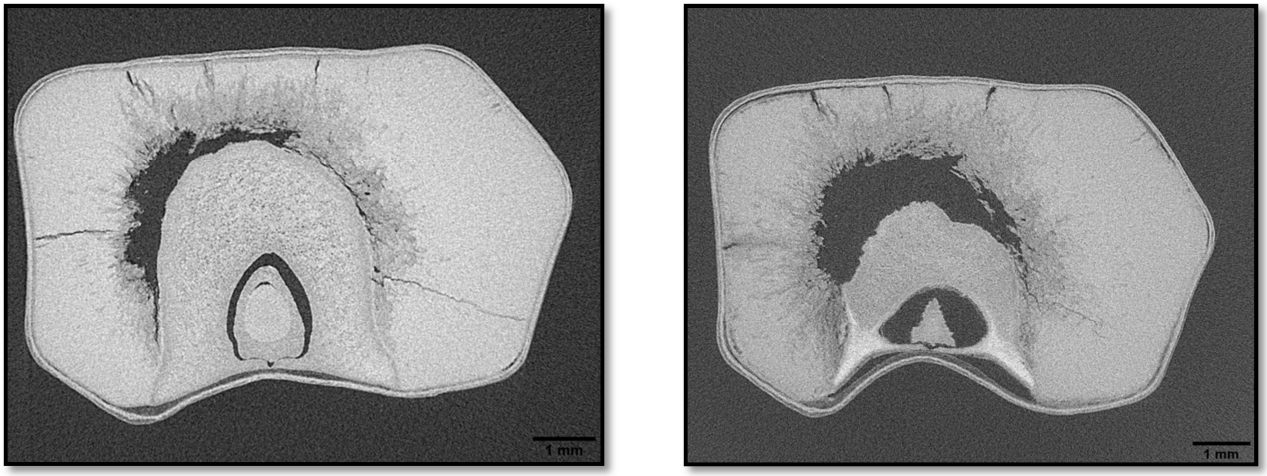

Figure 6.7. Tomograms of (a) t1 and (b) t29 at approximately the same slice in the image stack, viewed from the top.

(a) (b)

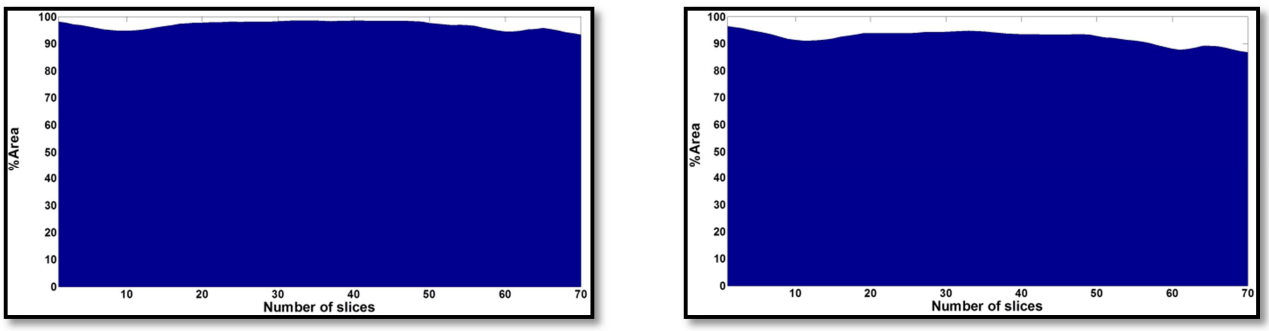

Figure 6.8. Area plots of (a) t11, 168 h after inoculation and (b) t20, 380 h after inoculation.

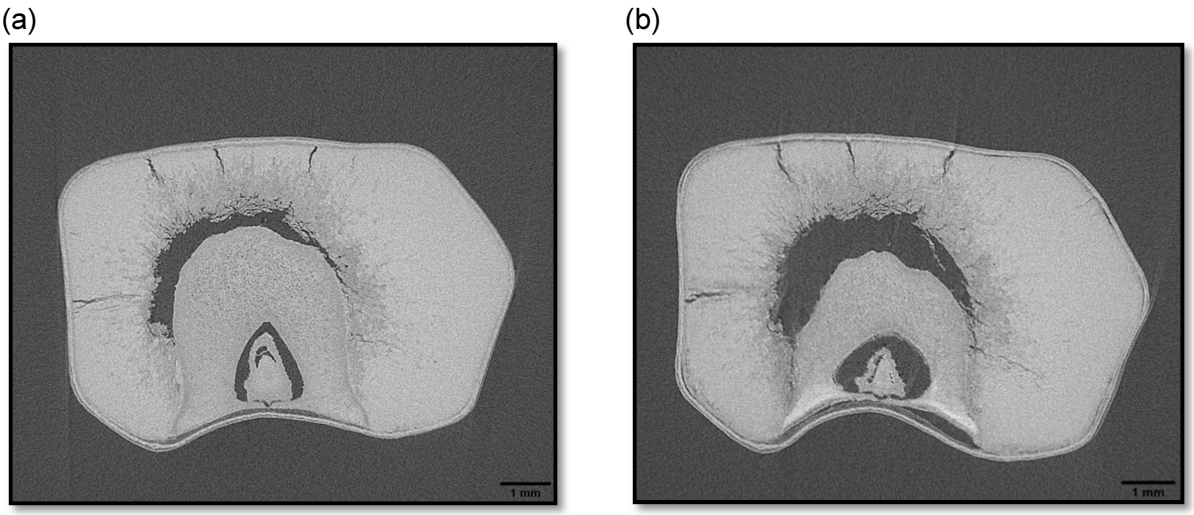

Figure 6.9. Tomograms of (a) t11 and (b) t20 at approximately the same slice in the image stack, viewed from the top.

It has been reported that early fungal growth is localised in the germ and the succeeding mycelial growth extends to the endosperm (Lillehoj *et al.*, 1976). This was obvious in the tomograms (Fig. 6.7a and b; Fig. 6.9a and b) The fungus uses the kernels food reserves (starch and protein) for energy (Boyacioglu & Hettiarachchy, 1995) to proliferate and grow. In a study on mango weevils infestation Thomas *et al.* (1995) reported that darker grey areas corresponded with insect infestation whereas lighter grey were healthy.

Histogram analyses

Histogram analyses have been used for the differentiation of adrenal adenomas from non-adenomas of X-ray computed tomography 3D images (Halefoglu *et al.*, 2010). Neethirajan *et al.* (2007) observed a decline in the low grey level values for sprouted wheat kernels to that of non-sprouted kernels when comparing their histograms. In a similar study on wheat, Karunakaran *et al.* (2004b) reported lower mean grey values for kernels infested with the red flour beetle compared to un-infested ones. The histogram of a 2D image is a plot of the grey level versus the number of pixels in the image at each grey level, and the number of voxels in the 3D tomogram at each grey level (Thum, 1983; Umbaugh, 2011b). Histograms are valuable for image analysis as they offer an immediate illustration of the spread of pixel or voxel intensities across a given image. A histogram with a small spread has low contrast, while a histogram with a wide spread represents a high contrast (Umbaugh, 2011a). An image with its histogram grouped at the low end of the grey value range is dark, and a histogram with values clustered at the high end of the range corresponds to a bright image or part of an image. Often this is used globally, *i.e.* on the entire image, however in this case it was decided to do a histogram analysis on only the regions of interest.

The data in Figure 6.10 shows the ROI grey scale tomogram slices of the maize kernel for t1 and t29, and their accompanying histograms. Both ROIs were extracted from slice 1 (the first slice from the bottom of the kernel, Fig. 6.2) for each time point, respectively. The voids and airspaces that appear in t1 (Fig. 6.10a) are natural and inherent to the kernels, and were expected. Even

though it was reported that conidia and hyphae infections were detected as early as 24 h post inoculation (Duncan & Howard, 2010), this was only found on the surface of the kernels. It was not expected to observe structural damage in t1, since the fungus would not have entered the kernel at this time. T1 was thus used for comparison with the rest of the time points. At t29 (Fig. 6.10c) there was a vast difference in the ROI compared to t1, the voids were larger and more prominent. The widening of the existing voids as well as the presence of additional ones was observed. This was likely due to the degradation of starch by the fungus as it is known that the fungus utilises the starch as an energy source during growth, and then depletes the kernel reserves causing structural instability and changes.

There were dissimilarities in the histograms of the two time points with Fig. 6.10b showing more high intensity grey values than Fig. 6.10d. In Fig. 6.10d there is more low intensity grey values and these are associated with the void presence. The x-axis in the histograms is also slightly shifted; t1 is centred on the 190-200 grey level intensity, while t29 is centred on the 160-180 grey level intensity. Overall, t1 had higher pixel counts between 150 and 250 grey level intensities than t29. This is clearly illustrated in Fig. 6.11, where the mean of the histogram groups of the two time points are shown. There is a vast difference in the region between 100 and 200. Between the histogram group values 50 and 100, t29 had higher pixel counts than t1, and this was due to the presence of more voids. As expected, similar results were obtained with different slices, at the same position, in the image stacks of t1 and t29 respectively. The closer the slice was to the tip of the kernel, for both time points (Figs. 6.12a, 6.12c, 6.14a and 6.14c), the more voids and airspaces there were (Fig. 6.2 and Fig. 6.3). However, there were more differences in this region for all slices of t29, and this was also evident in the accompanying histograms (Figs. 6.12b, 6.12d, 6.14b and 6.14d) that always had lower pixel counts for grey level intensities between 100 and 250. Histograms for t29 were generally shifted to the lower intensity grey values end of the grey level spectrum. There was also an overall increase in pixel counts for grey level intensities between 50 and 100 for all slices of t29. The discrepancies of the aforementioned histograms are clearly illustrated in their mean histograms (Figs. 6.13 and 6.15). These differences are easily interpreted and it is obvious that t1 has higher grey level intensities than t29. Furthermore, t29 always had higher pixel counts in the 50-100 grey value region than t1. It is evident that a distinction between these time points can be made, and thus the difference between infected and non-infected internal regions.

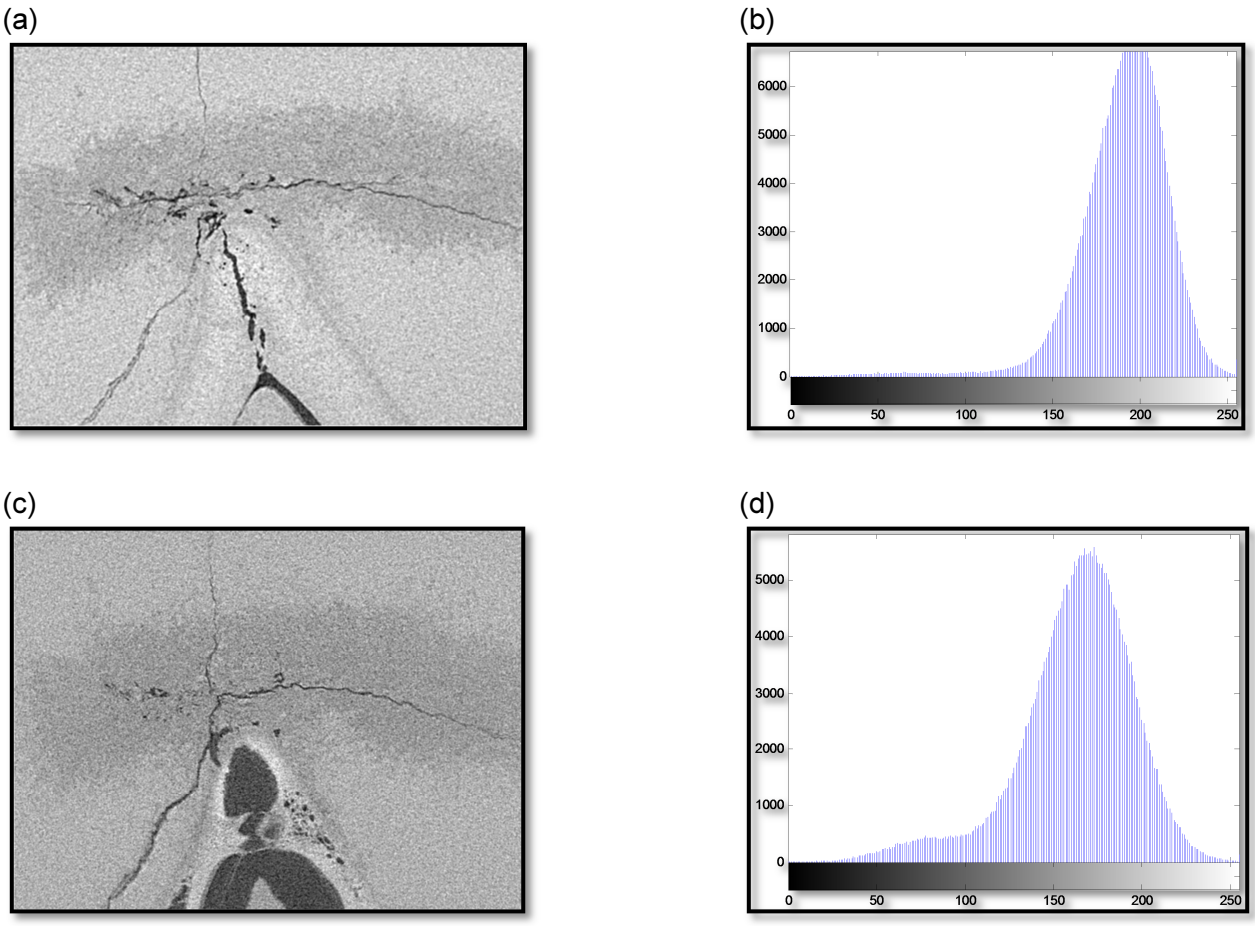

Figure 6.10. (a) ROI of t1, 20 h after inoculation and (b) histogram of grey level counts; (c) ROI of t29, 596 h after inoculation and (d) histogram of grey level counts. Both images were taken at slice one of the respective time point stacks.

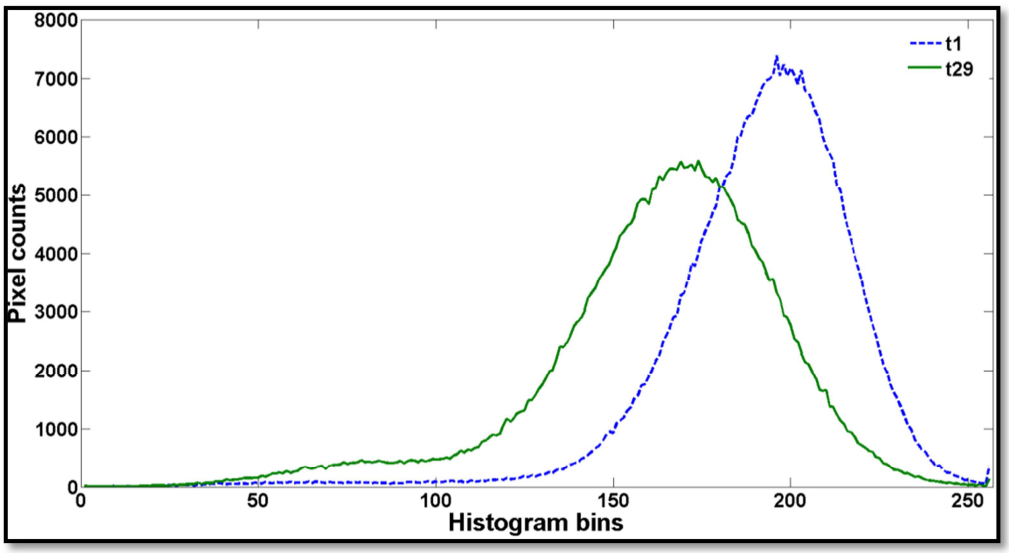

Figure 6.11. Mean histogram group values of t1 and t 29; slice 1, depicting vast its differences from 100-200.

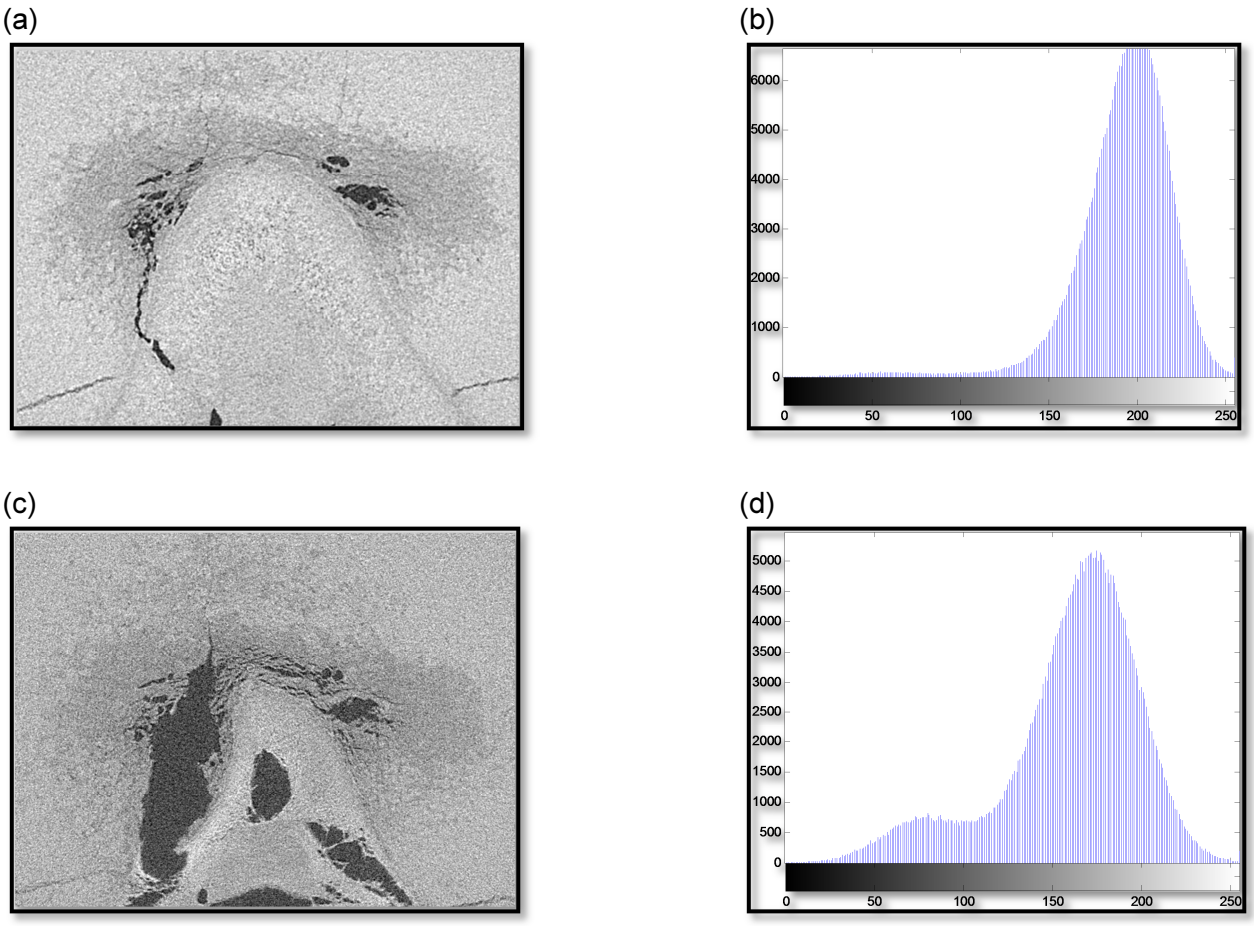

Figure 6.12. (a) ROI of t1, 20 h after inoculation and (b) histogram of grey level counts; (c) ROI of t29, 596 h after inoculation and (d) histogram of grey level counts. Both images were taken at slice 35 of the respective time point stacks.

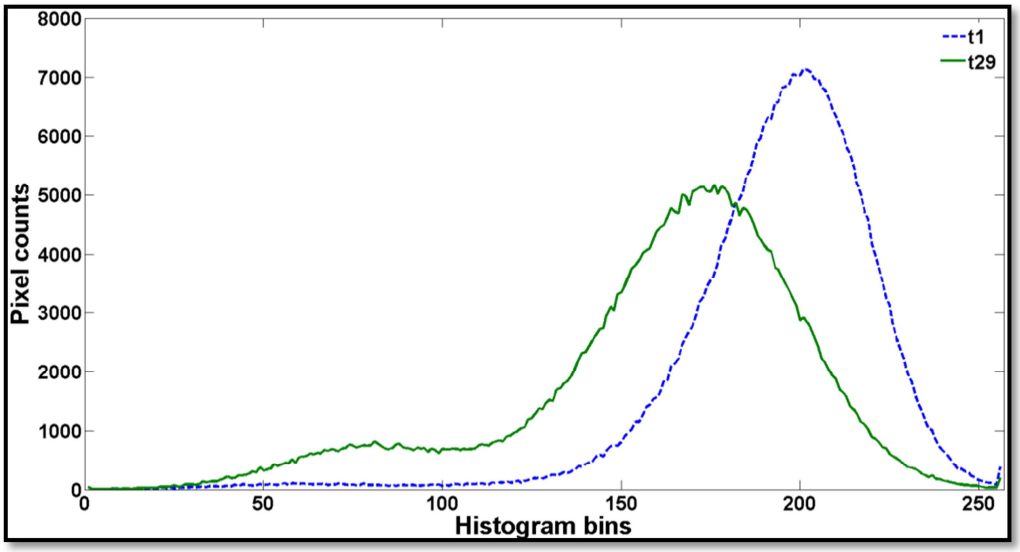

Figure 6.13. Mean histogram group values of t1 and t 29, slice 35, showing differences between 50 and100, and 150 and 250.

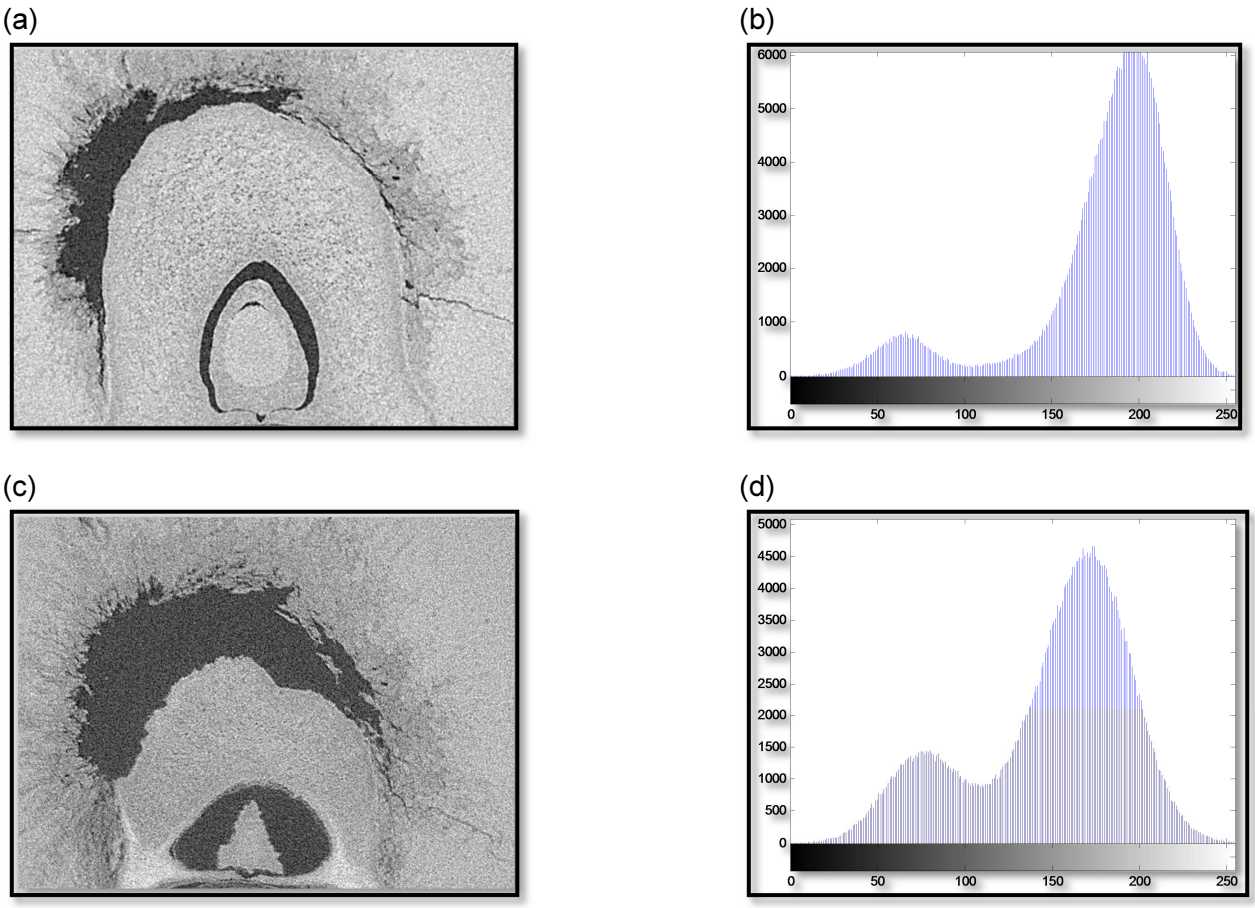

Figure 6.14. ROI of t1, 20 h after inoculation and (b) histogram of grey level counts; (c) ROI of t29, 596 h after inoculation and (d) histogram of grey level counts. Both images were taken at slice 70 of the respective time point stacks.

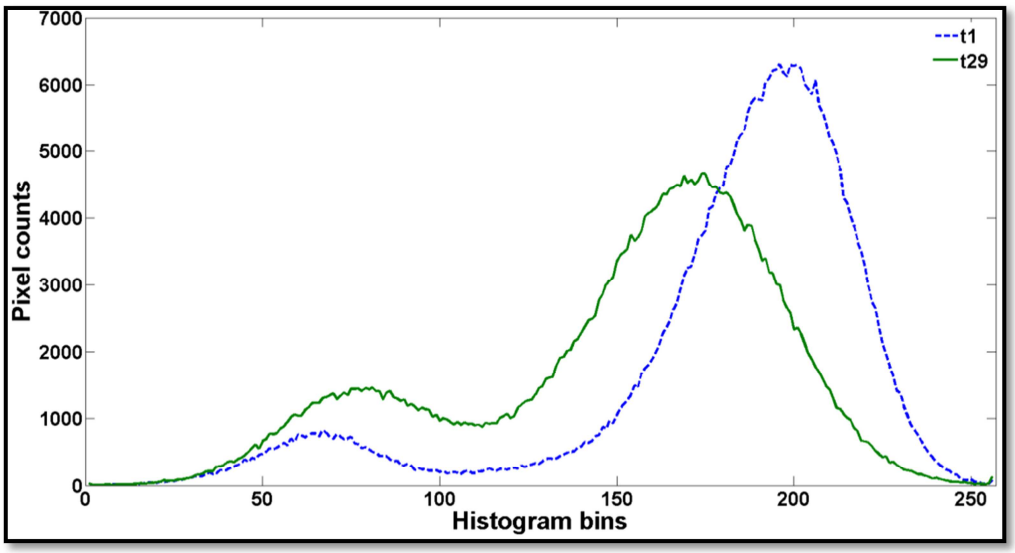

Figure 6.15. Mean histogram group values of t1 and t 29, slice 70, showing differences between 50 and100, and 150 and 250.

Histogram equalisation is a technique for adjusting image intensities to enhance contrast (Vij & Singh, 2009). It allows areas of lower contrast to gain a higher contrast, and it produces an output image with an evenly distributed histogram. Thus, it is the re-distribution of grey level values uniformly. In this study this technique was applied to the ROIs to determine whether it improved the contrast, and in so doing, if the ability to distinguish between infected and non-infected regions was improved.

The histogram equalised ROIs, as shown in Fig. 6.16, are considerably different to those shown in Figs. 6.10a and c even though they are the same images. As anticipated, there was an improvement in contrast and certain details when comparing those in Figs. 6.10a and c, and those in Figs. 6.16a and b. The central area of the ROIs in Figs. 6.16a and c are more apparent with a definite increase in contrast. This central region was darker in t1 (Fig. 6.16a) than in t29 (Fig. 6.16c). Although both ROIs are grainy, the ROI of t1 was coarse while that of t29 was finer and smoother. These were the major differences between the histogram equalised images but no improvement in the contrast of the voids was observed. Furthermore, the effect of the histogram equalization is evident in the histograms of both t1 and t29 (Figs. 6.16b and d), where the grey values are uniformly distributed when compared with those of Figs. 6.10b and d. For slices 35 (Fig. 6.17a and b) and 70 (Fig. 6.17c and d) for both t1 and t29 similar results were found. It was found that t1 was always more coarse than t29, and the central zone was continually darker in t1 than in t29. In all the slices from the various time points this trend was observed, where the central zone was always darker for slices after a short period of inoculation. From t1 to t7 the central zone was consistently darker, and then from t11 to t29 the central zone was considerably lighter. This could be linked to the action of the fungi that, with time, alters the structural integrity of the endosperm and germ region resulting in less attenuation of X-rays. And, this could be the cause of the whitening of the central zone after 168 h post inoculation. The coarseness and fineness of these images cannot be ignored. These features are related to image texture and give an indication to the spatial arrangement of the pixels and grey values.

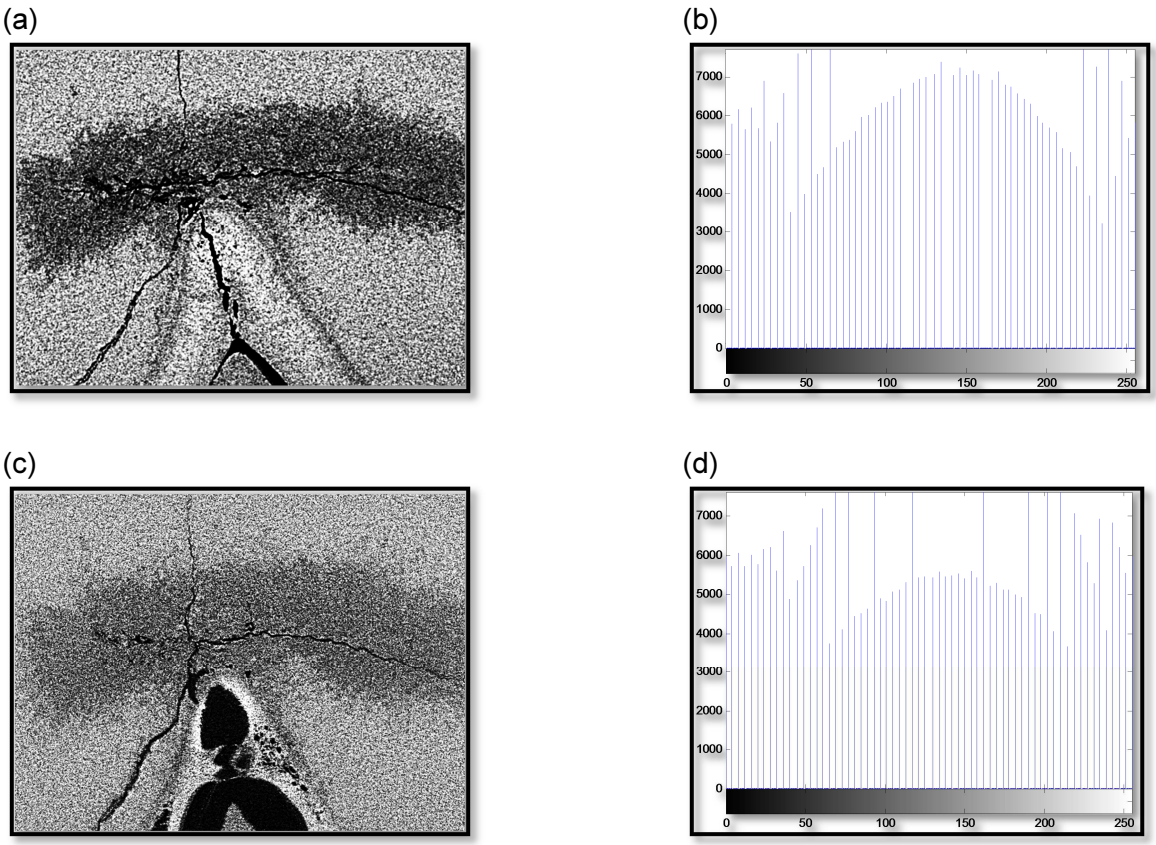

Figure 6.16. Histogram equalization enhanced ROIs of Fig. 6.10 illustrating improved contrast in both (a) t1 and (b) t29. (c) Uniformly distributed grey level histogram for t1 and (d) t29.

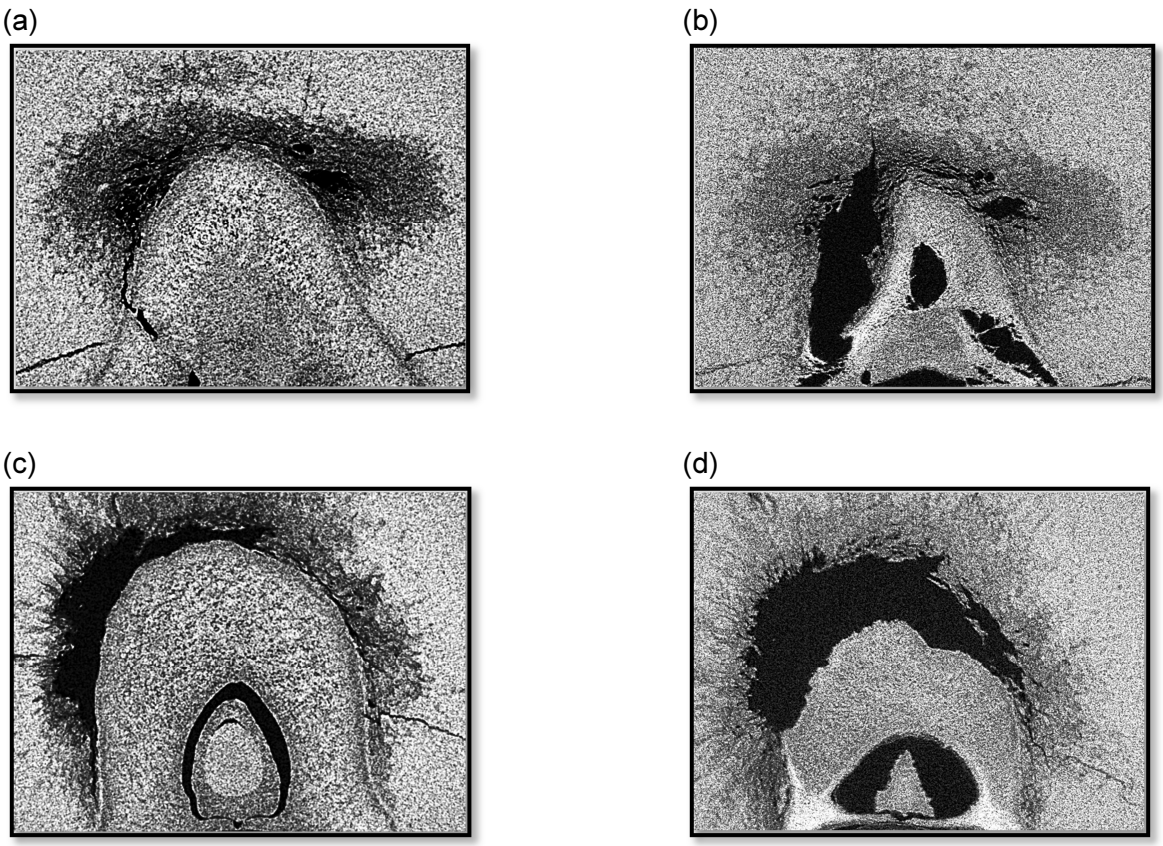

Figure 6.17. Histogram equalized images of ROIs; (a) t1 and (b) t29 at slice 35; (c) t1 and (d) t29 at slice 70.

Texture analyses of the original ROIs

Texture is an important characteristic that is used to identify objects or regions of interest in an image, and can be assessed as either fine, coarse, smooth, rippled, grainy or lineated (Haralick *et al.*, 1973). Image texture can be defined as a function of the spatial organisation and variation in pixel intensity or grey values (Haralick *et al.*, 1973; Tuceryan & Jain, 1993). Image texture can also be used for the recognition of image regions.

Entropy is a measure of the degree of randomness in an image, and high entropy has been reported to be associated with an image that is in focus while a low entropy indicates an image with bad focus (Thum, 1984). Furthermore, it was reported by Gadkari (2004) that entropy is a measure of the complexity of an image. Entropy is high when the image is not texturally uniform, and complex textures are inclined to have high entropy.

Even though it appears that Fig. 6.18b has a sharper focus than Fig. 6.18a, useful information regarding fungal damage can still be observed. The entropy images of t1 and t29 (Figs. 6.18c and d) differ with a fair amount of variation being present within each one. The high intensity grey values correspond to high entropy while the lower intensity grey values indicate low entropy. A wider spread of these pixels was observed in t1 than in t29. The high entropy regions in the individual images corresponded with the outline of the voids and airspaces when compared with the original images. It served as a means of identifying only the outlines of these regions as those were bordering the regions that were not homogenous in the images. Although t1 had more areas of high intensity grey values, t29, as a whole, had fewer low intensity grey values and thus appeared lighter. When the average entropy was computed t29 had a value of 7.00 and for t1 a value of 6.58. While t29 appeared to have a smoother texture, t1 was coarser. This was due to more evenly spread entropy values for t29 as opposed to t1.

Similar results were obtained with the standard deviation images where the outline of the voids and airspaces where identified as regions with a higher standard deviations compared to the rest of the image. This was expected since these regions differed markedly from the rest of the image. Here too this distinction was clearer in t1 than t29; however it was obvious that there were differences between t29 and t1 (Figs. 6.18e and f). Where the entropy images gave information regarding the voids and airspaces, the standard deviation showed similar results but in more detail, particularly for t1. The standard deviation image of t1 was clearer than t29, and the texture for t29 was coarse compared to t1 that looked smooth. Nevertheless, t29 had a more uniform distribution of high and low standard deviation pixels in contrast to those found for t1. These observations were made on slice one for both stacks. Comparable results were obtained for slice 35 (Fig. 6.19) and slice 70 (Fig. 6.20) for both t1 and t29. These texture techniques illustrate the differences between the structure, arrangement and intensity of the pixels, and also indicate the location of the boundaries of the voids and airspaces. These could be used to detect the location of the voids and airspaces, and thus the regions of interest where changes due to fungal growth could occur. Tomograms from t6 and t11 were also included and comparable results were obtained (Fig. 6.21).

Generally the entropy and the standard deviation increased with time after inoculation, i.e. as the fungus grew, spread and caused structural damage.

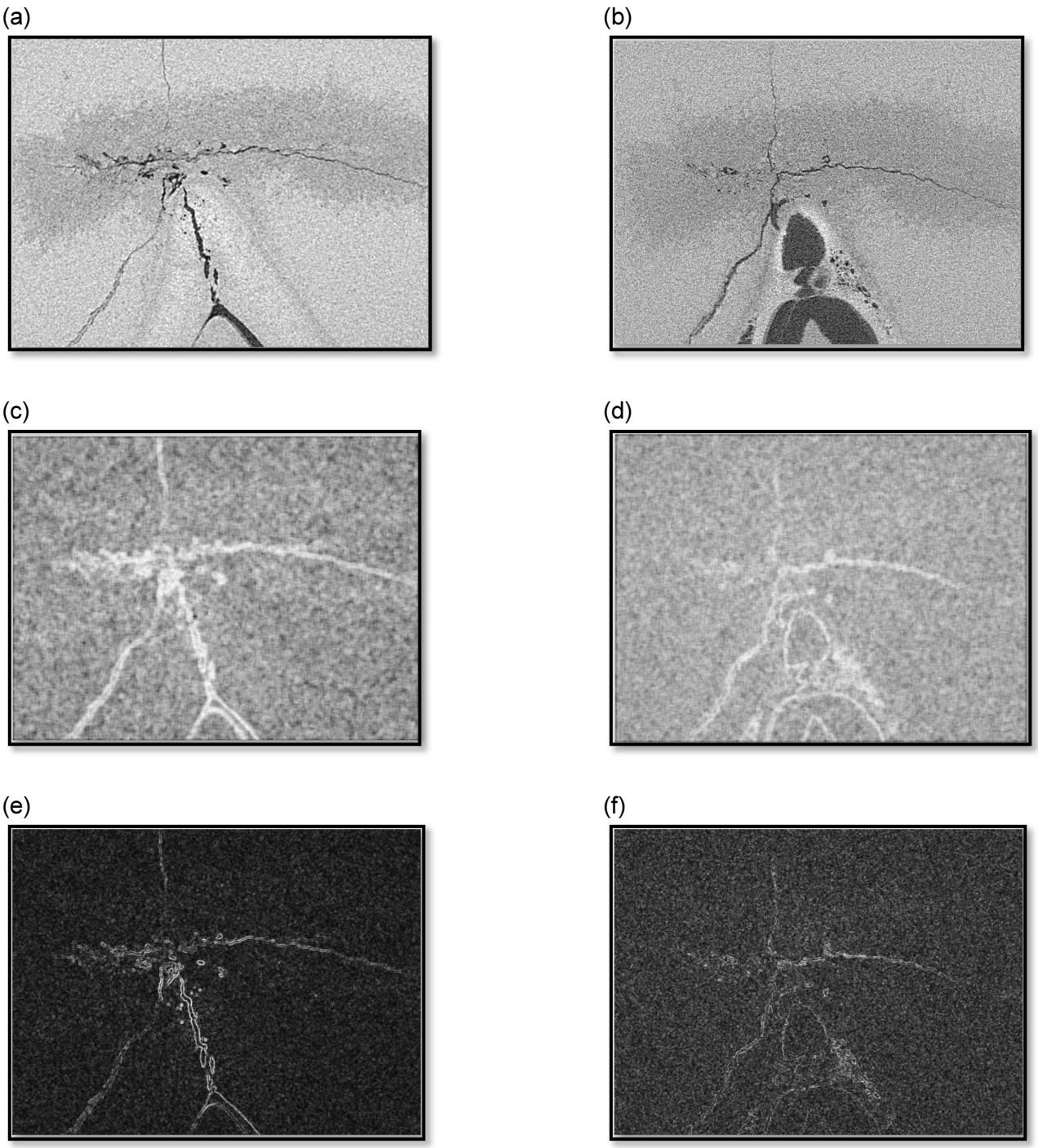

Figure 6.18. (a) T1 raw grey scale tomogram and (b) t29 raw grey scale tomogram both used to calculate (c) Entropy image of t1 and (d) entropy image of t29. (e) Standard deviation image of t1 and (f) standard deviation image of t29. Both original images were taken at slice one of the respective time point stacks.

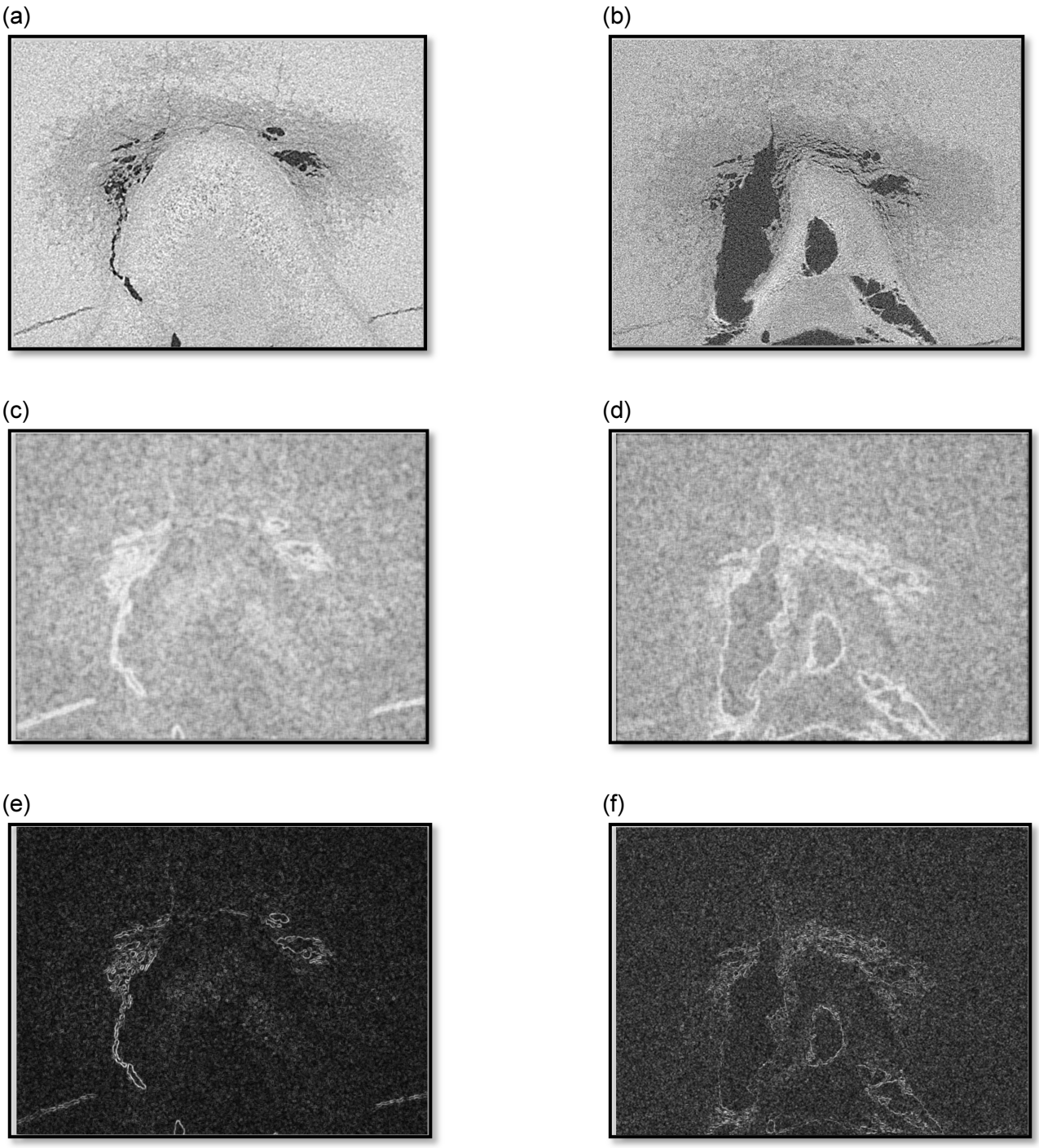

Figure 6.19. (a) T1 raw grey scale tomogram and (b) t29 raw grey scale tomogram both used to calculate (c) Entropy image of t1 and (d) entropy image of t29. (e) Standard deviation image of t1 and (f) standard deviation image of t29. Both original images were taken at slice 35 of the respective time point stacks.

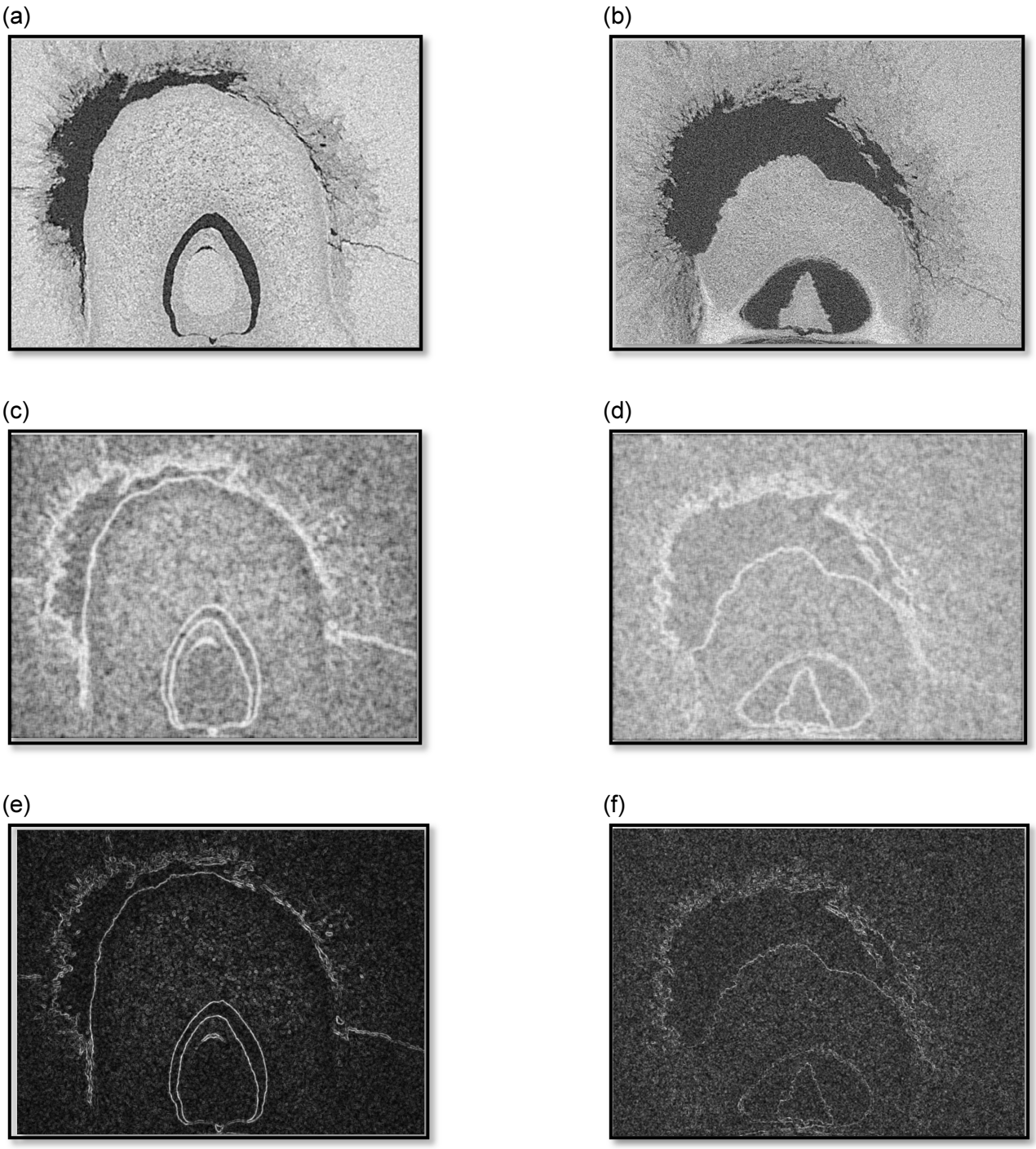

Figure 6.20. (a) T1 raw grey scale tomogram and (b) t29 raw grey scale tomogram both used to calculate (c) Entropy image of t1 and (d) entropy image of t29. (e) Standard deviation image of t1 and (f) standard deviation image of t29. Both original images were taken at slice 70 of the respective time point stacks.

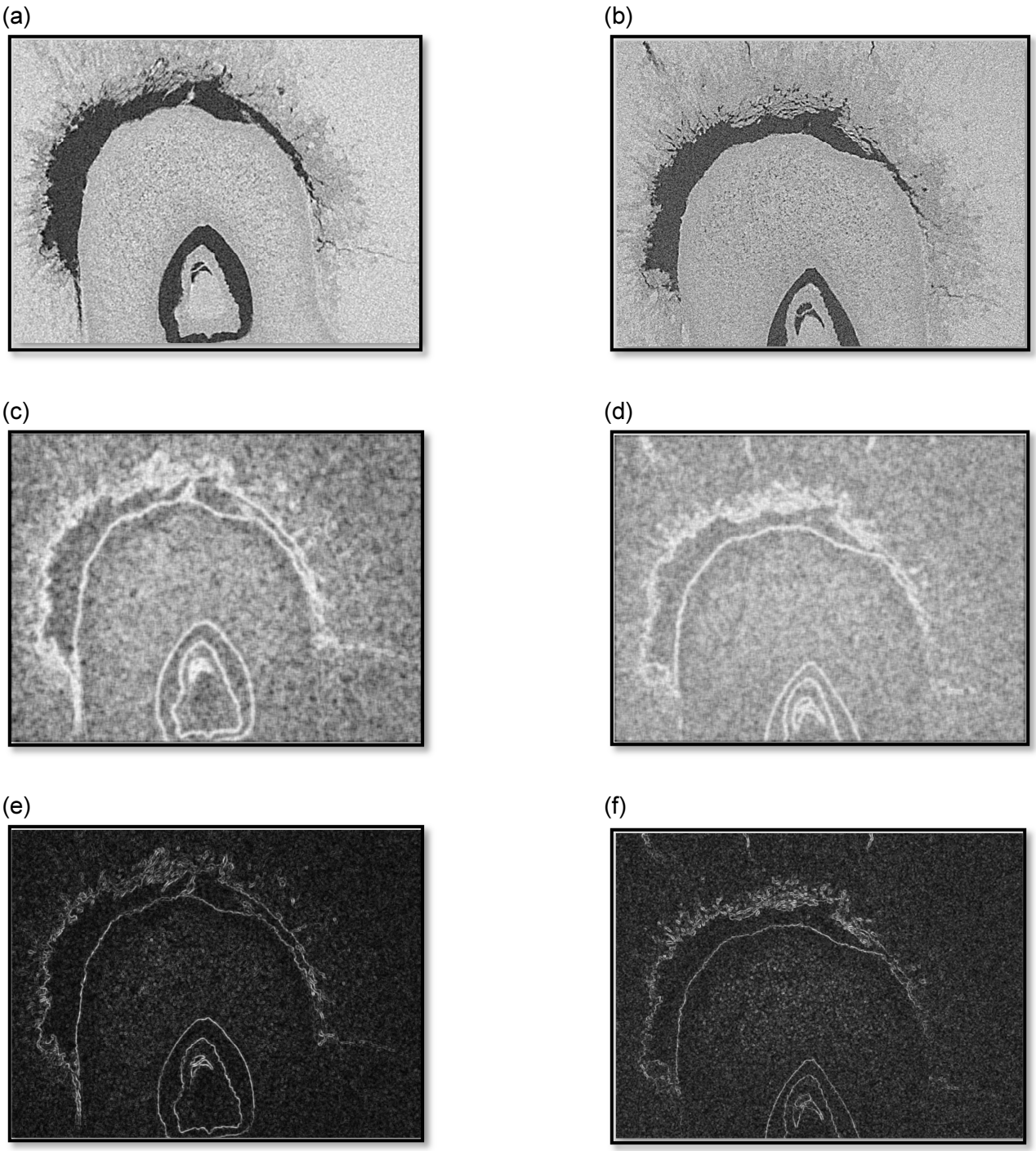

Figure 6.21. (a) T6 raw grey scale tomogram and (b) t11 raw grey scale tomogram both used to calculate (c) Entropy image of t6 and (d) entropy image of t11. (e) Standard deviation image of t6 and (f) standard deviation image of t11. Both original images were taken at slice 70 of the respective time point stacks.

Texture analysis using grey level co-occurrence matrices and principal component analysis

The output of the texture analyses of the 10 GLCMs, one for each time point with 70 images each, yielded a 700 x 4 data set used as the input for PCA. Figure 6.22 illustrates the achieved unsupervised classification of the image slices for all the time points in the score space of PCA. There are two clear groups (encircled in Fig. 6.22) with a clear separation along PC1 (92.61% sum of squares (SS)). The group labelled A corresponds to the time points t1, t6 and t7. The other group (B) was associated with the remaining time points. This was a distinct separation based on

time post inoculation, thus a differentiation between non-infected and infected regions. It was shown in Chapter 3 of this dissertation (Williams *et al.*, 2012) that chemical differences on maize kernels inoculated with *F. verticillioides* were apparent after 17 h post inoculation. Based on the chemical differences it was unlikely that, at this stage, the fungus had gained entry into the kernel and thus it was not be possible to observe any structural damage. In the case where X-rays were used variations in density were observed. Unless the kernel was damaged, it was unlikely that the fungus would have gained entry to the kernel at this early stage and cause internal structural damage. The direction of separation was dominated by principal component (PC) 1 (Fig. 6.23). This plot illustrates the variables in the PC loading space. These are the weights or influence of the variables found on the first two PCs. These reveal which variables are responsible for the patterns observed in the score space. It is clear that the variable responsible for the clustering along PC1 was contrast. The group labelled B had higher contrast values than those in A. It was clear that PCA was successful in finding the direction of maximum variation, thus making a simple distinction between infected and non-infected regions possible.

Contrast measures the spatial frequency of an image and is the difference moment of the GLCM (Gadkari, 2004). It is the difference between the highest and the lowest values of a contiguous set of pixels and it measures the amount of local variations present in the image (Haralick *et al.*, 1973). Group B had more local variation than group A. Therefore group B had a higher frequency of high and low grey levels than group A. The increased variation could be due to the increasing presence of voids and airspaces because of the destruction caused by the fungi. The breakdown of the germ and endosperm leads to structural instability and a softening of this region resulting in less X-ray attenuation and this equates to lower grey level values in the tomograms. It could also be observed from the loading plot (Fig. 6.23) that contrast, homogeneity and energy are negatively correlated. Homogeneity is also known as the inverse difference moment and is inversely correlated to contrast (Gadkari, 2004). It returns a value that measures the closeness of the distribution of elements in the GLCM to the GLCM diagonal. The diagonal elements all represent pixel pairs with no grey level difference. If there are high probabilities in these elements, then the image does not show much contrast: most pixels are identical to their neighbours. Energy is also called angular second-moment (ASM) and is a measure of the homogeneity of the image (Haralick et al., 1973). Energy values close to or equal to 1 indicates a homogenous image. Thus the grey level distribution is constant across the image. The negative correlation of contrast and homogeneity was reported by (Gadkari, 2004), and this correlation was also found in this study (Fig. 6.23). The relationship between the variables and the samples is easily illustrated in a PCA bi-plot (Fig. 6.24). The bi-plot allows one to visualize the magnitude and direction of each variable's contribution to the first two principal components, and how each observation is represented in terms of those components.

The grouping of the clusters in Fig. 6.23 was so extreme that it concealed the patterns, if any, in the individual groups. It thus was decided to calculate PCA on only one group at a time to

determine whether similar patterns existed. Figure 6.25 depicts the PC score plot of PC1 vs. PC3 after group A had been removed. There was a subtle separation along PC1 where the time points were grouped in ascending order of time post-inoculation from left to right i.e. from t11 to t25. Although this separation was not well-defined it was evident that a gradient existed from left to right along PC1. From the loadings plot in (Fig. 6.26) it could be seen that the correlation textural feature was the variable contributing to the distribution along PC1. Correlation is a measure of the grey tone linear-dependencies in the image (Haralick et al., 1973): how correlated a pixel is to its neighbour over the whole image. Thus from the data there was a change in correlation the longer the kernel was exposed to the fungi. Neighbouring pixels in these time points were more correlated with each other, and became more correlated with time. This means there were more consistent grey tone values or pixels with similar grey tone values at these time points, along the direction the GLCM was calculated. The angle chosen to extract the textural features was 0° or an East-West direction. This was chosen as such as it was the direction in which most of the changes could be observed.

As the fungus caused damage in the germ and endosperm region, this affected the ability of the starch to attenuate the X-rays leading to a change in grey tone values. There were inconsistencies observed within the time points as the slices at either end of the sampled region (Fig. 6.2) differed. When PCA was recalculated for group A, a similar trend was observed in the score plot (Fig. 6.27). A division between the time points could be seen in the direction of PC1. This was found to be due to the correlation textural feature (Fig. 6.28). Within in each group there were differences in contrast, however the variation between the two groups was greater than the variance within each group. This resulted in the data in Fig. 6.22 concealing the within group variation. Still, it was possible to distinguish between the time points based on their texture features.

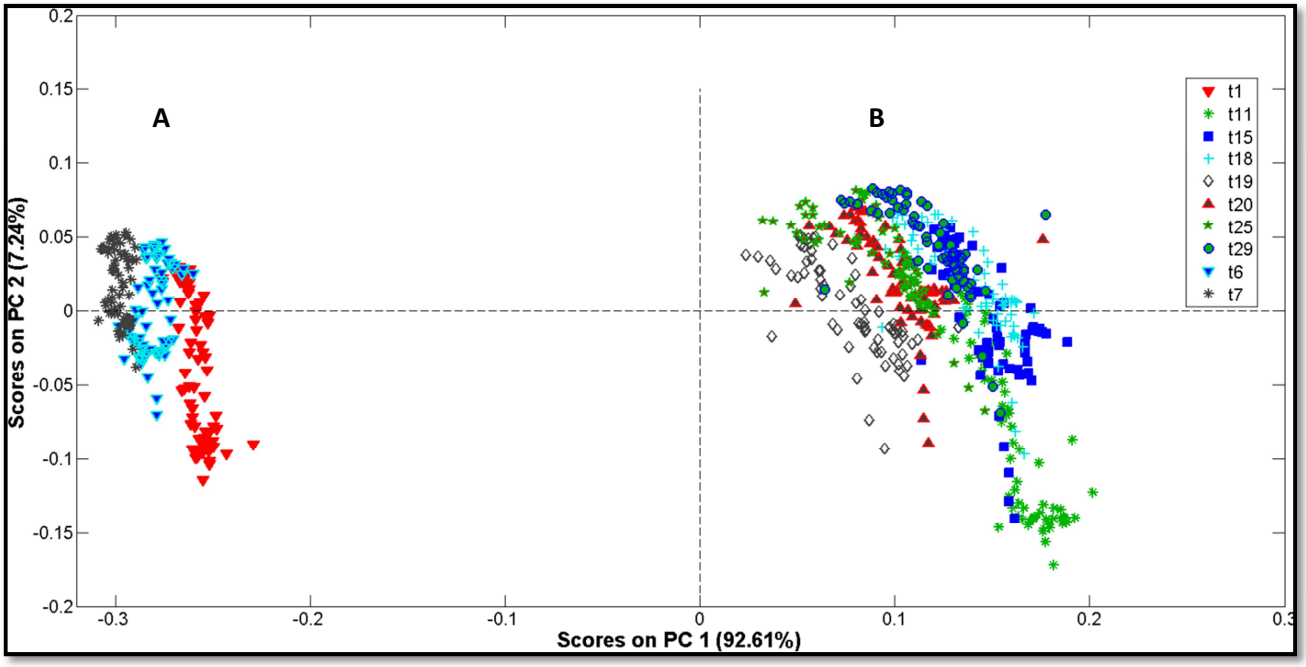

Figure 6.22. PCA scores plot of PC1 vs. PC2 for all time points with the extracted textural features as input. Encircled regions correspond with duration post-inoculation, where A is t1, t6 and t7 and B t11-t29.

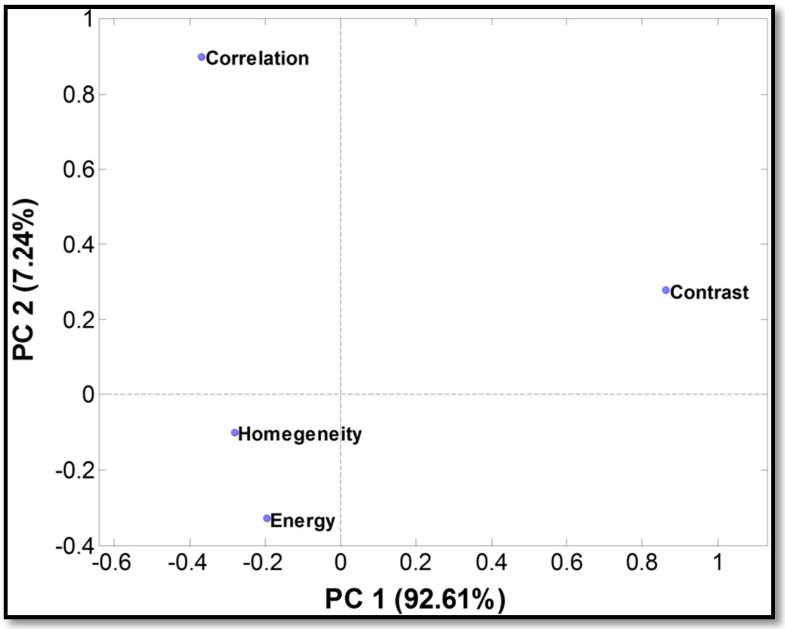

Figure 6.23. PC loading plot of PC1 vs. PC2 illustrating components describing the direction associated with the textural descriptors.

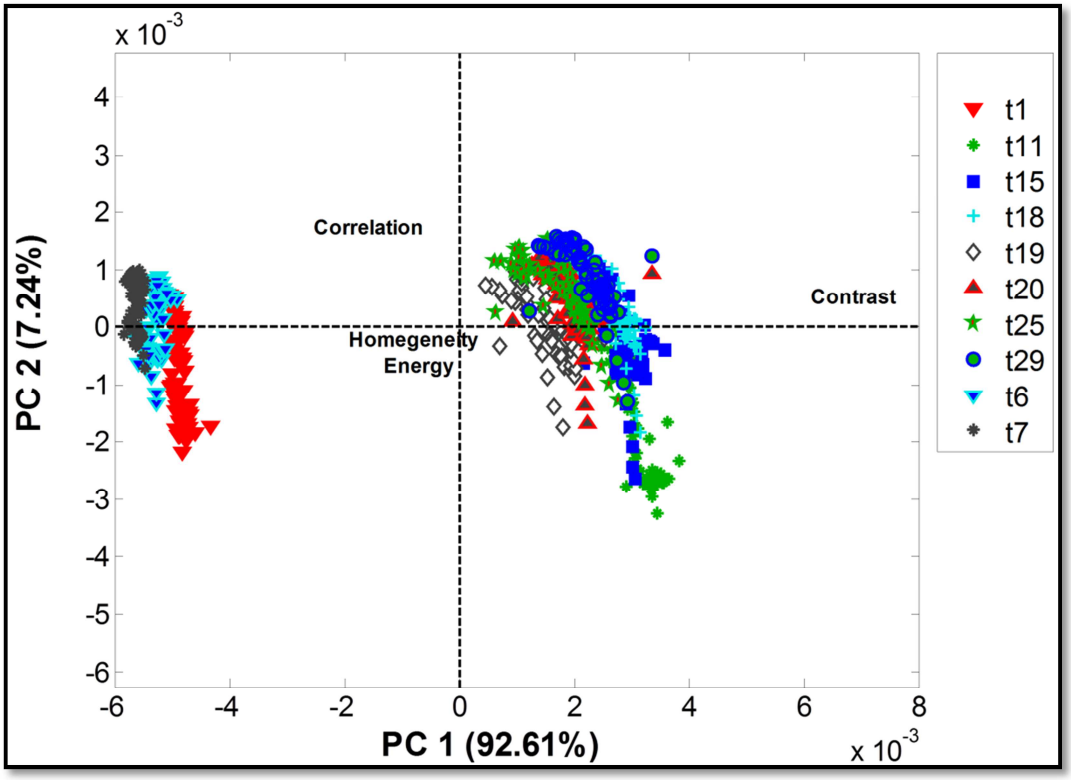

Figure 6.24. Bi-plot showing the magnitude and direction of each variable's contribution to the first two principal components, and how each observation is represented in terms of those components.

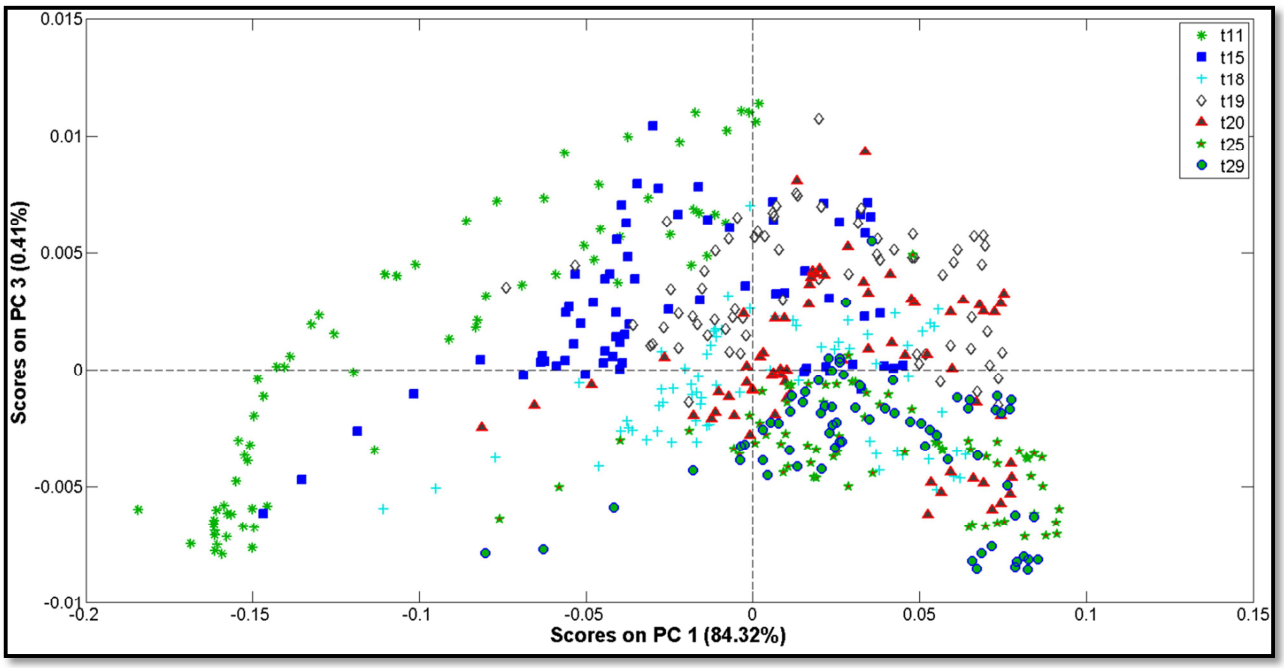

Figure 6.25. PCA scores plot of PC1 vs. PC3 for only t11-t29.

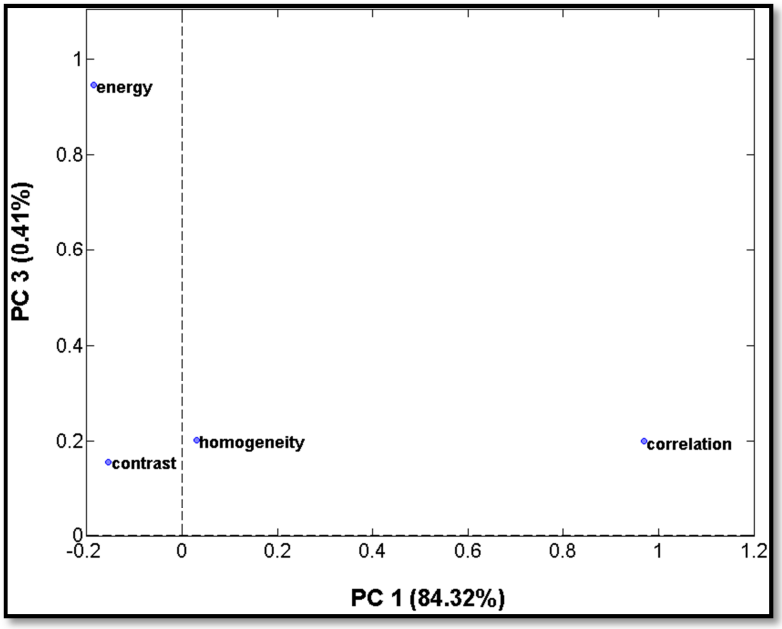

Figure 6.26. PC loading plot of PC1 vs. PC3 illustrating components describing the direction associated with the textural descriptors for group B.

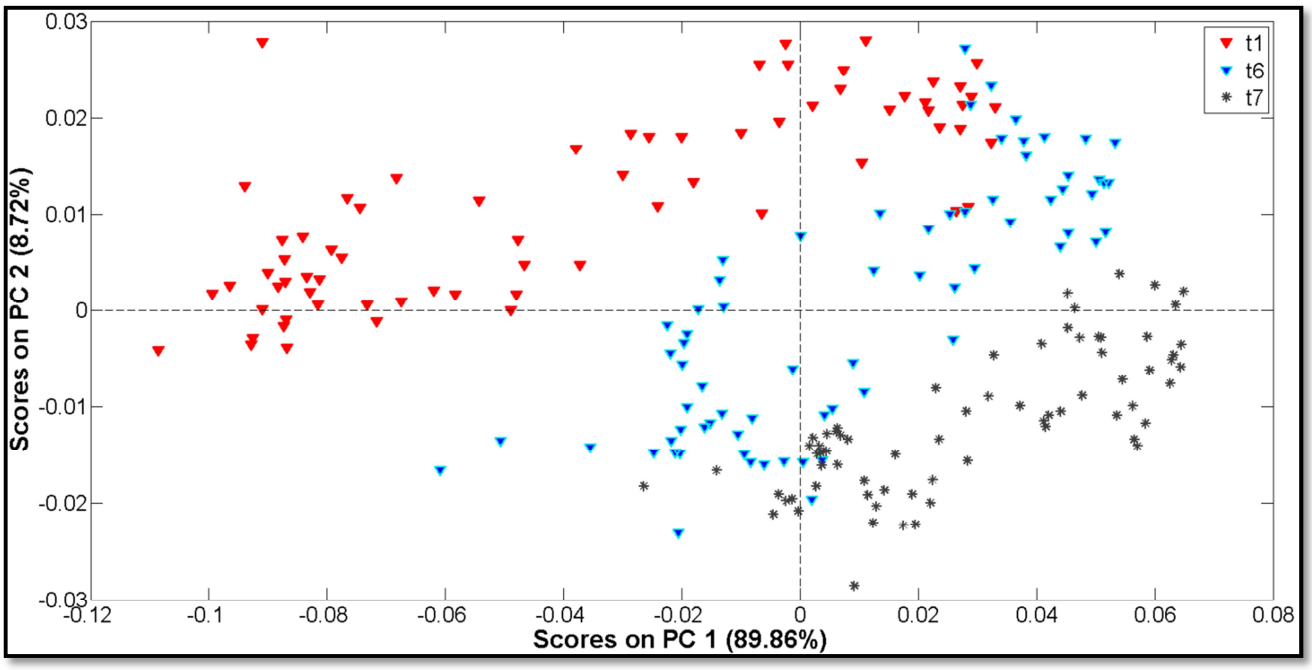

Figure 6.27. PCA scores plot of group A as illustrated in Fig.6.22, showing separation in the direction of PC1.

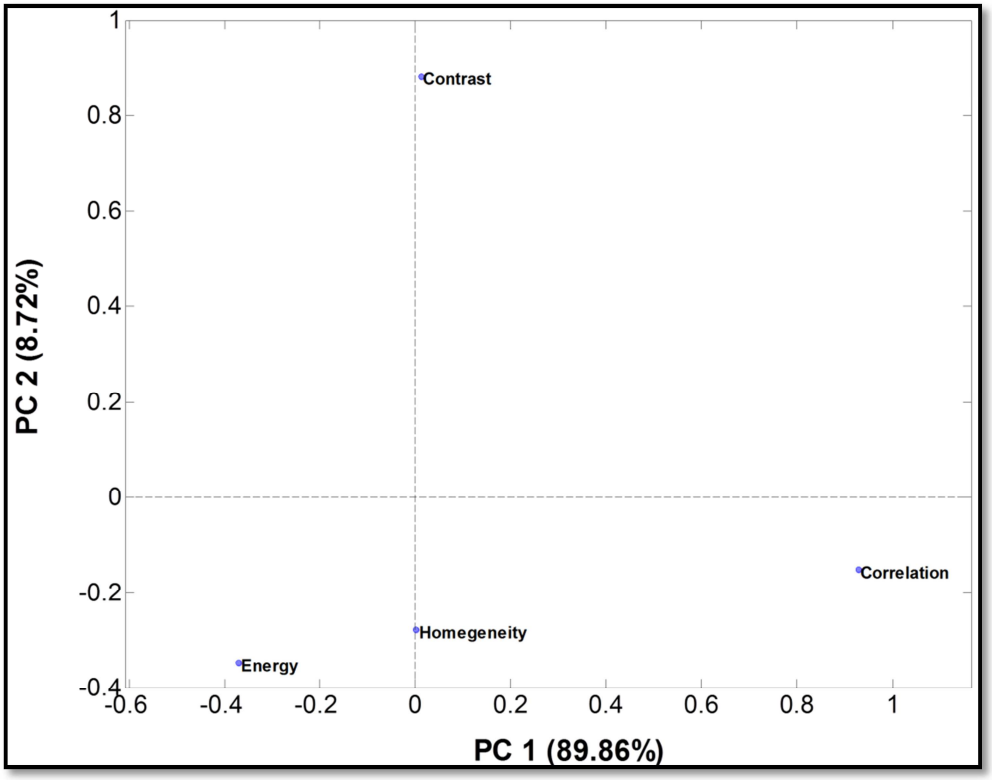

Figure 6.28. PC loading plot of PC1 vs. PC2 illustrating components describing the direction associated with the textural descriptors for group A.

Conclusion

In this study where high resolution X-ray micro-computed tomography was applied, it was possible to study the internal damage caused by *Fusarium verticillioides* in maize kernels over time through a series of 3D tomography scans repeatedly. A combination of conventional image analysis, GLCMs and texture features and multivariate techniques made the interpretation of this data possible. Although distinct visible changes were apparent, the challenge to find techniques to quantify this variation was successful. Physical changes in the kernels, over time, could already be observed in the 2D X-ray images, and were further confirmed in the tomograms, histogram and texture analyses. The physical damage to the germ and endosperm of the maize kernel, affected the integrity and physical texture of this region. These all contributed to the ability of this material to attenuate X-rays. With time this weakening of the material attenuated the X-rays less resulting in the changes observed. Image texture is an important feature that allows for discrimination of seemingly similar regions in images based on arrangement and frequency of grey tone values. This could be successfully used to distinguish between infected and non-infected regions overtime. PCA was crucial in understanding the relationship between the extracted textural descriptors and the ROIs, and how this changed with time.

It was shown that high resolution X-ray micro-computed tomography is a powerful analytical technique for studying the microstructure of food and agricultural produce and is being increasingly used as a research tool. It permits the study of fine detail of samples in high resolution. Practically

it would be ideal to use 2D X-ray imaging techniques in the food industry because it is rapid and analyses can be done in real-time.

References

Bacon, C.W., Bennett, R.M., Hinton, D.M. & Voss, K.A. (1992). Scanning electron microscopy of *Fusarium moniliforme* within asymptomatic corn kernels and kernels associated with leukoencephalomalacia. *Plant Disease*, **76**, 144-148.

Bacon, C.W., Glenn, A.E. & Yates, I.E. (2008). *Fusarium verticillioides*: managing the endophytic association with maize for reduced fumonisins accumulation. *Toxin Reviews*, **27**, 411-446.

Bacon, C.W., Hinton, D.M. & Richardson, M.D. (1994). A corn seedling assay for resistance to *Fusarium moniliforme*. *Plant Disease*, **78**, 302-305.

Bharati, M.H., Liu, J.J. & MacGregor, J.F. (2004). Image texture analysis: methods and comparisons. *Chemometrics and Intelligent Laboratory Systems*, **72**, 57-71.

Boyacioglu, D. & Hettiarachchy, N.S. (1995). Changes in some biochemical components of wheat grain that was infected with *Fusarium graminearum*. *Journal of Cereal Science*, **21**, 57-62.

Bull, C.R., Zwiggelaar, R. & Speller, R.D. (1997). Review of inspection techniques based on the elastic and inelastic scattering of X-rays and their potential in the food and agricultural industry. *Journal of Food Engineering*, **33**, 167-179.

Castells, M., Marín, S., Sanchis, V. & Ramos, A.J. (2008). Distribution of fumonisins and aflatoxins in corn fractions during industrial cornflake processing. *International Journal of Food Microbiology*, **123**, 81-87.

Chang, C. (1988). Measuring density and porosity of grain kernels using a gas pycnometer. *Cereal Chemistry*, **65**, 13-15.

Cleveland, T.E., Hussey, D.S., Chen, Z.Y., Jacobson, D.L., Brown, R.L., Carter-Wientjes, C., Cleveland, T.E. & Arif, M. (2008). The use of neutron tomography for the structural analysis of corn kernels. *Journal of Cereal Science*, **48**, 517-525.

Del Fiore, A., Reverberi, M., Ricelli, A., Pinzari, F., Serranti, S., Fabbri, A.A., Bonifazi, G. & Fanelli, C. (2010). Early detection of toxigenic fungi on maize by hyperspectral imaging analysis. *International Journal of Food Microbiology*, **144**, 64-71.

Duncan, K.E. & Howard, R.J. (2010). Biology of maize kernel infection by *Fusarium verticillioides*. *Molecular Plant-Microbe Interactions*, **23**, 6-16.

Frisullo, P., Laverse, J., Marino, R. & Nobile, M.A.D. (2009). X-ray computed tomography to study processed meat microstructure. *Journal of Food Engineering*, **94**, 283-289.

Frisullo, P., Marino, R., Laverse, J., Albenzio, M. & Del Nobile, M.A. (2010). Assessment of intramuscular fat level and distribution in beef muscles using X-ray microcomputed tomography. *Meat Science*, **85**, 250-255.

Gadkari, D. (2004). *Image quality analysis using GLCM*. *MSc in Modeling and Simulation*. University of Central Florida, Orlando, Florida, USA.

Haff, R. & Toyofuku, N. (2008). X-ray detection of defects and contaminants in the food industry. *Sensing and Instrumentation for Food Quality and Safety*, **2**, 262-273.

Halefoglu, A.M., Bas, N., Yasar, A. & Basak, M. (2010). Differentiation of adrenal adenomas from nonadenomas using CT histogram analysis method: A prospective study. *European Journal of Radiology*, **73**, 643-651.

Haralick, R.M., Shanmugam, K. & Dinstein, I.H. (1973). Textural features for image classification. *IEEE Transactions on Systems, Man and Cybernetics*, **3**, 610-621.

Helgason, S. (1999). *The radon transform.* Pp. 188. Birkhäuser Boston.

Hesseltine, C.W. & Shotwell, O. (1973). New methods for rapid detection of aflatoxin. *Pure and Applied Chemistry*, **35**, 259-266.

Jacobs, P., Sevens, E. & Kunnen, M. (1995). Principles of computerised X-ray tomography and applications to building materials. *Science of the Total Environment*, **167**, 161-170.

Kak, A.C. & Slaney, M. (1988). *Computerized tomographic imaging.* Pp. 344. New York: The Institute of Electrical and Electronics Engineers, Inc.

Kalender, W.A. (2006). X-ray computed tomography. *Physics in Medicine and Biology*, **51**, R29.

Karunakaran, C., Jayas, D.S. & White, N.D.G. (2004a). Detection of internal wheat seed infestation by *Rhyzopertha dominica* using X-ray imaging. *Journal of Stored Products Research*, **40**, 507-516.

Karunakaran, C., Jayas, D.S. & White, N.D.G. (2004b). Identification of wheat kernels damaged by the red flour beetle using X-ray images. *Biosystems Engineering*, **87**, 267-274.

Kotwaliwale, N., Singh, K., Kalne, A., Jha, S.N., Seth, N. & Kar, A. (2011). X-ray imaging methods for internal quality evaluation of agricultural produce. *Journal of Food Science and Technology*, http://dx.doi.org/10.1007/s13197-13011-10485-y.

Laverse, J., Mastromatteo, M., Frisullo, P. & Del Nobile, M.A. (2012). X-ray microtomography to study the microstructure of mayonnaise. *Journal of Food Engineering*, **108**, 225-231.

Lillehoj, E., Kwolek, W., Peterson, R., Shotwell, O. & Hesseltine, C. (1976). Aflatoxin contamination, fluorescence, and insect damage in corn infected with *Aspergillus flavus* before harvest. *Cereal Chemistry*, **53**, 505-512.

Medina-Martinez, M.S. & Martinez, A.J. (2000). Mold occurrence and aflatoxin B1 and fumonisin B1 determination in corn samples in Venezuela. *Journal of Agricultural and Food Chemistry*, **48**, 2833-2836.

Munkvold, G.P. (2003). Epidemiology of *Fusarium* diseases and their mycotoxins in maize ears. *European Journal of Plant Pathology*, **109**, 705-713.

Muthomi, J.W., Ndung'u, J.K., Gathumbi, J.K., Mutitu, E.W. & Wagacha, J.M. (2008). The occurrence of *Fusarium* species and mycotoxins in Kenyan wheat. *Crop Protection*, **27**, 1215-1219.

Narvankar, D.S., Singh, C.B., Jayas, D.S. & White, N.D.G. (2009). Assessment of soft X-ray imaging for detection of fungal infection in wheat. *Biosystems Engineering*, **103**, 49-56.

Neethirajan, S., Jayas, D.S. & White, N.D.G. (2007). Detection of sprouted wheat kernels using soft X-ray image analysis. *Journal of Food Engineering*, **81**, 509-513.

Neethirajan, S., Karunakaran, C., Jayas, D.S. & White, N.D.G. (2006). X-ray computed tomography image analysis to explain the airflow resistance differences in grain bulks. *Biosystems Engineering*, **94**, 545-555.

Paepens, C., Saeger, S.D., Sibanda, L., Barna-Vetró, I., Léglise, I., Van Hove, F. & Peteghem, C.V. (2004). A flow-through enzyme immunoassay for the screening of fumonisins in maize. *Analytica Chimica Acta*, **523**, 229-235.

Pittia, P., Sacchetti, G., Mancini, L., Voltolini, M., Sodini, N., Tromba, G. & Zanini, F. (2011). Evaluation of microstructural properties of coffee beans by synchrotron X-Ray microtomography: a methodological approach. *Journal of Food Science*, **76**, 222-231.

Sydenham, E.W., Shephard, G.S., Thiel, P.G., Bird, C. & Miller, B.M. (1996). Determination of fumonisins in corn: evaluation of competitive immunoassay and HPLC techniques. *Journal of Agricultural and Food Chemistry*, **44**, 159-164.

Thomas, P., Kannan, A., Degwekar, V.H. & Ramamurthy, M.S. (1995). Non-destructive detection of seed weevil-infested mango fruits by X-ray imaging. *Postharvest Biology and Technology*, **5**, 161-165.

Thum, C. (1983). Hybrid measurements of image histograms, with an application to texture discrimination. *Optica Acta: International Journal of Optics*, **30**, 1665-1673.

Thum, C. (1984). Measurement of the entropy of an image with application to image focusing. *Optica Acta: International Journal of Optics*, **31**, 203-211.

Tournier, C., Grass, M., Zope, D., Salles, C. & Bertrand, D. (2012). Characterization of bread breakdown during mastication by image texture analysis. *Journal of Food Engineering*, **113**, 615-622.

Tuceryan, M. & Jain, A.K. (1993). Texture analysis. In: *Handbook of pattern recognition and computer vision* (edited by C.H. Chen, L.F. Pau & P.S.P. Wang). Pp. 235-276. World Scientific Publishing Company.

Umbaugh, S.E. (2011a). *Digital image processing and analysis: human and computer vision applications with CVIPtools.* Pp. 456-463. Boca Raton: CRC Press.

Umbaugh, S.E. (2011b). *Digital image processing and analysis: human and computer vision applications with CVIPtools.* Pp. 105-107. Boca Raton: CRC Press.

Vij, K. & Singh, Y. (2009). Enhancement of images using histogram processing techniques. *International Journal of Computer Technology and Applications*, **2**, 309-313.

Williams, P.J., Geladi, P., Britz, T.J. & Manley, M. (2012). Investigation of fungal development in maize kernels using NIR hyperspectral imaging and multivariate data analysis. *Journal of Cereal Science*, **55**, 272-278.

Zwiggelaar, R., Bull, C.R. & Mooney, M.J. (1996). X-ray simulations for imaging applications in the agricultural and food industries. *Journal of Agricultural Engineering Research*, **63**, 161-170.

CHAPTER 7
GENERAL DISCUSSION AND CONCLUSIONS

Maize (*Zea mays* L.) is used for human and animal consumption in diverse forms, from specialised foods in developed countries, to staple food in developing countries. Maize is prone to infection by *Fusarium verticillioides, F. proliferatum* and *F. subglutinans* and their presence is associated with the high incidence of mycotoxins, specifically fumonisins that have cancer-promoting activity (Gelderblom *et al.*, 1988; Rheeder *et al.*, 2002). If the fungal contamination of maize plants and kernels is not detected early on, contamination in the form of mycotoxins can enter the food chain. *Fusarium* mycotoxins are a relevant problem in the cereal supply chain (Bergamini *et al.*, 2010) and are known to be carcinogenic to humans. *Fusarium verticillioides* is capable of asymptomatic infection, where infected kernels show no sign of fungal growth, but may be contaminated with fumonisins. Rapid and accurate methods are required to detect, identify and distinguish between pathogens to enable swift decisions regarding the fate of a batch or consignment of cereal.

In this study near infrared (NIR) hyperspectral imaging and high resolution X-ray micro-computed tomography (µCT) combined with statistical and multivariate image analysis (MIA) was used to study *Fusarium* infection in maize. The data from this study clearly showed that it was possible to monitor development of fungal growth in infected maize kernels over time using NIR hyperspectral imaging and MIA. A key discovery was that discrimination between the images of the control kernels (sterilised with no inoculation) and the images of the inoculated kernels was possible even before visual symptoms of infection appeared (20 h after inoculation). Wavelength variables that were used to show variation were: 1405 nm (associated with starch); 1660-1668 nm (associated with an aromatic structure); 1900 nm (associated with starch); and 2136 nm (associated with protein). These were attributed to the activity of the germinating fungal spores beneath and on the surface of the maize kernels. It was thus possible to detect early infection of maize kernels and prevent infected grains from entering the food chain.

Once fungal contamination has been detected it is important to identify the *Fusarium* species present. Presently grains are evaluated microbiologically which involves plating out on appropriate growth medium prior to further analyses. The conventional methods for enumeration and identification of moulds/fungi to the species level can take as long as two weeks. These methods are: time-consuming; destructive; require specialised growth media and tedious sample preparation; as well as staining and inspection using microscopy.

On growth media the organisms that commonly contaminate maize have a similar colonial appearance and are difficult to differentiate, especially to the untrained eye. Being able to distinguish between these three fungi is crucial since *F. verticillioides* and *F. proliferatum* are prolific producers of fumonisin while *F. subglutinans* produces far less (Munkvold & Desjardins, 1997). In this study the three *Fusarium* spp. could be discriminated with reasonable accuracy by

NIR hyperspectral imaging and the use of test sets. For *F. subglutinans*, 78–100% pixels were correctly predicted depending on the training and test sets used. Similarly, the percentage correctly predicted pixels of *F. proliferatum* were 60–80%. *Fusarium verticillioides* had the least correctly predicted pixels (16-47%). The poorer prediction for *F. verticillioides* could be due to the culture having lost its virulence because of repeated culturing under laboratory conditions.

It was also observed that when including different strains in the training set, identification in principal component (PC) score images was complicated. This complication was enhanced due to the presence of clear radial growth rings, with older growth in the centre and younger growth on the periphery of mycelium. This led to a number of questions: what happens when the fungi grow on growth medium? What were the growth rings and why were they different in the PC score images?

It is known that colonies of filamentous fungi growing on solid media spread outwards at a constant rate, radially (Pirt, 1967). With the use of cytochemical analyses Yanagita and Kogané (1962) showed that these radial rings are growth zones differing in composition, function and structure. NIR hyperspectral imaging and MIA techniques made visualisation of the radial growth rings possible by studying the mycelial growth of the three *Fusarium* spp. on solid medium over time. As these zones differed chemically, it was possible to make a distinction between them in the PC score images. Three prominent bands at 1166, 1380 and 1918 nm (protein) were found, and these were considered to be responsible for the differences between the growth zones. Variations in the bands at 1166 and 1380 nm were correlated with the depletion of carbohydrates as the fungus grew while the band at 1918 nm was a possible indication of spore and new mycelial formation. The growth rings were thus shown to be zones at different stages of maturity, and they differed in the PC score images because they varied chemically.

It is well known that bacterial and fungal colonies exhibit exponential growth. Constructing growth curves are painstaking and time-consuming, but by integrating images of whole mycelium as the sum of pixels over time, it was possible to construct curves that resembled microbial growth profiles. Despite a lack of data points at certain time intervals, an approximation of fungal growth was shown and these curves compared well with those obtained using conventional microbiological techniques.

By plotting the pixels from the individual growth zones as a function of time, it was possible to study the growth characteristics in more detail. This made it possible to visualise the emergence and interaction of the growth zones as separate growth profiles that would not have been possible with conventional microbiological techniques. This is of value as, with the use of NIR hyperspectral imaging and MIA techniques, fungal growth characteristics can be studied in a more constructive manner.

It was also shown that with NIR hyperspectral imaging, chemical changes on and just beneath the surface of maize kernels, infected with *F. verticillioides,* were observed. The biology of maize kernel infection by *F. verticillioides* was recently characterised using scanning electron microscopy

and transmission electron microscopy (Duncan & Howard, 2010). They reported that the fungus enters the kernel and spreads extracellularly, passes into the pericarp and fills the mesocarp cells. This was followed by extensive dissolution of the thick pericarp cell walls. These chemical changes were most likely what was detected when using NIR hyperspectral imaging. However, it was not possible to visualise the physical changes within the maize kernels with NIR hyperspectral imaging.

NIR hyperspectral imaging gives chemical information in two dimensional (2D) images offering only limited information regarding the internal microstructure of a sample. The long, low energy levels of wavelengths (1100-2500 nm) in the NIR region (as used in this study) are thus not adequate to determine changes in the centre of the sample and shorter, high energy wavelengths are required. To visualise the physical changes caused by the fungus inside the kernel, µCT three dimensional (3D) images will be required. X-rays, having a wavelength in the range of 0.01 to 10 nm, should be able to traverse through the samples.

The data obtained by using 3D µCT scans in this study showed that it was possible to visualise the internal damage caused by *F. verticillioides* in maize kernels over. The fungal degradation affected the integrity of the maize kernel and this was particularly prominent in the germ and immediate surroundings. The dissolution of the cell walls affected the overall density of the endosperm and germ regions and was visible with the X-rays. This was observed as the appearance of voids and clear microstructural differences were found between kernels infected for 20 and 596 h, respectively. Although it was not possible to view the presence of the fungi, the damage caused was evident. For all the kernels scanned, the region most affected by the fungus appeared to be in the germ and endosperm nearest to the germ, this is where most of the nutrients are located. The germ is also the gateway to the rest of the kernel, if fungus enters through the stylar canal as proposed by Duncan and Howard (2010). It was reported that the hyphae spread out radially, so when it arrives at a nutrient rich location it proliferates rapidly and spreads more.

In contrast to other techniques, NIR hyperspectral imaging in the 1100-2498 nm spectral range made it possible to detect early *F. verticillioides* infection in maize kernels. This spectral range also allowed for the discrimination of three closely related *Fusarium* species on growth medium. Because these species appear the same on growth media, discrimination would not have been possible within the visible spectrum. It was also shown that kinetic studies could be done in a simpler way and the growth characteristics of the three *Fusarium* species could be studied. Additionally, X-ray computed tomography was used to study the internal damage caused by *F. verticillioides* in individual maize kernels.

NIR hyperspectral imaging offers the ability to rapidly screen cereal grains for fungal infection, preventing contaminated grains from entering the food chain but additional work on the early detection on cereal grains is still required. There have been developments in automated systems for selecting individual kernels based on specific quality characteristics (Dowell *et al.*, 2006). These could be adapted using NIR hyperspectral imaging for detection and removal of infected grains.

For rapid detection, identification, differentiation of pathogens and studying growth, NIR hyperspectral imaging would be an excellent addition to the microbiology laboratory to screen for pathogens. This work should be extended for other fungal species associated with maize, particularly *Aspergillus* which poses problems in tropical climates. In this dissertation the optimal temperature for fungal growth was chosen to be 28°C on potato dextrose agar, so future research should consider other temperatures and growth media. This work has the potential to be extended to detection and identification of bacteria, specifically food-borne pathogens.

Although µCT is a time-consuming technique (ca. an hour to collect an image), high resolution images are acquired non-destructively. It also offers the possibility to explore the reconstructed images, allowing, 3D visualisation of imaged objects. This allows for the study of fine detail of samples in high resolution. It would have been ideal if NIR hyperspectral imaging and µCT was done on the same infected kernels over time. Here too, with µCT, future work should investigate other fungal species associated with maize infection. The applications of this technique are endless.

Imaging techniques are important for rapid, accurate and objective evaluation of products for quality and safety. They offer the ability to visualise information hidden to the naked eye. NIR hyperspectral imaging offers rapid chemical evaluation of samples in 2D images while µCT offers 3D microstructural information. Combining these image techniques added more value and gave a comprehensive evaluation of *Fusarium* infection in maize.

References

Bergamini, E., Catellani, D., Dall'asta, C., Galaverna, G., Dossena, A., Marchelli, R. & Suman, M. (2010). Fate of *Fusarium* mycotoxins in the cereal product supply chain: the deoxynivalenol (DON) case within industrial bread-making technology. *Food Additives and Contaminants Part A*, **27**, 677-687.

Dowell, F., Maghirang, E., Graybosch, R., Baenziger, P., Baltensperger, D. & Hansen, L. (2006). An automated near-infrared system for selecting individual kernels based on specific quality characteristics. *Cereal Chemistry*, **83**, 537-543.

Duncan, K.E. & Howard, R.J. (2010). Biology of maize kernel infection by *Fusarium verticillioides*. *Molecular Plant-Microbe Interactions*, **23**, 6-16.

Gelderblom, W.C.A., Jaskiewicz, K., Marasas, W.F.O., Thiel, P.G., Horak, R.M., Vleggaar, R. & Kriek, N.P.J. (1988). Fumonisins novel mycotoxins with cancer-promoting activity produced by *Fusarium moniliforme*. *Applied and Environmental Microbiology*, **54**, 1806-1811.

Munkvold, G.P. & Desjardins, A.E. (1997). Fumonisins in maize: can we reduce their occurrence? *Plant Disease*, **81**, 556-565.

Pirt, S.J. (1967). A kinetic study of the mode of growth of surface colonies of bacteria and fungi. *Journal of General Microbiology*, **47**, 181-197.

Rheeder, J.P., Marasas, W.F.O. & Vismer, H.F. (2002). Production of fumonisin analogs by *Fusarium* species. *Applied and Environmental Microbiology*, **68**, 2101-2105.

Yanagita, T. & Kogané, F. (1962). Growth and cytochemical differentiation of mold colonies. *The Journal of General and Applied Microbiology*, **8**, 201-213.